

UNIVERSIDADE FEDERAL DO RIO GRANDE DO SUL
INSTITUTO DE GEOCIÊNCIAS
PROGRAMA DE PÓS-GRADUAÇÃO EM GEOCIÊNCIAS

**HETEROGENEIDADE GEOQUÍMICA E ISOTÓPICA
(Sr-Nd-Pb E GASES NOBRES) DO MANTO SUPERIOR
PATAGÔNICO: DEPLEÇÃO E METASSOMATISMO EM
UM AMBIENTE DE *BACK-ARC* CONTINENTAL**

TIAGO LUIS REIS JALOWITZKI

ORIENTADORES:

Prof. Dr. Rommulo Vieira Conceição (UFRGS, Brasil)

Prof. Dr. Yuji Orihashi (Universidade de Tóquio, Japão)

Prof. Dr. Hirochika Sumino (Universidade de Tóquio, Japão)

BANCA EXAMINADORA

Prof. Dr. Edinei Koester - Instituto de Geociências, Universidade Federal do
Rio Grande do Sul (UFRGS)

Profa. Dra. Gabriela Isabel Massaferro - Facultad de Ciencias Naturales,
Universidad Nacional de la Patagonia San Juan Bosco

Prof. Dr. Lauro Valentim Stoll Nardi - Instituto de Geociências, Universidade
Federal do Rio Grande do Sul (UFRGS)

Tese de Doutorado apresentada como
requisito parcial para a obtenção do
Título de Doutor em Ciências.

Porto Alegre - 2015

UNIVERSIDADE FEDERAL DO RIO GRANDE DO SUL
INSTITUTO DE GEOCIÊNCIAS
PROGRAMA DE PÓS-GRADUAÇÃO EM GEOCIÊNCIAS

**HETEROGENEIDADE GEOQUÍMICA E ISOTÓPICA
(Sr-Nd-Pb E GASES NOBRES) DO MANTO SUPERIOR
PATAGÔNICO: DEPLEÇÃO E METASSOMATISMO EM
UM AMBIENTE DE *BACK-ARC* CONTINENTAL**

TIAGO LUIS REIS JALOWITZKI

ORIENTADORES:

Prof. Dr. Rommulo Vieira Conceição (UFRGS, Brasil)

Prof. Dr. Yuji Orihashi (Universidade de Tóquio, Japão)

Prof. Dr. Hirochika Sumino (Universidade de Tóquio, Japão)

Tese de Doutorado apresentada como
requisito parcial para a obtenção do
Título de Doutor em Ciências.

Porto Alegre - 2015

UNIVERSIDADE FEDERAL DO RIO GRANDE DO SUL

Reitor: Carlos Alexandre Netto

Vice-Reitor: Rui Vicente Oppermann

INSTITUTO DE GEOCIÊNCIAS

Diretor: André Sampaio Mexias

Vice-Diretor: Nelson Luiz Sambaqui Gruber

Jalowitzki, Tiago Luís Reis

Heterogeneidade geoquímica e isotópica (Sr-Nd-Pb e gases nobres) do manto superior patagônico: depleção e metassomatismo em um ambiente de back-arc continental . / Tiago Luís Reis Jalowitzki. - Porto Alegre: IGEO/UFRGS, 2015.
[254 f.] il.

Tese (Doutorado).- Universidade Federal do Rio Grande do Sul. Programa de Pós-Graduação em Geociências. Instituto de Geociências. Porto Alegre, RS - BR, 2015.

Orientador(es): Rommulo Vieira Conceição
Coorientador(es): Yuji Orihashi e Hirochika Sumino

1. Heterogeneidade mantélica 2. Xenólitos mantélicos 3. Patagônia
4. Isótopos de Sr-Nd-Pb e gases nobres I. Título.

CDU 55

Catálogo na Publicação

Biblioteca Instituto de Geociências - UFRGS

Veleida Ana Blank

CRB 10/571

*“Now there's a look in your eyes,
like black holes in the sky”*

Roger Waters

AGRADECIMENTOS

Agradeço ao Conselho Nacional de Desenvolvimento Científico e Tecnológico (CNPq) pela concessão do projeto de pesquisa Universal 475990/2004-8, viabilizando a realização de trabalhos de campo na Patagônia Argentina e a geração de análises químicas. Da mesma maneira agradeço ao CNPq pelas bolsas de doutorado no Brasil (GD, processo nº 141188/2010-3) e no Japão (SWE, processo nº 201513/2011-0).

À Universidade Federal do Rio Grande do Sul através do Laboratório de Geologia Isotópica (LGI), Instituto de Geociências, pelas facilidades e infraestrutura oferecidas.

Ao meu orientador, Rommulo Vieira Conceição, que tem sido um importante parceiro durante a minha trajetória acadêmica desde 2003, quando começamos a trabalhar juntos.

Quero fazer um agradecimento especial aos professores Yuji Orihashi, Hirochika Sumino e Keisuke Nagao pelas oportunidades, incentivo e confiança.

Sou extremamente grato por ter ao meu lado a minha esposa Ivana, uma pessoa rara e inspiradora. Amor, obrigado pelo apoio incondicional e pela família linda que tu me deste. A Hana e tu são tudo na minha vida. Aos queridos Hercílio e Vera Figueiredo, que sempre contribuíram para a nossa felicidade.

Da mesma maneira agradeço à minha mãe, Liane, e irmãos, Taís e Tomás, pois “se enxerguei longe, foi porque me apoiei nos ombros de gigantes” (Sir Isaac Newton).

À amizade e apoio recebidos pela querida amiga Fernanda Gervasoni. Obrigado por estar sempre presente!

Agradeço aos colegas e amigos que foram fundamentais na construção da minha vida profissional até o presente momento, a saber: Gustavo Walter Bertotto, Manuel Schilling, Edinei Koester, Mariana Assis, André Abreu Martins, Gisela Raupp, e Natsumi Hokanishi.

Por fim, aos amigos que sempre propiciaram enriquecedoras discussões sobre ciência e vida ao longo dessa jornada. Obrigado, Paulo Cesar, Raphael Morales, Eduardo Fontana, Gustavo Salerno, Iágaro Settin, Cesar Bermudez e Eduardo Balbinot.



Meseta de las Vizcachas, Patagônia, Argentina

Sumário

1. APRESENTAÇÃO	6
2. INTRODUÇÃO	6
3. CARACTERIZAÇÃO DO PROBLEMA	7
4. OBJETIVOS	9
5. ISÓTOPOS DE GASES NOBRES APLICADOS AO ESTUDO DE RESERVATÓRIOS MANTÉLICOS	9
6. CONTEXTO GEOLÓGICO	12
7. MÉTODOS ANALÍTICOS	16
7.1. Amostragem	16
7.2. Preparação de amostras	17
7.2.1. <i>Confecção de lâminas delgadas</i>	17
7.2.2. <i>Rocha total</i>	17
7.3. Petrografia e contagem modal	17
7.4. Geoquímica de rocha total	18
7.5. Datação K-Ar	20
7.6. Sistemas isotópicos Sr-Nd-Pb	21
7.7. Determinação de isótopos de gases nobres	22
8. ANÁLISE INTEGRADORA DOS MANUSCRITOS SUBMETIDOS	26
REFERÊNCIAS	30

RESUMO

A região de *back-arc* continental da Patagônia oferece a oportunidade de estudar a composição do manto terrestre, pois amostras de xenólitos mantélicos trazidas à superfície por lavas basálticas. Ambas fornecem valiosas informações sobre a fonte, bem como dos processos metassomáticos que promovem heterogeneidades geoquímicas e isotópicas no manto subcontinental. Com o objetivo de compreender a gênese e a contribuição de agentes metassomáticos em amostras de xenólitos mantélicos e de basaltos alcalinos, o presente estudo reporta novos dados geoquímicos, idades K-Ar, isótopos de Sr-Nd-Pb e isótopos de gases nobres.

Com base nas composições mineralógicas, geoquímicas e isotópicas (Sr-Nd-Pb), o primeiro manuscrito desta tese propõe dois novos grupos de basaltos datados do Cenozoico com assinatura intraplaca, Grupo I e Grupo II. A área de estudo está amplamente distribuída através do *back-arc* continental da Patagônia. Os basaltos do Grupo I são resultantes de baixos graus de fusão parcial (<3%) a partir de uma fonte astenosférica com flogopita estável na zona de estabilidade de granada-peridotitos (113-134 km) com razões isotópicas de Sr-Nd-Pb representativas de OIB depletado. Essas características sugerem que o vulcanismo intraplaca tem relação com anomalias composicionais (“*wetspots*”), o que poderia estar relacionado a uma anomalia térmica abaixo da Patagônia ($T_P = 1400-1563^\circ\text{C}$). Por outro lado, sugerimos que a fusão parcial (5-10%) de veios piroxeníticos próximos ao limite litosfera-astenosfera (89-94 km) foram capazes de produzir as características geoquímicas e isotópicas de manto enriquecido (EMI) observadas nos basaltos do Grupo II sem a influência de anomalia térmica ($T_P = 1305-1364^\circ\text{C}$). Em geral, a quantidade de componentes derivados da placa diminui em direção à leste, refletindo variação geoquímica a partir da distância do arco vulcânico.

O segundo manuscrito apresenta novos dados geoquímicos e isotópicos (Sr-Nd-Pb) de amostras de espinélio-lherzolitos e de seus basaltos hospedeiros. A área de estudo é representada por um fluxo de lava próximo à cidade de Coyhaique, *back-arc* chileno. Essa ocorrência é uma das mais próximas da margem convergente, estando a ~320 km da fossa do Chile. A idade K-Ar obtida para as amostras do basalto hospedeiro são de 54 Ma. Com base nos dados geoquímicos e isotópicos, esse basalto alcalino apresenta assinatura do tipo OIB (OIB-like), foi gerado a partir de baixos graus de fusão parcial (até 6%) dentro do campo de estabilidade da granada e, provavelmente, é o resultado da ressurgência astenosférica através da abertura de uma janela astenosférica como consequência da subducção da dorsal de Farallón-Aluk. Os

espinélio-lherzolitos mostram características marcantes de metassomatismo relacionado à zona de subducção, tais como pronunciadas anomalias negativas de Nb-Ta-Ti. No entanto, com base nos dados geoquímicos e isotópicos, essas rochas requerem um SCLM heterogêneo, resultante da mistura entre um componente depletado (DMM ou PREMA) e até 15% de componentes derivados da placa oceânica de Aluk. O agente metassomatizante é representado por diferentes proporções de líquidos resultantes da fusão de sedimentos da fossa do Chile (até 60%) e de uma crosta oceânica modificada (mais de 40%).

Por fim, o terceiro manuscrito é baseado em composições inéditas de gases nobres e em novas razões isotópicas de Sr-Nd-Pb de xenólitos mantélicos do Campo Vulcânico de Pali-Aike e de Gobernador Gregores. Os dados isotópicos de gases nobres indicam que o SCLM patagônico reflete a mistura entre o ar e dois membros finais mantélicos. Os peridotitos de Pali-Aike representam o SCLM desgaseificado e intrínseco com assinatura fortemente radiogênica/nucleogênica, como mostrado pelas elevadas razões de $^4\text{He}/^3\text{He}$, $^{21}\text{Ne}/^{22}\text{Ne}$, e $^{40}\text{Ar}/^{36}\text{Ar}$ comparadas à fonte de MORB. Em relação aos componentes mantélicos, os peridotitos de Gobernador Gregores representam uma mistura entre o SCLM (Pali-Aike) e o MORB. O metassomatismo de um componente do tipo MORB pode ser observado através das composições isotópicas de He e Ne, podendo ser tectonicamente explicado pela ressurgência do manto astenosférico em resposta à abertura de uma janela astenosférica abaixo da Patagônia como consequência da subducção da dorsal do Chile. Adicionalmente, essas rochas mostram composições depletadas de Sr-Nd-Pb e uma idade de $13,64 \pm 0,83$ Ma foi obtida através de uma isócrona de Rb-Sr baseada na composição isotópica da rocha-total, clinopiroxênio e flogopita. Esses dados representam a idade de formação da flogopita, que é um mineral essencial para determinar a idade do metassomatismo e sua potencial associação com eventos geotectônicos. Sendo assim, é possível relacionar a formação desse mineral com a colisão da dorsal do Chile contra a fossa do Chile e a subsequente abertura da janela astenosférica.

ABSTRACT

Patagonian continental back-arc offers the opportunity to study the mantle composition because of mantle xenoliths brought to the surface by basaltic lavas. Both provide valuable information about the mantle source, as well as metasomatic processes that promote geochemical and isotopic heterogeneities in the subcontinental mantle. In order to understand the mantle source and contribution of metasomatic agents in samples of mantle xenoliths and alkaline basalts, this study reports new geochemical data, K-Ar ages, Sr-Nd-Pb isotopes and noble gas isotopes.

Based on mineralogical, geochemical and Sr-Nd-Pb isotope compositions, the first manuscript of this thesis suggests two new groups of Cenozoic Patagonian basalts with intraplate signatures, Group I and Group II. The studied area is widely distributed through Patagonian continental *back-arc*. Group I basalts results from small degrees of partial melting (<3%) of a phlogopite-bearing garnet peridotite mantle source at asthenospheric depths (113-134 km) with Sr-Nd-Pb isotopic ratios that represent a depleted OIB-like component. These features suggest a relation between intraplate volcanism and compositional anomalies (“wetspot”), which could be related to a thermal anomaly beneath Patagonia ($T_P = 1400-1563^\circ\text{C}$). On the other hand, partial melting (5-10%) of pyroxenite veins close to the lithosphere-asthenosphere boundary (89-94 km) were capable to produce the geochemical and isotopic features of enriched mantle component (EMI) of Group II basalts without thermal anomaly ($T_P = 1305-1364^\circ\text{C}$). In general, the amount of slab components decreases eastward, reflecting across-arc geochemical variation.

The second manuscript presents new geochemical and Sr-Nd-Pb isotopic data for spinel-lherzolites and its host basalt. The studied area is represented by a lava flow near Coyhaique, Chilean back-arc. This occurrence is one of the closest to the convergent margin, being ~320 km from the Chile trench. New K-Ar ages for host basalt yielded 54 Ma. Based on geochemical and isotopic data, this OIB-like alkaline basalt was generated by small degrees of partial melting (up to 6%) within the garnet stability field, probably resulting from asthenospheric upwelling through slab window within the subducting Farallón-Aluk spreading ridge. Spinel-lherzolites show marked features of subduction zone metasomatism, such as pronounced negative Nb-Ta-Ti anomalies. However, based on the geochemical and isotopic data, these rocks require a heterogeneous SCLM resulting from mixing between depleted component (DMM or PREMA) and up to 15% of slab-derived components associated to subduction of Aluk oceanic plate. The enriched component added to the SCLM was metasomatized by

different extents of melts from subducted Chile trench sediments (up to 60%) and modified oceanic crusts (more than 40%).

Finally, the third manuscript is based on inedited noble gas compositions and on new Sr-Nd-Pb isotopic ratios of mantle xenoliths from Pali-Aike Volcanic Field and Gobernador Gregores. Noble gas data indicate that Patagonian SCLM reflects a mixing between air and two mantle endmembers. Pali-Aike peridotites represent degassed and intrinsic SCLM with strongly radiogenic/nucleogenic signature by higher $^4\text{He}/^3\text{He}$, $^{21}\text{Ne}/^{22}\text{Ne}$, and $^{40}\text{Ar}/^{36}\text{Ar}$ ratios than MORB source. In terms of mantle components, GG peridotites represent a mixing between SCLM (Pali-Aike) and MORB. The metasomatism with MORB-like signature can be tectonically explained by asthenospheric mantle upwelling in response to the opening of a slab window beneath Patagonia because of Chile Ridge subduction. Additionally, these rocks show depleted Sr-Nd-Pb isotopic data and an age of 13.64 ± 0.83 Ma was obtained by Rb-Sr isochron including whole-rock, clinopyroxene and phlogopite. This data represents the formation age of phlogopite, which is a key mineral to determine the time of metasomatic imprint and its potential association with geotectonic events. Thus, it is possible to associate the formation of this mineral to collision of Chile Ridge against Chile trench, and the subsequent opening of slab window.

ESTRUTURA DA TESE

Esta tese de doutorado tem como base três manuscritos submetidos a periódicos internacionais a saber: 1) *Journal of Petrology*; 2) *Lithos*; e 3) *Earth and Planetary Science Letters*. Conseqüentemente, sua estrutura está apresentada da seguinte forma:

- 1) Apresentação
- 2) Introdução
- 3) Caracterização do problema
- 4) Objetivos
- 5) Isótopos de gases nobres aplicados ao estudo de reservatórios mantélicos
- 6) Contexto geológico
- 7) Métodos analíticos
- 8) Análise integradora dos manuscritos submetidos
 - Referências
 - Manuscritos submetidos a periódicos internacionais de alto fator de impacto, corpo editorial permanente e revisores independentes. É importante ressaltar que os manuscritos apresentados nessa tese de doutorado foram escritos pelo candidato a Doutor em Ciências.

1. APRESENTAÇÃO

A presente tese corresponde ao produto final do projeto de doutorado intitulado: “*Heterogeneidade geoquímica e isotópica (Sr-Nd-Pb e gases nobres) do manto superior patagônico: depleção e metassomatismo em um ambiente de back-arc continental*”. As atividades desenvolvidas durante o período de doutorado contaram com as facilidades e infraestrutura oferecidas pelo Instituto de Geociências (IG) da Universidade Federal do Rio Grande do Sul (UFRGS), e pelo *Graduate School of Science* e *Earthquake Research Institute*, ambos da Universidade de Tóquio. O estudo realizado na UFRGS teve a orientação do Prof. Dr. Rommulo Vieira Conceição, enquanto que as atividades realizadas na Universidade de Tóquio tiveram a orientação dos Profs. Drs. Yuji Orihashi e Hirochika Sumino.

2. INTRODUÇÃO

Ao longo do tempo geológico, o manto terrestre tem registrado uma complexa história envolvendo depleção e enriquecimento de elementos maiores, traço e terras raras em resposta à fusão parcial e ao metassomatismo, como revelado por estudos de xenólitos derivados do manto de todo o mundo (e.g., Stern *et al.*, 1999; Gorryng & Kay, 2000; Grégoire *et al.*, 2000; Kilian & Stern, 2002; Niu, 2004; Workman & Hart, 2005; Mukasa *et al.*, 2007; Ntaflos *et al.*, 2007; Godard *et al.*, 2008). Dessa forma, as heterogeneidades observadas em basaltos alcalinos continentais, por vezes, não são facilmente explicadas pela fusão parcial de um manto peridotítico, exigindo um manto com heterogeneidade litológica (piroxenitos ou eclogitos) para explicar sua petrogênese (e.g., Herzberg, 2011). Adicionalmente, eventos metassomáticos desempenham papel importante na composição mineralogia e na química do manto, estando o metassomatismo modal relacionado à ocorrência de fases hidratadas (e.g., pargasita e flogopita), enquanto que o metassomatismo críptico está relacionado à presença de fluidos ou líquidos enriquecidos em elementos incompatíveis. Assim, diferentes fontes mantélicas têm sido propostas para explicar a fonte de basaltos alcalinos e de xenólitos mantélicos, tais como a relação eclogito/piroxenito (Hirschmann *et al.*, 2003; Kogiso *et al.*, 2003; Kogiso & Hirschmann, 2006; Yang & Zhou, 2013), metassomatismo modal (e.g., glimerito e/ou hornblendito; McKenzie & O’Nions, 1995; Späth *et al.*, 2001; Yang *et al.*, 2003; Pilet *et al.*, 2005, 2008; Johnson *et al.*, 2005; Mayer *et al.*, 2013), metassomatismo relacionado à líquidos/fluidos

derivados da placa subductante (e.g., Gazel *et al.*, 2011; Dyhr *et al.*, 2013; Kay *et al.*, 2013), e metassomatismo relacionados à líquidos carbonatíticos (Gorring & Kay, 2000; Dasgupta *et al.*, 2007; Zeng *et al.*, 2010).

3. CARACTERIZAÇÃO DO PROBLEMA

O estudo das características do manto, de sua heterogeneidade e dos processos relacionados à sua evolução é restrito a algumas rochas de ocorrência e volumes limitados (e.g. magmas alcalinos) ou a pequenos fragmentos deste manto hospedados em rochas basálticas (e.g., xenólitos mantélicos). A área de estudo (Fig. 1) está amplamente distribuída na região de *back-arc* continental da Patagônia (Argentina e Chile; 36°S - 52°S) e oferece a oportunidade de estudar as características petrográficas, geoquímicas e isotópicas do manto sob essa região, uma vez que seja coberta por vulcanismo basáltico recente datado do Cenozoico, que por vezes hospeda xenólitos ultramáficos, amostras diretas do manto superior.

Nessas latitudes, a interação do manto depletado com componentes enriquecidos é possível pela formação de subducções pretéritas e da configuração atual da margem oeste da América do Sul, que é caracterizada pela subducção das placas oceânicas de Nazca e Antártica sob a placa continental Sul-americana. Portanto, o limite convergente andino favorece à fertilização da cunha do manto através da introdução de sedimentos terrígenos/pelágicos, fluidos ricos em H₂O, crosta oceânica (alterada ou não), e líquidos adakiticos. Outro processo tectônico, com importante participação na evolução geoquímica do manto patagônico durante o Cenozoico, é a colisão de dorsais oceânicas, tais como a de Farallón-Aluk durante o Paleoceno-Eoceno e atualmente a do Chile. Em ambos os casos esse fenômeno teve a abertura de janelas astenosféricas e a consequente ressurgência do manto astenosférico como resultado.

Estudos prévios realizados a partir de dados geoquímicos e isotópicos em amostras de xenólitos mantélicos (litosfera) (e.g., Stern *et al.*, 1999; Gorring & Kay, 2000; Laurora *et al.*, 2001; Rivalenti *et al.*, 2004, 2007; Bjerg *et al.*, 2005, 2009; Conceição *et al.*, 2005; Schilling *et al.*, 2005, 2008; Ntaflos *et al.*, 2007; Gervasoni *et al.*, 2012; Dantas *et al.*, 2009; Jalowitzki *et al.*, 2010; Bertotto *et al.*, 2013; Faccini *et al.*, 2013; Mundl *et al.*, 2015) e de basaltos alcalinos (litosfera/astenosfera) (e.g., Stern *et al.*, 1990; Ramos & Kay, 1992; Gorring *et al.*, 1997, 2003; Espinoza *et al.*, 2005;

Guivel *et al.*, 2006; Kay *et al.*, 2004, 2006a, 2007, 2013; Jalowitzki *et al.*, 2008; D'Orazio *et al.*, 2000, 2004; Bruni *et al.*, 2008; Bertotto *et al.*, 2009; Varekamp *et al.*, 2010; Dyhr *et al.*, 2013; Søger & Holm, 2013; Søger *et al.*, 2013, 2015; Massaferrero *et al.*, 2014) têm mostrado que processos metassomáticos exercem importante contribuição na mineralogia e na assinatura geoquímica do manto da Patagônia, que é bastante heterogêneo.

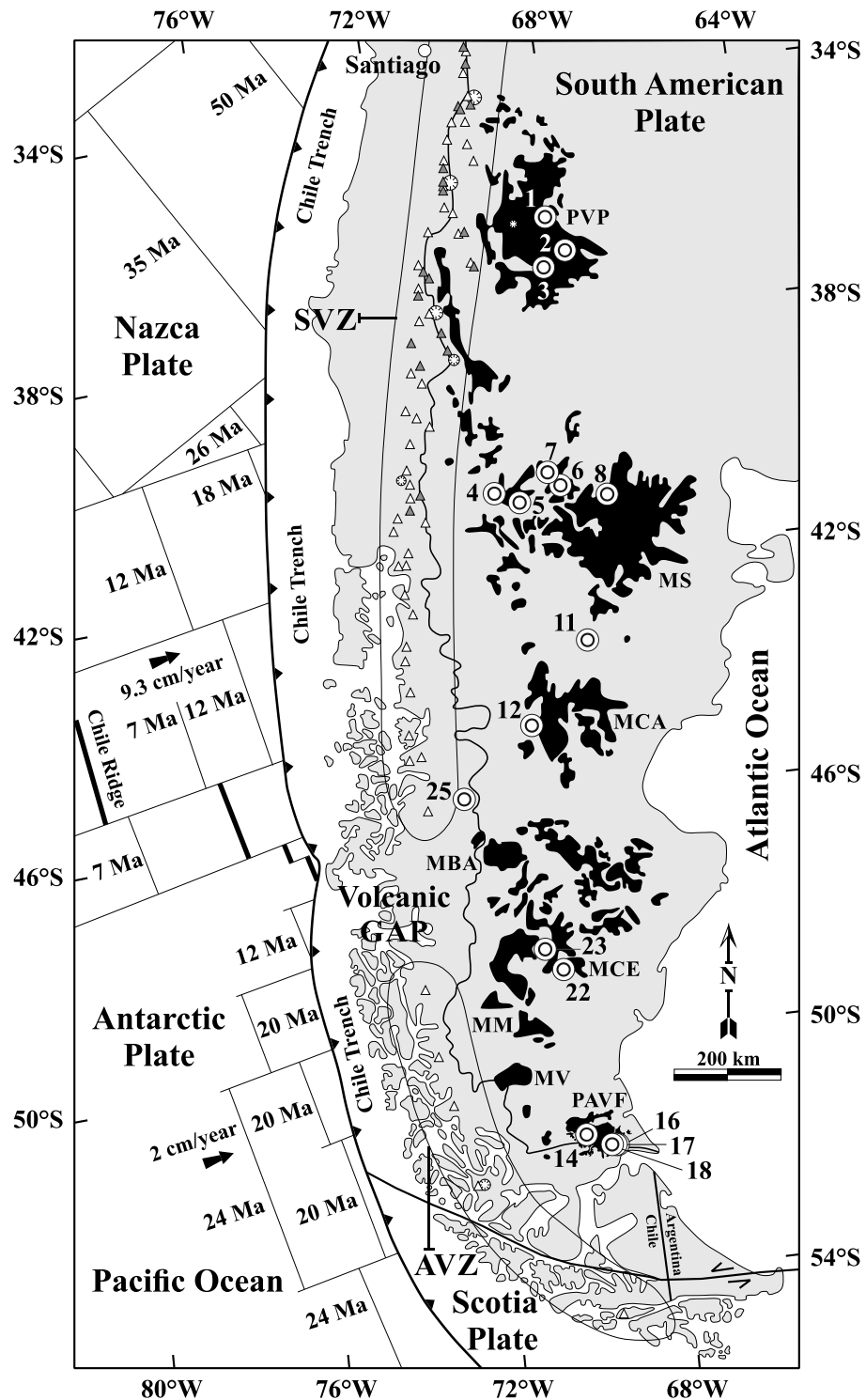


Figura 1. Mapa da localização da área de estudo (modificado de Stern *et al.*, 1990) mostrando o sul da América do Sul na sua configuração tectônica atual. A região de coleta das amostras está indicada por números: De la Laguna (1), Agua Poca (2), Huanul (3), El Mojón (PM4), Ingeniero Jacobacci (5), Aznares (6), Estancia Alvarez (7), Prahuaniyeu (8), Matilde (11) de los Chenques (12), Laguna Ana (14), Estancia Brazo Norte (16), Cueva de Fell (17), Laguna Timone (18), Cerro Redondo (22), Gobernador Gregores (23), Coyhaique (25).

4. OBJETIVOS

A geoquímica de elementos, bem como o estudo isotópico de Sr-Nd-Pb (e.g., Zindler & Hart, 1986; Hart *et al.*, 1992; Workman *et al.*, 2004; Stracke *et al.*, 2005; Jackson & Dasgupta, 2008; Salters & Sachi-Kocher, 2010; Hanyu *et al.*, 2014), e de gases nobres (e.g., Sarda *et al.*, 1988; Hiyagon *et al.*, 1992; Dunai & Baur, 1995; Burnard *et al.*, 1997; Moreira *et al.*, 1998; Trierloff *et al.*, 2000; Hopp *et al.*, 2004; Buikin *et al.*, 2005; Gautheron *et al.*, 2005; Sumino *et al.*, 2006, 2010; Parai *et al.*, 2009, 2012; Tucker *et al.*, 2012; Tucker & Mukhopadhyay, 2014), são poderosas ferramentas na identificação de reservatórios mantélicos e de agentes metassomáticos. Portanto, com o intuito de fornecer informações sobre a fonte mantélica, condições de pressão e temperatura, grau de fusão parcial, assim como da contribuição de eventos metassomáticos de diferentes porções do manto da Patagônia (litosfera/astenosfera), serão apresentados dados de elementos maiores e traços, juntamente com idades K-Ar e composições isotópicas nos sistemas Sr-Nd-Pb e gases nobres.

Cabe ressaltar que estudos prévios envolvendo a aplicação de isótopos de gases nobres em amostras de xenólitos mantélicos da região de *back-arc* continental da Patagônia são escassos e se limitam à publicação de uma tese de doutorado que apresentou dados isótopos de He em apenas 6 amostras do campo vulcânico de Pali-Aike (Bruni, 2004) e de resumos em congressos científicos nacionais e internacionais (Conceição *et al.*, 2007, 2009; Jalowitzki *et al.*, 2012, 2014), sem ainda terem sido publicados em periódicos científicos indexados.

5. ISÓTOPOS DE GASES NOBRES APLICADOS AO ESTUDO DE RESERVATÓRIOS MANTÉLICOS

Os isótopos de gases nobres são uma poderosa ferramenta na identificação de reservatórios mantélicos (e.g., manto superior, manto inferior, crosta continental e

atmosfera) devido à sua abundância, que é muito baixa (exceto pelo Ar), já que foram excluídos dos materiais sólidos durante a formação planetária no interior do sistema solar (Graham, 2002). Nesse contexto, xenólitos mantélicos, basaltos de cadeias meso-oceânicas (*mid-ocean ridge basalts*; MORBs) e basaltos de ilhas oceânicas (*ocean island basalts*; OIBs) fornecem valiosas informações acerca de reservatórios mantélicos. A erupção de lavas oceânicas é a melhor oportunidade para o estudo de gases nobres, pois a rápida formação de vidro vulcânico durante o contato com a água do mar favorece o aprisionamento de voláteis. Alternativamente, as inclusões fluidas aprisionadas em feno ou xenocristais de basaltos alcalinos ou de peridotitos (e.g., olivina, ortopiroxênio e clinopiroxênio) também podem ser analisadas com precisão para a obtenção da composição dos gases nobres.

Mudanças mensuráveis nas composições de isótopos de gases nobres estão intimamente relacionadas aos processos geoquímicos que controlam a distribuição de K, U e Th. A composição isotópica de cada gás nobre é modificada pelo decaimento radioativo de um ou mais desses elementos. A distribuição geoquímica de He está diretamente relacionada a uma produção de partículas α por U e Th. A composição isotópica Ne em sistemas terrestres é modificada por processos em que o ^{21}Ne é predominantemente produzido quando nêutrons ou partículas α colidem com átomos de Mg e O. Já o decaimento radioativo de ^{40}K geralmente controla a composição isotópica de Ar. Pequenas quantidades de ^{84}Kr e ^{86}Kr foram produzidas ao longo do tempo geológico pela fissão espontânea do ^{238}U . A produção de $^{131,132,134,136}\text{Xe}$ ocorreu ao longo do tempo geológico pela fissão espontânea do ^{238}U e do extinto ^{244}Pu (meia-vida $t_{1/2} = 82$ Ma), enquanto a produção de ^{129}Xe ocorreu através do decaimento radioativo do extinto ^{129}I ($t_{1/2} = 17$ Ma). Em síntese, os isótopos de gases nobres são caracterizados por componentes de diferentes origens, tais como primordial (e.g., razões enriquecidas em ^3He , ^{20}Ne , ^{22}Ne , ^{36}Ar , ^{38}Ar , ^{130}Xe , ^{132}Xe), radiogênica (razões enriquecidas em ^4He , ^{40}Ar e ^{129}Xe), fissiogênica (razões enriquecidas em ^{84}Kr , ^{86}Kr e ^{126}Xe), nucleogênica (razões enriquecidas em ^{21}Ne), e cosmogênica (e.g., razões enriquecidas em ^3He e ^{21}Ne).

A concentração de He na atmosfera é extremamente baixa (5,24 ppm) e, portanto, os efeitos de contaminação do ar que normalmente afetam as análises dos gases nobres pesados (Ne-Ar-Kr-Xe) estão ausentes nesse sistema isotópico. O manto superior, definido como fonte de MORBs, é desgaseificado e composicionalmente homogêneo em relação à He ($^3\text{He}/^4\text{He} = 8 \pm 1 R_A$; Sarda *et al.*, 1988; Moreira *et al.*, 1998) onde R_A é a razão atmosférica atual de $^3\text{He}/^4\text{He}$ ($1,4 \times 10^{-6}$).

(Ozima & Podosek, 1983). O manto inferior, definido como fonte de OIBs, tem natureza relativamente não desgaseificada e aquelas localidades relacionadas à ocorrência de plumas mantélicas (e.g., Havaí, Islândia e Réunion) usualmente têm elevadas razões $^3\text{He}/^4\text{He}$ quando comparadas a MORBs, podendo chegar a 50 R_A (e.g., Stuart *et al.*, 2003). Entretanto, alguns HIMU-OIBs (high- μ = elevado $^{238}\text{U}/^{204}\text{Pb}$; Hart *et al.*, 1992) (e.g., Açores, Santa Helena, Mangaia, Tubuaii e Tristão da Cunha), apresentam razões $^3\text{He}/^4\text{He}$ inferiores a MORBs (entre 4 a 8 R_A), que refletem elevadas razões $(\text{U}+\text{Th})/^3\text{He}$ na fonte. As fontes de OIB são mais enriquecidas em U e Th que as de MORB, o que indica que as fontes relacionadas às plumas mantélicas são enriquecidas em ^3He primordial quando comparadas à MORB devido às suas elevadas razões $^3\text{He}/^4\text{He}$. O manto litosférico subcontinental (SCLM) é uma parte importante do manto superior isolada do manto convectivo (MORB) e apresenta razão $^3\text{He}/^4\text{He}$ radiogênica (6 ± 1 ; Gautheron & Moreira, 2002; Gautheron *et al.*, 2005).

Os isótopos de Ne, assim como os demais isótopos de gases nobres pesados, são mais abundantes na atmosfera e isso pode resultar na contaminação quase inevitável de Ne proveniente do ar em rochas mantélicas. O aumento da razão $^{21}\text{Ne}/^{22}\text{Ne}$ associado com razões $^{20}\text{Ne}/^{22}\text{Ne}$ inferiores à atmosférica, juntamente com o enriquecimento de ^3He devido à exposição de rochas mantélicas na superfície terrestre caracterizam a contribuição de um componente cosmogênico. As razões isotópicas de Ne definidas para MORBs, OIBs e SCLM são mais elevadas que a atmosférica ($^{20}\text{Ne}/^{22}\text{Ne} = 9,8$; $^{21}\text{Ne}/^{22}\text{Ne} = 0,029$) e formam tendências que são interpretadas como a mistura entre a contaminação atmosférica e membros finais mantélicos enriquecidos em ^{20}Ne e ^{21}Ne . Os membros finais desgaseificados (MORB, HIMU e SCLM) mostram progressivo enriquecimento seletivo de ^{21}Ne [elevadas razões $(\text{U}+\text{Th})/^{22}\text{Ne}$] (Fig. 2).

A razão $^{40}\text{Ar}/^{36}\text{Ar}$ da atmosfera terrestre é de 296 e todas as outras rochas terrestres têm razões mais elevadas devido ao decaimento radioativo do ^{40}K ($t_{1/2} = 1,25$ Ga), que resulta na produção de ^{40}Ar . Os isótopos de ^{36}Ar e ^{38}Ar são primordiais em sua origem e não têm contribuições significativas no interior do planeta. As razões $^{38}\text{Ar}/^{36}\text{Ar}$ geralmente têm valores próximos a razão atmosférica (0,188) em rochas mantélicas.

Dados isotópicos de Kr e Xe não são comuns na literatura, pois a composição isotópica de Kr e Xe em rochas mantélicas é praticamente a mesma da atmosfera (atualmente). O único reservatório mantélico relativamente bem definido para Xe é o MORB (e.g., Staudacher & Allègre, 1982; Kunz *et al.*, 1998; Tucker *et al.*, 2012).

Adicionalmente, [Holland *et al.* \(2009\)](#) obtiveram dados de Kr e Xe para amostras de gás de Bravo Dome, Novo México, Estados Unidos. Com base em análises de alta precisão, eles sugeriram que o interior do planeta tem composições similares às aquelas definidas para a média de condritos carbonáceos (AVCC).

Uma série de estudos com base em isótopos de gases nobres (principalmente isótopos de He) tem sido realizada através da análise de xenólitos mantélicos de diferentes localidades: 1) Europa ([Dunai & Baur, 1995](#); [Gautheron & Moreira, 2002](#); [Gautheron *et al.*, 2005](#)); 2) Austrália ([Matsumoto *et al.*, 1998, 2000](#); [Czuppon *et al.*, 2009](#)); 3) Estados Unidos ([Dodson & Brandon, 1999](#)); 4) extremo leste russo ([Yamamoto *et al.*, 2004](#)); 5) Península coreana ([Kim *et al.*, 2005](#)); 6) Ásia Central ([Barry *et al.*, 2007](#)); 7) Tasmânia ([Czuppon *et al.*, 2010](#)).

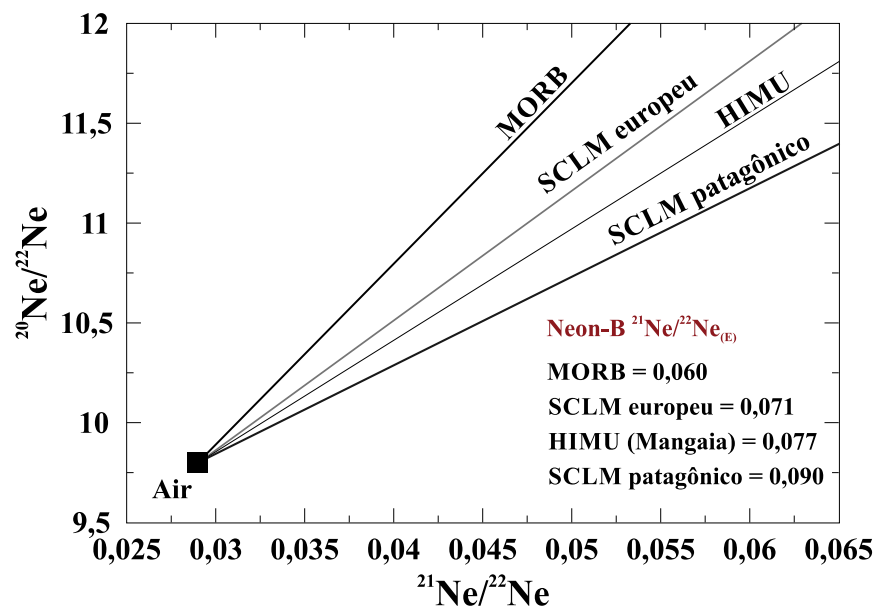


Figura 2. $^{20}\text{Ne}/^{22}\text{Ne}$ versus $^{21}\text{Ne}/^{22}\text{Ne}$. Esse diagrama mostra o nítido enriquecimento de ^{21}Ne em diferentes membros finais do manto.

6. CONTEXTO GEOLÓGICO

A cordilheira dos Andes se estende por mais de 7.500km ao longo da margem oeste da América do Sul, desde a costa do Caribe (ao norte) até Cabo Horn (ao sul). A atividade vulcânica de arco continental, entretanto, está restrita a quatro regiões separadas a partir das variações do ângulo de subducção das placas oceânicas ao longo da margem ativa e da presença de dorsais meso-oceânicas subductantes: Zona Vulcânica Norte (ZVN; 5°N - 2°S), Zona Vulcânica Central (ZVC; 14°S - 27°S), Zona

Vulcânica Sul (ZVS; 33°S - 46°S) e Zona Vulcânica Austral (ZVA; 49°S - 55°S) (e.g., Ramos, 1999; Stern, 2004) (Fig. 1).

A Cordilheira dos Andes é atualmente caracterizada por um complexo sistema de placas tectônicas no qual as placas oceânicas de Nazca, Antártica, Scotia e Cocos subductam a placa continental Sul-americana com diferentes velocidades e ângulos de mergulho (Fig. 1). Adicionalmente, a margem oeste da América do Sul, na latitude das ZVS e ZVA, foi submetida a uma vasta história de colisões e consequente subducção de dorsais oceânicas ao longo do Cenozoico, tais como a de Farallón-Aluk durante o Paleoceno-Eoceno e atualmente a do Chile (e.g., Aragón *et al.*, 2013; Breitsprecher & Thorkelson, 2009; Cande & Leslie, 1986). Esses processos permitiram a abertura de sucessivas janelas astenosféricas abaixo da Patagônia, como registrado pelos basaltos alcalinos de platô eocênicos da Patagônia Central (Espinoza *et al.*, 2005; Morata *et al.*, 2000; Parada *et al.*, 2001; Ramos & Kay, 1992).

Ainda no Cenozoico, as erupções de grandes volumes de lava basáltica na margem oriental da Cordilheira dos Andes deram lugar a extensos platôs e a centenas de cones monogenéticos de composição basáltica e/ou piroclástica em um ambiente geotectônico de *back-arc* continental. Os produtos vulcânicos aflorantes no extra *back-arc* andino são caracterizados por um volumoso magmatismo toleítico do tipo platô, seguido por um magmatismo do tipo pós-platô, que é menos volumoso e apresenta afinidade alcalina (Stern *et al.*, 1990; Gorrington *et al.*, 1997). A maioria dessas lavas, especialmente aquelas com afinidade alcalina, tem características geoquímicas típicas de um ambiente intraplaca (OIB-like), com razões isotópicas de Sr-Nd-Pb moderadamente depletadas (Gorrington & Kay, 2001).

Devido à vasta extensão territorial da Patagônia, que de norte a sul se estende por mais de 2000 km, e para simplificar os modelos geodinâmicos propostos para a evolução tectono-magmática da região, a área de estudo será seccionada com base nas mais importantes províncias vulcânicas: 1) Província Vulcânica de Payenia (34°S a 38°S), 2) Província de Somún Curá e seu prolongamento meridional (de 40°S a 45°S), e 3) Patagônia austral (49°S a 52°S).

O vulcanismo de Payenia (Mioceno inferior aos tempos históricos) está relacionado a um período transitório de subducção sub-horizontal que teve início a aproximadamente 20 Ma e culminou em aproximadamente 5 Ma, quando a atividade vulcânica se tornou progressivamente mais enriquecida em componentes derivados de placa devido à migração para leste do arco vulcânico (e.g., Kay *et al.*, 2004, 2006a-b). Estes processos estão relacionados com o aumento do ângulo de subducção

durante o processo de *roll-back* (alívio de pressão pela inversão do esforço da placa subductante) (e.g., Ramos & Kay, 2006; Ramos *et al.*, 2014). Posteriormente, o volumoso vulcanismo plio-pleistocênico foi associado ao aumento da inclinação da placa de Nazca após um período de subducção de baixo ângulo, o que favorece à ressurgência do manto astenosférico (e.g., Kay & Mancilla, 2001; Kay *et al.*, 2004, 2006a-b; Kay & Copeland, 2006; Folguera *et al.*, 2009; Germa *et al.*, 2010; Gudnason *et al.*, 2012; Dyhr *et al.*, 2013; Søger & Holm, 2013; Søger *et al.*, 2013, 2015).

A província magmática de Somún Curá (41°S - 43°S) data do Eoceno superior ao Pleistoceno (e.g., Ardolino, 1981; Orihashi *et al.*, 2005, 2006; Kay *et al.*, 2007) e representa o platô de maior extensão da Patagônia (55000 km², acrescido 6600 km² das mesetas adjacentes; Kay *et al.*, 2006a). A origem da província de Somún Curá e de seu prolongamento austral tem sido atribuída: 1) às anomalias térmicas (*hotspots*) transitórias associadas a dinâmica e reorganização da placa subductante (Kay *et al.*, 1993, 2004); 2) às plumas de ascensão astenosférica (*asthenospheric corner flow*) em decorrência de combinação de *roll-back* e topografia da placa com convexidade voltada para cima (de Ignacio *et al.*, 2001); 3) ao afinamento litosférico extensional atribuído a ressurgência da astenosfera através da formação de uma janela astenosférica em resposta a mudanças na geometria da zona de subducção (Muñoz *et al.*, 2000); ou 4) à ressurgência de uma astenosfera hidratada causada pela fusão induzida pela desidratação da zona de transição do manto (Orihashi *et al.*, 2005, 2006; Honda *et al.*, 2006).

Modelos petrológicos prévios para a região mais ao sul da Patagônia (sul de 47°S) foram propostos com base em dados geoquímicos e cronológicos, estando a maioria deles relacionada com a sucessiva subducção de diferentes segmentos da dorsal do Chile (*Chile Ridge*) (e.g., Charrier *et al.*, 1979; Stern *et al.*, 1990; Ramos & Kay, 1992; Gorryng *et al.*, 1997, 2003; D'Orazio *et al.*, 2000, 2001; Guivel *et al.*, 2006; Boutonnet *et al.*, 2010; Espinoza *et al.*, 2010; Ramírez de Arellano *et al.*, 2012). Com base em idades K-Ar, Charrier *et al.* (1979) definiram que não há evidências que relacionem o magmatismo da Meseta del Lago Buenos Aires (MLBA) com a subducção da dorsal do Chile. Entretanto, de acordo com Ramos & Kay (1992), a maioria dos basaltos de platô datados do Mioceno superior ao recente entre 46°S e 49°S tem afinidade geoquímica com basaltos do tipo OIB; e quase todos podem ser relacionados com a abertura de janelas astenosférica em resposta à colisão dos segmentos da dorsal do Chile com a fossa do Chile. Para a mesma latitude, Gorryng *et al.* (1997, 2003) definiram que todos as lavas pós-platô (3,4-0,1 Ma) foram geradas

após a passagem da dorsal do Chile a aproximadamente 6 Ma, sobrepondo as lavas de platô, que são de 2 a 5 Ma mais antigas. Esses basaltos mais antigos teriam erupcionado durante ou imediatamente após a colisão da dorsal do Chile. Com base nos dados geocronológicos disponíveis, a aproximadamente 47°S, um modelo alternativo foi proposto por [Guivel et al. \(2006\)](#), onde tanto os magmas do tipo OIB quanto os intermédios teriam sido gerados a partir de um manto astenosférico profundo que ascendeu através do rompimento da placa oceânica (*slab tear model*) a aproximadamente 15 Ma, quando os segmentos mais ao sul da dorsal do Chile colidiram com a fossa do Chile. O modelo de rompimento de placa implica na formação de uma única janela astenosférica subparalela à fossa, e que a atividade vulcânica pré-data a subducção da dorsal do Chile. [Boutonnet et al. \(2010\)](#) e [Espinoza et al. \(2010\)](#) estudaram a relação espaço-temporal entre o magmatismo bimodal na Patagônia Central (aproximadamente 47°S). Esses autores supuseram que a migração do arco vulcânico para o leste está associada à diminuição do ângulo de subducção, seguido por uma subducção sub-horizontal transitória, que promoveu a geração de uma hidratação secundária devido à desidratação da placa oceânica na cunha do manto até 300 km a leste da presente localização da fossa oceânica. Alternativamente, [Ramírez de Arellano et al. \(2012\)](#) propuseram que a transição entre o magmatismo cálcio-alcálico para alcálico, bem como a ocorrência do magmatismo transicional a alcálico a aproximadamente 1 a 2 Ma antes de subducção dos segmentos da dorsal do Chile, não estão restritas ao modelo de janela astenosférica. Eles também sugeriram que os basaltos transicionais refletem a diminuição de componentes derivados da placa na cunha do manto, o que provavelmente está relacionado com a migração para o leste do arco magmático durante o Mioceno. O modelo de janela astenosférica também foi proposto para Estancia Glencross Area (EGA) e Pali-Aike *Volcanic Field* (PAVF) (aproximadamente 52°S; [D’Orazio et al., 2000, 2001](#)). Este modelo implica na ressurgência de uma astenosfera primitiva através de uma janela astenosférica a aproximadamente 14 Ma como consequência da colisão da dorsal do Chile com a fossa do Chile. Em um estudo regional, envolvendo basaltos alcálicos amplamente distribuídos na Patagônia (34°S - 52°S), [Stern et al. \(1990\)](#) dividiu essas rochas em basaltos “cratônicos” e “transicionais”. Eles atribuíram a geração dos basaltos “cratônicos” aos baixos graus de fusão parcial de uma astenosfera do tipo “pudim de ameixa” (“*plume-pudding*”), como resultado da subducção da litosfera oceânica. Por outro lado, os basaltos “transitórios” representam a composição geoquímica intermediária entre os basaltos “cratônicos” e basaltos

andinos, com a incorporação de componentes derivados de placa em quantidades menores do que as observadas abaixo do arco vulcânico andino.

Suítes de xenólitos mantélicos de natureza máfica e ultramáfica são comumente hospedadas por lavas alcalinas na região de *back-arc* patagônico. Essas amostras representam fragmentos intrínsecos do manto litosférico continental e apresentam uma complexa história de depleção e enriquecimento relacionadas, respectivamente, a processos de fusão parcial e eventos metassomáticos. Portanto, essas rochas fornecem valiosas informações sobre a heterogeneidade mineralógica e química dessa região do planeta.

Diversas localidades da Patagônia têm sido objeto de numerosos estudos, estando entre as mais importantes: Agua Poca (e.g., Bertotto, 2000; Jalowitzki *et al.*, 2010; Bertotto *et al.*, 2013), Prahuaniyeu (Bjerg *et al.*, 2009), Cerro de los Chenques (e.g., Rivalenti *et al.*, 2007; Dantas *et al.*, 2009), Tres Lagos (Ntaflos *et al.*, 2007), Cerro del Fraile (e.g., Kilian & Stern, 2002; Faccini *et al.*, 2013), Cerro Redondo (Schilling *et al.*, 2005), Gobernador Gregores (e.g., Gorrying & Kay, 2000; Laurora *et al.*, 2001; Rivalenti *et al.*, 2004; Zaffarana *et al.*, 2014), Cerro Clark (Dantas *et al.*, 2009); Pali-Aike (e.g., Stern *et al.*, 1999; Gervasoni *et al.*, 2012; Zaffarana *et al.*, 2014). Adicionalmente, alguns estudos discutiram as diferenças petrográficas, geoquímicas e isotópicas em escala regional, onde amostras de diferentes localidades foram comparadas (e.g., Rivalenti *et al.*, 2004; Bjerg *et al.*, 2005; Conceição *et al.*, 2005; Schilling *et al.*, 2008; Mundl *et al.*, 2015). Entretanto, a natureza e a evolução dos vários domínios do manto, assim como a influência de componentes relacionados à zona de subducção ou de líquidos de origem astenosférica permanecem em debate.

7. MÉTODOS ANALÍTICOS

As atividades desenvolvidas durante o período de doutorado contaram com as facilidades e infraestrutura oferecidas pelo IG-UFRGS, e pelos *Graduate School of Science* e *Earthquake Research Institute*, ambos da Universidade de Tóquio.

7.1. Amostragem

Amostras de basaltos alcalinos e xenólitos mantélicos de 17 pequenos vulcões extintos localizados na Patagônia (Argentina e Chile; 36°S - 52°S) foram coletadas durante três campanhas de campo (2004, 2007 e 2010). A coleta de amostras foi

realizada nas áreas pertencentes às Províncias de La Pampa, Mendoza, Rio Negro, Chubut e Santa Cruz (Argentina) e no Parque Nacional de Pali-Aike (Chile).

7.2. Preparação de amostras

7.2.1. Confeção de lâminas delgadas

Fatias de aproximadamente 2 cm de espessura de basaltos e de xenólitos foram serradas e, quando necessário, impregnadas a vácuo com resina colorida para posterior identificação em microscópio binocular, permanecendo na estufa a 100°C até que toda a umidade fosse evaporada. Na etapa seguinte uma fina fatia foi separada, lixada com lixas de distintos potenciais de desbaste (120, 220, 600, 1200, 2500 e 4000 grana), e submetida a processos de abrasão com abrasivos de carbeto de silício (900 µm) e óxido de alumínio (9,5 µm). O acabamento final das lâminas (polimento) é feito com politriz com a aplicação de 100 rotações por minuto (rpm) durante aproximadamente 5 minutos com abrasivo composto por alumina (0,3 µm).

7.2.2. Rocha total

O restante das amostras foi fragmentado, quarteado, e parte desses fragmentos foi reduzida com auxílio de cadinho (grau) de ágata e pistilo. Posteriormente, a amostra foi submetida ao processo de pulverização com a utilização de pulverizador de bolas de ágata, que permite a obtenção de frações inferiores a 200 mesh para realização das análises químicas de rocha total (XRF, LA-ICPMS e isótopos de Sr-Nd-Pb). A rotação e o período de duração do processo de pulverização das amostras são de 300 rpm e 30 minutos, respectivamente.

7.3. Petrografia e contagem modal

A descrição petrográfica e dos aspectos texturais dos xenólitos mantélicos e dos basaltos alcalinos foram realizadas com auxílio de microscópio óptico petrográfico e com análises no Microscópio Eletrônico de Varredura (MEV), com sistema EDS (*Energy Dispersive System*). O MEV utilizado foi o Jeol 6610-LV, instalado no Laboratório de Geologia Isotópica da UFRGS.

As observações petrográficas aplicadas aos xenólitos mantélicos tiveram como objetivo principal identificar a paragênese mineral e as principais texturas, que tiveram como base o artigo de [Mercier & Nicolas \(1975\)](#). As composições modais das amostras de xenólitos mantélicos foram calculadas e, posteriormente, a soma das proporções minerais foi recalculada para 100%. A análise petrográfica dos basaltos foi realizada com o intuito de determinar texturas e a assembleia mineralógica representativa das rochas em estudo.

7.4. Geoquímica de rocha total

Com o objetivo de correlacionar quimicamente as rochas basálticas estudadas, foram realizadas análises geoquímicas em rocha total para elementos maiores, traços e terras raras com a colaboração do Prof. Dr. Yuji Orihashi (*Earthquake Research Institute, the University of Tokyo*).

Os elementos maiores e as concentrações de alguns elementos (Sc, V, Cr, Co, Ni, Zn, Ga, Rb, Sr, Y, Zr, Nb e Ba) foram determinados por fluorescência de raios-X (XRF, PW2400; Philips Japan Ltd.) e as concentrações de outros elementos traço foram obtidas através do método LA-ICPMS (Plasma Quad 3; VG Scienta Holdings AB) durante os meses de setembro a novembro de 2010. O sistema de *laser ablation* é o UP-213 *laser system* (*New Wave Research*) de frequência quadruplicada Nd-YAG UV ($\lambda = 213 \text{ nm}$) com comprimento de onda de 266 nm e diâmetro de amostragem de 40 μm . O sistema do laser foi operado na modalidade do Q-interruptor, com energia de pulso de $\sim 100 \text{ mJ/cm}^2$, repetição do pulso de 10 Hz e ablação de 120 s. Em ordem, para minimizar o fracionamento elementar durante a ablação, o ponto da ablação foi alterado a cada 20 s, totalizando seis crateras de ablação com 3x2 de grade e um intervalo de 100 μm foi produzido dentro do período da integração (120 s).

No caso específico deste estudo foram adotados os padrões JB-2 (basalto). As pastilhas fundidas de vidro para análise de XRF foram preparadas a partir da mistura de 1,8 g de pó da amostra com 3,6 g de metaborato/tetraborato de lítio. 0,54 g de nitrato do lítio foram adicionados como oxidante do ferro na amostra de rocha total e misturado por três minutos. Esta mistura foi aquecida até 1200°C durante 15 minutos em um cadinho 95%Pt-5%Au com diâmetro interno de 30 mm, usado em um amostrador automático de pastilha de vidro fundida. O procedimento detalhado e teste de homogeneização da pastilha de vidro fundida para análise de elementos maiores na XRF são descritas por [Tanaka & Orihashi \(1997\)](#) e [Tani *et al.* \(2002\)](#). A descrição

detalhada sobre o método empregado na obtenção dos dados por XRF e LA-ICPMS foram descritos por Tani *et al.* (2002) e por Orihashi & Hirata (2003), respectivamente.

A geoquímica de rocha total das amostras de xenólitos mantélicos foi realizada no *The Earth Resources Research and Analysis* (TERRA), do Departamento de Ciências da Terra, Memorial University of Newfoundland, Canadá. As abundâncias de elementos maiores e traço foram obtidas através da fluorescência de raios-X (Bruker S8 Tiger sequential wavelength-dispersive XRF) e ICP-MS (PerkinElmer ELAN DRCII). Os dados de XRF foram obtidos através de pastilhas fundidas, que foram preparadas pela mistura de 1,5 g de pó de rocha com 6,0 g de metaborato de lítio e 1,5 g de tetraborato de lítio. A mistura foi colocada num cadinho de platina e algumas gotas de brometo de lítio foram adicionadas como um agente umedecedor. Os cadinhos foram então colocados no *Leco Fluxer* e aquecidos a $\sim 850^\circ\text{C}$ durante 8,5 minutos e fundido a $\sim 1050^\circ\text{C}$ durante 11,5 minutos. Dados de ICP-MS foram obtidos por análise de solução, onde 0,1 g de pó de amostra foi digerida com a técnica de digestão de alta pressão desenvolvida por Diegor *et al.* (2001). Para esse método, utilizam-se frascos de politetrafluoretileno ao invés dos convencionais frascos de teflon (Savilex®). A vantagem desse método é sua rapidez na total digestão das amostras, sendo realizado em apenas 4 dias, e a eficiência em dissolver minerais mais resistentes, como granada e espinélio. As amostras (0,1 g cada), junto de 3 ml de HNO_3 8 M e 2 ml HF 30%, foram acopladas às bombas de politetrafluoretileno, que então foram condicionadas a uma temperatura de 200°C em um forno por 24 horas. Depois do aquecimento, as bombas foram abertas, e sobre uma chapa quente (70°C), a digestão deu continuidade. Após a evaporação dos primeiros reagentes, foram realizados mais dois ciclos de ataque químico com HNO_3 sobre chapa quente e bomba aberta. Este procedimento de digestão durou três dias. No final do ataque, foram adicionados à solução 1,35 ml de ácido oxálico (0,22 M) para complexar o Fe e outros elementos traços em solução, 0,665 ml de mistura de HF-HBr (0,1 M HF / 0,45 M HBr) para estabilizar os elementos Nb e Ta, e ácido bórico para complexar o excesso de íons F^- .

Apenas 0,5 ml das amostras dissolvidas são então condicionadas em tubos de ensaio junto de 4,5 ml de 0,2 N HNO_3 e mais 5 ml da solução de padrão interno funcionando como um *spike*. Outro tubo de ensaio com mais 0,5 ml de amostra dissolvida e 9,5 ml de 0,2 N HNO_3 também foram analisados. Para as análises, o tempo de contagem total por massa foi de 10 s e o tempo de permanência por massa foi de 0,05 s. Três padrões externos foram usados com diferentes elementos e com

diferentes concentrações de cada um deles. Padrões internos também foram aplicados (Sc, Na, Re e U) com diferentes concentrações. O Índio (In) foi usado como padrão interno e seu sinal foi utilizado para correção do *drift*. A sensibilidade das massas foi determinada por calibrações externas. Para as determinações das massas de Nb, Ta e Mo, utilizou-se calibrações por substituição (*surrogate calibration*) usando os elementos Zr e Hf (Jenner *et al.*, 1990). A aplicação dos padrões internos, o uso dos padrões externos e a calibração por substituição são estratégias para lidar com os efeitos da matriz, interferências e o *drift* durante as análises. Informações detalhas sobre o método aplicado encontra-se no trabalho realizado por Jenner *et al.* (1990). A redução dos dados foi feita depois das análises, em uma planilha Excel pertencente ao laboratório.

7.5. Datação K-Ar

As idades obtidas para basaltos alcalinos que hospedam xenólitos mantélicos provenientes de 13 vulcões extintos da Patagônia foram determinadas através do método K-Ar sem *spike* (*unspiked*), na qual a concentração do ^{40}Ar radiogênico é determinada por uma comparação direta entre a razão $^{40}\text{Ar}/^{36}\text{Ar}$, a intensidade de sinal do ^{40}Ar das amostras e do volume de Ar atmosférico volumetricamente calibrado nas mesmas condições no espectrômetro de massa. O método pode datar precisamente rochas mais jovens que 0,1 Ma, uma vez que permite a medição de pequenas quantidades de ^{40}Ar radiogênico e determina a composição isotópica do Ar inicial na amostra por medir a razão $^{38}\text{Ar}/^{36}\text{Ar}$ sem assumir que a razão $^{40}\text{Ar}/^{36}\text{Ar}$ na amostra é igual ao valor atmosférico atual de 296 (ver Nagao *et al.*, 1991 e Orihashi *et al.*, 2004).

As análises de Ar foram realizadas com o uso de um espectrômetro de massa com linha de gás acoplada MS-III (modified-VG5400) no *Geochemical Research Center* (antigo *Earthquake Chemistry Laboratory*), *Graduate School of Science*, the University of Tokyo. Amostras de rocha total foram trituradas e peneiradas na fração entre 60-80 mesh e tiveram os minerais ferromagnéticos removidos com uso de imã de mão, posteriormente foram lavadas com água Milli-Q, postas em um ultrassom por 15 minutos e, por fim, foram secas a 110°C em uma estufa. Parte da amostra (0,3-0,6 g) foi fundida a 1700°C e o gás evaporado foi purificado. As análises isotópicas de Ar foram realizadas com uma quantidade relativamente pequena de gás Ar ($<2 \times 10^{-7} \text{cm}^3$ STP). Se a quantidade de gás Ar extraído da amostra excede esse limite, a quantidade de gás Ar é reduzida usando-se a linha de purificação. Incertezas sobre a

sensibilidade do ^{40}Ar e a razão $^{40}\text{Ar}/^{36}\text{Ar}$ são estimados em 5% e 0,2%, respectivamente, com base em medições repetidas do padrão atmosférico contendo $1,5 \times 10^{-7} \text{cm}^3$ STP de ^{40}Ar . A qualidade das idades K-Ar obtidas neste estudo foi baseada no uso de dois padrões de referência. Um deles é o YZ1, que é um basalto quaternário do vulcão Zao (Japão), cuja idade de referência obtida pelo método de diluição isotópica é 0.227 ± 0.009 Ma; e o outro é o Baba tuff, que é biotita com idade de referência de 11.81 ± 0.10 Ma (Nagao *et al.*, 1996).

As concentrações de K foram determinadas na fluorescência de raios-X (XRF) (Phillips PW2400) com o uso de uma alíquota da fração de rocha total triturada e peneirada utilizada para a análise de Ar. As análises de XRF foram realizadas no *Earthquake Research Institute*, the University of Tokyo. Maiores detalhes dos procedimentos empregados na obtenção dos dados são descritos em Nagao *et al.* (1991) e Orihashi *et al.* (2004).

7.6. Sistemas isotópicos Sr-Nd-Pb

As análises isotópicas em rocha total nos sistemas isotópicos Sr-Nd-Pb foram geradas no Laboratório de Geologia Isotópica (LGI) do Centro de Estudos em Petrologia e Geoquímica (CPGq) - IG da UFRGS com a utilização de dois espectrômetros de massa multi-coletores por ionização termal TIMS (*Sector 54*; VG Scienta Holdings e Triton; Thermo Scientific). As análises de basaltos alcalinos foram realizadas sem adição de traçadores (*spikes*), pois as idades absolutas das amostras estudadas foram determinadas através do método K-Ar. Entretanto, as análises isotópicas de xenólitos mantélicos tiveram adição de *spikes*.

As amostras pulverizadas de rocha total (< 200 mesh) foram pesadas (0,1 g) em frascos de teflon (Savillex®) e ainda na balança de precisão foram adicionadas 15 gotas de HNO_3 concentrado. Para realização das análises de Rb-Sr e Sm-Nd foram adicionadas quantidades específicas de *spikes* mistos. As análises de Pb foram realizadas sem adição de *spikes*. Procedimentos específicos foram utilizados na dissolução total das amostras (processo de “abertura”) com diferentes volumes e concentrações de HF, HNO_3 e HCl. Após a dissolução, as amostras foram diluídas em 3ml de HCl 2,5N e dispostas em tubos de ensaio.

A separação do Rb, Sr, Sm e Nd foi feita através de colunas preenchidas por resina de troca catiônica AG-50W-X8 (200-400 mesh) e aniônica LN-B50-A (100-150 μm) de acordo com procedimentos envolvendo HCl. As amostras de soluções

individuais de Rb, Sr, Sm e Nd foram secas na chapa elétrica e depositadas com auxílio de 2 μ de H₃PO₄ com concentrações específicas para cada um dos elementos sobre filamentos simples de Ta (Rb, Sr e Sm) e triplo de Ta-Re-Ta (Nd). As razões isotópicas foram determinadas no modo *static* multi-coletor, utilizando coletores Faraday. As razões de Sr e Nd foram normalizadas para $^{86}\text{Sr}/^{88}\text{Sr} = 0.1194$ e $^{146}\text{Nd}/^{144}\text{Nd} = 0.7219$, respectivamente.

Para as medições isotópicas de Pb-Pb, uma alíquota de 1 ml da mesma solução de rocha total foi utilizada. A separação do Pb foi feita através de colunas cromatográficas preenchidas por resina aniônica (200-400 mesh, AG1X; Bio-Rad Laboratories Inc.) de acordo com procedimentos envolvendo HBr. As razões isotópicas de Pb das amostras de basaltos alcalinos foram determinadas por espectrometria de massa com plasma indutivamente acoplado (ICP-MS, Neptune; Finnigan MAT GmbH). Uma solução de HNO₃ com 50 ppb de TI foi utilizada para corrigir o fracionamento de Pb durante as análises. As razões isotópicas de Pb para amostras de xenólitos mantélicos foram determinadas no Triton. Nesse caso, as soluções de Pb foram secas na chapa elétrica e depositadas com auxílio de 2 μ de sílica gel e 2 μ de H₃PO₄ em filamento simples de Ta. Para os valores dos padrões de referências, veja mais detalhes nos capítulos referentes aos manuscritos.

7.7. Determinação de isótopos de gases nobres

As análises de gases nobres em xenólitos mantélicos foram realizadas em amostras de rocha total (todos minerais que compõem a rocha) e em minerais separados de olivina. Em ambos os casos as amostras foram desagregadas com o uso de um gral de ágata e a porção mais superficial das amostras foi descartada com o intuito de evitar a contaminação gerada pelo contato do xenólito mantélico com o basalto hospedeiro, pela alteração superficial (intemperismo) e pela exposição das amostras aos raios cósmicos. As amostras desagregadas foram peneiradas e separadas em três frações (0,5-1; 1-2 e > 2 mm), sendo que apenas as frações entre 1-2 e > 2 mm foram utilizadas para esse estudo. Após selecionar cuidadosamente os minerais sem alteração com auxílio de uma lupa binocular, as amostras foram dispostas em *beckers* com etanol (EtOH 99,5%), levadas a um ultrassom durante 30 minutos por duas vezes e, posteriormente, foram levadas ao forno (T = 150°C) durante 24 horas. Na etapa seguinte, as amostras foram pesadas em uma balança de precisão (~0,5 g para análises por fusão e ~1 g para análises envolvendo a quebra dos

minerais; ver detalhes a seguir). No caso das amostras destinadas às análises por fusão as mesmas foram embrulhadas em papel alumínio de 10 µm de espessura e dispostas no porta amostras, que comporta até 24 amostras sem que ocorra a quebra da condição de vácuo. Aqueles minerais destinados às análises por quebra foram dispostos diretamente nos tubos de aço inoxidável utilizados nos procedimentos de análise.

A metodologia empregada nesse estudo foi baseada em três etapas:

- i) Análises isotópicas de He, Ne e Ar através do método de fusão total (*single step heating*). Essa etapa da pesquisa teve a finalidade de determinar a concentração de gases nobres que cada uma das amostras possui {[⁴He], [²⁰Ne] e [⁴⁰Ar]}. No total foram analisadas 82 amostras representativas de rocha total e cada amostra demorou pouco mais de 3 horas para ser analisada. Vale salientar que essa metodologia foi empregada na obtenção de dados em xenólitos mantélicos de Agua Poca, El Mojón, Estancia Alvarez, Cerro Chenque, Cerro de los Chenques, Tres Lagos, Cerro Redondo, Laguna Ana, e Laguna Timone.
- ii) Análises isotópicas envolvendo todos os gases nobres (He, Ne, Ar, Kr, Xe) foram determinadas através do método de quebra de minerais (*crushing*). Nessa etapa, as localidades com a maior concentração de gases nobres foram selecionadas como prioridade de estudo. Dessa forma, as 3 amostras mais enriquecidas em gases nobres de Laguna Ana (PM14), Laguna Timone (PM18) e Gobernador Gregores (PM23) foram selecionadas para análise, que durou pouco mais de 4 horas para cada amostra. Nesse caso foram aplicados diferentes números de *strokes* (batidas) para triturar as amostras e, conseqüentemente, liberar os gases que estão aprisionados em suas inclusões fluidas. O número de *strokes* aplicado foi de 100, 500, 1000 e 2000 (o último foi aplicado diversas vezes enquanto a amostra apresentava enriquecimento na concentração de gases nobres). Sendo assim, uma mesma amostra pôde ser analisada até 8 vezes. No total foram realizadas 61 análises isotópicas através desse método.
- iii) A terceira etapa da pesquisa levou em consideração os resultados obtidos na segunda (*crushing*) para determinar que localidades e que amostras deveriam ser selecionadas para que minerais de olivina fossem separados

e analisados. A análise de minerais separados foi necessária naqueles casos em que foram observadas variações significativas nas razões isotópicas de He durante os diferentes números de *strokes* aplicados ou quando amostras de uma mesma localidade mostraram diferentes assinaturas isotópicas de Ne. Essa variação sugere que a diferença nas razões isotópicas de He e Ne está relacionada à ocorrência de minerais com diferentes assinaturas isotópicas ou a processos secundários de enriquecimento em ^3He cosmogênico, ^4He radiogênico e ^{21}Ne cosmogênico ou nucleogênico. No total foram realizadas 21 análises isotópicas em minerais separados de olivina.

Os gases nobres foram extraídos dos minerais selecionados (tamanho de cristal > 1 mm, mas sempre priorizando a análise dos minerais de maior dimensão) sob condição de vácuo através do método descrito por Nagao *et al.* (1996) e Sumino *et al.* (2001). A extração dos gases nobres é realizada de duas maneiras: 1) durante o processo de fusão total (*single step heating*), onde aproximadamente 0,5 g da amostra é completamente fundida a 1800°C; e 2) na quebra de minerais (*crushing*), onde aproximadamente 1 g de amostra é depositado na base do tubo de aço inoxidável (*crusher*) e é triturada com o uso de um pistão de níquel movido a partir de bobinas magnéticas.

As composições elementares e isotópicas dos gases nobres foram obtidas através de uma linha de gás acoplada em um espectrômetro de massa. É na linha de gás que ocorrem as etapas de separação dos diferentes isótopos e a purificação, que consiste na eliminação dos gases residuais durante a análise. Os espectrômetros de massa utilizados nas leituras isotópicas e é do tipo *sector*, versão modificada de um VG5400 (MS-III e MS-IV). A sensibilidade e os fatores de correção de discriminação de massa para o sistema de espectrometria de massa são determinados através da medição de constantes atmosféricas conhecidas através do mesmo procedimento aplicado para análise de amostras. Incertezas experimentais nas concentrações de cada um dos gases nobres foram estimadas em 5% para He e Ar; e em 10% para Ne, Kr e Xe com base na reprodutibilidade das medições dos padrões de gás (e.g., HESJ = He *standard of Japan*). As incertezas admitidas para as razões isotópicas estão em um desvio-padrão (1σ), incluindo incertezas de correção em branco e discriminação em massa.

Antes das análises terem início, a linha de gás e o porta amostras (forno ou *crushers*, dependendo do método aplicado) é aquecido com temperatura superior a 250°C por mais de 24 horas com o objetivo de reduzir a contaminação atmosférica. Após essa etapa ter sido concluída, os gases nobres aprisionados nas amostras são liberados de acordo com cada um dos métodos de extração (fusão ou quebra) e, em seguida, são inseridos na linha de gás. Cada um dos processos descritos abaixo envolve a abertura e fechamento de válvulas que isolam ou conectam as diferentes partes da linha de gás.

Branco foram determinados antes do início das análises isotópicas envolvendo amostras de rocha. Para cada conjunto de amostra depositada e analisada por fusão (geralmente 20 ou 24 amostras) um valor de branco foi determinado e aplicado para corrigir os valores de He, Ne e Ar. No caso específico das análises por *crushing*, brancos individuais foram determinados para cada uma das amostras. Os valores dos brancos referentes aos experimentos por fusão são: (2-4) x 10⁻¹¹ cm³ STP para ⁴He; (1-9) x 10⁻¹² cm³ STP para ²⁰Ne e (2-12) x 10⁻⁹ cm³ STP para ⁴⁰Ar. Os valores dos brancos referentes aos experimentos por *crushing* são: (2-4) x 10⁻¹¹ cm³ STP para ⁴He; (2-4) x 10⁻¹³ cm³ STP para ²⁰Ne e (3-5) x 10⁻¹⁰ cm³ STP para ⁴⁰Ar. A contribuição dos brancos às amostras analisadas é muito próxima no caso do He em ambos os métodos empregados, mas ele é menor nos experimentos por *crushing* nos casos do Ne e Ar. O procedimento aplicado na análise isotópica propriamente dita é explicado a seguir.

Primeiramente, os gases nobres liberados são purificados com o uso de uma armadilha aquecida a ~800°C composta por Ti e Zr (Ti1; Ti-Zr *getter*) que aprisiona os demais gases (e.g. H, CO₂⁺⁺, CO₂⁺). A seguir, o Ar, Kr e Xe são aprisionados em uma armadilha de carvão (*charcoal trap*, CH1), que é resfriada com nitrogênio líquido. O He e o Ne, que não são aprisionados durante esses processos iniciais de purificação e separação isotópica (permanecendo na linha de gás), são submetidos a um segundo processo de purificação através de uma segunda armadilha de Ti-Zr aquecida a ~800°C (Ti2) e por uma segunda *charcoal trap* (CH2) resfriada com nitrogênio líquido. Finalmente, o Ne é separado do He com o uso de uma terceira armadilha resfriada a 15 K (-260°C; *Cryo trap*).

Cada um dos gases nobres separados é sucessivamente introduzido e analisado no espectrômetro de massas (VG5400 modificado). Os isótopos de He são os primeiros a serem medidos e a análise é realizada com o uso de dois coletores: Axial no caso do ³He e High Faraday no caso do ⁴He. A seguir, os isótopos de Ne são

liberados da *Cryo* aplicando-se uma temperatura de 45 K (-230°C) e analisados no espectrômetro de massas através do Axial. Com o objetivo de reduzir a interferência do $^{40}\text{Ar}^{++}$ e CO_2^{++} ($M = 44$) sobre os isótopos de ^{20}Ne e ^{22}Ne , respectivamente, uma outra armadilha composta pelo mesmo material da *Cryo* está localizada na entrada do espectrômetro de massas (armadilha CHns). A CHns é resfriada com nitrogênio líquido pouco antes do Ne ser introduzido no espectrômetro de massas e volta a ser aquecida após a análise isotópica. As alturas dos picos definidos para ^{40}Ar e CO_2 são medidos no início e no final de cada análise de Ne para que os valores obtidos sejam corrigidos. Os gases nobres que ficaram aprisionados na CH1 (Ar, Kr e Xe) são liberados através da remoção do nitrogênio líquido. Para que o aquecimento ocorra com maior eficácia, a CH1 é previamente aquecida como uso de um recipiente contendo água quente e de uma pipeta. Em seguida o forno é recolocado na CH1 e os gases presentes na linha de gás são novamente purificados pelas duas armadilhas aquecidas de Ti-Zr (Ti1 e Ti2). A seguir o Kr e o Xe são aprisionados na *Cryo* a uma temperatura de 95 K (-180°C) e o Ar é introduzido no espectrômetro de massas para ser analisado através do multi-coletor *Daly* (*Daly multiplier collector*). O Kr é liberado da *Cryo* a 135 K (-140°C) e é introduzido no espectrômetro de massas. Por fim, o Xe é liberado da *Cryo* a 200 K (-73°C) e é introduzido no espectrômetro de massas. Ambos são analisados pelo Axial.

8. ANÁLISE INTEGRADORA DOS MANUSCRITOS SUBMETIDOS

ARTIGO 1

Submetido ao *Journal of Petrology* em 19 de maio de 2015.

Geochemistry and geochronology of Cenozoic alkaline basalts from Patagonia (36°S - 52°S): Constraints for their mantle sources and petrogenesis.

A separação de dois novos grupos de basaltos Cenozoicos de composição alcalina do tipo OIB coletados em uma vasta extensão territorial do *back-arc* continental da Patagônia (36°S - 52°S) foi possível através de dados geoquímicos de elementos maiores, traço e isótopos de Sr-Nd-Pb, além de novas idades K-Ar. Com base nos resultados obtidos foi possível identificar que a fonte mantélica do magmatismo alcalino patagônico é mineralógica e composicionalmente heterogênea, com a contribuição de fluidos provenientes de diferentes origens. Ambos os grupos

são enriquecidos em elementos terras raras leves (ETRL) em relação aos pesados (ETRP), o que demonstra forte afinidade com basaltos do tipo OIB. Além disso, estimativas de pressão obtidas com base no método empírico proposto por [Albarède \(1992\)](#) demonstram que as amostras estudadas foram geradas na zona de estabilidade da granada. As principais considerações acerca do presente estudo estão a seguir.

Grupo I: Basanitos e nefelinitos são o resultado de baixas taxas de fusão parcial ($F < 3\%$) a partir de um granada-peridotito com flogopita estável na fonte. Pronunciadas anomalias negativas de Rb, K, Pb e Ti acompanhadas de forte enriquecimento em Nb-Ta no diagrama multielementar, assim como baixas razões Rb-Sr, K/(La, Ce) e elevadas razões Ce/Pb, corroboram com a presença de flogopita residual na fonte. Elevadas razões $^{143}\text{Nd}/^{144}\text{Nd}$ associadas às baixas razões $^{87}\text{Sr}/^{86}\text{Sr}$ observadas nas amostras do Grupo I sugerem que a formação da flogopita no manto abaixo da Patagônia está relacionada ao evento de subducção atual, em que as placas oceânicas de Nazca e Antártica subductam sob a placa continental Sul-americana. Estimativas de P-T foram definidas e sugerem a participação do manto astenosférico com profundidade variando de 113 a 134 km na gênese dessas rochas. A origem da flogopita na fonte dos basaltos do Grupo I pode estar relacionada com a desidratação de serpentinitos, que fornece Rb, K, e H₂O em quantidade suficiente para formar este mineral. Posteriormente, a quebra da flogopita favoreceu o processo envolvendo baixos graus de fusão parcial de um líquido silicático hidratado rico em álcalis derivado da interação de uma astenosfera mais quente no meio da cunha do manto. A presença de flogopita estável no manto astenosférico anormalmente quente ($T_P = 1400\text{-}1563^\circ\text{C}$) pode sugerir que a gênese do vulcanismo intraplaca está relacionada a anomalias composicionais (“*wetspots*”). As estimativas de temperatura foram calculadas pelos métodos de [Albarède \(1992\)](#) e [Herzberg & Asimow \(2008\)](#).

Grupo II: Traquibasaltos, basanitos e mugearitos são o resultado de baixas taxas de fusão parcial ($F = 5\text{-}10\%$) a partir de um granada-piroxenito com metassomatismo críptico na fonte (enriquecimento em LILE e Pb). Além disso, esses basaltos têm elevadas anomalias de K/K* e Pb/Pb* (usualmente >1) e razões isotópicas ligeiramente mais radiogênicas quando comparadas aos basaltos do Grupo I. Estimativas de P-T foram definidas e sugerem que a fonte do magmatismo dos basaltos do Grupo II está restrita ao limite litosfera-astenosfera (<100 km, [Stern *et al.*](#),

1999), com profundidade variando de 89 a 94 km. Portanto, as amostras do Grupo II são o resultado do processo de fusão parcial do manto litosférico metassomatizado por veios ou cumalatos de composição piroxenítica, cuja origem está relacionada à subducção atual das placas oceânicas de Nazca e Antártica sob a placa continental Sul-americana.

Adicionalmente, de acordo com variações espaço-temporais, as profundidades estimadas para as fontes mantélicas desempenham um papel importante na gênese dos basaltos dos Grupos I e II. No entanto, localmente também foi possível distinguir os Grupos I e II devido as idades K-Ar, através da proximidade com o arco vulcânico e pelas variações e latitudes.

ARTIGO 2

Submetido à *Lithos* em 30 de novembro de 2015.

Slab-derived components in the subcontinental lithospheric mantle of the Paleocene-Eocene subduction zone beneath Chilean Patagonia: Geochemistry and Sr-Nd-Pb isotopes of mantle xenoliths and their host basalts.

A área de estudo está localizada próxima à cidade de Coyhaique, Patagônia Chilena. Juntamente com Cerro del Fraile e Chile Chico, que também estão localizados entre 280-300 km da fossa do Chile, os spinélio-lherzolitos anidros de Coyhaique fornecem a rara oportunidade de estudar fragmentos do manto litosférico próximo à placa de Nazca. Esses lherzolitos foram trazidos até a superfície por um magmatismo alcalino eocênico (54 Ma). A determinação da idade do magmatismo de composição alcalina, assim como das características geoquímica e isotópicas tanto do basalto hospedeiro quanto dos lherzolitos, foi possível através de datações K-Ar e geoquímica de rocha total. Com base nesses dados, foi possível determinar que o basalto hospedeiro é do tipo OIB, sendo resultado de baixas taxas de fusão parcial (até 6%) dentro do campo de estabilidade granada. A provável origem desse magmatismo está relacionada a ressurgência do manto astenosférico através da abertura de uma janela astenosférica associada a colisão da dorsal de Farallón-Aluk contra a placa Sul-americana durante o Paleoceno-Eoceno. Os spinélio-lherzolitos anidros de Coyhaique, em sua totalidade, têm características típicas de zonas de subducção, tais como pronunciadas anomalias negativas de Nb-Ta-Ti. Entretanto, variações composicionais significativas evidenciam que o manto litosférico nessa região é bastante heterogêneo. As composições isotópicas menos radiogênicas de

Sr-Pb e mais radiogênicas de Nd sugerem a participação de um componente depletado [*Depleted MORB mantle* (DMM; Workman & Hart, 2005) ou *Prevalent Mantle* (PREMA; Wörner *et al.*, 1986)] na gênese das amostras que apresentam padrão subhorizontalizado a depletado em ETRL em relação aos ETRP no diagrama multielementar. Seguindo a mesma lógica, aquelas amostras com elevadas razões de Sr-Pb e baixas razões de Nd apresentam enriquecimento de ETRL em relação aos ETRP, o que sugere um processo metassomático tardio com características de manto enriquecido (EM-2; Workman *et al.*, 2004). Portanto, a mistura de um componente depletado (DMM ou PREMA) com até 15% de componentes derivados da placa oceânica de Aluk é necessária para explicar o SCLM abaixo de Coyhaique. Nesse caso, o agente metassomatizante é representado por diferentes proporções de líquidos resultantes da fusão de sedimentos da fossa do Chile (até 60%) e de uma crosta oceânica modificada (mais de 40%).

ARTIGO 3

Submetido à *Earth and Planetary Science Letters* em 01 de dezembro de 2015.

Noble gas composition of subcontinental lithospheric mantle: an extensively degassed Earth reservoir of Southern Hemisphere.

Embora as composições de gases nobres de MORBs e OIBs sejam bem definidas (e.g., Sarda *et al.*, 1988; Hiyagon *et al.*, 1992; Burnard *et al.*, 1997; Moreira *et al.*, 1998; Tieloff *et al.*, 2000; Mukhopadhyay, 2012), a composição do SCLM permanece pouco conhecida. Amostras de rocha total e de olivina foram utilizadas para a obtenção de dados inéditos de gases nobres (He, Ne, Ar, Kr, Xe) em xenólitos mantélicos de duas localidades inseridas no contexto tecno-magmático da Zona Vulcânica Austral (49°S - 55°S). Os locais de coleta de amostras foram o Campo Vulcânico de Pali-Aike e o centro eruptivo de Gobernador Gregores. Os resultados obtidos indicam que o SCLM da Patagônia é isotopicamente heterogêneo, pois reflete a mistura entre três componentes: o ar e dois membros finais mantélicos. É importante ressaltar que a discussão dos resultados está baseada nos dados obtidos através do método por quebra (*crushing*), pois ele minimiza o efeito do hélio radiogênico (^4He) e cosmogênico (^3He) aprisionados na matriz da rocha. Os xenólitos mantélicos de Pali-Aike representam o SCLM desgaseificado e intrínseco, sendo caracterizado por apresentar razões mais radiogênicas/nucleogênicas que as observadas em MORBs. Esse reservatório mantélico é definido por elevados valores de $(\text{U}+\text{Th}+\text{K})/({}^3\text{He}, {}^{22}\text{Ne},$

^{36}Ar). Pali-Aike apresenta razões de $^3\text{He}/^4\text{He}_{\text{AVERAGE}} = 6,87 \pm 0,04 \text{ RA}$ (SCLM = 6 ± 1 ; Gautheron & Moreira, 2002; Gautheron *et al.*, 2005) (onde 1RA corresponde a razão atmosférica de 1.4×10^{-6} ; Ozima & Podosek, 1983). As razões de $^{21}\text{Ne}/^{22}\text{Ne}_{(\text{E})}$ variam entre 0.085 e 0.094 [onde (E) = razão extrapolada para Neon-B $^{20}\text{Ne}/^{22}\text{Ne} = 12,5$] (SCLM europeu $^{21}\text{Ne}/^{22}\text{Ne}_{(\text{E})} = 0.07$; Hopp *et al.*, 2004; Buikin *et al.*, 2005). As medidas de $^{40}\text{Ar}/^{36}\text{Ar}$ variam de valores próximos às razões atmosféricas (510) e alcançam 16400, com $^{40}\text{Ar}/^{36}\text{Ar}_{(\text{E})}$ variando entre 31100^{+9400}_{-6800} e 54000^{+14200}_{-9600} (SCLM europeu $^{40}\text{Ar}/^{36}\text{Ar} = 34000\text{-}52000$; Buikin *et al.*, 2005). Adicionalmente, as razões $^3\text{He}/^{22}\text{Ne}$ do SCLM patagônico (entre 12,00-13,70) são mais elevadas do que as definidas para MORBs ($^3\text{He}/^{22}\text{Ne} = 8.30\text{-}9.80$; Tucker & Mukhopadhyay, 2014), corroborando com o fato de o SCLM ser mais desgaseificado, radiogênico e nucleogênico. Comparativamente, as razões apresentadas acima de fato são mais radiogênicas/nucleogênicas que as de MORBs (e.g., $^3\text{He}/^4\text{He} = 8 \pm 1 \text{ RA}$; $^{21}\text{Ne}/^{22}\text{Ne} = 0.06$; $^{40}\text{Ar}/^{36}\text{Ar} \sim 40000$) (e.g., Sarda *et al.*, 1988; Moreira *et al.*, 1998; Tucker *et al.*, 2012). Diferentemente, os peridotitos de Gobernador Gregores representam uma mistura entre o SCLM (Pali-Aike) e o MORB. Esse metassomatismo é evidenciado pelas composições isotópicas de He e Ne, podendo ser tectonicamente explicado pela ressurgência do manto astenosférico em resposta à abertura de uma janela astenosférica abaixo da Patagônia como consequência da subducção da dorsal do Chile. Xenólitos mantélicos costumam não apresentar dados de Xe suficientemente diferentes do ar devido à sua baixa concentração. Entretanto, considerando-se 1σ de incerteza, algumas amostras de Pali-Aike e Gobernador Gregores mostram composições claramente distintas das do ar, mas similares as definidas para MORBs. Isso sugere que o excesso de ^{129}Xe a ^{136}Xe observado no SCLM é pelo menos igual ao de MORBs. Assim como é amplamente observado em estudos prévios de amostras de xenólitos mantélicos de várias partes do planeta, as composições de Kr são muito próximas às da atmosfera, o que inviabiliza tecer qualquer tipo de interpretação com base nos resultados obtidos. Adicionalmente, os peridotitos de Pali-Aike e Gobernador Gregores mostram composições depletadas de Sr-Nd-Pb. Uma idade de $13,64 \pm 0,83 \text{ Ma}$ foi obtida para PAVF através de uma isócrona de Rb-Sr baseada na composição isotópica da rocha-total, clinopiroxênio e flogopita. Esses dados representam a idade de formação da flogopita, que é um mineral essencial para determinar a idade do metassomatismo e sua potencial associação com eventos geotectônicos. Sendo assim, é possível relacionar a formação desse mineral com a colisão da dorsal do Chile contra a fossa do Chile e a subsequente abertura da janela astenosférica.

REFERÊNCIAS

- Albarède, F. (1992). How deep do common basalts form and differentiate? *Journal of Geophysical Research* **97**, 10997-11009.
- Aragón, E., Pinotti, L., D'Eramo, F., Castro, A., Rabbia, O., Coniglio, J., Demartis, M., Hernando, I., Cavarozzi, C. E. & Aguilera, Y. E. (2013). The Farallón-Aluk ridge collision with South America: Implications for the geochemical changes of slab window magmas from fore- to back-arc. *Geoscience Frontiers* **4**, 377-388.
- Ardolino, A. A. (1981). El vulcanismo cenozoico del borde suroriental de la meseta de Somún Curá, provincia del Chubut. In: VIII Congreso Geológico Argentino, San Luis, Actas, Vol. III, pp. 7-23.
- Barry, T. L., Ivanov, A. V., Rasskazov, S. V., Demonterova, E. I., Dunai, T. J., Davies, G. R. & Harrison, D. (2007). Helium isotopes provide no evidence for deep mantle involvement in widespread Cenozoic volcanism across Central Asia. *Lithos* **95**, 415-424.
- Bertotto, G. W. (2000). Cerro Agua Poca, un cono basáltico cuaternario portador de xenolitos ultramáficos, en el oeste de la provincia de La Pampa, Argentina. *Revista de la Asociación Geológica Argentina* **55**, 59-71.
- Bertotto, G. W., Cingolani, C. A. & Bjerg, E. A. (2009). Geochemical variations in Cenozoic back-arc basalts at the border of La Pampa and Mendoza provinces, Argentina. *Journal of South American Earth Sciences* **28**, 360-373.
- Bertotto, G. W., Mazzucchelli, M., Zanetti, A. & Vannucci, R. (2013). Petrology and geochemistry of the back-arc lithospheric mantle beneath eastern Payunia (La Pampa, Argentina): Evidence from Agua Poca peridotite xenoliths. *Geochemical Journal* **47**, 219-234.
- Bjerg, E. A., Ntaflos, T., Kurat, G., Dobosi, G. & Labudía, C. H. (2005). The upper mantle beneath Patagonia, Argentina, documented by xenoliths from alkali basalts. *Journal of South American Earth Sciences* **18**, 125-145.

Bjerg, E. A., Ntaflou, T., Thöni, M., Aliani, P. & Labudis, C. H. (2009). Heterogeneous Lithospheric Mantle beneath Northern Patagonia: Evidence from Prahuanique Garnet- and Spinel-Peridotites. *Journal of Petrology* **50**, 1267-1298.

Boutonnet, E., Arnaud, E., Guivel, C., Lagabrielle, Y., Scalabrino, B. & Espinoza, F. (2010). Subduction of the South Chile active spreading ridge: A 17 Ma to 3 Ma magmatic record in central Patagonia (western edge of Meseta del Lago Buenos Aires, Argentina). *Journal of Volcanology and Geothermal Research* **189**, 319-339.

Breitsprecher, K. & Thorkelson, D. J. (2009). Neogene kinematic history of Nazca-Antarctic-Phoenix slab windows beneath Patagonia and the Antarctic Peninsula. *Tectonophysics* **464**, 10-20.

Bruni, S. (2004). The Cenozoic back-arc magmatism of Central Patagonia (44°-46°S): activation of different mantle domains in space and time. Tesi di Dottorato. Università di Pisa, Corso di Dottorato in Scienze della Terra, Italia. 144p.

Bruni, S., D'Orazio, M., Haller, M. J., Innocenti, F., Manetti, P., Pécskay, Z. & Tonarini, S. (2008). Time-evolution of magma sources in a continental back-arc setting: the Cenozoic basalts from Sierra de San Bernardo (Patagonia, Chubut, Argentina). *Geological Magazine* **145**, 714-732.

Buikin, A., Tieloff, M., Hopp, J., Althaus, T., Korochantseva, E., Schwarz, W. H. & Altherr, R. (2005). Noble gas isotopes suggest deep mantle plume source of late Cenozoic mafic alkaline volcanism in Europe. *Earth and Planetary Science Letters* **230**, 143-162.

Burnard, P. G., Graham, D. W. & Turner, G. (1997). Vesicle-specific noble gas analyses of "popping rock": Implications for primordial noble gases in Earth. *Science* **276**, 568-571.

Cande, S. C. & Leslie, R. B. (1986). Late Cenozoic tectonics of the Southern Chile trench. *Journal Geophysical Research* **91**, 471-496.

Charrier, R., Linares, E., Niemeyer, H. & Skarmeta, J. (1979). K-Ar ages of basalt flows of the Meseta Buenos Aires in southern Chile and their relation to the southeast Pacific triple junction. *Geology* **7**, 436-439.

Conceição, R. V., Mallmann, G., Koester, E., Schilling, M., Bertotto, G. W. & Rodriguez-Vargas, A. (2005). Andean subduction-related mantle xenoliths: isotopic evidence of Sr-Nd decoupling during metasomatism. *Lithos* **82**, 273-287.

Conceição, R. V., Sumino, H., Orihashi, Y. & Nagao, K. (2007). Mantle heterogeneity evidence from South Patagonia, Argentina indicated by noble gas analysis on mantle xenoliths. *Geochimica et Cosmochimica Acta* **71**, A185.

Conceição, R. V., Sumino, H., Orihashi, Y., Jalowitzki, T. L. R. & Gervasoni, F. (2009). Noble gases analysis on mantle xenoliths from South Patagonia, Argentina. In: Simpósio 45 anos de Geocronologia no Brasil, 2009, São Paulo. Boletim de Resumos Expandidos do Simpósio 45 anos de Geocronologia no Brasil, 2009. p. 162-164.

Czuppon, Gy., Matsumoto, T., Handler, M. R. & Matsuda, J. (2009). Noble gases in spinel peridotite xenoliths from Mt Quincan, North Queensland, Australia: Undisturbed MORB-type noble gases in the subcontinental lithospheric mantle. *Chemical Geology* **266**, 19-28.

Czuppon, Gy., Matsumoto, T., Matsuda, J., Everard, J. & Sutherland, L. (2010). Noble gases in anhydrous mantle xenoliths from Tasmania in comparison with other localities from eastern Australia: Implications for the tectonic evolution. *Earth and Planetary Science Letters* **299**, 317-327.

Dantas, C., Grégoire, M., Koester, E., Conceição, R. V. & Rieck Jr., N. (2009). The lherzolite-websterite xenolith suite from Northern Patagonia (Argentina): Evidence of mantle-melt reaction processes. *Lithos* **107**, 107-120.

Dasgupta, R., Hirschmann, M. M. & Smith, N. D. (2007). Partial melting experiments of peridotite+CO₂ at 3 GPa and genesis of alkalic ocean island basalts. *Journal of Petrology* **48**, 2093-2124.

- de Ignacio, C., López, I., Oyarzun, R. & Márquez, A. (2001). The northern Patagonia Somuncura plateau basalts: a product of slab-induced, shallow asthenospheric upwelling? *Terra Nova* **13**, 117-121.
- Diegor, W., Longerich, H., Abrajano, T. & Horn, I. (2001). Applicability of a high pressure digestion technique to the analysis of sediment and soil samples by inductively coupled plasma-mass spectrometry. *Analytica Chimica Acta* **431**, 195-207.
- Dodson, A. & Brandon, A. D. (1999). Radiogenic helium in xenoliths from Simcoe, Washington, USA: implications for metasomatic processes in the mantle wedge above subduction zones. *Chemical Geology* **160**, 371-385.
- D'Orazio, M., Agostini, S., Mazzarini, F., Innocenti, F., Manetti, P., Haller, M. & Lahsen, A. (2000). The Pali Aike Volcanic Field, Patagonia: slab-window magmatism near the tip of South America. *Tectonophysics* **321**, 407-427.
- D'Orazio, M., Agostini, S., Innocenti, F., Haller, M., Manetti, P. & Mazzarini, F. (2001). Slab window-related magmatism from southernmost South America: the Late Miocene mafic volcanics from the Estancia Glencross Area (~52°S, Argentina-Chile). *Lithos* **57**, 67-89.
- D'Orazio, M., Innocenti, F., Manetti, P. & Haller, M. (2004). Cenozoic back-arc magmatism of the southern extra-Andean Patagonia (44°30'-52°S): a review of geochemical data and geodynamic interpretations. *Revista de la Asociación Geológica Argentina* **59**, 525-538.
- Dunai, T. J. & Baur, H. (1995). Helium, neon, and argon systematics of the European subcontinental mantle: implications for its geochemical evolution. *Geochimica et Cosmochimica Acta* **59**, 2767-2783.
- Dyhr, C. T., Holm, P. M., Llambías, E. J. & Scherstén, A. (2013). Subduction controls on Miocene back-arc lavas from Sierra de Huantraico and La Matancilla and new ⁴⁰Ar/³⁹Ar dating from the Mendoza Region, Argentina. *Lithos* **179**, 67-83.

Espinoza, F., Morata, D., Pelleter, E., Maury, R. C., Suárez, M., Lagabrielle, Y., Polvé, M., Bellon, H., Cotten, J., De la Cruz, R. & Guivel, C. (2005). Petrogenesis of the Eocene and Mio-Pliocene alkaline basaltic magmatism in Meseta Chile Chico, southern Patagonia, Chile: Evidence for the participation of two slab windows. *Lithos* **82**, 315-343.

Espinoza, F., Morata, D., Polvé, M., Lagabrielle, Y., Maury, R., de la Rupelle, A., Guivel, C., Cotten, J., Bellon, H. & Suárez, M. (2010). Middle Miocene calc-alkaline volcanism in Central Patagonia (47°S): Petrogenesis and implication for slab dynamics. *Andean Geology* **37**, 300-328.

Faccini, B., Bonadiman, C., Coltorti, M., Grégoire, M. & Siena, F. (2013). Oceanic Material Recycled within the Sub-Patagonian Lithospheric Mantle (Cerro del Fraile, Argentina). *Journal of Petrology* **54**, 1211-1258.

Folguera, A., Naranjo, J. A., Orihashi, Y., Sumino, H., Nagao, K., Polanco, E. & Ramos, V. A. (2009). Retroarc volcanism in the northern San Rafael Block (34°-35°30'S), southern Central Andes: Occurrence, age, and tectonic setting. *Journal of Volcanology and Geothermal Research* **186**, 169-185.

Gautheron, C. E. & Moreira, M. (2002). Helium signature of the subcontinental lithospheric mantle. *Earth and Planetary Science Letters* **199**, 39-47.

Gautheron, C. E., Moreira, M. & Allègre, C. (2005). He, Ne and Ar composition of the European lithospheric mantle. *Chemical Geology* **217**, 97-112.

Gazel, E., Hoernle, K., Carr, M. J., Herzberg, C., Saginor, I., van den Bogaard, P., Hauff, F., Feigenson, M. & Swisher III, C. (2011). Plume-subduction interaction in southern Central America: Mantle upwelling and slab melting. *Lithos* **121**, 117-134.

Germa, A., Quidelleur, X., Gillot, P. Y. & Tchilinguirian, P. (2010). Volcanic evolution of the back-arc Pleistocene Payun Matru volcanic field (Argentina). *Journal of South American Earth Sciences* **29**, 717-730.

Gervasoni, F., Conceição, R. V., Jalowitzki, T. L. R., Schilling, M. E., Orihashi, Y., Nakai, S. & Sylvester, P. (2012). Heterogeneidades do manto litosférico subcontinental no extremo sul da Placa Sul-americana: influência da subducção atual e interações litosfera-astenosfera sob o Campo Vulcânico de Pali Aike. *Pesquisas em Geociências* **39**, 269-285.

Godard, M., Lagabrielle, Y., Alard, O. & Harvey, J. (2008). Geochemistry of the highly depleted peridotites drilled at ODP Sites 1272 and 1274 (Fifteen-Twenty Fracture Zone, Mid-Atlantic Ridge): Implications for mantle dynamics beneath a slow spreading ridge. *Earth and Planetary Science Letters* **267**, 410-425.

Gorring, M. L. & Kay, S. M. (2000). Carbonatite metasomatized peridotite xenoliths from southern Patagonia: implications for lithospheric processes and Neogene plateau magmatism. *Contributions to Mineralogy and Petrology* **140**, 55-72.

Gorring, M. L. & Kay, S. M. (2001). Mantle processes and sources of Neogene slab window magmas from Southern Patagonia, Argentina. *Journal of Petrology* **42**, 1067-1094.

Gorring, M. L., Kay, S. M., Zeitler, P. K., Ramos, V. A., Rubiolo, D., Fernandez, M. I. & Panza, J. L. (1997). Neogene Patagonian plateau lavas: continental magmas associated with ridge collision at the Chile Triple Junction. *Tectonics* **16**, 1-17.

Gorring, M. L., Singer, B., Gowers, J. & Kay, S. M. (2003). Plio-Pleistocene basalts from the Meseta del Lago Buenos Aires, Argentina: evidence for asthenosphere-lithosphere interactions during slab window magmatism. *Chemical Geology* **193**, 215-235.

Graham, D. W. (2002). Noble Gas Isotope Geochemistry of Mid-Ocean Ridge and Ocean Island Basalts: Characterization of Mantle Source Reservoirs. Porcelli, D.; Ballentine, C. J. & Wieler, R. (editors). *Reviews in Mineralogy and Geochemistry*, Mineralogical Society of America, Washington-DC, 247-318pp.

Grégoire, M., Moine, B. N., O'Reilly, S. Y., Cottin, J. Y. & Giret, A. (2000). Trace Element Residence and Partitioning in Mantle Xenoliths Metasomatized by Highly

Alkaline, Silicate- and Carbonate-rich Melts (Kerguelen Islands, Indian Ocean).

Journal of Petrology **41**, 477-509.

Gudnason, J., Holm, P. M., Søger, N. & Llambías, E. J. (2012). Geochronology of the late Pliocene to recent volcanic activity in the Payenia back-arc volcanic province, Mendoza Argentina. *Journal of South American Earth Sciences* **37**, 191-201.

Guivel, C., Morata, D., Pelleter, E., Espinoza, F., Maury, R. C., Lagabrielle, Y., Polvé, M., Bellon, H., Cotton, J., Benoit, M., Suárez, M. & de la Cruz, R. (2006). Miocene to Late Quaternary Patagonian basalts (46-47°S): Geochronometric and geochemical evidence for slab tearing due to active spreading ridge subduction. *Journal of Volcanology and Geothermal Research* **149**, 346-370.

Hanyu, T., Kawabata, H., Tatsumi, Y., Kimura, J.-I., Hyodo, H., Sato, K., Miyazaki, T., Chang, Q., Hirahara, Y., Takahashi, T., Senda, R. & Nakai, S. (2014). Isotope evolution in the HIMU reservoir beneath St. Helena: Implications for the mantle recycling of U and Th. *Geochimica et Cosmochimica Acta* **143**, 232-252.

Hart, S. R., Hauri, E. H., Oschmann, L. A. & Whitehead, J. A. (1992). Mantle Plumes and Entrainment: Isotopic Evidence. *Science* **256**, 517-520.

Herzberg, C. (2011). Identification of Source Lithology in the Hawaiian and Canary Islands: Implications for Origins. *Journal of Petrology* **52**, 113-146.

Herzberg, C. & Asimow, P. D. (2008). Petrology of some oceanic island basalts: PRIMELT2.XLS software for primary magma calculation. *Geochemistry, Geophysics, Geosystems* **9**: 1-25. <http://dx.doi.org/10.1029/2008GC002057>.

Hirschmann, M. M., Kogiso, T., Baker, M. B. & Stolper, E. M. (2003). Alkalic magmas generated by partial melting of garnet pyroxenite. *Geology* **31**, 481-484.

Hiyagon, H., Ozima, M., Marty, B., Zashu, S. & Sakai, H. (1992). Noble gases in submarine glasses from mid-oceanic ridges and Loihi seamount: Constraints on the early history of the Earth. *Geochimica et Cosmochimica Acta* **56**, 1301-1316.

- Holland, G., Cassidy, M. & Ballentine, C. J. (2009). Meteorite Kr in Earth's Mantle Suggests a Late Accretionary Source for the Atmosphere. *Science* **326**, 1522-1525.
- Honda, S., Orihashi, Y., Mibe, K., Motoki, A., Sumino, H. & Haller, M. J. (2006). Mantle wedge deformation by subducting and rotating slab and its possible implication. *Earth, Planets and Space* **58**, 1087-1092.
- Hopp, J., Trierloff, M. & Altherr, R. (2004). Neon isotopes in mantle rocks from the Red Sea region reveal large-scale plume-lithosphere interaction. *Earth and Planetary Science Letters* **219**, 61-76.
- Jackson, M. G. & Dasgupta, R. (2008). Compositions of HIMU, EM1, and EM2 from global trends between radiogenic isotopes and major elements in ocean island basalts. *Earth and Planetary Science Letters* **276**, 175-186.
- Jalowitzki, T. L. R., Conceição, R. V., Bertotto, G. W. & Orihashi, Y. (2008). Contribuição de fluidos da placa de Nazca à fonte do magma alcalino do tipo OIB associado a uma pluma mantélica no norte da Patagônia, Argentina. *Geochimica Brasiliensis* **22**, 073-090.
- Jalowitzki, T. L. R., Conceição, R. V., Orihashi, Y., Bertotto, G. W., Nakai, S. & Schilling, M. (2010). Evolução geoquímica de peridotitos e piroxenitos do Manto Litosférico Subcontinental do vulcão Agua Poca, Terreno Cuyania, Argentina. *Pesquisas em Geociências* **37**, 143-167.
- Jalowitzki, T. L. R., Sumino, H., Conceição, R. V., Orihashi, Y. & Nagao, K. (2012). Noble gas isotopes of mantle-derived xenoliths from Patagonian subcontinental lithospheric mantle (37-52°S). In: Annual Meeting of Geochemical Society of Japan, Fukuoka.
- Jalowitzki, T. L. R., Sumino, H., Conceição, R. V., Orihashi, Y., Nagao, K., Bertotto, G. W., Schilling, M., Gervasoni, F. (2014). Helium and neon isotopes in mantle-derived xenoliths from Southern Patagonia: MORB-like and radiogenic/nucleogenic noble gas components in the subcontinental lithospheric mantle. In: 9th South American symposium on isotope geology - 9th SSAGI, 2014, São Paulo.

Jenner, G. A., Longerich, H. P., Jackson, S. E. & Fryer, B. J. (1990). ICP-MS - a powerful tool for high-precision trace-element analysis in earth sciences: evidence from analysis of selected U.S.G.S. reference samples. *Chemical Geology* **83**, 133-148.

Johnson, J. S., Gibson, S. A., Thompson, R. N. & Nowell, G. M. (2005). Volcanism in the Vitim Volcanic Field, Siberia: geochemical evidence for a mantle plume beneath the Baikal Rift zone. *Journal of Petrology* **46**, 1309-1344.

Kay, S. M. & Mancilla, O. (2001). Neogene shallow subduction segments in the Chilean/Argentine Andes and Andean-type margins. *Geological Society of America* **63**, A156.

Kay, S. M. & Copeland, P. (2006). Early to middle Miocene backarc magmas of the Neuquén Basin: Geochemical consequences of slab shallowing and the westward drift of South America. *Geological Society of America, Special Paper* **407**, 185-213.

Kay, S. M., Ardolino, A. A., Franchi, M. & Ramos, V. A. (1993). Origen de la Meseta de Somuncura: distribución and geoquímica de sus rocas volcánicas máficas. In: XII Congreso Geológico Argentino, Buenos Aires, Actas, Vol. IV, pp. 236-248.

Kay, S. M., Gorrington, M. & Ramos, V. (2004). Magmatic sources, setting and causes of Eocene to Recent Patagonian plateau magmatism (36°S to 52°S latitude). *Revista de la Asociación Geológica Argentina* **59(4)**: 556-568.

Kay, S. M., Burns, W. M., Copeland, P., Mancilla, O. (2006a). Upper Cretaceous to Holocene magmatism and evidence for transient Miocene shallowing of the Andean subduction zone under the northern Neuquén Basin. *Geological Society of America, Special Paper* **407**, 19-60.

Kay, S. M., Copeland, P., Mancilla, O. (2006b). Evolution of the late Miocene Chachahuén volcanic complex at 37°S over a transient shallow subduction zone under the Neuquén Andes. *Geological Society of America, Special Paper* **407**, 215-246.

- Kay, S. M., Ardolino, A., Gorring, M. & Ramos, V. (2007). The Somuncura Large Igneous Province in Patagonia: Interaction of a Transient Mantle Thermal Anomaly with a Subducting Slab. *Journal of Petrology* **48**, 43-77.
- Kay, S. M., Jones, H. A. & Kay, R. W. (2013). Origin of Tertiary to Recent EM- and subduction-like chemical and isotopic signatures in Auca Mahuida region (37°-38°S) and other Patagonian plateau lavas. *Contributions to Mineralogy and Petrology* **166**, 165-192.
- Kilian, R. & Stern, C. R. (2002). Constraints on the interaction between slab melts and the mantle wedge from adakitic glass in peridotite xenoliths. *European Journal of Mineralogy* **14**, 25-36.
- Kim, K. H., Nagao, K., Tanaka, T., Sumino, H., Nakamura, T., Okuno, M., Lock, J.B., Youn, J.S. & Song, J. (2005). He-Ar and Nd-Sr isotopic compositions of ultramafic xenoliths and host alkali basalts from the Korean peninsula. *Geochemical Journal* **39**, 341-356.
- Kogiso, T. & Hirschmann, M. M. (2006). Partial melting experiments of biminerally eclogite and the role of recycled mafic oceanic crust in the genesis of ocean island basalts. *Earth and Planetary Science Letters* **249**, 188-199.
- Kogiso, T., Hirschmann, M. M. & Frost, D. J. (2003). High-pressure partial melting of garnet pyroxenite: possible mafic lithologies in the source of ocean island basalts. *Earth and Planetary Science Letters* **216**, 603-617.
- Kunz, J., Staudacher, T. & Allègre, C. J. (1998). Plutonium-fission xenon found in Earth's mantle. *Science* **280**: 877-880.
- Laurora, A., Mazzucchelli, M., Rivalenti, G., Vannucci, R., Zanetti, A., Barbieri, M. A. & Cingolani, C. A. (2001). Metasomatism and melting in carbonated peridotite xenoliths from the mantle wedge: the Gobernador Gregores case (Southern Patagonia). *Journal of Petrology* **42**, 69-87.

Massaferro, G. I., Haller, M. J., Dostal, J., Pécskay, Z., Prez, H., Meister, C. & Alric, V. (2014). Possible sources for monogenetic Pliocene-Quaternary basaltic volcanism in northern Patagonia. *Journal of South American Earth Sciences* **55**, 29-42.

Matsumoto, T., Honda, M., McDougall, I. & O'Reilly, S. Y. (1998). Noble gases in anhydrous lherzolites from the newer volcanics, southeastern Australia: a MORB-like reservoir in the subcontinental mantle. *Geochimica et Cosmochimica Acta* **62**, 2335-2345.

Matsumoto, T., Honda, M., McDougall, I., O'Reilly, S.Y., Norman, M. & Yaxley, G. (2000). Noble gases in pyroxenites and metasomatised peridotites from the Newer Volcanics, southeastern Australia: implications for mantle metasomatism. *Chemical Geology* **168**, 49-73.

Mayer, B., Jung, S., Romer, R. L., Stracke, A., Haase, K. M. & Garbe-Schönberg, C. -D. (2013). Petrogenesis of Tertiary Hornblende-bearing Lavas in the Rhön, Germany. *Journal of Petrology* **54**, 2095-2123.

McKenzie, D. A. N. & O'Nions, R. K. (1995). The source regions of ocean island basalts. *Journal of Petrology* **36**, 133-159.

Mercier, J-C. C. & Nicolas, A. (1975). Textures and fabrics of upper mantle peridotites as illustrated by basalts xenoliths. *Journal of Petrology* **16**, 454-487.

Morata, D., de la Cruz, R., Suárez, M. & Demant, A. (2000). Mantle xenoliths and xenocrysts in the late Paleocene Patagonian continental flood basalts from Aysen, S. Chile. In: IX Congreso Geológico Chileno. Actas 2, 226-229.

Moreira, M., Kunz, J. & Allègre, C. (1998). Rare gas systematics in popping rock: isotopic and elemental compositions in the upper mantle. *Science* **279**, 1178-1181.

Mukasa, S. B., Blatter, D. L. & Andronikov, A. V. (2007). Mantle peridotite xenoliths in andesite lava at El Peñon, central Mexican Volcanic Belt: Isotopic and trace element evidence for melting and metasomatism in the mantle wedge beneath an active arc. *Earth and Planetary Science Letters* **260**, 37-55.

Mukhopadhyay, S. (2012). Early differentiation and volatile accretion recorded in deep-mantle neon and xenon. *Nature* **486**, 101-104.

Mundl, A., Ntaflos, Th., Ackerman, L., Bizimis, M., Bjerg, E. A. & Hauzenberger, C. A. (2015). Mesoproterozoic and Paleoproterozoic subcontinental lithospheric mantle domains beneath southern Patagonia: Isotopic evidence for its connection to Africa and Antarctica. *Geology* **43**, 39-42.

Muñoz, J., Troncoso, R., Duhart, P., Crignola, P., Farmer, L. & Stern, C. R. (2000). The Mid-Tertiary coastal magmatic belt in south-central Chile (36°-43°S): its relation to crustal extension, mantle upwelling, and the late Oligocene increase in the rate of oceanic plate subduction beneath South America. *Andean Geology* **27**(2), 177-203.

Nagao, K., Ogata, A., Miura, Y., Matsuda, J. & Akimoto, S. (1991). Highly reproducible 13 and 17 ka K-Ar ages of two volcanic rocks. *Geochemical Journal* **25**, 447-451.

Nagao, K., Ogata, A., Miura, Y. N. & Yamaguchi, K. (1996). Ar isotope analysis for K-Ar dating using two modified-VG5400 mass spectrometers-I: isotope dilution method. *Journal of Mass Spectrometry Society of Japan* **44**, 39-61.

Niu, Y. (2004). Bulk-rock Major and Trace Element Compositions of Abyssal Peridotites: Implications for Mantle Melting, Melt Extraction and Post-melting Processes Beneath Mid-Ocean Ridges. *Journal of Petrology* **45**, 2423-2458.

Ntaflos, Th., Bjerg, E. A., Labudia, C. H. & Kurat, G. (2007). Depleted lithosphere from the mantle wedge beneath Tres Lagos, southern Patagonia, Argentina. *Lithos* **94**, 46-65.

Orihashi, Y. & Hirata T. (2003). Rapid quantitative analysis of Y and REE abundances in XRF glass bead for selected GSJ reference rock standards using UV laser ablation ICP-MS. *Geochemical Journal* **37**, 401-412.

Orihashi, Y., Naranjo, J. A., Motoki, A., Sumino, H., Hirata, D., Anma, R. & Nagao, K. (2004). Quaternary volcanic activity of Hudson and Lautaro volcanoes, Chilean Patagonia: new constraints from K-Ar ages. *Andean Geology* **31**, 207-224.

Orihashi, Y., Motoki, A., Haller, M. J. & CHRISTMASSY Project Volcanic Group. (2005). Petrogenesis of relatively large-volume basalts on extra-back arc province: Somuncura plateau, north Patagonia. *Earth Monthly* **27**, 438-447.

Orihashi, Y., Motoki, A., Haller, M., Sumino, H. & CHRISMASSEY Group. (2006). Petrogenesis of Somuncura plateau basalt in an extra-back arc province: Melting of hydrous wadsleyite beneath northern Patagonia. *Geochimica et Cosmochimica Acta* **70**, A463.

Ozima, M. & Podosek, F. A. (1983). Noble Gas Geochemistry (Cambridge Univ. Press, Cambridge, 367p).

Parada, M. A., Lahsen, A. & Palacios, C. (2001). Ages and geochemistry of Mesozoic-Eocene back-arc volcanic rocks in the Aysén region of the Patagonian Andes, Chile. *Andean Geology* **28**, 25-46.

Parai, R., Mukhopadhyay, S. & Lassiter, J. C. (2009). New constraints on the HIMU mantle from neon and helium isotopic compositions of basalts from the Cook-Austral Islands. *Earth and Planetary Science Letters* **277**, 253-261.

Parai, R., Mukhopadhyay, S. & Standish, J. J. (2012). Heterogeneous upper mantle Ne, Ar and Xe isotopic compositions and a possible Dupal noble gas signature recorded in basalts from the Southwest Indian Ridge. *Earth and Planetary Science Letters* **359-360**, 227-239.

Pilet, S., Hernandez, J., Sylvester, P. & Poujol, M. (2005). The metasomatic alternative for ocean island basalt chemical heterogeneity. *Earth and Planetary Science Letters* **236**, 148-166.

Pilet, S., Baker, M. B. & Stolper, E. M. (2008). Metasomatized lithosphere and the origin of alkaline lavas. *Science* **320**, 916-919.

Ramos, V. A. (1999). Plate tectonic setting of the Andean Cordillera. *Episodes* **22**, 183-190.

Ramos, V. A. & Kay, S. M. (2006). Overview of the tectonic evolution of the southern Central Andes of Mendoza and Neuquén (35°-39°S latitude). *Geological Society of America*, Special Paper **407**, 1-17.

Ramos, V. A., Litvak, V. D., Folguera, A. & Spagnuolo, M. (2014). An Andean tectonic cycle: From crustal thickening to extension in a thin crust (34°-37°SL). *Geoscience Frontiers* **5**, 351-367.

Rivalenti, G., Mazzucchelli, M., Laurora, A., Ciuffi, S. I. A., Zanetti, A., Vannucci, R., & Cingolani, C. A. (2004). The backarc mantle lithosphere in Patagonia, South America. *Journal of South American Earth Sciences* **17**, 121-152.

Rivalenti, G., Mazzucchelli, M., Zanetti, A., Vannucci, R., Bollinger, C., Hémond, C. & Bertotto, G. W. (2007). Xenoliths from Cerro de los Chenques (Patagonia): An example of slab-related metasomatism in the backarc lithospheric mantle. *Lithos* **99**, 45-67.

Salter, V. J. M. & Sachi-Kocher, A. (2010). An ancient metasomatic source for the Walvis Ridge basalts. *Chemical Geology* **273**, 151-167.

Schilling, M., Conceição, R. V., Mallmann, G., Koester, E., Kawashita, K., Hervé, F., Morata, D. & Motoki, A. (2005). Spinel-facies mantle xenoliths from Cerro Redondo, Argentine Patagonia: Petrographic, geochemical, and isotopic evidence of interaction between xenoliths and host basalt. *Lithos* **72**, 209-229.

Schilling, M., Carlson, R. W., Conceição, R. V., Dantas, C., Bertotto, G. W. & Koester, E. (2008). Re-Os isotope constraints on subcontinental lithospheric mantle evolution of southern South America. *Earth and Planetary Science Letters* **268**, 89-101.

Sarda, P., Staudacher, T., Allègre, C. J. (1988). Neon isotopes in submarine basalts. *Earth and Planetary Science Letters* **91**, 73-88.

Søager, N. & Holm, P. M. (2013). Melt-peridotite reactions in upwelling eclogite bodies: Constraints from EM1-type alkaline basalts in Payenia, Argentina. *Chemical Geology* **360-361**: 204-219.

- Søager, N., Holm, P. M. & Llambías, E. J. (2013). Payenia volcanic province, southern Mendoza, Argentina: OIB mantle upwelling in a backarc environment. *Chemical Geology* **349-350**: 36-53.
- Søager, N., Holm, P. M. & Thirlwall, M. F. (2015). Sr, Nd, Pb and Hf isotopic constraints on mantle sources and crustal contaminants in the Payenia volcanic province, Argentina. *Lithos* **212-215**: 368-378.
- Späth, A., le Roex, A. P. & Opiyo-Akech, N. (2001). Plume-lithosphere interaction and the origin of continental rift-related alkaline volcanism-the Chyulu Hills volcanic province, southern Kenya. *Journal of Petrology* **42**, 765-787.
- Staudacher, Th. & Allègre, C.J. (1982). Terrestrial xenology. *Earth and Planetary Science Letters* **60**, 389-406.
- Stern, C. R. (2004). Active Andean volcanism: its geologic and tectonic setting. *Andean Geology* **31**, 161-206.
- Stern, C. R., Frey, F. A., Futa, K., Zartman, R. E., Peng, Z. & Kyser, T. K. (1990). Trace element and Sr, Nd, Pb, and O isotopic composition of Pliocene and Quaternary alkali basalts of the Patagonian plateau lavas of southernmost South America. *Contributions to Mineralogy and Petrology* **104**, 294-308.
- Stern, C. R., Kilian, R., Olker, B., Hauri, E. H. & Kyser, T. K. (1999). Evidence from mantle xenoliths for relatively thin (<100 km) continental lithosphere below the Phanerozoic crust of southernmost South America. *Lithos* **48**, 217-235.
- Stracke, A., Hofmann, A. W. & Hart, S. R. (2005). FOZO, HIMU, and the rest of the mantle zoo. *Geochemistry, Geophysics, Geosystems* **6**, 1-20.
- Stuart, F. M., Lass-Evans, S., Fitton, J. G., Ellam, R. M. (2003). High $^3\text{He}/^4\text{He}$ ratios in picritic basalts from Baffin Island and the role of a mixed reservoir in mantle plumes. *Nature* **424**, 57-59.

Sumino, H., Nagao, K. & Notsu, K. (2001). Highly sensitive and precise measurement of helium isotopes using a mass spectrometer with double collector system. *Journal of the Mass Spectrometry Society of Japan* **49**, 61-68.

Sumino, H., Kaneoka, I., Matsufuji, K. & Sobolev, A. V. (2006). Deep mantle origin of kimberlite magmas revealed by neon isotopes. *Geophysical Research Letters* **33**, L16318. doi:10.1029/2006GL027144.

Sumino, H., Burgess, R., Mizukami, T., Wallis, S. R., Holland, G. & Ballentine, C. J. (2010). Seawater-derived noble gases and halogens preserved in exhumed mantle wedge peridotite. *Earth and Planetary Science Letters* **294**, 163-172.

Tanaka, R. & Orihashi, Y. (1997). XRF analysis of major and trace elements for silicate rocks using low dilution ratio fused glass. Technical Research Report (ERI, University of Tokyo), 2: 1-20.

Trieloff, M., Kunz, J., Clague, D. A., Harrison, D., Allègre, C. J. (2000). The nature of pristine noble gases in mantle plumes. *Science* **288**, 1036-1038.

Tucker, J. M. & Mukhopadhyay, S. (2014). Evidence for multiple magma ocean outgassing and atmospheric loss episodes from mantle noble gases. *Earth and Planetary Science Letters* **393**, 254-265.

Tucker, J. M., Mukhopadhyay, S. & Schilling, J.-G. (2012). The heavy noble gas composition of the depleted MORB mantle (DMM) and its implications for the preservation of heterogeneities in the mantle. *Earth and Planetary Science Letters* **355-356**, 244-254.

Varekamp, J. C., Hesse, A. & Mandeville, C. W. (2010). Back-arc basalts from the Loncopue graben (Province of Neuquen, Argentina). *Journal of Volcanology and Geothermal Research* **197**, 313-328.

Wörner, G., Zindler, A., Staudigel, H. & Schmincke, H. U. (1986). Sr, Nd, and Pb isotope geochemistry of Tertiary and Quaternary alkaline volcanics from West Germany. *Earth and Planetary Science Letters* **79**, 107-119.

Workman, R. K. & Hart, S. R. (2005). Major and trace element composition of the depleted MORB mantle (DMM). *Earth and Planetary Science Letters* **231**, 53-72.

Workman, R. K., Hart, S. R., Jackson, M., Regelous, M., Farley, K. A., Blusztajn, J., Kurz, M. & Staudigel, H. (2004). Recycled metasomatized lithosphere as the origin of the Enriched Mantle II (EM2) end-member: Evidence from the Samoan Volcanic Chain. *Geochemistry, Geophysics, Geosystems* **5**, 1-44.

Yamamoto, J., Nishimura, K., Sugimoto, T., Takemura, K., Takahata, N. & Sano, Y. (2009). Diffusive fractionation of noble gases in mantle with magma channels: Origin of low He/Ar in mantle-derived rocks. *Earth and Planetary Science Letters* **280**, 167-174.

Yang, H. -J., Frey, F. A. & Clague, D.A. (2003). Constraints on the source components of lavas forming the Hawaiian North Arch and Honolulu volcanics. *Journal of Petrology* **44**, 603-627.

Yang, Z. F. & Zhou, J. H. (2013). Can we identify source lithology of basalt? *Scientific Report* **3**, 1856. doi:10.1038/srep01856.

Zaffarana, C., Tommasi, A., Vauchez, A. & Grégoire, M. (2014). Microstructures and seismic properties of south Patagonian mantle xenoliths (Gobernador Gregores and Pali Aike). *Tectonophysics* **621**, 175-197.

Zindler, A. & Hart, S. (1986). Chemical Geodynamics. *Annual Review of Earth and Planetary Sciences* **14**, 493-57.

ARTIGO 1

GEOCHEMISTRY AND GEOCHRONOLOGY OF CENOZOIC ALKALINE BASALTS FROM PATAGONIA (36°S – 52°S): CONSTRAINTS FOR THEIR MANTLE SOURCES AND PETROGENESIS

Manuscrito submetido à revista científica *Journal of Petrology*

Assunto Journal of Petrology - Manuscript ID JPET-May-15-0058
Remetente <J.Petrology@earth.leeds.ac.uk>
Para <tiago.jalowitzki@ufrgs.br>
Cópia <tiago.jalowitzki@ufrgs.br>, <oripachi@eri.u-tokyo.ac.jp>, <rommulo.conceicao@ufrgs.br>, <gwbertotto@yahoo.com.ar>, <manuel.schilling@uach.cl>, <sumino@eqchem.s.u-tokyo.ac.jp>, <gervasoni.fe@uni-muenster.de>, <nagao@eqchem.s.u-tokyo.ac.jp>
Data 2015-05-19 17:27



19-May-2015

Dear Mr. Jalowitzki:

Your manuscript entitled "Geochemistry and geochronology of Cenozoic alkaline basalts from Patagonia (36°S - 52°S): Constraints for their mantle sources and petrogenesis" has been successfully submitted online and is presently being given full consideration for publication in the Journal of Petrology.

Your manuscript ID is JPET-May-15-0058.

Please mention the above manuscript ID in all future correspondence or when calling the office for questions. If there are any changes in your street address or e-mail address, please log in to Manuscript Central at <https://mc.manuscriptcentral.com/jpet> and edit your user information as appropriate.

You can also view the status of your manuscript at any time by checking your Author Center after logging in to <https://mc.manuscriptcentral.com/jpet>.

Thank you for submitting your manuscript to the Journal of Petrology.

Regards,

Alastair Lumsden
Editorial Manager Journal of Petrology

1 **Geochemistry and geochronology of Cenozoic alkaline basalts**
2 **from Patagonia (36°S – 52°S): Constraints for their mantle sources**
3 **and petrogenesis**

4

5 Tiago Jalowitzki ^{a,b*}, Yuji Orihashi ^c, Rommulo V. Conceição ^a, Gustavo W. Bertotto ^d, Manuel
6 Schilling ^e, Hirochika Sumino ^b, Fernanda Gervasoni ^f and Keisuke Nagao ^b

7

8 ^a Programa de Pós-graduação em Geociências, Instituto de Geociências, Universidade Federal do Rio
9 Grande do Sul (UFRGS). Av. Bento Gonçalves, 9500 - Prédio 43129, Bairro Agronomia, Porto Alegre
10 - RS, Brazil. CEP: 91501970, E-mail: tiago.jalowitzki@ufrgs.br, rommulo.conceicao@ufrgs.br

11 ^b Geochemical Research Center, Graduate School of Science, the University of Tokyo, Bunkyo-ku,
12 Tokyo 113-0033, Japan. E-mail: sumino@eqchem.s.u-tokyo.ac.jp, nagao@eqchem.s.u-tokyo.ac.jp

13 ^c Earthquake Research Institute, the University of Tokyo, Yayoi 1-1-1, Bunkyo-Ku, 113-0032, Tokyo,
14 Japan. E-mail: oripachi@eri.u-tokyo.ac.jp

15 ^d INCITAP, CONICET – Universidad Nacional de La Pampa, Uruguay 151 (6300), Santa Rosa, La
16 Pampa, Argentina. E-mail: gwbertotto@yahoo.com.ar

17 ^e Instituto de Ciencias de la Tierra, Facultad de Ciencias, Universidad Austral de Chile, Valdivia,
18 Región de Los Ríos, Chile. Código postal 5090000. E-mail: manuel.schilling@uach.cl

19 ^f Institut für Mineralogie, Westfälische-Wilhelms-Universität Münster, Germany. E-mail:
20 gervasoni.fe@uni-muenster.de

21

22 ***Corresponding author:** Programa de Pós-graduação em Geociências, Instituto de Geociências,
23 Universidade Federal do Rio Grande do Sul (UFRGS). Av. Bento Gonçalves, 9500 – Prédio 43129,
24 Bairro Agronomia, Porto Alegre - RS, Brazil. CEP: 91501970. Telephone number: +55(51)3308-7287.
25 **E-mail address:** tiago.jalowitzki@ufrgs.br (T. Jalowitzki).

26

1 **ABSTRACT**

2

3 The Patagonian Basaltic Province, located on the extra-Andean back-arc (Argentina and
4 Chile), is characterized mainly by large volumes of Cenozoic mafic magmas. Based on their
5 mineralogy, geochemical and Sr–Nd–Pb isotope compositions, we newly defined two groups
6 of the Cenozoic Patagonian basaltic rocks with intraplate signatures.

7 Group I basalts comprise basanites and nephelinites with prominent negative Rb, K, Pb, and
8 Ti anomalies coupled with positive Nb–Ta anomalies. These basaltic rocks have low Rb/Sr
9 and K/(La, Ce) ratios, negative K/K* (0.14–0.34) anomalies, and high Ce/Pb ratio, which
10 have indicated that phlogopite existed as a residual phase during small degrees of partial
11 melting (<3%) of a garnet-peridotite at asthenospheric depths (113–134 km). The Group I
12 Sr–Nd–Pb isotopic ratios ($^{87}\text{Sr}/^{86}\text{Sr}_i = 0.703179\text{--}0.703403$; $^{143}\text{Nd}/^{144}\text{Nd}_i =$
13 $0.512776\text{--}0.512967$; $^{206}\text{Pb}/^{204}\text{Pb} = 18.597\text{--}19.186$; $^{207}\text{Pb}/^{204}\text{Pb} = 15.563\text{--}15.660$; $^{208}\text{Pb}/^{204}\text{Pb} =$
14 $38.423\text{--}38.997$) represent a depleted OIB-like component. Moreover, they show identical
15 isotopic ratios of phlogopites from Patagonian mantle xenoliths. These isotope signatures
16 suggest a relation of intraplate volcanism with compositional anomalies (“wet spot”). The
17 calculated potential temperatures (T_P) for Group I basalts are higher (1400–1563°C) than
18 normal ambient mantle temperature (1350±50°C), perhaps because of a thermal anomaly
19 beneath Patagonia.

20 Group II basalts consist of trachybasalts, basanites and mugearites characterized by variable
21 enrichments in LILE (e.g., Cs, Ba, K, Sr) and Pb with respect to HFSE (e.g., Nb–Ta) and REE
22 (e.g., La, Ce), as well as positive K/K* and Pb/Pb* anomalies. These basalts have slight
23 radiogenic Sr–Nd and less radiogenic Pb–Pb isotopic ratios than those of Group I basalts,
24 indicating the contribution of an enriched mantle component (EMI). In general, the amount of
25 slab components decreases eastward, reflecting across-arc geochemical variation. Although

1 Group II basalts display EM affinity, they have high Nb/Ta (>18), Ce/Pb (>20), Nb/U (>37),
2 and Nb/Nb* (>1) ratios, and low La/Nb (<1) ratios, similar to basalts of Group I and to
3 worldwide intraplate basalts from continental and oceanic settings. The calculated T_P for
4 Group II basalts (1305–1364°C) overlap the normal ambient mantle temperature (1350±50°C),
5 which excludes the influence of any thermal anomaly. Therefore, we argue that the mixing
6 process among a depleted mantle-wedge, a melt with ancient OIB-like composition and the
7 subducted oceanic lithosphere allowed the generation of pyroxenite veins close to the
8 lithosphere–asthenosphere boundary (89–94 km), with partial melting (5–10%) capable of
9 producing the features of EMI Group II basalts.

10 Finally, based on spatiotemporal variations (K–Ar ages, latitude, longitude and depths), the
11 Cenozoic Patagonian basalts presented in this study show a complex tectono-magmatic
12 evolution. In general, the mantle source depth seems to play an important role in the genesis
13 of all Group I and II basalts. However, in Payenia volcanic province, it was possible to divide
14 Group I and II basalts based on their eruption ages, where Group II (Pleistocene) are younger
15 than Group I (Miocene). The across-arc geochemical variation was identified in
16 Plio–Pleistocene basalts from Meseta de Somún Curá, where Group II basalts are located
17 nearer the volcanic arc than Group I basalts are. In southern Patagonia, Group I and II basalts
18 can be divided based on the westward increase of slab-derived components, latitude and
19 eruption ages. The interaction with enriched components is restricted to older lavas located
20 close to the Austral Volcanic Zone and at the latitude of Meseta Central.

21

22 **KEY WORDS:** Patagonian alkaline basalts; Subcontinental mantle sources; Sr–Nd–Pb
23 isotopes; K–Ar ages; Wet spot.

24

25

1 INTRODUCTION

2

3 Geochemical and isotopic heterogeneities observed worldwide in continental alkaline
4 basalts cannot always be explained as the result of simple partial melting of a peridotitic mantle
5 source. Instead, they require a mantle with lithological heterogeneities (pyroxenite or eclogite)
6 to explain their petrogenesis (e.g., Herzberg, 2011; Zhang *et al.*, 2012). Consequently, to
7 elucidate the origin of intraplate alkaline basalts, different mantle sources have been suggested
8 in previous reports of the literature: 1) the eclogite/pyroxenite relation (Hirschmann *et al.*,
9 2003; Kogiso *et al.*, 2003; Kogiso & Hirschmann, 2006; Yang & Zhou, 2013), 2) hydrous
10 metasomatism [e.g., glimerite and/or hornblendite – McKenzie & O’Nions (1995); Späth *et al.*
11 (2001); Yang *et al.* (2003); Johnson *et al.* (2005); Pilet *et al.* (2005, 2008, 2010); Mayer *et al.*
12 (2013)], 3) slab-derived metasomatism (Gazel *et al.*, 2011; Dyhr *et al.*, 2013; Kay *et al.*, 2013),
13 and 4) carbonatitic metasomatism [carbonated peridotite – Gorryng & Kay (2000); Dasgupta *et*
14 *al.* (2007); Zeng *et al.* (2010)].

15 Although the mantle source of continental alkaline basalts remains a matter of considerable
16 debate, the Patagonian Basaltic Province offers an opportunity to investigate the previously
17 described mantle processes. This volcanic province, located in the extra-Andean continental
18 back-arc (approx. 36°S – 52°S), represents one of the largest Cenozoic magmatic events in the
19 world (e.g., Kay *et al.*, 2004). Several reports have described that OIB-like alkaline basalts
20 collected in Patagonia reflect different sources and a rather complex history of metasomatism
21 (e.g., Stern *et al.*, 1990; Gorryng *et al.*, 1997, 2003; D’Orazio *et al.*, 2000, 2004; Kay *et al.*,
22 2004, 2007, 2013; Espinoza *et al.*, 2005; Guivel *et al.*, 2006; Bruni *et al.*, 2008; Jalowitzki *et al.*,
23 2008, 2009; Bertotto *et al.*, 2009; Varekamp *et al.*, 2010, 2015; Dyhr *et al.*, 2013; Søgager &
24 Holm, 2013; Søgager *et al.*, 2013, 2015; Massaferrero *et al.*, 2014).

1 Based on major and trace elements as well as Sr–Nd–Pb–O isotopic composition, *Stern et*
2 *al.* (1990) classified the Pliocene to Quaternary alkali basalts from Patagonian plateaus as
3 “cratonic” and “transitional”. The cratonic basalts do not include slab-derived components and
4 display strong geochemical similarity with ocean island basalts (OIBs). The geochemical
5 features of transitional basalts suggest the introduction of slab-derived components in lesser
6 amounts than those observed below the Andean volcanic arc.

7 To provide insights into the mantle source, as well as partial melting and metasomatic
8 processes related to the genesis of these rocks, e.g., we present major and trace elements data
9 (including REEs), together with Sr–Nd–Pb isotopic compositions, and K–Ar ages of 35
10 volcanic rocks collected from the whole Patagonian Basaltic Province (36°S – 52°S).
11 Consequently, these new data contribute to a better understanding of the origin and evolution
12 of this important igneous province.

13

14 **GEOLOGICAL SETTING**

15

16 The Patagonian western margin is currently characterized by a complex subduction zone,
17 where the Nazca and Antarctic oceanic plates subduct beneath the South American continental
18 plate with different speeds and angles of dip (Fig. 1). The Andean volcanic arc, at the same
19 latitude as Patagonian Basaltic Province, has been divided into the Southern Volcanic Zone
20 (SVZ, 33°S – 46°S) and the Austral Volcanic Zone (AVZ, 49°S – 55°S) (e.g., Ramos, 1999).
21 Between the SVZ and AVZ (46.3°S – 49°S), a volcanic gap exists because of the subduction of
22 the South Chile Ridge (SCR), where the Nazca, Antarctic and South American plates join at a
23 place designated as the Chile Triple Junction (between 47°S – 48°S). This singular tectonic
24 feature has migrated northward since 16 Ma ago, when the SCR started its subduction under
25 the southern edge of the continent at 55°S (e.g., Cande & Leslie, 1986). e.g., e.g.,

1 **Figure 1**

2

3 The Patagonian Basaltic Province, located on the extra-Andean back-arc (Argentina and
4 Chile), is characterized mainly by large volumes of Cenozoic mafic magmas, which sometimes
5 host crustal and mantle xenoliths. The Eocene–Pleistocene volcanism has been divided into
6 large plateau and post-plateau lavas (e.g., *Gorring et al., 1997*), which mainly comprise basaltic
7 lava flows and monogenetic cinder cones. Previous petrological studies of the Patagonian
8 basalts have documented a wide compositional range from tholeiitic to alkaline basaltic rocks
9 (*Stern et al., 1990; Gorring et al., 1997*). Most of these lavas, especially those with alkaline
10 affinity, are characterized by OIB-like geochemical signatures and moderately depleted Sr–Nd
11 isotope compositions (e.g., *Gorring & Kay, 2001*). Based on the across-arc geochemical
12 variation, *Stern et al. (1990)* and *Gorring & Kay (2001)* pointed out that both the plateau and
13 post-plateau lava compositions show an eastwardly decreasing amount of slab components.

14 Several geodynamic models have been proposed to explain the volcanism of the earliest
15 Miocene to historical times in the Payenia volcanic province (34°S – 38°S), in which most of
16 them are focused on the Plio–Pleistocene volcanism. A transient period of shallow subduction
17 that initiated at ca. 20 Ma culminated at ca. 5 Ma when the volcanic activity became
18 progressively more enriched in slab-derived components because of eastward migration of the
19 volcanic arc (e.g., *Kay et al., 2004, 2006a-b*). These processes are related to the increase of the
20 subduction angle during trench roll-back (e.g., *Ramos & Kay, 2006; Ramos et al., 2014*). Later,
21 voluminous Plio–Pleistocene volcanism has been associated to the steepening of the Nazca
22 plate after a period of shallow subduction, which engenders to an influx of asthenospheric
23 mantle (e.g., *Kay & Mancilla, 2001; Kay et al., 2004, 2006a-b; Kay & Copeland, 2006;*
24 *Folguera et al., 2009; Germa et al., 2010; Gudnason et al., 2012; Dyhr et al., 2013; Søager &*
25 *Holm, 2013; Søager et al., 2013, 2015*).

1 The late Eocene to Pleistocene Somún Curá igneous province is the largest volcanic field of
2 Northern Patagonia (40°S – 46°S; Ardolino, 1981; Orihashi *et al.*, 2005, 2006; Kay *et al.*,
3 2007). It is partially contemporary with the breakup of the Farallón plate. The origin of Somún
4 Curá province and its austral prolongation have been attributed to: 1) transient “hot-spot”-like
5 thermal anomaly associated with slab dynamics during times of plate reorganization (Kay *et al.*,
6 1993, 2004); 2) thermal anomaly related to a shallow asthenospheric upwelling induced by a
7 concave-up slab geometry (de Ignácio *et al.*, 2001); 3) extensional lithospheric thinning
8 attributed to asthenospheric upwelling through a slab window that formed in response to
9 changes in subduction zone geometry (Muñoz *et al.*, 2000), or 4) “wet” asthenospheric
10 upwelling caused by dehydration-induced melting of mantle transition zone in central
11 Patagonia (Orihashi *et al.*, 2005, 2006; Honda *et al.*, 2006). However, the geodynamic model
12 suggested to the Sierra de San Bernardo and Valle del Río Genoa areas implies an
13 asthenospheric upwelling to compensate a westward drift of the mantle wedge attached to the
14 South American lithosphere (Bruni *et al.*, 2008).

15 Previous petrological models for the southern Patagonia (South of 47°S) have been
16 proposed based on geochemical and chronological data, most of them being related to the
17 successive subduction of different segments of the Chile Ridge (e.g., Charrier *et al.*, 1979; Stern
18 *et al.*, 1990; Ramos & Kay, 1992; Gorrington *et al.*, 1997, 2003; D’Orazio *et al.*, 2000, 2001;
19 Guivel *et al.*, 2006; Boutonnet *et al.*, 2010; Espinoza *et al.*, 2010; Ramírez de Arellano *et al.*,
20 2012). Based on K-Ar ages, Charrier *et al.* (1979) defined that no clear relation exist between
21 the magmatism of Meseta del Lago Buenos Aires (MLBA) and subduction of the Chile Ridge.
22 However, according to Ramos & Kay (1992), most of Late Miocene to Recent plateau basalts
23 between 46°S and 49°S have OIB-like geochemical affinity; almost all can be related to
24 time-transgressive slab windows in response to the collision of Chile Ridge segments with the
25 Chile trench. For the same latitude, Gorrington *et al.* (1997, 2003) defined that all post-plateau

1 lavas (3.4–0.1 Ma) erupted after the passage of the Chile Ridge at ca. 6 Ma, overlaying the
2 main-plateau lavas, which are 2–5 million years older. These older basalts would have erupted
3 at or immediately after the time of ridge collision. Based on the available geochronological data
4 at ca. 47°S, an alternative model was proposed by [Guivel *et al.* \(2006\)](#), where both OIB and
5 intermediate magmas were derived from deep sub-slab asthenospheric mantle, which ascended
6 through a tear-in-the-slab around 15 Ma, when the southernmost segments of the South Chile
7 Ridge (SCR) collided with the Chile trench. The slab–tear model implies that the volcanic
8 activity pre-dates the subduction of the Chile Ridge and a unique slab window subparallel to the
9 trench. [Boutonnet *et al.* \(2010\)](#) and [Espinoza *et al.* \(2010\)](#) studied the spatiotemporal relation
10 between bimodal magmatism in Central Patagonia (ca. 47°S). These authors surmised that the
11 migration of the volcanic arc eastward attributable to slab shallowing followed by a transitory
12 flat-slab subduction configuration, which promoted the generation of a secondary hydration
13 front by a slab dehydration and mantle-wedge up to 300 km east of the present trench.
14 Alternatively, [Ramírez de Arellano *et al.* \(2012\)](#) proposed that the transition from calc-alkaline
15 to alkaline magmatism is not restricted to the slab window model, as well as the occurrence of
16 transitional to alkaline magmatism ca. 1 to 2 Ma before subduction of the Chile Ridge segments
17 with the Chile trench. They also suggested that the transitional signature reflects a decrease of
18 fluid-rich slab-derived components to the sub-arc mantle wedge, which is probably related to
19 eastward migration of the magmatic arc during the Miocene. The arc migration was explained
20 as a result of substantial shortening and subduction erosion in the fore-arc region attributable to
21 the increase of subduction speed after major plate motion changes in the early Miocene. The
22 slab window model was also proposed to the Estancia Glencross Area (EGA) and Pali-Aike
23 Volcanic Field (PAVF), southern South America (ca. 52°S; [D’Orazio *et al.*, 2000, 2001](#)). This
24 model implies the upwelling of a pristine sub-slab asthenosphere through a slab window at ca.
25 14 Ma as a consequence of the collision of the Chile Ridge with the Chile trench. In a previous

1 regional study, involving alkaline basalts widely distributed in Patagonia (34°S – 52°S), Stern
2 *et al.* (1990) divided these rocks into “cratonic” and “transitional”. They attributed the
3 generation of the “cratonic” basalts to low degrees of partial melting of a “plume-pudding”
4 asthenosphere as a result of the subducted oceanic lithosphere. On the other hand, the
5 “transitional” basalts represent intermediate geochemical composition between the “cratonic”
6 and Andean basalts with incorporation of slab-derived components in lesser amounts than those
7 observed below the Andean volcanic arc.

8

9 **SAMPLES, PETROGRAPHY AND CLASSIFICATION**

10

11 The basaltic rock samples collected in this study cover the whole Patagonian Basaltic
12 Province. Their sites (name, latitude and longitude) are portrayed in [Figure 1](#). The main
13 volcanic fields sampled for this study are 1) Payenia volcanic province (10 samples from sites
14 PM1–PM3), 2) Meseta de Somún Curá province (11 samples from sites PM4–PM8), 3) Paso de
15 Indios and Valle del Río Genoa (5 samples from sites PM11–PM12), 4) Meseta Central (3
16 samples from PM22 site) and 5) Pali-Aike Volcanic Field (6 samples from sites PM16–PM17).
17 The acronym PM stands for Projeto Manto (Mantle Project), which is a scientific project
18 undertaken by the Universidade Federal do Rio Grande do Sul (UFRGS), Brazil. From 13
19 cinder cones and lava flows, 35 basaltic samples hosting mantle xenoliths were collected.
20 Based on differences in their petrographic, geochemical, and isotopic characteristics, the
21 volcanic rocks collected in this study were divided into two groups, Group I and II, as described
22 below.

23 – Group I comprises melanephelinites (PM8 site; normative nepheline <20%) and basanites
24 (PM1, PM11, PM12, PM16 and PM17 sites), of which geochemical characteristics show some
25 similarity with those of the cratonic basalts defined by Stern *et al.* (1990).

1 – Group II comprises basanites (PM4 site), trachybasalts (PM2, PM3, PM6 and PM7 sites)
2 and mugearites (PM5 and PM22 sites), which have some similarity with the transitional basalts
3 defined by Stern *et al.* (1990).

4 Group I basaltic rocks have porphyritic–glomeroporphyritic to subaphyric textures. Olivine
5 is the main phase, subhedral or euhedral, and commonly contains small Cr-spinel inclusions.
6 Clinopyroxene is euhedral or prismatic, usually exhibiting oscillatory and sector zoning; it is
7 high-Ca Ti-augite or diopside. Rare plagioclase phenocrysts occur in some samples, varying
8 from euhedral to anhedral. They are characterized by well-developed twinning and normal
9 zoning. Fe-Ti oxides (Ti-magnetite and ilmenite) are abundant, occurring as microphenocrysts
10 and small inclusions. The apatite microphenocrysts are rare. The groundmass, which is
11 fine-grained hyalopilitic, intergranular, intersertal, or pilotaxitic, consists of olivine,
12 clinopyroxenes, nepheline, glass, plagioclase, and K-feldspar microlites and laths. Abundant
13 carbonates occur as disseminated or filling cavities in PM8 basalts.

14 Group II basaltic rocks are coarse-grained, with porphyritic to glomeroporphyritic textures.
15 Olivine is the dominant phase, except for PM5 basalts, which have plagioclase as main
16 phenocrysts. Phenocrysts of olivine are mainly subhedral and are to a lesser degree euhedral.
17 Clinopyroxenes (Ti-augite and diopside) are subhedral to anhedral, showing oscillatory and
18 sectorial zoning. Plagioclase is euhedral to subhedral, often exhibiting polysynthetic and rarely
19 Carlsbad twins. Ti-magnetite and ilmenite occur as abundant microphenocrysts. The
20 groundmass is coarse-grained hyalopilitic, intersertal, or intergranular, containing abundant
21 plagioclase with subordinate clinopyroxene, olivine, Ti-magnetite, ilmenite, nepheline and
22 smaller quantities of glass. Accessory minerals are K-feldspar, and apatite.

23 The basalts of both groups are fresh, with only a few showing incipient alteration of olivine
24 phenocrysts along their rims, which were partially replaced by low-temperature iddingsite and
25 in some cases, olivine with embayed and skeletal textures.

1 ANALYTICAL TECHNIQUES

2

3 Major and trace elements

4

5 The whole-rock geochemistry of 35 basaltic rocks was achieved using the facilities of the
6 Earthquake Research Institute at the University of Tokyo. Major and selected trace element
7 abundances (Sc, V, Cr, Co, Ni, Zn, Ga, Rb, Sr, Y, Zr, Nb, and Ba) were analyzed using X-ray
8 fluorescence (XRF, PW2400; Philips Japan Ltd.), whereas the abundances of other trace
9 elements (Cs, REEs, Ta, Hf, Pb, Th and U) were obtained using ICP–MS (Plasma Quad 3; VG
10 Scienta Holdings AB), connected to a laser ablation system using a frequency-quadrupled 213
11 nm Nd: YAG laser (UP-213; New Wave Research Inc.). Both data were analyzed using the
12 same glass beads, which were prepared by mixing 1.8 g of rock powder with 3.6 g of lithium
13 metaborate/tetraborate flux. Then 0.54 g of lithium nitrate was added into the sample powder as
14 an oxidizer for the iron. It was mixed in a torch-mixer for 3 min. This mixture was heated to
15 1200°C for 15 min in a 95%Pt-5%Au crucible with 30 mm inner diameter, used in an automatic
16 bead sampler. More detailed analytical procedures of the XRF and LA-ICPMS methods used
17 were described respectively by Tani *et al.* (2002) and by Orihashi & Hirata (2003).

18

19 Unspiked Sr–Nd–Pb isotopes

20

21 Sr–Nd–Pb isotopic ratios for 26 samples were measured at the Laboratório de Geologia
22 Isotópica, Universidade Federal do Rio Grande do Sul (UFRGS), Porto Alegre, Brazil. The
23 samples (0.1 g) were leached with cold 0.25 N HCl in an ultrasonic bath for 30 min to eliminate
24 impurities. Subsequently the dried samples were weighed and processed using standard
25 dissolution procedures with HF, HNO₃, and HCl in Teflon vials (Savillex®), warmed on a hot

1 plate until complete material dissolution. In the next stage, the sample solutions were diluted in
2 3 ml of HCl 2.5 N and were stored in test tubes, from which 1 ml was used to separate the Sr and
3 Nd, respectively, via Cationic AG-50W-X8 (200–400 mesh) and Anionic exchange resin
4 columns LN-B50-A (100–150 μ). Individual solutions of Sr and Nd were dried in Teflon vials
5 (Savillex®) on a hot plate. Then the residue for each sample and element was deposited with
6 0.25N H₃PO₄ onto a single Ta (for Sr), and Re (for Nd) filaments.

7 Mass spectrometric analyses for Sr and Nd isotopes were performed respectively on two
8 thermal ionization mass spectrometers (Sector 54; VG Scientia Holdings AB and Triton;
9 Thermo Scientific). Both Sr–Nd isotopic ratios were determined in multi-collector static mode
10 using Faraday collectors. The data were corrected for mass fractionation by normalization to
11 $^{86}\text{Sr}/^{88}\text{Sr} = 0.1194$ and $^{146}\text{Nd}/^{144}\text{Nd} = 0.7219$. Replicate analyses of NIST SRM987 and JNd-I
12 standards gave $^{87}\text{Sr}/^{86}\text{Sr} = 0.710254 \pm 12$ (2σ , $n = 7$) and $^{143}\text{Nd}/^{144}\text{Nd} = 0.512101 \pm 8$ (2σ , $n = 4$).

13 Pb isotope ratios were determined using multicollector-inductively coupled plasma-mass
14 spectrometry (ICP-MS, Neptune; Finnigan MAT GmbH). For Pb–Pb isotopic measurements,
15 an aliquot of 1 ml from dissolved whole-rock samples used for Sr–Nd analyses was taken.
16 Thereby, Pb was separated using anionic resin (200–400 mesh, AG1X; Bio-Rad Laboratories
17 Inc.) in HBr solution. Each sample was dried to a solid, with added solution of HNO₃ with 50
18 ppb Tl to correct the Pb fractionation during the analyses. The values obtained for common lead
19 isotopic standard (NIST SRM981) were $^{206}\text{Pb}/^{204}\text{Pb} = 16.9414 \pm 22$, $^{207}\text{Pb}/^{204}\text{Pb} = 15.4892 \pm 25$,
20 and $^{208}\text{Pb}/^{204}\text{Pb} = 36.7278 \pm 27$.

21

22 **K–Ar ages**

23

24 The K–Ar ages of 20 samples were analyzed using the unspiked sensitivity method. Ar
25 analyses were performed using a noble gas mass spectrometry system (MS-III) at the

1 Geochemical Research Center, Graduate School of Science, the University of Tokyo. The
2 whole-rock samples (0.3–0.6 g), crushing and sieving to 60–80 mesh, were wrapped in 10 μm
3 thick aluminum foil and were loaded in a glass sample holder, which was connected to an
4 extraction oven in which the sample was fused at 1700°C in vacuum and into which the
5 evaporated gas for Ar purification was introduced directly using a vacuum line. The Ar isotope
6 analyses were performed using an in-house modified VG-5400 on a small amount of Ar gas
7 ($<2 \times 10^{-7} \text{ cm}^3 \text{ STP}$). When the amount of Ar gas extracted from the sample exceeded this limit,
8 it was reduced using a known volume of the purification line. Errors on ^{40}Ar sensitivity and
9 $^{40}\text{Ar}/^{36}\text{Ar}$ ratio are estimated respectively as 5% and 0.2%, based on repeated measurements of
10 the atmospheric standard containing $1.5 \times 10^{-7} \text{ cm}^3 \text{ STP}$ of ^{40}Ar . The K concentration for an
11 aliquot of the rock fractions used for Ar analysis was determined using X-ray fluorescence
12 (XRF, PW2400; Philips Japan Ltd.) at the Earthquake Research Institute, the University of
13 Tokyo. Details of procedures applied for K–Ar dating were described by Nagao *et al.* (1991)
14 and by Orihashi *et al.* (2004).

15 The unspiked method enables measurement of small amounts of radiogenic ^{40}Ar and
16 determines the isotopic composition of the initial Ar in the sample by measuring $^{38}\text{Ar}/^{36}\text{Ar}$
17 without assuming that the $^{40}\text{Ar}/^{36}\text{Ar}$ ratio in the sample is equal to the modern atmospheric
18 value of 296 (Nier, 1950). Most $^{38}\text{Ar}/^{36}\text{Ar}$ ratios for the samples show good agreement with the
19 modern atmospheric value of 0.1880 within the range of analytical error by 2σ . One sample
20 (PM1-A4) has a higher $^{38}\text{Ar}/^{36}\text{Ar}$ ratio than the atmospheric value beyond the range of the
21 analytical error, resulting in an older K–Ar age obtained when calculated using the
22 conventional method than that obtained when using the correct age. In this case, the mass
23 fractionation effect was corrected using the measured $^{38}\text{Ar}/^{36}\text{Ar}$ ratios. Then the K–Ar age was
24 recalculated.

25

1 RESULTS

2

3 Major and trace element abundances

4

5 Representative geochemical compositions for Group I and II basaltic rocks are presented
6 respectively in Tables 1 and 2. These rocks, which have mildly to strongly alkaline affinities
7 ($\text{Na}_2\text{O} + \text{K}_2\text{O} = 3.54\text{--}6.56$ wt.%), are shown in the total alkalis vs. silica (TAS) diagram (Fig. 2).
8 The Group I samples are in the fields of nephelinites and basanites, while those of Group II
9 were classified as basanites, trachybasalts and mugearites. CIPW-norm calculations (Table 3)
10 show the presence of normative hypersthene+olivine (PM22 site), hypersthene+quartz (PM5
11 site) and nepheline+olivine (all Group I basaltic samples and Group II basaltic samples from
12 PM2, PM3, PM4, PM6 and PM7 sites).

13

14 Figure 2

15

16 Although basaltic rocks from both groups span a similar range with high values of Mg#
17 [$\text{Mg}/(\text{Mg} + \text{Fe}_{\text{total}})$] and MgO (mostly >60 ; and >9 wt.%, respectively), the selected variation
18 diagrams show great differences in major elements abundances for a given MgO content (Fig.
19 3). Group I basaltic rocks tend to exhibit lower SiO_2 (<44 wt.%), Al_2O_3 (<13 wt.%), K_2O (<1
20 wt.%) and alkalis ($\text{Na}_2\text{O} + \text{K}_2\text{O} < 5.1$) coupled with higher MgO (>10 wt.%), TiO_2 (>3 wt.%),
21 Fe_2O_3 (as total iron; >12.8 wt.%) and CaO (>10 wt.%) contents compared with those from
22 Group II (Tables 1 and 2; Figs. 2 and 3a–f). Only the rock samples from the PM1 site (Group I)
23 differ and sometimes overlap the values of Group II basaltic rocks (e.g., MgO, TiO_2 , Al_2O_3 and
24 Fe_2O_3). The contents of Na_2O and P_2O_5 (not shown) scatter somewhat, being broadly similar in
25 both groups. The $\text{CaO}/\text{Al}_2\text{O}_3$ ratio varies considerably (0.39–1.14 wt.%), with the lowest values

1 observed in Group II basaltic rocks (0.39–0.62 wt.%), whereas the Group I basaltic rocks range
2 from 0.75 to near-chondritic values (e.g., ~1.1; McDonough & Sun, 1995). The Ni and Cr
3 contents from both groups span a similar range and exhibit a good positive correlation with
4 MgO (Figs. 3g–h). The Ni concentration range from 522 ppm for the most primitive samples
5 (e.g., PM8 site – Group I basalts) up to 51 ppm for those with evolved compositions (e.g., PM5
6 site – Group II basalts), whereas Cr contents range from 540 ppm (PM12 site) to 31 ppm (PM5
7 site). Except for evolved samples (PM5 site), their high MgO, Ni, and Cr contents indicate that
8 they crystallized from primitive magmas.

9 Compared to cratonic and transitional basalts defined by Stern *et al.* (1990), the Group I
10 samples display similar distributions of TiO₂, Al₂O₃, and Fe₂O₃ (Fig. 3) to those of cratonic
11 basalts. However, in terms of SiO₂, CaO, K₂O, MgO, Cr, and Ni, no differences were found
12 between cratonic and transitional basalts. For this reason, in terms of these elements, it is
13 impossible to establish a relation between the groups of basalts defined by Stern *et al.* (1990)
14 with our samples.

15

16 **Figure 3**

17

18 The multi-element diagrams (Figs. 4a–b), normalized to primitive mantle (PM, Sun &
19 McDonough, 1989), show that all basaltic samples are enriched in LILE, HFSE, and light to
20 middle REE, resembling the pattern observed for typical intraplate basalts from continental and
21 oceanic settings. Group I basalts show prominent negative Rb, U, K, Pb, and Ti anomalies
22 coupled with positive Nb-Ta anomalies, whereas Group II basalts show selective enrichment in
23 mobile and incompatible elements (e.g., Ba, K, Pb, and Sr). In Group II basalts, positive Nb-Ta
24 anomalies are identified in the basaltic rocks of PM6 and PM7 sites, whereas the PM4 site
25 shows negative anomalies. Group I basalts have higher LREE and similar HREE (Figs. 4c–d),

1 lower LILE/HFSE-REE ratios [e.g., Ba/(Th, Nb, La), K/(Nb, La, Ce), Rb/Nb], and higher
2 Ce/Pb and Nb/U ratios than those of Group II basalts (Table 3). Selected trace element ratio
3 diagrams (Ba/Nb vs. K/Nb, Ba/La vs. Rb/Nb and Ce/Pb vs. Nb/U; Fig. 5) show that Group I
4 basalts have more affinity with cratonic basalts (Stern *et al.*, 1990) and with a depleted OIB
5 component (e.g., HIMU; Willbold & Stracke, 2006), whereas Group II basalts are
6 geochemically correlated with the transitional basalts (Stern *et al.*, 1990) and with the Enriched
7 Mantle I (EMI) reservoir (Willbold & Stracke, 2006). In this respect, the affinity of Group I and
8 II basalts with the groups defined by Stern *et al.* (1990) is also observed through incompatible
9 trace element ratios [e.g., Ba/(Nb, La), K/Nb, Rb/Nb, and Ce/Pb), where Group I basalts
10 broadly resemble cratonic basalts, whereas Group II basalts have comparable ratios with
11 transitional basalts. The basaltic rocks of both groups have no significant Eu-anomaly $Eu/Eu^* =$
12 $0.92-1.22$; $Eu/Eu^* = Eu_N / (Sm_N * Gd_N)^{1/2}$], suggesting that plagioclase is not a major
13 fractionated phase. Therefore, the slightly positive Eu anomalies shown in Group II basalts
14 (Fig. 4d), especially in PM5 site's samples, merely reflect moderate plagioclase accumulation.

15

16 **Figure 4**

17

18 **Figure 5**

19

20 **Influence of weathering and crustal contamination**

21

22 The basaltic samples of both groups were chosen based on their freshness: they show no
23 petrographic evidence of alteration, except for the presence of iddingsite, which sometimes
24 partially replaces olivine. All basaltic samples collected from the sites are characterized by the

1 occurrence of mantle-derived xenoliths, which implies a rapid ascent of these basaltic magmas
2 to the surface with less interaction with crustal wall rocks.

3 Most samples have MgO >9 wt.%, Mg# >60 and FeO*/MgO <1.5, indicating near-primary
4 melt composition. Furthermore, most Group I and II basalts have high Ce/Pb and Nb/U ratios
5 (Table 3) that are similar to those derived from N-type MORB (normal mid-ocean ridge basalts)
6 or OIB-like sources unaffected by crustal contamination (Ce/Pb = 25 ± 5 ; Nb/U = 47 ± 10 ;
7 Hofmann *et al.*, 1986; Sun & McDonough, 1989). Compared to the other samples from Group I
8 and II (Table 1), the basaltic samples from PM4 site show the lowest Ce/Pb and Nb/U ratios.
9 The geochemical characteristics of these rocks might be justified by the selective enrichment in
10 mobile elements, such as Pb and U, typically observed in basalts from the Andean arc-volcanic
11 zone. The two basaltic rocks from PM5 site are markedly evolved, as shown by their normative
12 compositions (hyperthene+quartz), very high FeO*/MgO (~2.5) and low MgO (<5 wt.%)
13 contents. These samples do not represent the mantle source. Therefore, we do not consider
14 these samples further.

15

16 **Sr–Nd–Pb isotopes**

17

18 Twenty-six representative basaltic rocks of Groups I and II were analyzed in this study for
19 Sr–Nd–Pb isotopes (Table 4). Although all basaltic rocks studied are generally young, with
20 little radiogenic in-growth, age correction has been done based on their respective ages
21 following the K–Ar dating (Table 5) for the Sr–Nd isotopic ratios.

22 The basaltic rocks examined here have initial $^{87}\text{Sr}/^{86}\text{Sr}$ ratios of 0.703179–0.704498 and
23 initial $^{143}\text{Nd}/^{144}\text{Nd}$ ratios of 0.512591–0.512967 (Fig. 6a). The Pb isotope ratios for Group I and
24 II basalts vary over the ranges of $^{206}\text{Pb}/^{204}\text{Pb} = 17.986\text{--}19.186$, $^{207}\text{Pb}/^{204}\text{Pb} = 15.504\text{--}15.660$,
25 and $^{208}\text{Pb}/^{204}\text{Pb} = 37.973\text{--}38.997$ (Figs. 6b–c). In the Sr–Nd–Pb diagrams (Fig. 6a–c), most of

1 these samples fall between depleted OIBs, which represents a mixture of depleted mid-ocean
2 ridge MORBs (DMM – e.g., Chile Ridge MORBs; Klein & Karsten, 1995; Bach *et al.*, 1996),
3 HIMU (high- μ = elevated $^{238}\text{U}/^{204}\text{Pb}$), and EMI components (Hart *et al.*, 1992). Furthermore,
4 they are similar to other Patagonian basalts at 36°S – 52°S (Gorring *et al.*, 1997, 2003;
5 D’Orazio *et al.*, 2000, 2001; Gorring & Kay, 2001; Kay *et al.*, 2004, 2007, 2013; Espinoza *et*
6 *al.*, 2005; Guivel *et al.*, 2006; Kay & Copeland, 2006; Bruni *et al.*, 2008; Choo *et al.*, 2012;
7 Dyhr *et al.*, 2013; Søgager & Holm, 2013; Søgager *et al.*, 2013).

8 Group I basaltic rocks generally have lower $^{87}\text{Sr}/^{86}\text{Sr}$ followed by higher $^{143}\text{Nd}/^{144}\text{Nd}$ and
9 $^{206}\text{Pb}-^{207}\text{Pb}-^{208}\text{Pb}/^{204}\text{Pb}$ ratios when compared to Group II (Figs. 6a–c). However, basaltic
10 samples at the PM8 site show slightly higher Sr isotope ratios than the other Group I basaltic
11 rocks ($^{87}\text{Sr}/^{86}\text{Sr} = 0.703938-0.703941$) that overlap the ratios of less-enriched basaltic rocks
12 from Group II (PM2 and PM3 sites).

13 The Sr–Nd–Pb isotopic ratios for basaltic rocks of Group I resemble those of cratonic
14 basalts defined by Stern *et al.* (1990), as well as those basalts from Pali-Aike Volcanic Field
15 (PAVF) and the Estancia Glencross area [51°S – 52°S; D’Orazio *et al.* (2000, 2001); Choo *et*
16 *al.* (2012)]. However, compared with most Group I samples, basalts from the PM1 and PM8
17 sites have lower $^{206}\text{Pb}-^{207}\text{Pb}-^{208}\text{Pb}/^{204}\text{Pb}$, respectively showing strong affinity with samples
18 from Payenia province (Kay *et al.*, 2004, 2013 and references therein; Kay & Copeland, 2006;
19 Søgager & Holm, 2013; Søgager *et al.*, 2013, 2015) and Somún Curá province (Kay *et al.*, 2004,
20 2007). Furthermore, all Group I basalts are isotopically identical to phlogopites from Estancia
21 Lote 17 (Gobernador Gregores; Gorring & Kay, 2000) and PAVF (Stern *et al.*, 1999) (Fig. 6).
22 In contrast, Group II basalts have Sr–Nd isotopic ratios that are more radiogenic than Group I
23 basalts, plotted closer to the present-day Bulk Silicate Earth (BSE; Zindler & Hart, 1986),
24 showing some affinity with transitional basalts defined by Stern *et al.* (1990). These rocks
25 overlap the previously published data for Sr–Nd–Pb from Meseta de Somún Curá, Paso de

1 Indios and Valle del Río Genoa areas [40°S – 45°S; Kay *et al.* (2004, 2007); Bruni *et al.*
2 (2008)], as well as from the more enriched samples from Payenia province (Fig. 6). This
3 behavior indicates that both groups of basalts studied here are originated from isotopically
4 heterogeneous sources with contrasting contributions from depleted (Group I basalts) and
5 enriched (EMI, Group II basalts) mantle components.

6

7 **Figure 6**

8

9 **K–Ar age**

10

11 Results for K–Ar ages obtained in this study are shown in Table 5. The errors are 1σ of
12 single analysis for each sample, including statistical errors associated to the ion collection of Ar
13 isotopes; errors are in blank correction (less than 1% of the sample gases) and in the sensitivity
14 and discrimination factors of the mass spectrometer. The new K–Ar ages for the basaltic rocks
15 range from 32.1 to 0.73 Ma. Results of K–Ar ages for each of the five main volcanic fields are
16 summarized as described below.

17

18 *Payenia volcanic province*

19

20 The De la Laguna volcano (PM1 site) is located in the northwestern part of the Las Matras
21 Block, where rocks of Choiyoi Group are widely distributed (Bertotto *et al.*, 2009, and
22 references therein). The Agua Poca volcano (PM2 site) is located in the Payún Matru volcanic
23 field, which shows the most important volcanic activity of the Payenia volcanic province, and
24 was included on the Puente Group (Pleistocene; Bertotto *et al.*, 2000). The Huanul volcano
25 (PM3 site), located in the Southern segment of Payenia volcanic province was included on the

1 Chapúa Group (Plio–Pleistocene; Bermúdez *et al.*, 1993). Bertotto (2000) and Bertotto *et al.*
2 (2006) reported K–Ar ages for volcanic rocks from those three sites, but from different lava
3 flows, yielding 14.87 ± 0.87 Ma at the PM1 site, 0.6 ± 0.1 Ma and 0.64 ± 0.04 Ma at the PM2
4 site, and 0.84 ± 0.05 Ma at the PM3 site. New K–Ar ages were determined for the PM1 site (1
5 sample), PM2 site (2 samples) and PM3 site (2 samples), yielding 19.3 ± 1.1 Ma at the PM1
6 site, 0.81 ± 0.05 and 0.78 ± 0.04 Ma at the PM2 site; and 0.99 ± 0.06 and 0.95 ± 0.05 Ma at the
7 PM3 site (Figs. 1 and 7b–c). Compared to those of earlier studies, our five new K–Ar ages were
8 slightly older at each site, but the results accord with geological observations, considering
9 multiple stages of volcanic activity at a single site.

10

11 *Meseta de Somún Curá province*

12

13 Nine new K–Ar ages for two samples from the PM4 site, two samples from the PM5 site,
14 two samples from the PM6 site, one sample from the PM7 site and two samples from the PM8
15 site were obtained in this study, yielding 0.75 ± 0.04 Ma and 0.73 ± 0.04 Ma from the PM4 site,
16 23.8 ± 1.3 Ma and 21.4 ± 1.2 Ma from the PM5 site, 29.6 ± 1.6 Ma and 29.4 ± 1.6 Ma from the
17 PM6 site, 31.6 ± 1.7 Ma from the PM7 site, and 3.76 ± 0.21 Ma and 3.57 ± 0.20 Ma from the
18 PM8 (Figs. 1 and 7b–c).

19 Ardolino (1981), Orihashi *et al.* (2005, 2006), and Kay *et al.* (2007) defined the volcanic
20 activity of basaltic lava flows forming Meseta de Somún Curá basalts as starting in the
21 Oligocene (partly in late Eocene). Ardolino (1981) proposed two peaks of volcanism between
22 33–31 and 27–25 Ma. Orihashi *et al.* (2005, 2006) reported that the main activity in the northern
23 Meseta de Somún Curá was at 23–22 Ma with a vast magmatic event, of which the whole
24 activity ranged 36–20 Ma (stage I), toward 18–10 Ma (stage II), but traceable in the
25 surrounding area down to 5.6–0.34 Ma (stage III). Kay *et al.* (2007) proposed a pre-plateau

1 stage (33–29 Ma), a plateau stage (29–25 Ma), and a post-plateau magmatism (24–17 Ma),
2 being the oldest stage coincident with that determined by [Ardolino \(1981\)](#). Based on the
3 paleontological contents of the Bajada de Los Ingleses Formation, the youngest units were
4 covered with basalts from Estancia Alvarez (PM7 site) and Aznares (PM6 site); their lava flows
5 were included previously in the Chaiful Formation (Pleistocene; [Labudía & Bjerg, 1994](#)), and
6 later, at the Basalto Meseta Coli Toro Unit (Late Oligocene – Early Miocene; [Cucchi *et al.*, 2001](#)). Our K–Ar ages from basaltic rocks at the PM6 and PM7 sites were 31.6–29.4 Ma, which
7 are consistent with the age of Meseta Coli Toro basalts and with the pre-plateau stage defined
8 by [Kay *et al.* \(2007\)](#).

10 [Coira *et al.* \(1985\)](#) reported K–Ar ages of 24 ± 5 and 20 ± 1 Ma for basalts located in
11 southeastern area of Meseta de Cari Laufquen, near to the Ingeniero Jacobacci and PM5 site,
12 which closely resemble our new K–Ar ages (23.75 ± 1.27 and 21.36 ± 1.15 Ma). These ages
13 also coincide with the main stage of the Somún Curá plateau basalt defined by [Orihashi *et al.*](#)
14 ([2005, 2006](#)) and with the post-plateau stage defined by [Kay *et al.* \(2007\)](#).

15 [Labudía *et al.* \(2011\)](#) obtained an age of 3.2 ± 0.7 Ma for the lava flows of Cerro Medina, 16
16 km southwest of the village of Prahuaniyeu, whereas basaltic rocks from Cerro El Mojón
17 (PM4), situated near Comallo area, were assigned by geological relations to the Pliocene
18 ([González *et al.*, 2003](#)). Our K–Ar ages for basaltic rocks from Prahuaniyeu on the PM8 site
19 also show a late Pliocene age (3.8–3.6 Ma), however basaltic rocks from Cerro El Mojón show
20 Pleistocene age (0.75–0.73 Ma). The new ages defined for PM4 site allow us to redefine the
21 stratigraphic position of the Campana Formation, which was defined previously by geological
22 relations as being Pliocene ([González *et al.*, 2003](#)). Our new young K–Ar ages are still
23 consistent with other Plio–Pleistocene ages that have been documented in the Somún Curá area
24 (5.65 – 0.23 Ma; [Orihashi *et al.* 2005, 2006](#); [Pécskay *et al.*, 2007](#); [Massaferro *et al.*, 2014](#)).

1 Therefore, these nine new K–Ar ages determined here for Somún Curá area are consistent
2 with long-lived volcanism extending from the Oligocene to the Pleistocene (Figs. 7b–c).

3
4 *Paso de Indios and Valle del Río Genoa areas*

5
6 Two new K–Ar ages for one sample on Cerro Matilde (Paso de Indios area; PM11 site)
7 and one sample on the Valle del Río Genoa area (PM12 site) were determined here,
8 respectively yielding 32.1 ± 1.7 Ma and 2.39 ± 0.13 Ma (Figs. 1 and 7b–c).

9 Alric (1996) calculated the Ar–Ar ages for several outcrops situated in the Paso de Indios
10 area and surroundings, including Cerro Matilde (49.35 ± 0.74 Ma). This author reported
11 Paleocene ($62.87 \pm 0.20 - 61.64 \pm 0.24$ Ma) and Eocene volcanic activity ($52.01 \pm 0.09 - 40.92$
12 ± 0.45 Ma). Our K–Ar age is considerably younger than the Ar–Ar ages reported by Alric
13 (1996) but it is consistent with other K–Ar ages dated in this area, such as Cerro Ponte (31 ± 3
14 Ma; Pesce, 1978; Ardolino & Franchi, 1993). The K–Ar ages for these basaltic rocks closely
15 resemble the austral culmination of southern pre-plateau stage of Somún Curá basalts (Kay *et*
16 *al.*, 2007), suggesting that the early Oligocene volcanism on Paso de Indios area differs from
17 the Eocene volcanism reported by Alric (1996).

18 The PM12 site of Cerro de los Chenques is an isolated monogenetic volcano along the
19 west side of Meseta de Canquel. Bruni *et al.* (2008) reported early Pleistocene age (2.5–2.3 Ma)
20 for the lava flow, which is identical to our new K–Ar data (2.39 ± 0.13 Ma).

21
22 *Meseta Central area*

23
24 New K–Ar ages were ascertained for two samples at Cerro Redondo (PM22 site):
25 yielding 9.50 ± 0.51 Ma and 9.75 ± 0.53 Ma (Figs. 1 and 7b–c). Cerro Redondo is an eroded

1 cinder cone situated in the southern part of Meseta Central, Santa Cruz province (Schilling *et*
2 *al.*, 2005). Our K–Ar ages of 9.8–9.5 Ma show agreement with the Late Miocene volcanic rocks
3 from the main basaltic plateau sequence defined by Goring *et al.* (1997) for Meseta Central,
4 Northeast region of Meseta Central, Meseta Belgrano, and Meseta de la Muerte ($^{40}\text{Ar}/^{39}\text{Ar}$ age
5 of 11.5–5.1 Ma). Moreover, they can be correlated with volcanic rocks of similar ages at the
6 Meseta del Lago Buenos Aires (K–Ar age of 12.4–5.6 Ma; Guivel *et al.*, 2006), with the upper
7 basaltic sequence of Meseta de Chile Chico (K–Ar age of 8.2–7.6 Ma; Espinoza *et al.*, 2005)
8 and with basaltic lava flows near Cerro Pampa (K–Ar age of 8.7 Ma; Orihashi *et al.*, 2013).

9

10 *Pali-Aike Volcanic Field (PAVF)*

11

12 Two new K–Ar ages for one sample on Estancia Brazo Norte (PM16 site) and one sample
13 on Cueva de Fell (PM17 site) were determined here, respectively yielding 1.73 ± 0.10 Ma and
14 1.53 ± 0.09 Ma (Figs. 1 and 7b–c).

15 The PAVF is characterized by the occurrence of the southernmost and youngest Cenozoic
16 back-arc Patagonian plateau lavas (e.g., Stern *et al.*, 1999; D’Orazio *et al.*, 2000). Available
17 K–Ar and $^{40}\text{Ar}/^{39}\text{Ar}$ ages (Meglioli, 1992; Corbella, 2002 and references therein; Mejia *et al.*,
18 2004) for the erupted lavas vary from 9.22–0.17 Ma (Figs. 1 and 7b–c), being the oldest rock
19 outcropping in the western sector of the volcanic field, with similar ages to those of Estancia
20 Glencross area (8.5–8.0 Ma; D’Orazio *et al.*, 2001). Our K–Ar ages presented here show
21 agreement with this interval, and with ages obtained previously by Meglioli (1992) for Estancia
22 Brazo Norte (1.5–1.4 Ma).

23

24

25

1 *Spatiotemporal distribution of Group I and II basalts*

2

3 In general, as observed by both Stern *et al.* (1990) and Gorrington & Kay (2001), the Group II
4 basalts display across-arc geochemical variation, with the amount of slab components
5 decreasing eastwardly (Fig. 7a). Indeed, it is possible to define an increasing tendency in
6 enriched mantle components, represented here by Ba/Nb ratios, from Payenia volcanic
7 province (36°S) to Meseta de Sumún Curá latitude (approx. 41°S). However, in southern
8 Patagonia (e.g., PM22), we identified an enriched mantle source component (EMI) weaker than
9 in central and northern Patagonian Group II basalts.e.g.,

10 Based on both K–Ar geochronology and bulk geochemical data of Payenia volcanic
11 province, it was possible to identify that the older basalts from PM1 site (Miocene), which is
12 located 90 km NNW from PM2 site, do not display any geochemical enrichment related to
13 slab-derived fluids. However, the younger PM2 and PM3 basalts (Pleistocene) display a slight
14 contribution from enriched mantle components (EMI) and are located in higher latitudes than
15 the PM1 site (Fig. 7b).

16 Plio–Pleistocene basalts from Meseta de Somún Curá display a relation between longitude
17 and K–Ar ages (Fig. 7c). The PM8 lavas (Pliocene) are located a great distance from the
18 Andean volcanic arc, presenting the strongest phlogopite-bearing signature of Group I basalts.
19 Differently, the PM4 samples (Pleistocene), located nearest the volcanic arc, are characterized
20 by the strongest contribution of slab-derived components of Group II basalts. Oligocene basalts
21 from Meseta de Somún Curá (PM6 and PM7 sites) show more similar enrichment in fluid
22 mobile elements than Group II basalts from Payenia volcanic province, but do not show
23 spatiotemporal relations. Considering the Group I samples from Valle del Río Genoa
24 (Pleistocene; PM12 site) and Paso de Indios (Oligocene; PM11 site) areas, no contribution of
25 subduction-related components exists in the mantle source of these rocks (Fig. 7a).

1 The basalts from Meseta Central (PM22) and Pali-Aike Volcanic Field (PM16 and PM17)
2 studied here suggest that interaction with enriched mantle components is restricted to the older
3 lavas located at the same latitude in the northern part of Austral Volcanic Zone, whereas the
4 outcrops located more southward are younger and display no interaction with slab-derived
5 components (Fig. 7b). Furthermore, those basalts nearest the volcanic arc (e.g., PM22 site)
6 display some slab-derived components (Fig. 7a), different from Pali-Aike Volcanic Field
7 outcrops, which are distant from the volcanic arc.

8

9 **Figure 7**

10

11 **DISCUSSION**

12

13 **Depths of magma segregation and mantle potential temperature (T_p) estimations**

14

15 Previous P–T estimations of Patagonian mantle xenoliths indicate that the lithosphere has
16 up to 80 km depth (e.g., Stern *et al.*, 1999; Laurora *et al.*, 2001; Kilian & Stern, 2002; Rivalenti
17 *et al.*, 2004, 2007; Bjerg *et al.*, 2005, 2009; Schilling *et al.*, 2005), which is consistent with the
18 estimated depth of the lithosphere–asthenosphere boundary in the region (Stern *et al.*, 1999;
19 <100 km).

20 The depth of magma generation, as well as mantle potential temperatures (see Table 6) can
21 be estimated using major oxide compositions of the most primitive basalts studied here (#Mg
22 >60; MgO >9 wt.%; Ni >200 ppm and Cr >240 ppm) because their geochemical features are
23 unaffected by crystal fractionation. Estimations of magma segregation pressures were obtained
24 based on the empirical equation of Albarède (1992) [$\ln P(\text{GPa}) = \{[5.04\text{MgO}/(\text{SiO}_2 + \text{MgO})] -$
25 $0.12\text{SiO}_2 + 7.47\}$]. Assuming an increase of 0.1 GPa per 3.3 km of depth in the mantle, the

1 calculation suggests that both Group I and II basaltic rocks were generated within the range of
2 the garnet stability field (Klemme & O'Neill, 2000) as 3.4–4.1 GPa and as 2.7–2.8 GPa, which
3 respectively correspond to depths of 113–134 km and 89–94 km (Table 6).

4 The estimated mantle potential temperature (T_P) of the Patagonian basalts were obtained
5 using methods proposed by Albarède (1992) [T (°C) = $2000\text{MgO}/(\text{SiO}_2+\text{MgO})+969$] and
6 Herzberg & Asimow (2008) [T (°C) = $935+33\text{MgO} - 0.37\text{MgO}^2+54\text{P}-2\text{P}^2$; P = GPa] (Table 6).
7 The mantle T_P calculated for Group I basalts (1398–1546°C and 1431–1563°C) are higher than
8 those estimated for Group II basalts (1305–1324°C and 1346–1364°C), using both methods.
9 The mantle potential temperature of Group II basalts overlaps those estimated as the normal
10 ambient mantle ($\sim 1350\pm 50^\circ\text{C}$; Herzberg & Asimow, 2008), which presents no evidence of a
11 thermal anomaly. However, Group I basalts have a higher estimated mantle potential
12 temperature than normal ambient mantle temperatures ($>1400^\circ\text{C}$); the temperatures partially
13 overlap those defined for OIB and mantle plume model (approx. 1430–1600°C; Green *et al.*,
14 2001; Herzberg & Asimow, 2008). The subducting slab often does not allow a thermal anomaly
15 in the mantle wedge. However, several tectonic models that have been proposed might provide
16 temporal and spatial scenarios for a hot subcontinental mantle as follows: 1) asthenospheric
17 upwelling through slab windows and slab-tearing within the subducting oceanic lithosphere in
18 southern Patagonia (Gorring & Kay, 2001; Guivel *et al.*, 2006); 2) roll-back of the subducting
19 slab in northern Patagonia (e.g., Muñoz *et al.*, 2000; de Ignácio *et al.*, 2001; Kay & Copeland,
20 2006; Kay *et al.*, 2006; Ramos & Kay, 2006; Ramos *et al.*, 2014); 3) “wet” asthenospheric
21 upwelling caused by dehydration-induced melting of mantle transition zone in central
22 Patagonia (Orihashi *et al.*, 2005, 2006; Honda *et al.*, 2006); and 4) oblique upwelling of thermal
23 flows from the hotspots in Atlantic Ocean during the Oligocene (Kay *et al.*, 2007).

24 In summary, the Patagonian primary magmas originated at great depths within the garnet
25 stability field. Group I basalts must have been generated by the hot asthenospheric upwelling.

1 Instead, Group II basalts have been generated at estimated depths overlapping the
2 lithosphere–asthenosphere boundary (LAB; <100 km).

3

4 **Insights into mantle sources beneath Patagonia**

5

6 *Discrimination of mantle source lithology*

7

8 During melting of garnet lherzolite or pyroxenite, the abundances of CaO and Al₂O₃ are
9 controlled predominantly by residual clinopyroxene and garnet (e.g., [Walter, 1998](#); [Klemme et](#)
10 [al., 2002](#)), which are generally more abundant in pyroxenites than in peridotites. Clinopyroxene
11 has a high $D_{\text{CaO}}/D_{\text{Al}_2\text{O}_3}$ ratio and is less refractory than garnet ([Walter, 1998](#)). Therefore, a high
12 CaO/Al₂O₃ ratio obtained in a primary magma results from low degrees of partial melting of
13 garnet–peridotite mantle source. The Group II basalts have CaO/Al₂O₃ ratios of 0.39–0.62.
14 They are plotted within the field obtained from compositions of pyroxenite partial melt. The
15 Group I basalts have CaO/Al₂O₃ ratios of 0.75–1.14. They are plotted within the field defined
16 for compositions of peridotite partial melts in the CaO vs. MgO diagram ([Fig. 3e](#); [Herzberg &](#)
17 [Asimow, 2008](#)). Group I basalts at the PM1 site are very close to the boundary separating the
18 peridotite and pyroxenite partial melt fields ([Fig. 3e](#)), suggesting a generation of large amounts
19 of high-pressure pyroxene fractionation in a garnet–peridotite mantle source ([Herzberg &](#)
20 [Asimow, 2008](#)).

21 According to [Yang & Zhou \(2013\)](#), it is possible to identify whether the mantle source of
22 OIB-like basaltic rocks with MgO >7.5 wt.% is peridotitic or pyroxenitic through their FC3MS
23 values (FC3MS = FeO/CaO-3*MgO/SiO₂, all in wt.%). The FC3MS values of normal mantle
24 peridotite melts are estimated as less than 0.5, but the upper limit for peridotite melts is 0.65.
25 When the FC3MS value is higher than 0.65, partial melting of a pyroxenite mantle source is

1 suggested. The FC3MS values of Group II basalts vary between 0.63–1.27, in agreement with a
2 garnet–pyroxenite as a mantle source for these basalts. Similarly, Group I basalts present low
3 FC3MS values (0.22–0.43) that are consistent with a peridotitic rock as the mantle source.

4 Some experimental studies have shown that garnet is stable in the mantle source and that it
5 is a residual solidus phase at depths greater than approx. 80 km (approx. 2.5 GPa) (e.g.,
6 Klemme & O'Neill, 2000). Experimental data of mineral/melt partition coefficients indicate
7 $D_{Th} < D_U$ and $D_{Tb} < D_{Yb}$ for garnet (e.g., Elkins *et al.*, 2008), which means that Group I and II
8 basalts having high Tb/Yb_N values (2–4) and high Th/U ratios (usually >4) are generated from
9 partial melts of the mantle source with residual garnet.

10

11 *Group I: Phlogopite-bearing peridotite as the mantle source*

12

13 The presence of residual amphibole or phlogopite in the mantle source regions of alkaline
14 basalts has been discussed in several reports (e.g., Class & Goldstein, 1997; Späth *et al.*, 2001;
15 Yang *et al.*, 2003; Johnson *et al.*, 2005; Mayer *et al.*, 2013). The stability field of amphibole is
16 restricted to temperatures of 1100–1250°C at pressures of 1–3 GPa (e.g., Niida & Green, 1999;
17 Green *et al.*, 2010), which does not agree to the P–T conditions for depth of magma segregation
18 or potential temperature calculated for the Group I basalts. In contrast, as pointed out by several
19 reports of the relevant literature (e.g., Luth, 1997; Enggist *et al.*, 2012), phlogopite is an
20 important K-bearing phase in the upper mantle at depths of 90–200 km (up to 9 GPa) with
21 temperatures of 1000–1550°C. In addition, alkali-rich magma can result from low-degree
22 partial melting of phlogopite-bearing peridotite.

23 In multi-element diagrams for Group I basalts (Fig. 4a), the pronounced negative K, Rb, Pb,
24 and variable Ti anomalies, together with a relative enrichment of Ba, suggest that phlogopite
25 played a key role in the magma genesis. According to the partition coefficient, melts with

1 residual phlogopite are expected to have low Rb/(Sr, Nb), Ba/(Th, La), and K/(Nb, La, Ce)
2 ratios, whereas basaltic rocks having phlogopite phenocrysts are expected to show higher ratios
3 of these elements (e.g., LaTourrette *et al.*, 1995). Similarly, all Group I basalts show lower
4 Rb/(Sr, Nb), Ba/(Th, La), and K/(Nb, La, Ce) ratios compared not only to Group II basalts but
5 also to primitive mantle and OIB average (Sun & McDonough, 1989). Aiming to clarify the
6 role of phlogopite or amphibole in the magma genesis of Group I basalts, we show melting
7 trajectory lines drawn using a compilation of partition coefficients between garnet
8 phlogopite-silicate and spinel amphibole-silicate melts in the PM-normalized Rb/Sr, K/Ce and
9 K/K* vs. K/La diagrams (Figs. 8a–c).

10 The K anomaly [$K/K^* = K_N/(Nb_N \times La_N)^{1/2}$] was applied here because it constitutes a
11 powerful tool to identify the presence of K-bearing minerals in the mantle source because K,
12 Nb, and La have similar bulk partition coefficients and behave highly incompatibly in both
13 spinel–peridotite and garnet–peridotite. Assuming that phlogopite is the residual mineral phase
14 that fractionates Rb and K relative to Sr and Ce even more efficiently than amphibole, the
15 Group I basalts show markedly low K-anomalies ($K/K^* = 0.14–0.34$) (Fig. 8). This result
16 suggests phlogopite as the most plausible phase in the mantle source of Group I basalt, and
17 excludes any amphibole participation.

18

19 **Figure 8**

20

21 Phlogopites and phlogopite-bearing basaltic rocks often present high Rb/Sr ratios and
22 consequently high $^{87}\text{Sr}/^{86}\text{Sr}$ ratios because of the time-integrated decay of Rb. Stern *et al.*
23 (1999) and Gorrington & Kay (2000) reported Sr–Nd–Pb isotope data of separated phlogopites of
24 mantle xenoliths from PAVF and Lote 17 (Gobernador Gregores), but they respectively
25 showed low $^{87}\text{Sr}/^{86}\text{Sr}$ (0.70344–0.70315) and high $^{143}\text{Nd}/^{144}\text{Nd}$ (0.51292–0.512816) ratios.

1 Based on their data, Gorryng & Kay (2000) reported the age of <25 Ma for the formation of
2 phlogopite in the Patagonian subcontinental lithospheric mantle. Group I basalts have identical
3 $^{87}\text{Sr}/^{86}\text{Sr}$ and $^{143}\text{Nd}/^{144}\text{Nd}$ ratios of phlogopites from Lote 17 and PAVF (Fig. 6a). Only Pliocene
4 Group I basalts at the PM8 site have a slightly radiogenic Sr isotopic composition, resulting
5 from longer time-integrated Rb/Sr ratios in their mantle source than the other Group I basalts.
6 Consequently, the absence of the more radiogenic Sr–Nd isotope signatures on the Group I
7 basalts suggests that the enrichment of their mantle source occurred during the Cenozoic, and
8 possibly in conjunction with the subduction of Nazca and Antarctic oceanic plates beneath the
9 South American continental plate.

10 The dehydration of serpentinite is a plausible explanation for the input of water up to
11 approximately 80–200 km depth (Evans *et al.*, 2013). Therefore, we suggest that the subduction
12 of serpentinitized olivine-rich mantle peridotite during deep dehydration of the subducting
13 oceanic plate can provide H₂O and fluid mobile elements (Deschamps *et al.*, 2013; Ribeiro *et*
14 *al.*, 2013; Spandler & Pirard, 2013) sufficient to form phlogopite, and to allow the precipitation
15 of an alkali-rich hydrous silicate melt derived from the interaction of a hotter asthenosphere on
16 the middle of the mantle wedge.e.g.,e.g., Consequently, the breakdown of phlogopite allowed
17 the lowering of the solidus temperature and induced small degrees of partial melting observed
18 in Group I basaltic magmas. This fact indicates that some intraplate volcanism might derive
19 from the past-metasomatized asthenosphere having compositional anomalies such as a
20 “wetspot” (Bonatti, 1990).

21

22 *Group II: Enriched pyroxenite-bearing veins as the mantle source*

23

24 The Group II basalts are characterized by variable enrichments of incompatible elements
25 (e.g., Cs, Ba, K, Pb, Sr) compared to other trace elements in the multi-element diagram.

1 Furthermore, geochemical signatures of Group II basalts having high K/K* (0.86–1.66, most >
2 1) and Pb/Pb* (1.19–2.26) anomalies [where $Pb^* = Pb_N / (Ce_N * Pr_N)^{1/2}$], supporting the influence
3 of a subduction component because of K and Pb additions from the subducting slab (*Gazel et*
4 *al.*, 2011). The positive anomalies of K/K* and Pb/Pb* greater than 1.0 suggest the contribution
5 of slab-derived fluids, whereas K/K* and Pb/Pb* ratios having less than 1.0 indicate relative
6 depletion in these elements that are typical of intraplate (OIB-type) magmatism (*Gazel et al.*,
7 2011). Except for Group II basalts at the PM6 and PM7 sites, which show less than 1.0 on K/K*
8 anomalies, Group II basalts have greater than 1.0 on both K/K* and Pb/Pb* anomalies (Table
9 3). However, it can be readily justified by their high Nb concentration (approx. 62 ppm)
10 compared to the other Group II basalts (< 50 ppm).

11 Group II basaltic rocks show high Nb/Ta (>18), Ce/Pb (>20), Nb/U (>37), and low La/Nb
12 (<1) ratios, coupled with high Nb/Nb* anomalies [>1 ; where $Nb/Nb^* = Nb_N / (Th_N * La_N)^{1/2}$;
13 *Gazel et al.*, 2011]. These results are similar to those of Group I basalts and to intraplate basalts
14 (*Hofmann et al.*, 1986; *Sun & McDonough*, 1989). The clear depletion of Nb–Ta and Ti, the
15 lowest Nb/Ta (ca. 14), Ce/Pb (ca. 12) and Nb/U (ca. 17) ratios, the highest La/Nb (ca. 1.4)
16 ratios and the low Nb/Nb* (ca. 0.7) anomalies of Group II basalts at the PM4 site might reflect
17 selective enrichment in incompatible elements in the mantle wedge because of the addition of
18 small amounts (1%) of pelagic sediments (e.g., Ce/Pb; Fig. 9) and/or because of the presence of
19 residual rutile in their mantle source (e.g., *Foley et al.*, 2000; *Klemme et al.*, 2005).

20 To explain the role of slab-derived components on the magma genesis of most Group II
21 basalts, based on an enriched garnet–pyroxenite, we used ratios of element pairs with similar
22 bulk partition coefficients because they do not vary in terms of fractional crystallization and
23 vary only slightly during partial melting. Considering the coefficient partition in an anhydrous
24 assemblage, the element pairs (e.g., Ce/Pb) are useful to identify fluids, sediments, and
25 slab-melt additions to the mantle wedge because Pb is soluble in aqueous fluids and enriched in

1 pelagic sediments, whereas Ce is immobile. A Ce/Pb vs. Ce diagram is presented in Figure 9,
2 portraying selective enrichment of Pb relative to Ce, compared to the OIB average (Sun &
3 McDonough, 1989) and to Group I basalts. Comparatively, most Group II basalts are markedly
4 less enriched in Pb than the average of Chile Triple Junction pelagic sediments (Kilian &
5 Behrmann, 2003; Shinjoe *et al.*, 2013), which exclude the participation of sediments in their
6 mantle source. The enrichment of Ce concentrations suggests that the Group II basalts can be
7 generated by simple partial melting of enriched garnet–pyroxenite as the mantle source. Based
8 mainly on incompatible element ratios (e.g., Ce/Pb; Fig. 9) and Sr–Nd–Pb isotopic data (Figs.
9 6a–c), we propose three-component-mixing among a depleted mantle-wedge, an OIB-like melt
10 and the subducted oceanic lithosphere to explain the mantle sources for Group II basalts. This
11 reaction is expected to form young pyroxenite-bearing veins close to the
12 lithosphere-asthenosphere boundary (89–94 km), with partial melting of 5–10% capable of
13 producing the geochemical features of EMI Group II basalts.

14

15 **Figure 9**

16

17 **REE modeling of partial melting**

18

19 To produce variable compositions of the Cenozoic Patagonian basalts, estimates of the
20 degrees of partial melting (F) were modeled respectively using the abundance of REEs based
21 on the Tb/Yb vs. Yb diagram with the primitive mantle (Sun & McDonough, 1989) and with
22 garnet–pyroxenite as the starting materials of Group I and II basalts (Figs. 10a–b). The degrees
23 of partial melting of Group I basalts were calculated assuming garnet–peridotite as a source
24 mode, whereas Group II basalts assumed as the mantle source were garnet–pyroxenite, both
25 with varying amounts of clinopyroxene and garnet (see Fig. 10b). The Group II mantle source

1 (enriched pyroxenite) assumed here is represented by a mixing of 90% of depleted lithospheric
2 mantle (DM; Salters & Stracke, 2004), 8% of the estimated oceanic crust, and 2% of OIB
3 average (Sun & McDonough, 1989). The oceanic crust was estimated according to Willbold &
4 Stracke (2006), consisting of a mixture of 40% MORB (sample D20-1 of Chile Ridge Segment
5 1; Klein & Karsten, 1995), 50% gabbro (Niu & O'Hara, 2003), and 10% altered MORB
6 (Staudigel *et al.*, 1996).

7 The calculations were done using the non-modal batch melting equation reported by Shaw
8 (2006) [$C^L = C^S / (D + F(1 - P))$], with application of different degrees of partial melting ($F < 15\%$).
9 The bulk distribution coefficients for both the mantle source (D) and the extracted melt (P)
10 were estimated using the mineral proportions and mineral/melt partition coefficients
11 (McKenzie & O'Nions, 1991; Grégoire *et al.*, 2000; Shaw, 2000). Source modes are shown in
12 Figure 10. The melt modes are those proposed by Johnson (1998).

13 The results for the modeling indicate that Group I basalts were generated from partial
14 melting of <3%, whereas Group II basalts vary over the range of 5–10%. The Group I basalts at
15 the PM8 site have an extremely high Tb/Yb ratio (approx. 0.85) and Yb content (2.2 ppm),
16 which results from extremely small fractions of melt ($F < 1\%$). The characteristics of Group I
17 basalts at the PM1 site also show the lowest amount of clinopyroxene compared to the other
18 Group I basalts (Fig. 10a). That amount is in agreement with efficient pyroxene fractionation in
19 a garnet–peridotite mantle source (see Fig. 3e).

20

21 **Figure 10**

22

23

24

25

1 **Magmatic model for the Patagonian Basaltic Province**

2

3 A tectono-magmatic model explaining the generation of Group I and II lavas of Patagonian
4 basaltic province (36°S – 52°S) is summarized below and in [Figure 11](#). This model was
5 constructed based on both geochemical characteristics and depth estimations discussed above,
6 and in previous works (e.g., [Somoza et al., 1998](#); [Gorring et al., 1997, 2003](#); [Gorring & Kay,](#)
7 [2001](#); [Orihashi et al., 2005, 2006](#); [Guivel et al., 2006](#); [Honda et al., 2006](#); [Boutonnet et al.,](#)
8 [2010](#); [Espinoza et al., 2010](#); [Ramírez de Arellano et al., 2012](#); [Kay et al., 2013](#)).e.g.,

9 Although some particularities are involved in the tectono-magmatic evolution of the three
10 segments defined here (36°S – 38°S; 40°S – 45°S; and 46°S – 52°S), we assumed that all Group
11 I basalts have their genesis related to a “wet” plume generated as a result of devolatilization of
12 hydrated serpentinite within the subducting oceanic lithosphere, which contributed to a
13 subsequent formation of phlogopite in a deep and hot OIB-like asthenosphere. Group II basalts
14 show geochemical similarities to “transitional” basalts proposed by [Stern et al. \(1990\)](#) and are
15 expected to represent back-arc basalts affected by arc widening during the Cenozoic, which
16 allowed the incorporation of slab-derived components in lesser amounts than those observed
17 beneath the Andean volcanic arc.

18 The magmatic model assumed here for Payenia volcanic province (36°S – 38°S; [Fig. 11a](#)) is
19 based on roll-back theory, whereby the Nazca plate displays a westward shift of volcanic
20 activity since the late Pliocene, facilitating the increase of slab-derived components from older
21 to younger volcanism (e.g., [Ramos & Kay, 2006](#); [Ramos et al., 2014](#)). This model shows
22 agreement with the occurrence of OIB-like EMI components in Group II basalts (PM2 and
23 PM3), which display Pleistocene ages, compared to Miocene phlogopite-bearing OIB-like
24 lavas from Group I (PM1) ([Fig. 7](#)). The geochemical and isotopic characteristics of PM1 basalts
25 are probably related to an eastward asthenospheric upwelling, which includes fossil plume

1 fragments (Tristan da Cunha mantle plume?; *Kay et al., 2007*), after changing of the slab dip
2 and the convergence from near-normal to oblique along the Chile trench from the late
3 Oligocene to the early Miocene (e.g., *Somoza et al., 1998; Kay et al., 2013*). Using information
4 from our sampling sites (eastern Payenia), *Bertotto et al. (2009)* showed that the Miocene lavas
5 have intraplate affinity with no slab input, whereas Plio–Pleistocene lavas have the contribution
6 of a slab-derived component. Furthermore, they described an increase of incompatible element
7 concentrations from the northern to the central and southern zones, excluding any relation with
8 the distance from the trench.

9 The geodynamic model presented for Cenozoic magmatism between 40°S and 45°S
10 includes basalts from the Meseta de Somún Curá (PM4, PM5, PM6, PM7 and PM8), Valle del
11 Río Genoa (PM12), and Paso de Indios (PM11) areas (*Fig. 11b*). This model incorporates the
12 upwelling of a deeper and hot OIB-like asthenosphere beneath central Patagonia that
13 experienced the interaction with deep slab serpentinite dehydration, triggered in response to the
14 changing of slab dip during the Oligocene (*Kay et al., 2007*). Consequently, the devolatilization
15 of the subducted serpentinite contributed to subsequent “wet” plume generation and Group I
16 basalt magmatism. Although the presence of volatile-bearing minerals such as amphibole and
17 phlogopite, in the sources of intraplate volcanism do not require a thermal anomaly in the
18 generation of these magmas (e.g., *Smith & Lewis, 1999*), the calculated potential temperatures
19 (T_p) for Group I basalts are high (1400–1563°C), which indicates the contribution of an ancient
20 mantle plume beneath Somún Curá province and its austral prolongation.

21 Our model used to explain the OIB-like volcanism in Somún Curá province is similar to that
22 proposed by *Orihashi et al. (2005, 2006)* and by *Honda et al. (2006)*, although they attributed
23 the origin of water to the wet asthenospheric upwelling caused by dehydration-induced melting
24 of mantle transition zone. On the other hand, after the breakup of Farallón plate, which allowed
25 the change of the slab dip from oblique to near-normal convergence along the Andean margin

1 during the Oligocene (Cande & Leslie, 1986; Somoza, 1998; Kay *et al.*, 2007), the shallow
2 mantle source of Group II basalts (89–94 km) became susceptible to interaction with H₂O-rich
3 fluids from the Nazca plate dehydration.

4 The geodynamic evolution of southernmost Patagonia at latitudes of the Meseta Central
5 (PM22) and PAVF (PM16 and PM17) (49°S – 52°S) presented here was constructed based on
6 models proposed previously by Gorrington *et al.* (1997, 2003), Gorrington & Kay (2001), Guivel *et*
7 *al.* (2006), Boutonnet *et al.* (2010), Espinoza *et al.* (2010), and Ramírez de Arellano *et al.*
8 (2012) (Fig. 11c). Our model includes a weak enriched mantle source component stored in the
9 supra-slab (near the lithosphere-asthenosphere boundary), as well as a phlogopite-bearing
10 OIB-like components (PM16 and PM17), which are explainable by the upwelling of a hotter
11 asthenosphere. The “conventional” slab window model proposed by Gorrington *et al.* (1997, 2003)
12 and by Gorrington & Kay (2001), determines that the “true” slab window is represented by all
13 post-plateau lavas that postdate the passage of the Nazca Plate edge ca. 7 to 1 Ma ago.
14 However, those basalts located further north (e.g., Meseta de Chile Chico, Meseta del Lago
15 Buenos Aires, and Northeast region of Meseta Central) require an alternative model because of
16 the absence of decreasing in the age of magmatism from South to North, as might be expected
17 for each segment of the Chile Ridge when its activity ended and its own slab window was
18 developed (Fig. 7 and Guivel *et al.*, 2006). This chronological inconsistency lead Guivel *et al.*
19 (2006) to propose a model based on the process of slab tearing at depth when collision starts at
20 the trench, followed by slab breakoff. Therefore, we attribute the eastward arc migration to slab
21 flattening (Boutonnet *et al.*, 2010; Espinoza *et al.*, 2010; Ramírez de Arellano *et al.*, 2012) to
22 explain the EMI component recognized in Group II basalts (PM22), whereas Group I basalts
23 from PAVF correspond to the opening of “true” (ridge-related) slab windows.

24

25 **Figure 11**

1 **CONCLUDING REMARKS**

2

3 We newly ascertained major and trace element and Sr–Nd–Pb isotope compositions, as well
4 as K–Ar ages, for the Cenozoic basaltic rocks from the Patagonian Basaltic Province to
5 evaluate their mantle sources and petrogenesis. Our conclusions include the following.

6 1) The alkaline basalts studied here were divisible into two mineralogical and
7 compositional groups: Group I basalts comprising basanites and nephelinites; Group II basalts
8 comprising trachybasalts, basanites and mugearites. Both groups show enrichment in LILE,
9 HFSE, and light to middle REE in primitive mantle-normalized multi-element diagrams,
10 which characterize intraplate basalts from continental and oceanic settings.

11 2) Fractionated HREE ratios (e.g., Tb/Yb_N = 2–4), as well as calculated depths of magma
12 generation of Groups I basalts (113–134 km) and Group II basalts (89–94 km) show that the
13 Patagonian basalts were generated within the garnet stability field. The difference between the
14 depths of the respective groups suggests an asthenospheric source for Group I basalts,
15 whereas Group II basalts most likely have their mantle source close to the
16 lithosphere–asthenosphere boundary (LAB; <100 km).

17 3) Regarding Group I basalts, the strong depletion of Rb, K, Pb, and Ti coupled with Nb–Ta
18 positive anomalies in the multi-element diagram, as well as low Rb/Sr and K/(La, Ce) ratios,
19 high Ce/Pb ratios and low K/K* (0.14–0.34) anomalies suggest that phlogopite was a residual
20 mantle phase during the basalt genesis. Sr–Nd–Pb isotopic ratios for Group I basalts are similar
21 to depleted OIB and are identical to phlogopites from Patagonian mantle xenoliths, which
22 suggests that the enrichment responsible by phlogopite formation in their mantle source
23 occurred during the Cenozoic, possibly in conjunction with the subduction of Nazca and
24 Antarctic oceanic plates beneath the South American continental plate. The origin of
25 phlogopite in the mantle source for Group I basalts might be related to serpentinite dehydration,

1 which provided Rb, K, and H₂O sufficient to form this mineral. Thereafter, the breakdown of
2 phlogopite allowed small degrees of partial melting of an alkali-rich hydrous silicate melt
3 derived from the interaction of a hotter asthenosphere with the middle of the mantle wedge. It
4 can still suggest that the genesis of intraplate volcanism is related to compositional anomalies
5 (“wetspots”).

6 4) Group II basalts are characterized by enrichment to some degree in LILE (e.g., Cs, Ba,
7 K, Sr) and Pb with respect to HFSE (e.g., Nb–Ta) and REE (e.g., La, Ce), suggesting that
8 these magmas had the contribution of slab-derived fluids. Furthermore, these basalts have
9 higher K/K* and Pb/Pb* anomalies and slightly higher radiogenic isotopic ratios than those of
10 Group I basalts. Curiously, the Group II basalts show high Nb/Ta (>18), Ce/Pb (>20), Nb/U
11 (>37), Nb/Nb* (>1), and low La/Nb (<1) ratios, similar to those of the Group I basalts and to
12 intraplate basalts elsewhere. Based on these features, we argue that Group II basalts reflect the
13 partial melting of metasomatized pyroxenite-bearing veins in the continental
14 lithosphere-asthenosphere boundary with EMI signature during the Cenozoic time.

15 5) The mantle potential temperatures (T_P) calculated for Group I basalts are higher
16 (1400–1563°C) than those estimated from Group II basalts (1305–1364°C). The Group II
17 basalt estimates overlap the normal ambient mantle temperature (approx. 1350±50°C),
18 whereas Group I basalts show high T_P (>1400°C), indicating evidence of a thermal anomaly
19 beneath Patagonia. The non-modal batch partial melting modeling results indicate that both
20 groups were generated by a small degree of partial melting. However, Group I from
21 phlogopite–garnet peridotite (Group I basalts; <3%) and Group II basalts originated from
22 enriched garnet–pyroxenite (Group II basalts; 5–10%) mantle sources.

23 6) According to spatiotemporal variations, the estimated depths of mantle sources
24 apparently play an important role in the genesis of all Group I and II basalts. However, in local
25 cases, it was also possible to discern Groups I and II basalts because of their eruption ages,

1 across-arc geochemical variations and latitudes. Consequently, in Payenia volcanic province,
2 the eruption ages of Group II lavas are younger (Pleistocene) than those of Group I (Miocene).
3 The Plio–Pleistocene basalts from Meseta de Somún Curá show across-arc geochemical
4 variation, where Group II basalts are located closer to the volcanic arc than Group I basalts are.
5 In southern Patagonia, Group I and II basalts are discernible based on the westward increase of
6 slab-derived components, latitude, and eruption ages because interaction with enriched
7 components is restricted to the older lavas located near the Austral volcanic zone and at the
8 Meseta Central latitude.

9

10 **ACKNOWLEDGMENTS**

11

12 The studies presented here were supported by National Council of Technological and
13 Scientific Development – CNPq, Brazil, JSPS KAKENHI Grant Number 21403012 awarded to
14 Y. O. and the Earthquake Research Institute (ERI) cooperative research program, the
15 University of Tokyo. We are thankful to N. Hokanishi for her help in XRF analysis, to M.
16 Assis, L. Gruber and G. Raupp for their help in Sr–Nd–Pb analysis and to M. Haller, J.A.
17 Naranjo, F. Hervé, R. Anma and S. Klemme for their useful comments. The authors are also
18 grateful to Drs. G. Massaferrro, J. C. Varekamp and C. Ramírez de Arellano for their kind
19 reviews and useful suggestions.

20

1 **REFERENCES**

2

3 Albarède, F. (1992). How deep do common basalts form and differentiate? *Journal of*
4 *Geophysical Research* **97**, 10997-11009.

5

6 Alric, V. I. (1996). *Los basaltos portadores de xenolitos aflorantes em las localidades Passo*
7 *de Indios y Cerro Condor, Departamento de Paso de Indios, Provincia del Chubut*. Tesis
8 Doctoral. Universidad Nacional de la Patagonia San Juan Bosco. 135 pp.

9

10 Ardolino, A. A. (1981). El vulcanismo cenozoico del borde suroriental de la meseta de
11 Somún Curá, provincia del Chubut. In: VIII Congreso Geológico Argentino, San Luis,
12 Actas, Vol. III, pp. 7-23.

13

14 Ardolino, A. A. & Franchi, M. R. (1993). El vulcanismo Cenozoico de la Meseta de Somun
15 Cura, Provincias de Rio Negro y Chubut. In: XII Congreso Geológico Argentino y II
16 Congreso de Exploración de Hidrocarburos, Mendoza, Actas, Vol. IV, pp. 225-235.

17

18 Bach, W., Erzinger, J., Dosso, L., Bollinger, C., Bougault, H., Etoubleau, J. & Sauerwein, J.
19 (1996). Unusually large Nb-Ta depletions in North Chile ridge basalts at 36°50' to
20 38°56'S: major element, trace element, and isotopic data. *Earth and Planetary Science*
21 *Letters* **142**, 223-240.

22

23 Bermúdez, A., Delpino, D., Frey, F., Saal, A. (1993). Los basaltos de retroarco
24 extraandinos. In: Ramos, V. A. (Ed.), *Geología y Recursos Naturales de Mendoza*,
25 Relatorio. XII Congreso Geológico Argentino y II Congreso de Exploración de
26 Hidrocarburos, pp. 161-173.

- 1
- 2 Bertotto, G. W. (2000). Cerro Agua Poca, un cono basáltico cuaternario portador de
3 xenolitos ultramáficos, en el oeste de la provincia de La Pampa, Argentina. *Revista de la*
4 *Asociación Geológica Argentina* **55**, 59-71.
- 5
- 6 Bertotto, G. W., Orihashi, Y., Nagao, K. & Motoki, A. (2006). New K-Ar ages on retroarc
7 basalts of Mendoza-La Pampa. In: Second scientific meeting of the ICES, Buenos Aires,
8 Actas, CD.
- 9
- 10 Bertotto, G. W., Cingolani, C. A. & Bjerg, E. A. (2009). Geochemical variations in Cenozoic
11 back-arc basalts at the border of La Pampa and Mendoza provinces, Argentina. *Journal of*
12 *South American Earth Sciences* **28**, 360-373.
- 13
- 14 Bjerg, E. A., Ntaflos, T., Kurat, G., Dobosi, G. & Labudía, C. H. (2005). The upper mantle
15 beneath Patagonia, Argentina, documented by xenoliths from alkali basalts. *Journal of*
16 *South American Earth Sciences* **18**, 125-145.
- 17
- 18 Bjerg, E. A., Ntaflos, T., Thöni, M., Aliani, P. & Labudia, C. H. (2009). Heterogeneous
19 Lithospheric Mantle beneath Northern Patagonia: Evidence from Prahuanियeu Garnet-
20 and Spinel-Peridotites. *Journal of Petrology* **50**, 1267-1298.
- 21
- 22 Bonatti, E. (1990). Not So Hot "Hot Spots" in the Oceanic Mantle. *Science* **250**, 107-111.
- 23
- 24 Boutonnet, E., Arnaud, E., Guivel, C., Lagabrielle, Y., Scalabrino, B. & Espinoza, F. (2010).
25 Subduction of the South Chile active spreading ridge: A 17 Ma to 3 Ma magmatic record
26 in central Patagonia (western edge of Meseta del Lago Buenos Aires, Argentina). *Journal*

1 *of Volcanology and Geothermal Research* **189**, 319-339.

2

3 Bruni, S., D’Orazio, M., Haller, M. J., Innocenti, F., Manetti, P., Pécskay, Z. & Tonarini, S.

4 (2008). Time-evolution of magma sources in a continental back-arc setting: the Cenozoic

5 basalts from Sierra de San Bernardo (Patagonia, Chubut, Argentina). *Geological*

6 *Magazine* **145**, 714-732.

7

8 Cande, S. C. & Leslie, R. B. (1986). Late Cenozoic tectonics of the Southern Chile trench.

9 *Journal Geophysical Research* **91**, 471-496.

10

11 Charrier, R., Linares, E., Niemeyer, H. & Skarmeta, J. (1979). K-Ar ages of basalt flows of

12 the Meseta Buenos Aires in southern Chile and their relation to the southeast Pacific

13 triple junction. *Geology* **7**, 436-439.

14

15 Choo, M. K., Lee, M. J., Lee, J. I., Kim, K. H. & Park, K. -H. (2012). Geochemistry and

16 Sr–Nd–Pb isotopic constraints on the petrogenesis of Cenozoic lavas from the Pali Aike

17 and Morro Chico area (52°S), southern Patagonia, South America. *Island Arc* **21**, 327-350.

18

19 Class, C. & Goldstein, S. L. (1997). Plume-lithosphere interactions in the ocean basins:

20 constraints from the source mineralogy. *Earth and Planetary Science Letters* **150**,

21 245-260.

22

23 Cobbold, P. R. & Rossello, E. A. (2003). Aptian to recent compressional deformation,

24 foothills of the Neuquén Basin, Argentina. *Marine and Petroleum Geology* **20**, 429-443.

25

26 Coira, B., Franchi, M. E. & Nullo, F. (1985). Vulcanismo Terciario al oeste de Somuncura y

1 su relación con el arco magmático de la Cordillera Norpatagónica, Argentina. In: IV
2 Congreso Geológico Chileno, Antofagasta, Actas, Vol. IV, pp. 68-88.

3

4 Corbella, H. (2002). El campo volcano-tectónico de Pali Aike. In: XV Congreso Geológico
5 Argentino, El Calafate, Actas, Vol. I-18, pp. 285-301.

6

7 Cucchi, R., Busteros, A., Lema, H., Dalponte, M. & Espejo, P. (2001). Hoja Geológica
8 4169-II, Los Menucos, provincia de Río Negro. Instituto de Geología y Recursos Minerales,
9 Servicio Geológico Minero Argentino, Boletín 265, 105 p., Buenos Aires.

10

11 Dasgupta, R., Hirschmann, M. M. & Smith, N. D. (2007). Partial melting experiments of
12 peridotite+CO₂ at 3 GPa and genesis of alkalic ocean island basalts. *Journal of Petrology*
13 **48**, 2093-2124.

14

15 de Ignacio, C., López, I., Oyarzun, R. & Márquez, A. (2001). The northern Patagonia
16 Somuncura plateau basalts: a product of slab-induced, shallow asthenospheric upwelling?
17 *Terra Nova* **13**, 117-121.

18

19 Deschamps, F., Godard, M., Guillot, S. & Hattori, K. (2013). Geochemistry of subduction
20 zone serpentinites: A review. *Lithos* **178**, 96-127.

21

22 D’Orazio, M., Agostini, S., Mazzarini, F., Innocenti, F., Manetti, P., Haller, M. & Lahsen, A.
23 (2000). The Pali Aike Volcanic Field, Patagonia: slab-window magmatism near the tip of
24 South America. *Tectonophysics* **321**, 407-427.

25

26 D’Orazio, M., Agostini, S., Innocenti, F., Haller, M., Manetti, P. & Mazzarini, F. (2001).

1 Slab window-related magmatism from southernmost South America: the Late Miocene
2 mafic volcanics from the Estancia Glencross Area (~52°S, Argentina–Chile). *Lithos* **57**,
3 67-89.

4

5 D’Orazio, M., Innocenti, F., Manetti, P. & Haller, M. (2004). Cenozoic back-arc
6 magmatism of the southern extra-Andean Patagonia (44°30’–52°S): a review of
7 geochemical data and geodynamic interpretations. *Revista de la Asociación Geológica*
8 *Argentina* **59**, 525-538.

9

10 Dyhr, C. T., Holm, P. M., Llambías, E. J. & Scherstén, A. (2013). Subduction controls on
11 Miocene back-arc lavas from Sierra de Huantraico and La Matancilla and new ⁴⁰Ar/³⁹Ar
12 dating from the Mendoza Region, Argentina. *Lithos* **179**, 67-83.

13

14 Elkins, L., Gaetani, G. & Sims, K. (2008). Partitioning of U and Th during garnet
15 pyroxenite partial melting: Constraints on the source of alkaline ocean island basalts.
16 *Earth and Planetary Science Letters* **265**, 270-286.

17

18 Enggist, A., Chu, L. & Luth, R. W. (2012). Phase relations of phlogopite with magnesite
19 from 4 to 8 GPa. *Contributions to Mineralogy and Petrology* **163**, 467-481.

20

21 Espinoza, F., Morata, D., Pelleter, E., Maury, R. C., Suárez, M., Lagabrielle, Y., Polvé, M.,
22 Bellon, H., Cotten, J., De la Cruz, R. & Guivel, C. (2005). Petrogenesis of the Eocene and
23 Mio–Pliocene alkaline basaltic magmatism in Meseta Chile Chico, southern Patagonia,
24 Chile: Evidence for the participation of two slab windows. *Lithos* **82**, 315-343.

25

26 Espinoza, F., Morata, D., Polvé, M., Lagabrielle, Y., Maury, R., de la Rupelle, A., Guivel, C.,

1 Cotten, J., Bellon, H. & Suárez, M. (2010). Middle Miocene calc-alkaline volcanism in
2 Central Patagonia (47°S): Petrogenesis and implication for slab dynamics. *Andean*
3 *Geology* **37**, 300-328.

4

5 Evans, B. W., Hattori, K. & Baronnet, A. (2013). Serpentinite: What, why, where?
6 *Elements* **9**, 99-106.

7

8 Foley, S. F., Barth, M. G. & Jenner, G. A. (2000). Rutile/melt partition coefficients for
9 trace elements and an assessment of the influence of rutile on the trace element
10 characteristics of subduction zone magmas. *Geochimica et Cosmochimica Acta* **64**,
11 933-938.

12

13 Folguera, A., Naranjo, J. A., Orihashi, Y., Sumino, H., Nagao, K., Polanco, E. & Ramos, V.
14 A. (2009). Retroarc volcanism in the northern San Rafael Block (34°-35°30'S), southern
15 Central Andes: Occurrence, age, and tectonic setting. *Journal of Volcanology and*
16 *Geothermal Research* **186**, 169-185.

17

18 Galland, O., Hallot, E., Cobbold, P. R., Ruffet, G. & de Bremond d'Ars, J. (2007).
19 Volcanism in a compressional Andean setting: A structural and geochronological study of
20 Tromen volcano (Neuquén province, Argentina). *Tectonics* **26**, TC4010,
21 doi:10.1029/2006TC002011.

22

23 Gazel, E., Hoernle, K., Carr, M. J., Herzberg, C., Saginor, I., van den Bogaard, P., Hauff,
24 F., Feigenson, M. & Swisher III, C. (2011). Plume–subduction interaction in southern
25 Central America: Mantle upwelling and slab melting. *Lithos* **121**, 117-134.

26

1 Gerlach, D. C., Frey, F. A., Moreno-Roa, H. & López-Escobar, L. (1988). Recent volcanism
2 in the Puyehue-Cordon Caulle region, Southern Andes, Chile (40.5°S): petrogenesis of
3 evolved lavas. *Journal of Petrology* **29**, 333-382.

4

5 Germa, A., Quidelleur, X., Gillot, P. Y. & Tchilinguirian, P. (2010). Volcanic evolution of
6 the back-arc Pleistocene Payun Matru volcanic field (Argentina). *Journal of South
7 American Earth Sciences* **29**, 717-730.

8

9 González, P., Coluccia, A. & Franchi, M. (2003). Hoja 4169-III Ingeniero Jacobacci, Carta
10 Geológica de la República Argentina, escala 1:250.000, Buenos Aires: Servicio Geológico
11 Minero Argentino.

12

13 Gorrington, M. L. & Kay, S. M. (2000). Carbonatite metasomatized peridotite xenoliths from
14 southern Patagonia: implications for lithospheric processes and Neogene plateau
15 magmatism. *Contributions to Mineralogy and Petrology* **140**, 55-72.

16

17 Gorrington, M. L. & Kay, S. M. (2001). Mantle processes and sources of Neogene slab window
18 magmas from Southern Patagonia, Argentina. *Journal of Petrology* **42**, 1067-1094.

19

20 Gorrington, M. L., Kay, S. M., Zeitler, P. K., Ramos, V. A., Rubiolo, D., Fernandez, M. I. &
21 Panza, J. L. (1997). Neogene Patagonian plateau lavas: continental magmas associated
22 with ridge collision at the Chile Triple Junction. *Tectonics* **16**, 1-17.

23

24 Gorrington, M. L., Singer, B., Gowers, J. & Kay, S. M. (2003). Plio-Pleistocene basalts from
25 the Meseta del Lago Buenos Aires, Argentina: evidence for asthenosphere–lithosphere
26 interactions during slab window magmatism. *Chemical Geology* **193**, 215-235.

1
2 Green, D. H., Falloon, T. J., Eggins, S. M. & Yaxley, G. M. (2001), Primary magmas and
3 mantle temperatures. *European Journal of Mineralogy* **13**, 437-451.
4
5 Green, D. H., Hibberson, W. O., Kovacs, I. & Rosenthal, A. (2010). Water and its influence
6 on the lithosphere-asthenosphere boundary. *Nature* **467**, 448-451.
7
8 Grégoire, M., Moine, B. N., O'Reilly, S. Y., Cottin, J. Y. & Giret, A. (2000). Trace Element
9 Residence and Partitioning in Mantle Xenoliths Metasomatized by Highly Alkaline,
10 Silicate- and Carbonate-rich Melts (Kerguelen Islands, Indian Ocean). *Journal of*
11 *Petrology* **41**, 477-509.
12
13 Gudnason, J., Holm, P. M., Søyger, N. & Llambías, E. J. (2012). Geochronology of the late
14 Pliocene to recent volcanic activity in the Payenia back-arc volcanic province, Mendoza
15 Argentina. *Journal of South American Earth Sciences* **37**, 191-201.
16
17 Guivel, C., Morata, D., Pelleter, E., Espinoza, F., Maury, R. C., Lagabrielle, Y., Polvé, M.,
18 Bellon, H., Cotton, J., Benoit, M., Suárez, M. & de la Cruz, R. (2006). Miocene to Late
19 Quaternary Patagonian basalts (46–47°S): Geochronometric and geochemical evidence
20 for slab tearing due to active spreading ridge subduction. *Journal of Volcanology and*
21 *Geothermal Research* **149**, 346-370.
22
23 Hart, S. R., Hauri, E. H., Oschmann, L. A. & Whitehead, J. A. (1992). Mantle Plumes and
24 Entrainment: Isotopic Evidence. *Science* **256**, 517-520.
25
26 Herzberg, C. (2011). Identification of Source Lithology in the Hawaiian and Canary

1 Islands: Implications for Origins. *Journal of Petrology* **52**, 113-146.

2

3 Herzberg, C. & Asimow, P. D. (2008). Petrology of some oceanic island basalts:
4 PRIMELT2.XLS software for primary magma calculation. *Geochemistry, Geophysics,*
5 *Geosystems* **9**: 1-25. <http://dx.doi.org/10.1029/2008GC002057>.

6

7 Hickey, R., Frey, F. A. & Gerlach, D. (1986). Multiple sources for basaltic arc rocks from
8 the Southern Volcanic Zone of the Andes (34°-41°S): trace element and isotopic evidence
9 for contributions from subducted oceanic crust, mantle, and continental crust. *Journal of*
10 *Geophysical Research* **91**, 5963-5983.

11

12 Hickey-Vargas, R., Moreno-Roa, H., López-Escobar, L. & Frey, F. A. (1989). Geochemical
13 variations in Andean basaltic and silicic lavas from the Villarrica-Lanin volcanic chain
14 (39.5°S): an evaluation of source heterogeneity, fractional crystallization and crustal
15 assimilation. *Contributions to Mineralogy and Petrology* **103**, 361-386.

16

17 Hirschmann, M. M., Kogiso, T., Baker, M. B. & Stolper, E. M. (2003). Alkalic magmas
18 generated by partial melting of garnet pyroxenite. *Geology* **31**, 481-484.

19

20 Hofmann, A. W., Jochum, K. P., Seufert, M. & White, W. M. (1986). Nb and Pb in oceanic
21 basalts: new constraints on mantle evolution. *Earth and Planetary Science Letters* **79**,
22 33-45.

23

24 Honda, S., Orihashi, Y., Mibe, K., Motoki, A., Sumino, H. & Haller, M. J. (2006). Mantle
25 wedge deformation by subducting and rotating slab and its possible implication. *Earth,*
26 *Planets and Space* **58**, 1087-1092.

- 1
- 2 Irvine, T. N. & Baragar, W. R. A. (1971). A guide to the chemical classification of the
3 common volcanic rocks. *Canadian Journal of Earth Sciences* **8**, 523-548.
- 4
- 5
- 6 Jacobsen, S. B. & Wasserburg, G. J. (1980). Sm-Nd isotopic evolution of chondrites. *Earth
7 and Planetary Science Letters* **50**, 139-155.
- 8
- 9 Jalowitzki, T. L. R., Conceição, R. V., Bertotto, G. W. & Orihashi, Y. (2008). Contribuição
10 de fluidos da placa de Nazca à fonte do magma alcalino do tipo OIB associado a uma
11 pluma mantélica no norte da Patagônia, Argentina. *Geochimica Brasiliensis* **22**, 073-090.
- 12
- 13 Jalowitzki, T. L. R., Conceição, R. V., Orihashi, Y., Bertotto, G. W. & Gervasoni, F. (2009).
14 Phlogopite-bearing fossil plume and EM II component evidences in Patagonia, registered
15 in alkaline basalts from Southern Argentina (36°S - 44°S). *Geochimica et Cosmochimica
16 Acta* **73**, A583.
- 17
- 18 Johnson, K. T. M. (1998). Experimental determination of partition coefficients for rare
19 earth and high-field-strength elements between clinopyroxene, garnet, and basaltic melt
20 at high pressures. *Contributions to Mineralogy and Petrology* **133**, 60-68.
- 21
- 22 Johnson, J. S., Gibson, S. A., Thompson, R. N. & Nowell, G. M. (2005). Volcanism in the
23 Vitim Volcanic Field, Siberia: geochemical evidence for a mantle plume beneath the
24 Baikal Rift zone. *Journal of Petrology* **46**, 1309-1344.
- 25
- 26 Kay, S. M. & Mancilla, O. (2001). Neogene shallow subduction segments in the

1 Chilean/Argentine Andes and Andean-type margins. *Geological Society of America* **63**,
2 A156.

3

4 Kay, S. M. & Copeland, P. (2006). Early to middle Miocene backarc magmas of the
5 Neuquén Basin: Geochemical consequences of slab shallowing and the westward drift of
6 South America. *Geological Society of America, Special Paper* **407**, 185-213.

7

8 Kay, S. M., Ardolino, A. A., Franchi, M. & Ramos, V. A. (1993). Origen de la Meseta de
9 Somuncura: distribución and geoquímica de sus rocas volcánicas máficas. In: XII
10 Congreso Geológico Argentino, Buenos Aires, Actas, Vol. IV, pp. 236-248.

11

12 Kay, S. M., Gorrington, M. & Ramos, V. (2004). Magmatic sources, setting and causes of
13 Eocene to Recent Patagonian plateau magmatism (36°S to 52°S latitude). *Revista de la*
14 *Asociación Geológica Argentina* **59(4)**: 556-568.

15

16 Kay, S. M., Burns, W. M., Copeland, P., Mancilla, O. (2006a). Upper Cretaceous to
17 Holocene magmatism and evidence for transient Miocene shallowing of the Andean
18 subduction zone under the northern Neuquén Basin. *Geological Society of America*,
19 *Special Paper* **407**, 19-60.

20

21 Kay, S. M., Copeland, P., Mancilla, O. (2006b). Evolution of the late Miocene Chachahuén
22 volcanic complex at 37 °S over a transient shallow subduction zone under the Neuquén
23 Andes. *Geological Society of America, Special Paper* **407**, 215-246.

24

25 Kay, S. M., Ardolino, A., Gorrington, M. & Ramos, V. (2007). The Somuncura Large Igneous
26 Province in Patagonia: Interaction of a Transient Mantle Thermal Anomaly with a

1 Subducting Slab. *Journal of Petrology* **48**, 43-77.

2

3 Kay, S. M., Jones, H. A. & Kay, R. W. (2013). Origin of Tertiary to Recent EM- and
4 subduction-like chemical and isotopic signatures in Auca Mahuida region (37°–38°S) and
5 other Patagonian plateau lavas. *Contributions to Mineralogy and Petrology* **166**, 165-192.

6

7 Kilian, R. & Stern, C. R. (2002). Constraints on the interaction between slab melts and
8 the mantle wedge from adakitic glass in peridotite xenoliths. *European Journal of*
9 *Mineralogy* **14**, 25-36.

10

11 Kilian, R. & Behrmann, J. H. (2003). Geochemical constraints on the sources of Southern
12 Chile Trench sediments and their recycling in arc magmas of the Southern Andes.
13 *Journal of the Geological Society* **160**, 57-70.

14

15 Klein, M. E. & Karsten, J. L. (1995). Ocean-ridge basalts with convergent-margin
16 geochemical affinities from the Chile Ridge. *Nature* **374**, 52-57.

17

18 Klemme, S. & O'Neill, H. S. C. (2000). The near-solidus transition from garnet lherzolite
19 to spinel lherzolite. *Contributions to Mineralogy and Petrology* **138**, 237-248.

20

21 Klemme, S., Blundy, J. D. & Wood, B. J. (2002). Experimental constraints on major and
22 trace element partitioning during partial melting of eclogite. *Geochimica et*
23 *Cosmochimica Acta* **66**, 3109-3123.

24

25 Klemme, S., van Miltenburg, J. C., Javorsky, P. & Wastin, F. (2005). Thermodynamic
26 properties of uvarovite garnet (Ca₃Cr₂Si₃O₁₂). *American Mineralogy* **90**, 663-666.

- 1
- 2 Kogiso, T. & Hirschmann, M. M. (2006). Partial melting experiments of biminerally
3 eclogite and the role of recycled mafic oceanic crust in the genesis of ocean island basalts.
4 *Earth and Planetary Science Letters* **249**, 188-199.
- 5
- 6 Kogiso, T., Hirschmann, M. M. & Frost, D. J. (2003). High-pressure partial melting of
7 garnet pyroxenite: possible mafic lithologies in the source of ocean island basalts. *Earth*
8 *and Planetary Science Letters* **216**, 603-617.
- 9
- 10 Labudía, C. H. & Bjerg, E. A. (1994). Geología del Sector Oriental de la Hoja Bajo Hondo
11 (39e), Provincia de Río Negro. *Revista de la Asociación Geológica Argentina* **49**, 284-296.
- 12
- 13 Labudía, C. H., Bjerg, E. A. & Ntaflou, Th. (2011). Nuevas dataciones del vulcanismo del
14 noroeste de la Meseta de Somoncurá, Argentina. S6 Evolución tectono-magmática cenozoica
15 del macizo norpatagónico. XVIII Congreso Geológico Argentino, Neuquén.
- 16
- 17 LaTourrette, T., Hervig, R. L. & Holloway, J. R. (1995). Trace element partitioning between
18 amphibole, phlogopite, and basanite melt. *Earth and Planetary Science Letters* **135**, 13-30.
- 19
- 20 Laurora, A., Mazzucchelli, M., Rivalenti, G., Vannucci, R., Zanetti, A., Barbieri, M. A. &
21 Cingolani, C. A. (2001). Metasomatism and melting in carbonated peridotite xenoliths
22 from the mantle wedge: the Gobernador Gregores case (Southern Patagonia). *Journal of*
23 *Petrology* **42**, 69-87.
- 24
- 25 Le Bas, M. J., Le Maitre, R. W., Strekeisen, A. & Zanetti, B. (1986). A chemical
26 classification of volcanic rock based on the total alkali-silica diagram. *Journal of Petrology*

1 **27**, 745-750.

2

3 Luth, R. W. (1997). Experimental study of the system phlogopite-diopside from 3.5 to 17

4 GPa. *American Mineralogist* **82**, 1198-1209.

5

6 Massaferro, G. I., Haller, M. J., Dostal, J., Pécskay, Z., Prez, H., Meister, C. & Alric, V.

7 (2014). Possible sources for monogenetic Pliocene–Quaternary basaltic volcanism in

8 northern Patagonia. *Journal of South American Earth Sciences* **55**, 29-42.

9

10 Mayer, B., Jung, S., Romer, R. L., Stracke, A., Haase, K. M. & Garbe-Schönberg, C. -D.

11 (2013). Petrogenesis of Tertiary Hornblende-bearing Lavas in the Rhön, Germany.

12 *Journal of Petrology* **54**, 2095-2123.

13

14 McDonough, W. F. & Sun, S. -S. (1995). Composition of the Earth. *Chemical Geology* **120**,

15 223-253.

16

17 McKenzie, D. P. & O’Nions, R. K. (1991). Partial melt distribution from inversion of rare

18 earth element concentrations. *Journal of Petrology* **32**: 1021-1991.

19

20 McKenzie, D. A. N. & O’Nions, R. K. (1995). The source regions of ocean island basalts.

21 *Journal of Petrology* **36**, 133-159.

22

23 Meglioli, A. (1992). Glacial geology and geochronology of south ernmost Patagonia and

24 Tierra del Fuego, Argentina and Chile. Ph.D. dissertation, Leigh University, Bethlehem,

25 PA.

26

1 Mejia, V., Opdyke, N. D., Vilas, J. F., Singer, B. S. & Stoner, J. S. (2004). Plio-Pleistocene
2 time-averaged field in southern Patagonia recorded in lava flows. *Geochemistry,*
3 *Geophysics, Geosystems* **5**, 1-15. <http://dx.doi.org/10.1029/2003GC000633>.
4

5 Muñoz, J., Troncoso, R., Duhart, P., Crignola, P., Farmer, L. & Stern, C. R. (2000). The
6 Mid-Tertiary coastal magmatic belt in south-central Chile (36°-43°S): it's relation to
7 crustal extension, mantle upwelling, and the late Oligocene increase in the rate of oceanic
8 plate subduction beneath South America. *Andean Geology* **27**(2), 177-203.
9

10 Nagao, K., Ogata, A., Miura, Y., Matsuda, J. & Akimoto, S. (1991). Highly reproducible 13
11 and 17 ka K-Ar ages of two volcanic rocks. *Geochemical Journal* **25**, 447-451.
12

13 Nier, A. O. (1950). A redetermination of the relative abundances of the isotopes of carbon,
14 nitrogen, oxygen, argon and potassium. *Physical Review* **77**, 789-793.
15

16 Niida, K. & Green, D. (1999). Stability and chemical composition of pargasitic amphibole
17 in MORB pyrolite under upper mantle conditions. *Contributions to Mineralogy and*
18 *Petrology* **135**, 18-40.
19

20 Niu, Y. & O'Hara, M. J. (2003). Origin of ocean island basalts: a new perspective from
21 petrology, geochemistry, and mineral physics considerations. *Journal of Geophysical*
22 *Research* **108**, 2209. doi:10.1029/2002JB002048.
23

24 Orihashi, Y. & Hirata T. (2003). Rapid quantitative analysis of Y and REE abundances in
25 XRF glass bead for selected GSJ reference rock standards using UV laser ablation
26 ICP-MS. *Geochemical Journal* **37**, 401-412.

1
2 Orihashi, Y., Naranjo, J. A., Motoki, A., Sumino, H., Hirata, D., Anma, R. & Nagao, K.
3 (2004). Quaternary volcanic activity of Hudson and Lautaro volcanoes, Chilean
4 Patagonia: new constraints from K-Ar ages. *Andean Geology* **31**, 207-224.
5
6 Orihashi, Y., Motoki, A., Haller, M. J. & CHRISTMASSY Project Volcanic Group. (2005).
7 Petrogenesis of relatively large-volume basalts on extra-back arc province: Somuncura
8 plateau, north Patagonia. *Earth Monthly* **27**, 438-447.
9
10 Orihashi, Y., Motoki, A., Haller, M., Sumino, H. & CHRISMASSEY Group. (2006).
11 Petrogenesis of Somuncura plateau basalt in an extra-back arc province: Melting of
12 hydrous wadsleyite beneath northern Patagonia. *Geochimica et Cosmochimica Acta* **70**,
13 A463.
14
15 Orihashi, Y., Anma, R., Motoki, A., Haller, M. J., Hirata, D., Iwano, H., Sumino, H. &
16 Ramos, V. A. (2013). Evolution history of the crust underlying Cerro Pampa, Argentine
17 Patagonia: Constraint from LA-ICPMS U-Pb ages for exotic zircons in the Mid-Miocene
18 adakite. *Geochemical Journal* **47**, 235-247.
19
20 Pécskay, Z., Haller, M. J. & Németh, K. (2007). Preliminary K/Ar geochronology of the
21 crater Basalt volcanic field (CBVF), Northern Patagonia. *Revista de la Asociación*
22 *Geológica Argentina* **62**, 25-29.
23
24 Pesce, A. H. (1978). Estratigrafía del arroyo Perdido en su tramo medio e inferior, provincia del
25 Chubut. In: VII Congreso Geológico Argentino, Neuquen, Actas, Vol. I, 315-333.
26

- 1 Pilet, S., Hernandez, J., Sylvester, P. & Poujol, M. (2005). The metasomatic alternative for
2 ocean island basalt chemical heterogeneity. *Earth and Planetary Science Letters* **236**, 148-166.
- 3 Pilet, S., Baker, M. B. & Stolper, E. M. (2008). Metasomatized lithosphere and the origin of
4 alkaline lavas. *Science* **320**, 916-919.
- 5
- 6 Pilet, S., Ulmer, P. & Villiger, S. (2010). Liquid line of descent of a basanitic liquid at 1.5 Gpa:
7 constraints on the formation of metasomatic veins. *Contributions to Mineralogy and Petrology*
8 **159**, 621-643.
- 9 Quidelleur, X., Carlut, J., Tchilinguirian, P., Germa, A. & Gillot, P. -Y. (2009). Paleomagnetic
10 directions from mid-latitude sites in the southern hemisphere (Argentina): Contribution to time
11 averaged field models. *Physics of the Earth and Planetary Interiors* **172**, 199-209.
- 12
- 13 Ramírez de Arellano, C., Putlitz, B., Müntener, O. & Ovtcharova, M. (2012). High precision
14 U/Pb zircon dating of the Chaltén Plutonic Complex (Cerro Fitz Roy, Patagonia) and its
15 relationship to arc migration in the southernmost Andes. *Tectonics* **31**, TC4009,
16 doi:10.1029/2011TC003048.
- 17
- 18 Ramos, V. A. (1999). Plate tectonic setting of the Andean Cordillera. *Episodes* **22**, 183-190.
- 19
- 20 Ramos, V. A. & Kay, S. M. (1992). Southern Patagonian plateau basalts and deformation:
21 back-arc testimony of ridge collisions, *Tectonophysics* **205**, 261-282.
- 22
- 23 Ramos, V. A. & Kay, S. M. (2006). Overview of the tectonic evolution of the southern
24 Central Andes of Mendoza and Neuquén (35°–39°S latitude). *Geological Society of*

1 *America*, Special Paper **407**, 1-17.

2

3 Ramos, V. A., Litvak, V. D., Folguera, A. & Spagnuolo, M. (2014). An Andean tectonic
4 cycle: From crustal thickening to extension in a thin crust (34°-37°SL). *Geoscience*
5 *Frontiers* **5**, 351-367.

6

7 Ribeiro, J. M., Stern, R. J., Kelley, K. A., Martinez, F., Ishizuka, O., Manton, W. I. &
8 Ohara, H. (2013). Nature and distribution of slab-derived fluids and mantle sources
9 beneath the Southeast Mariana forearc rift. *Geochemistry, Geophysics, Geosystems* **14**,
10 4585-4607. doi:10.1002/ggge.20244.

11

12 Rivalenti, G., Mazzucchelli, M., Laurora, A., Ciuffi, S. I. A., Zanetti, A., Vannucci, R., &
13 Cingolani, C. A. (2004). The backarc mantle lithosphere in Patagonia, South America.
14 *Journal of South American Earth Sciences* **17**, 121-152.

15

16 Rivalenti, G., Mazzucchelli, M., Zanetti, A., Vannucci, R., Bollinger, C., Hémond, C. &
17 Bertotto, G. W. (2007). Xenoliths from Cerro de los Chenques (Patagonia): An example of
18 slab-related metasomatism in the backarc lithospheric mantle. *Lithos* **99**, 45-67.

19

20 Salters, V. J. M. & Stracke, A. (2004). Composition of the depleted mantle. *Geochemistry,*
21 *Geophysics, Geosystems* **5**, 1-27. [http://dx.doi.org/ 10.1029/2003GC000597](http://dx.doi.org/10.1029/2003GC000597).

22

23 Schilling, M., Conceição, R. V., Mallmann, G., Koester, E., Kawashita, K., Hervé, F.,
24 Morata, D. & Motoki, A. (2005). Spinel-facies mantle xenoliths from Cerro Redondo,
25 Argentine Patagonia: Petrographic, geochemical, and isotopic evidence of interaction
26 between xenoliths and host basalt. *Lithos* **72**, 209-229.

1
2 Shaw, D. M. (2000). Continuous (dynamic) melting theory revisited. *Canadian*
3 *Mineralogy* **38**, 1041-1063.
4
5 Shaw, D. M. (2006). Trace Elements in Magmas: A Theoretical Treatment. Cambridge
6 University Press, 256pp.
7
8 Shinjoe, H., Orihashi, Y., Naranjo, J. A., Hirata, D., Hasenaka, T., Fukuoka, T., Sano, T. &
9 Anma, R. (2013). Boron and other trace element constraints on the slab-derived
10 component in Quaternary volcanic rocks from the Southern Volcanic Zone of the Andes.
11 *Geochemical Journal* **47**, 185-199.
12
13 Smith, A. D. & Lewis, C. (1999). The planet beyond the plume hypothesis. *Earth-Science*
14 *Reviews* **48**, 135-182.
15
16 Søgner, N. & Holm, P. M. (2013). Melt–peridotite reactions in upwelling eclogite bodies:
17 Constraints from EM1-type alkaline basalts in Payenia, Argentina. *Chemical Geology*
18 **360-361**: 204-219.
19
20 Søgner, N., Holm, P. M. & Llambías, E. J. (2013). Payenia volcanic province, southern
21 Mendoza, Argentina: OIB mantle upwelling in a backarc environment. *Chemical Geology*
22 **349-350**: 36-53.
23
24 Søgner, N., Holm, P. M. & Thirlwall, M. F. (2015). Sr, Nd, Pb and Hf isotopic constraints
25 on mantle sources and crustal contaminants in the Payenia volcanic province, Argentina.
26 *Lithos* **212-215**: 368-378.

1

2 Somoza, R. (1998). Updated Nazca (Farallon)–South America relative motions during the
3 last 49 My: implications for mountain building in the Central Andean region. *Journal of*
4 *South American Earth Sciences* **11**(3), 211-215.

5

6 Spandler, C. & Pirard, C. (2013). Element recycling from subducting slabs to arc crust: A
7 review. *Lithos* **170-171**, 208-223.

8

9 Späth, A., le Roex, A. P. & Opiyo-Akech, N. (2001). Plume-lithosphere interaction and the
10 origin of continental rift-related alkaline volcanism—the Chyulu Hills volcanic province,
11 southern Kenya. *Journal of Petrology* **42**, 765-787.

12

13 Staudigel, H., Plank, T., White, B. & Schminck, H. -U. (1996). Geochemical Fluxes During
14 Seafloor Alteration of the Basaltic Upper Oceanic Crust: DSDP Sites 417 and 418. In:
15 Subduction top to bottom. Geophysical Monograph. Bebout, G.E., Scholl, D.W., Kirby, S.H.
16 and Platt, J.P. (Editors), American Geophysical Union, Washington, D.C. 96: 19-38.

17

18 Stern, C. R., Frey, F. A., Futa, K., Zartman, R. E., Peng, Z. & Kyser, T. K. (1990). Trace
19 element and Sr, Nd, Pb, and O isotopic composition of Pliocene and Quaternary alkali
20 basalts of the Patagonian plateau lavas of southernmost South America. *Contributions to*
21 *Mineralogy and Petrology* **104**, 294-308.

22

23 Stern, C. R., Kilian, R., Olker, B., Hauri, E. H. & Kyser, T. K. (1999). Evidence from
24 mantle xenoliths for relatively thin (<100 km) continental lithosphere below the
25 Phanerozoic crust of southernmost South America. *Lithos* **48**, 217-235.

26

1 Sun, S. & McDonough, W. F. (1989). Chemical and isotopic systematics of oceanic basalts,
2 implications for mantle composition and processes. In: Magmatism in the Ocean Basins
3 (Saunders, A. D. & Norry, M. J., editors). *Geological Society* (Special Publications) **42**,
4 313-345.

5

6 Tani, K., Orihashi, Y. & Nakada, S. (2002). Major and trace component analysis of silicate
7 rocks using fused glass bead by X-ray Fluorescence spectrometer: Evaluation of
8 analytical precision for third, sixth and eleventh dilution fused glass beads. *Tech. Res.*
9 *Rep., ERI, Univ. Tokyo* **8**, 26-36.

10

11 Varekamp, J. C., Hesse, A. & Mandeville, C. W. (2010). Back-arc basalts from the
12 Loncopue graben (Province of Neuquen, Argentina). *Journal of Volcanology and*
13 *Geothermal Research* **197**, 313-328.

14

15 Varekamp, J. C., Zareski, J. E., Camfield, L. M. & Todd, E. (2015). Copahue Volcano and
16 Its Regional Magmatic Setting. In: Copahue, eds Tassi et al., chapter 5, p.81-117.
17 Springer Publishers.

18

19 Walter, M. J. (1998). Melting of Garnet Peridotite and the Origin of Komatiite and
20 Depleted Lithosphere. *Journal of Petrology* **39**, 29-60.

21

22 Willbold, M. & Stracke, A. (2006). Trace element composition of mantle end-members:
23 Implications for recycling of oceanic and upper and lower continental crust. *Geochemistry,*
24 *Geophysics, Geosystems* **7**, 1-30. <http://dx.doi.org/10.1029/2005GC001005>.

25

26 Yang, H. -J., Frey, F. A. & Clague, D.A. (2003). Constraints on the source components of

1 lavas forming the Hawaiian North Arch and Honolulu volcanics. *Journal of Petrology* **44**,
2 603-627.

3

4 Yang, Z. F. & Zhou, J. H. (2013). Can we identify source lithology of basalt? *Scientific*
5 *Report* **3**, 1856. doi:10.1038/srep01856.

6

7 Zeng, G., Chen, L. -H., Xu, X. -S. Jiang, S. -Y. & Hofmann, A. W. (2010). Carbonated
8 mantle sources for Cenozoic intra-plate alkaline basalts in Shandong, North China.
9 *Chemical Geology* **273**, 35-45.

10

11 Zhang, G. L., Zong, C. L., Yin, X. B. & Li, H. (2012). Geochemical constraints on a mixed
12 pyroxenite–peridotite source for East Pacific Rise basalts. *Chemical Geology* **330-331**,
13 176-187.

14

15 Zindler, A. & Hart, S. (1986). Chemical Geodynamics. *Annual Review of Earth and*
16 *Planetary Sciences* **14**, 493-57.

17

18 **Figure Captions**

19

20 **Figure 1.** Tectono-magmatic map showing Patagonian plateau lavas in southernmost South
21 America after Stern *et al.* (1990). Circles denote the following sample localities: De la Laguna
22 (PM1 – 36°13'19"S; 68°26'01"W), Agua Poca (PM2 – 37°01'05"S; 68°07'21"W), Huanul
23 (PM3 – 37°17'25"S; 68°32'27"W), Cerro El Mojón (PM4 – 41°06'18"S; 70°13'09"W),
24 Ingeniero Jacobacci (PM5 – 41°22'07"S; 69°47'44"W), Aznares (PM6 – 40°48'51"S;
25 68°41'01"W), Estancia Alvarez (PM7 – 40°46'08"S; 68°46'21"W), Prahuanियeu (PM8 –
26 41°20'09"S; 67°54'08"W), Cerro Matilde (PM11 – 43°48'42"S; 68°55'32"W), Cerro de los

1 Chenques (PM12 – 44°52'19"S; 70°03'58"W), Estancia Brazo Norte (PM16 – 52°02'55"S;
2 70°02'07"W), Cueva de Fell (PM17 – 52°02'39"S; 70°03'33"W), and Cerro Redondo (PM22
3 – 49°07'13"S; 70°08'44"W). The major plateau regions are Payenia Volcanic Province (PVP),
4 Meseta de Somún Curá (MS), Meseta de Canquel (MCA), Meseta de la Muerte (MM),
5 Meseta Central (MCE), Meseta de Buenos Aires (MBA), Meseta de las Viscachas (MV), and
6 Pali-Aike Volcanic Field (PAVF). Also shown are the Austral volcanic zone (AVZ), Southern
7 volcanic zone (SVZ), and the Patagonian volcanic GAP.

8
9 **Figure 2.** Total alkalis (Na₂O + K₂O; wt.%) vs. silica (wt.%) diagram (TAS; *Le Bas et al.*,
10 1986) for Groups I and II. The alkaline – sub-alkaline divide was reported by *Irvine &*
11 *Baragar (1971)*. For comparison, values of “cratonic” and “transitional” basalts reported by
12 *Stern et al. (1990)* are shown.

13
14 **Figure 3.** Variation diagrams for selected major (wt.%) and trace (ppm) elements vs. MgO
15 (wt.%) from Group I and II basalts (a–h). CaO vs. MgO diagram (e) were reported by
16 *Herzberg & Asimow (2008)*. For comparison, values of “cratonic” and “transitional” basalts
17 reported by *Stern et al. (1990)* are shown. Total iron is reported as Fe₂O₃. Symbols are the
18 same as those for *Figure 2*.

19
20 **Figure 4.** Primitive mantle-normalized incompatible trace elements (a–b) and REE (c–d)
21 diagrams. Normalized values were reported by *Sun & McDonough (1989)*.

22
23 **Figure 5.** Selected trace element ratio diagrams. (a) Ba/Nb, vs. K/Nb, (b) Ba/La vs. Rb/Nb
24 and (c) Ce/Pb vs. Nb/U diagrams illustrating the geochemical characteristics of the mantle
25 sources for Groups I and II. Shown for comparison are Andean volcanic arc basalts with Mg#

1 >55 and FeO*/MgO <1.5 (Hickey *et al.*, 1986; Gerlach *et al.*, 1988; Hickey-Vargas *et al.*,
 2 1989), “cratonic” and “transitional” basalts (Stern *et al.*, 1990), the average of Chile Triple
 3 Junction pelagic sediments (MR08-06 Leg1b; Shinjoe *et al.*, 2013), and the OIB average (Sun
 4 & McDonough, 1989). The fields for HIMU and EMI are based on data reported by Willbold
 5 & Stracke (2006). Symbols are the same as those for Figure 2.

6
 7 **Figure 6.** (a) $^{87}\text{Sr}/^{86}\text{Sr}$ vs. $^{143}\text{Nd}/^{144}\text{Nd}$; (b–c) $^{208-207}\text{Pb}/^{204}\text{Pb}$ vs. $^{206}\text{Pb}/^{204}\text{Pb}$ isotope variations
 8 of Group I and II basalts (see text for details). Errors are 2σ of the mean, referring to the last
 9 two digits of the $^{87}\text{Sr}/^{86}\text{Sr}$ and $^{143}\text{Nd}/^{144}\text{Nd}$ ratios. $(^{87}\text{Sr}/^{86}\text{Sr})_i = (^{87}\text{Sr}/^{86}\text{Sr})_{\text{sample}} -$
 10 $(^{87}\text{Rb}/^{86}\text{Sr})_{\text{sample}} \times (e^{\lambda t} - 1)$; $(^{143}\text{Nd}/^{144}\text{Nd})_i = (^{143}\text{Nd}/^{144}\text{Nd})_{\text{sample}} - (^{147}\text{Sm}/^{144}\text{Nd})_{\text{sample}} \times (e^{\lambda t} -$
 11 $1)$; $\epsilon\text{Nd} = \{[(^{143}\text{Nd}/^{144}\text{Nd})_{\text{sample}} - (^{143}\text{Nd}/^{144}\text{Nd})_{\text{CHUR}}] / [(^{143}\text{Nd}/^{144}\text{Nd})_{\text{CHUR}}] \times 10000\}$, are
 12 $^{143}\text{Nd}/^{144}\text{Nd}_{\text{CHUR}} = 0.512638$ (Jacobsen & Wasserburg, 1980). $\lambda\text{Sm} = 6.54 \times 10^{-12} \text{ year}^{-1}$, λRb
 13 $= 1.42 \times 10^{-11} \text{ year}^{-1}$, $t(\text{Ma})$. Symbols are the same as those for Figure 2. For comparison are
 14 shown alkaline basalts from: (1) Payenia volcanic province ($36^\circ\text{S} - 38^\circ\text{S}$); (2) Meseta de
 15 Somún Curá, Paso de Indios and Valle del Río Genoa areas ($40^\circ\text{S} - 45^\circ\text{S}$); (3) Meseta Central
 16 area ($46^\circ\text{S} - 49^\circ\text{S}$); and (4) Pali-Aike Volcanic Field ($51^\circ\text{S} - 52^\circ\text{S}$). See text for references.
 17 Isotopic data of “cratonic” and “transitional” basalts are shown (Stern *et al.*, 1990), plus
 18 phlogopites from Pali-Aike Volcanic Field (PAVF; Stern *et al.*, 1999) and Estancia Lote 17
 19 (L17; Gorryng & Kay, 2000). Mantle reservoirs are from Hart *et al.* (1992) and Chile Ridge
 20 MORBs are from Klein & Karsten (1995) and Bach *et al.* (1996).

21
 22 **Figure 7.** Ba/Nb vs. longitude (a); New K–Ar ages against latitude (b) and longitude (c) of
 23 Groups I and II (Errors are 1σ). For comparison, K–Ar ages (K–Ar and $^{40}\text{Ar}/^{39}\text{Ar}$ methods) of
 24 other Patagonian lavas are shown. Data sources: Payenia Volcanic Field ($36^\circ\text{S} - 38^\circ\text{S}$;
 25 Cobbold & Rossello, 2003; Kay *et al.*, 2004 and references therein; Kay & Copeland, 2006

1 and references therein; Bertotto *et al.*, 2006; Galland *et al.*, 2007; Folguera *et al.*, 2009;
2 Quidelleur *et al.*, 2009; Germa *et al.*, 2010; Gudnason *et al.*, 2012), Somún Curá, Paso de
3 Indios and Valle del Río Genoa areas (40°S – 45°S; Kay *et al.*, 2007; Pécskay *et al.*, 2007;
4 Labudia *et al.*, 2011; Bruni *et al.*, 2008; Massaferró *et al.*, 2014), Plateau basalts between
5 46°S – 49°S (Gorring *et al.*, 1997; Guivel *et al.*, 2006), and Pali-Aike Volcanic Field (51°S –
6 52°S; Corbela, 2002 and references therein; Mejia *et al.*, 2004). Abbreviations: Olig. =
7 Oligocene ($n = 8$), Mioc. = Miocene ($n = 60$), Plio. = Pliocene ($n = 38$), Pleist. = Pleistocene
8 ($n = 171$). Symbols are the same as those for Figure 2. The youngest samples display error
9 bars smaller than printed symbols. Black-filled circles and squares represent samples dated
10 previously from the same localities studied here.

11

12 **Figure 8.** K/La vs. (a) Rb/Sr, (b) K/Ce and (c) K/K*. All trace elements were normalized to
13 primitive mantle. Melt trajectories are drawn for phlogopite-bearing lherzolite (continuous
14 line; Ol = 0.56, Opx = 0.13, Cpx = 0.2, Grt = 0.09, Phlog = 0.02) and amphibole-bearing
15 lherzolite (dotted line; Ol = 0.62, Opx = 0.22, Cpx = 0.12, Sp = 0.02, Amp = 0.05) sources
16 using the non-modal batch partial melting of Shaw (2006). Melting of phlogopite-bearing and
17 amphibole-bearing lherzolites shows that Group I basalt is explainable by low degrees of
18 partial melting (<3%) of a mantle source with residual phlogopite. However, the participation
19 of amphibole in the genesis of these rocks is apparently inconsistent. Symbols are the same as
20 those for Figure 2.

21

22 **Figure 9.** Plot of Ce/Pb vs. Ce (ppm) showing melt curves obtained using non-modal batch
23 melting. Melt curves are drawn for both garnet–pyroxenite (A) and garnet–pyroxenite plus 1%
24 of average of Chile Triple Junction pelagic sediments (Shinjoe *et al.*, 2013) (B). See text and
25 Figure 8 for partition coefficient compilation, mode and melt mode. For comparison are shown

1 the average of Chile Triple Junction pelagic sediments (MR08-06 Leg1b; Shinjoe *et al.*, 2013),
2 South Chile Ridge Sediments (Kilian & Behrmann, 2003), and the OIB average of Sun &
3 McDonough (1989). Symbols are the same as those for Figure 2.

4

5 **Figure 10.** Tb/Yb vs. Yb diagram showing melt curves obtained using non-modal batch
6 melting of Shaw (2006). Continuous curves show non-modal batch melting models
7 considering the primitive mantle with lherzolite mode for Group I (A) (ol = 0.62, opx = 0.22,
8 and phlog = 0.02 are fixed, whereas the amounts of cpx and grt vary respectively: 0.05–0.1
9 and 0.09–0.03); and a garnet–pyroxenite mode for Group II (B) (ol = 0.3 and opx = 0.5 are
10 fixed, whereas the amounts of cpx and grt vary respectively: 0.12–0.16 and 0.08–0.04) as
11 starting materials. Numbers along the continuous curves represent the degrees of partial
12 melting (F). Symbols are the same as those for Figure 2.

13

14 **Figure 11.** Schematic tectono-magmatic models of Patagonian Basaltic Province: (a) Payenia
15 area (PM1, PM2 and PM3); (b) Somún Curá (PM4, PM5, PM6, PM7 and PM8), Valle del Río
16 Genoa (PM12) and Paso de Indios (PM11) areas; and (c) Meseta Central (PM22) and
17 Pali-Aike Volcanic Field (PM16 and PM17) areas. See text for discussion.

Figure 1

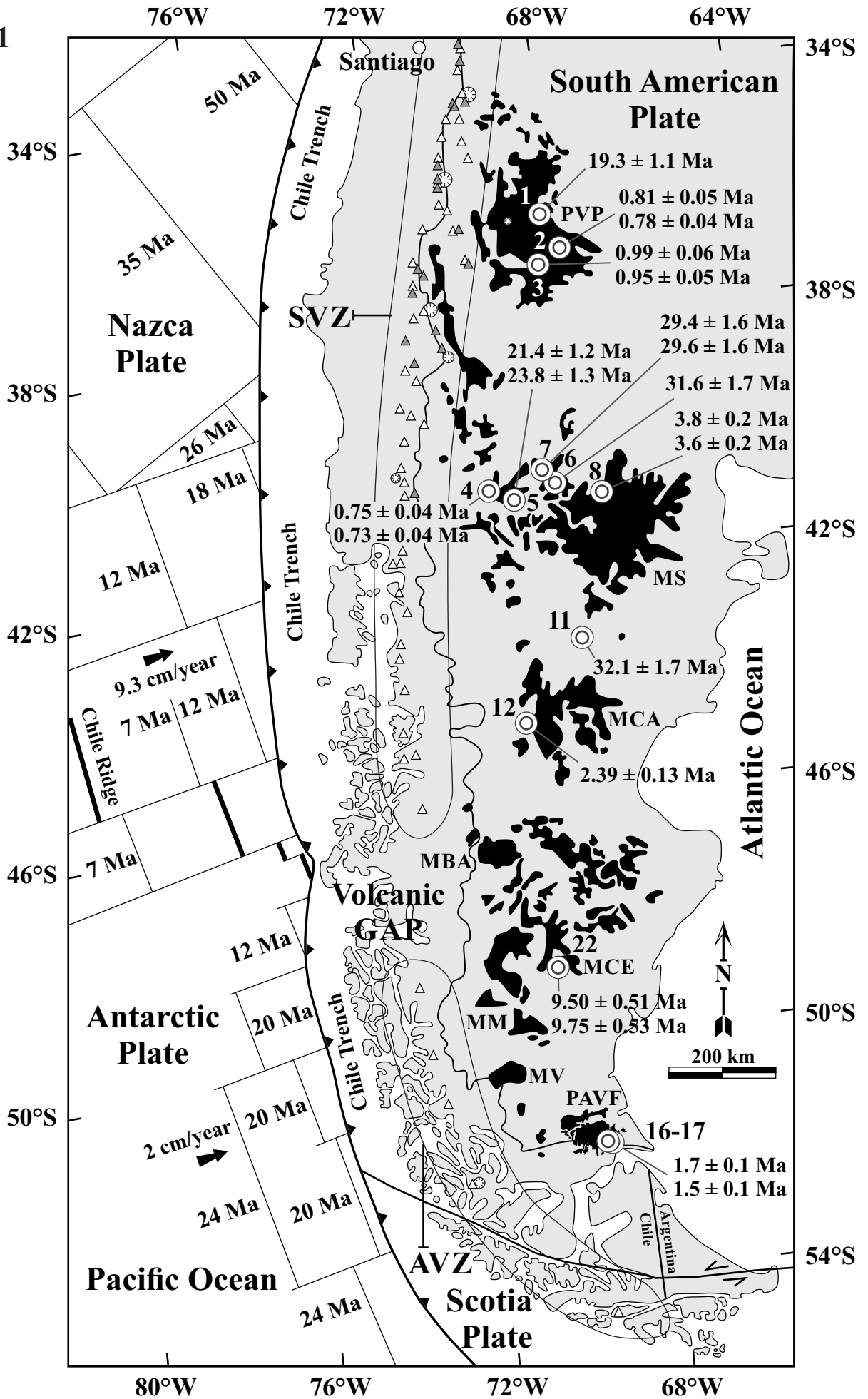


Figure 2

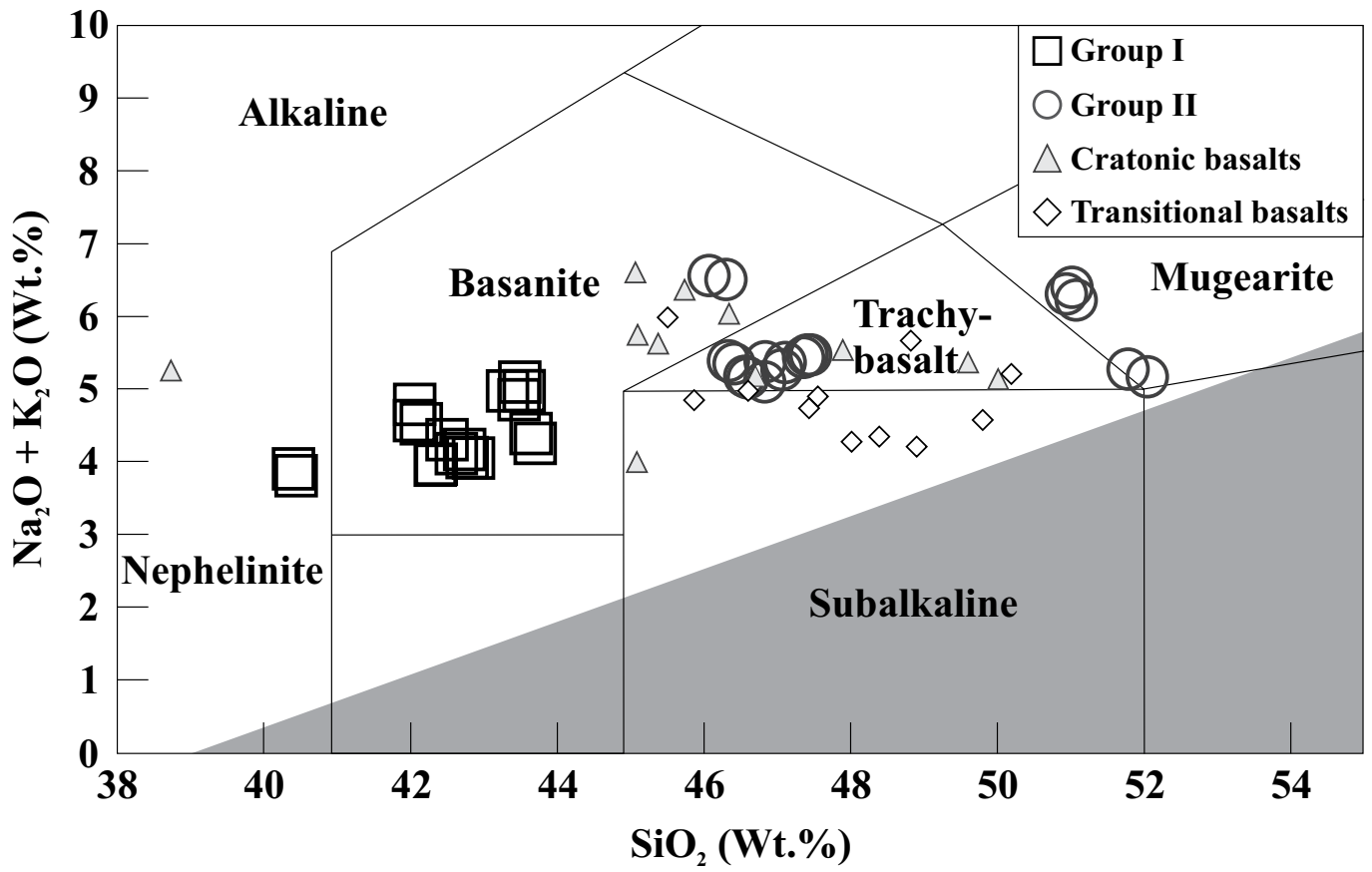


Figure 3

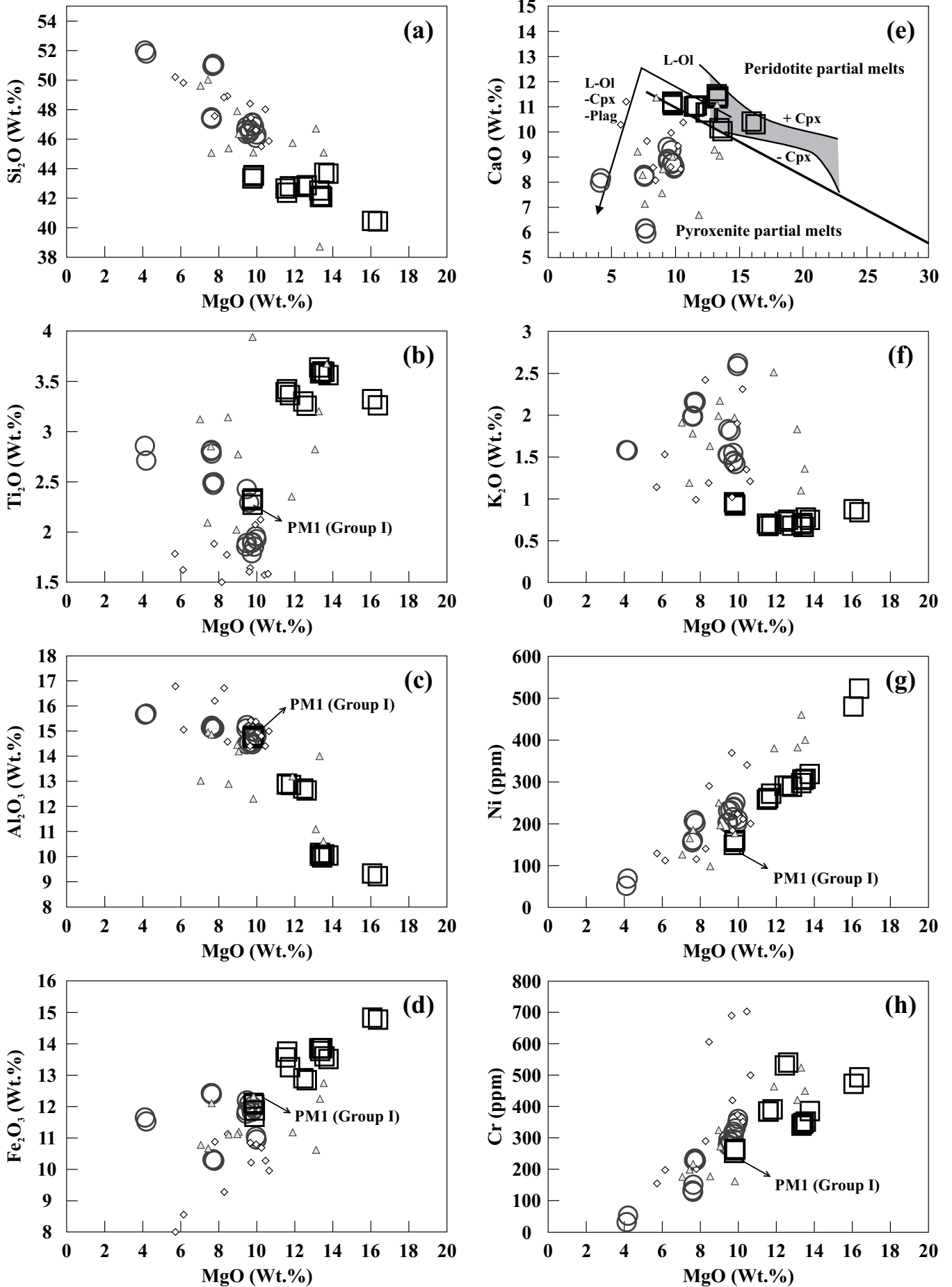


Figure 4

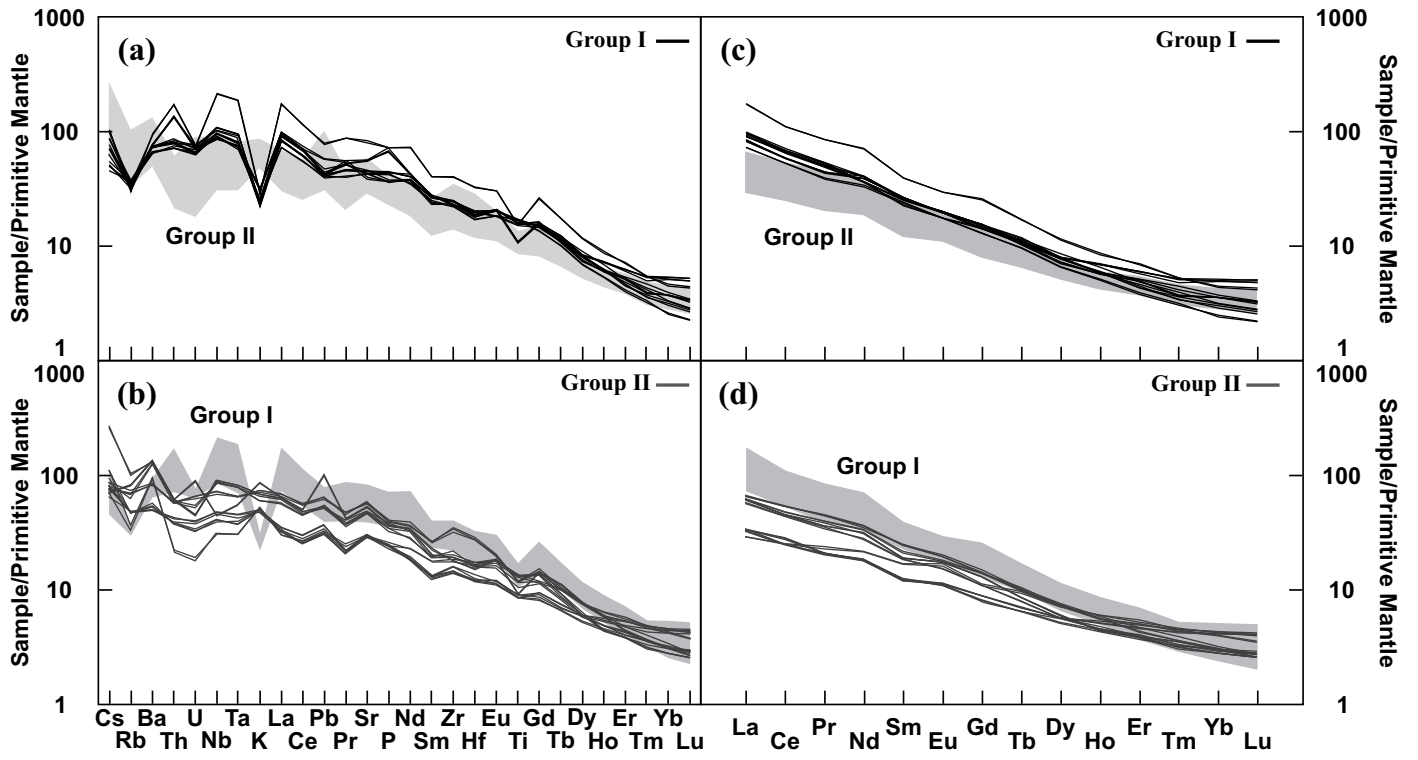


Figure 5

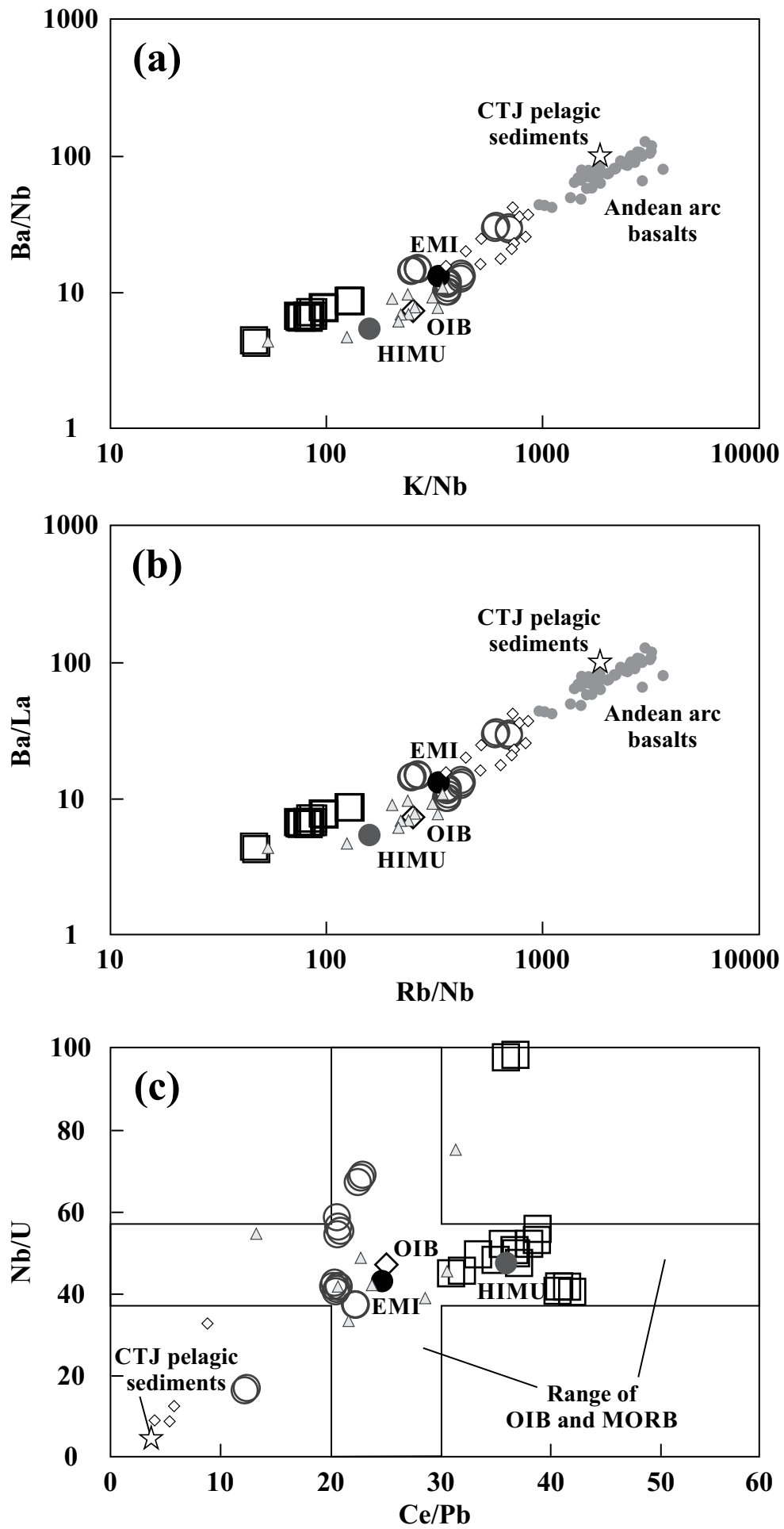


Figure 6

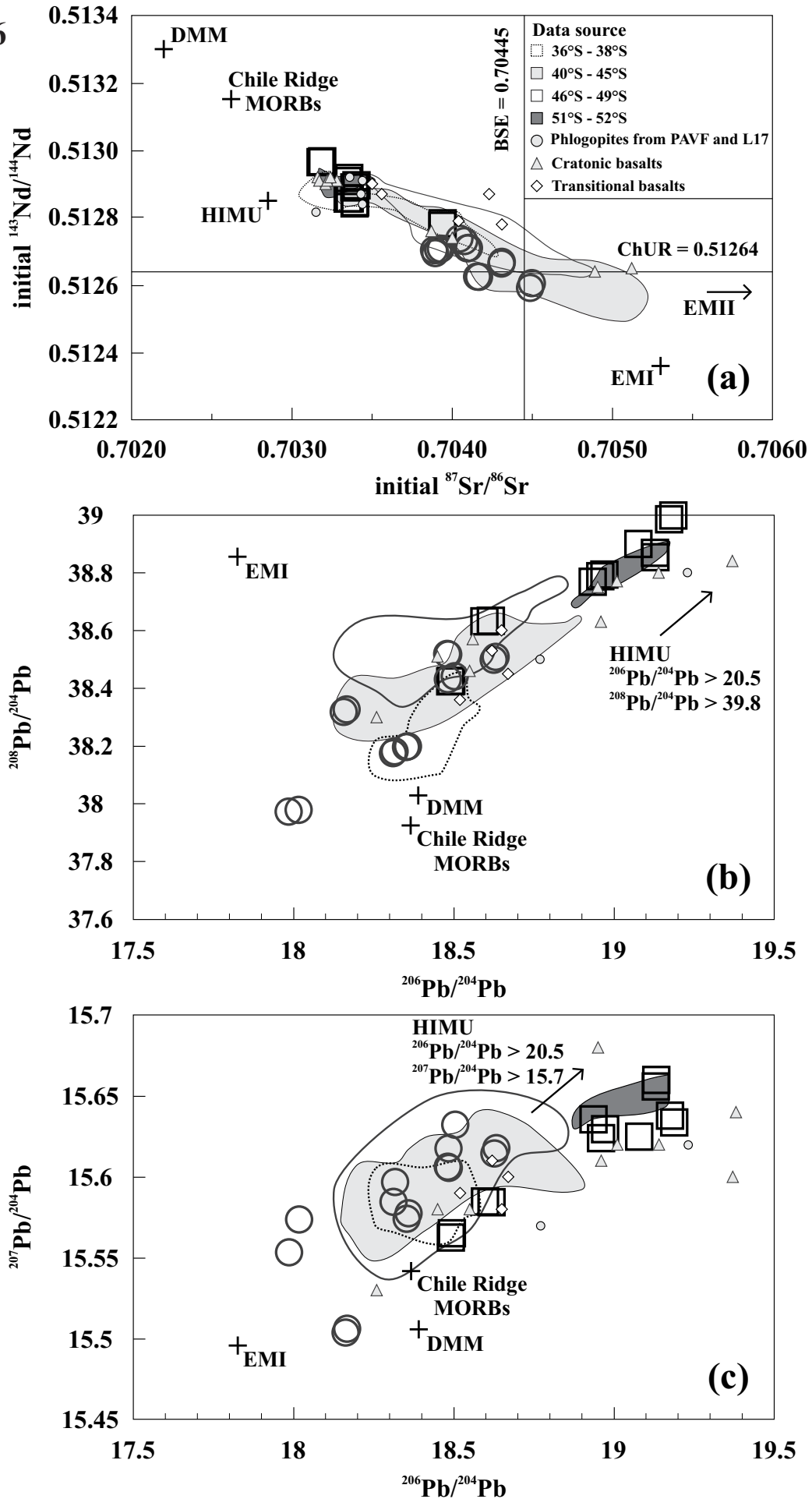


Figure 7

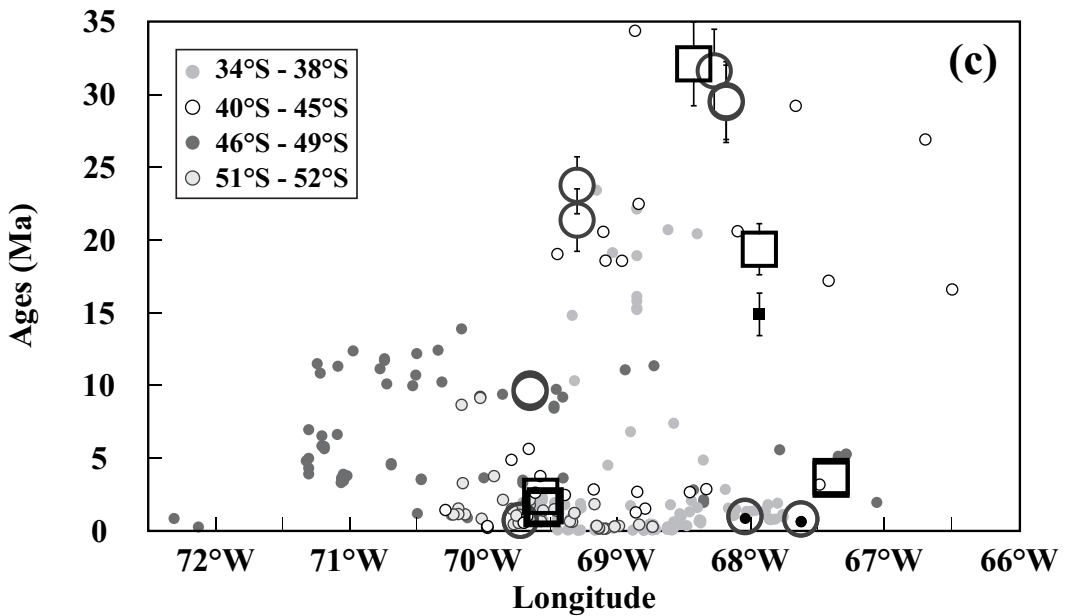
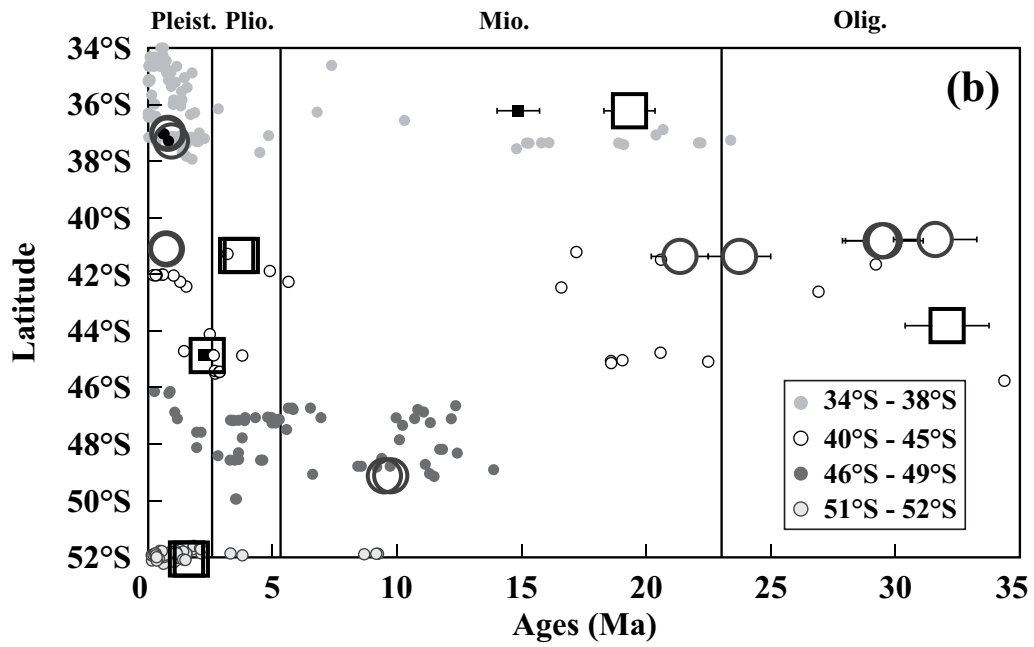
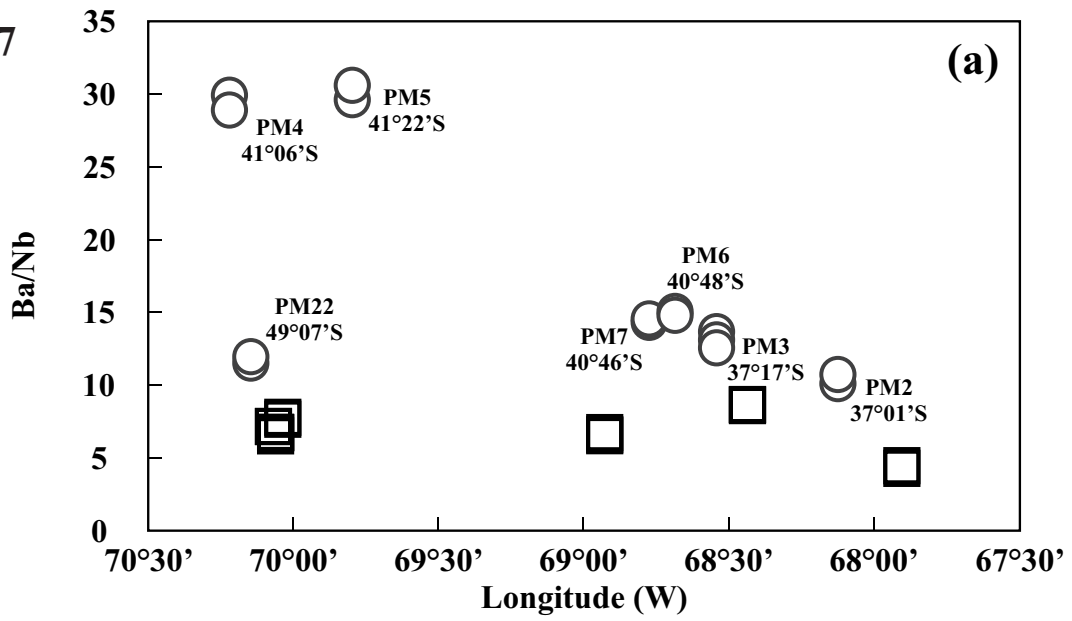


Figure 8

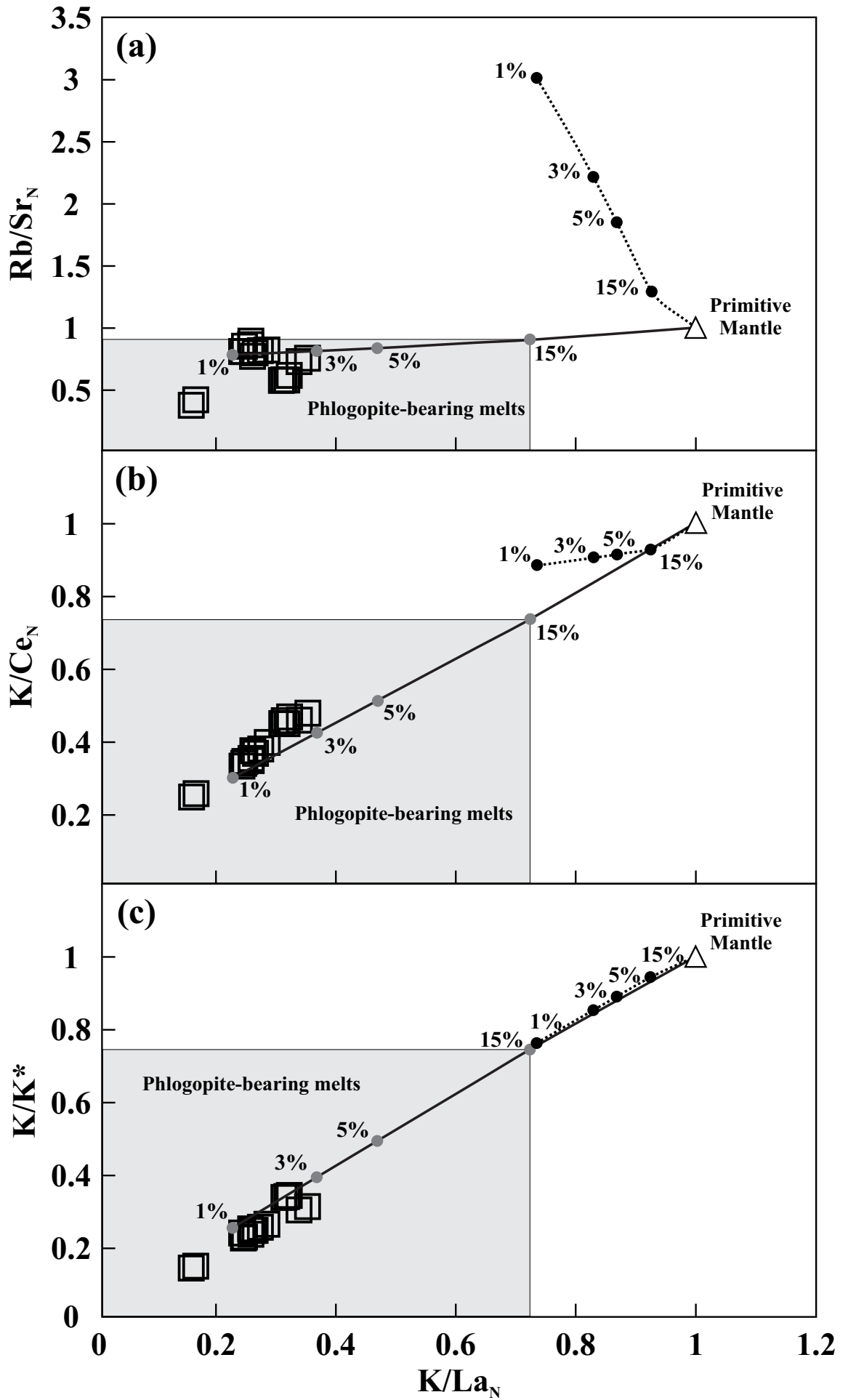


Figure 9

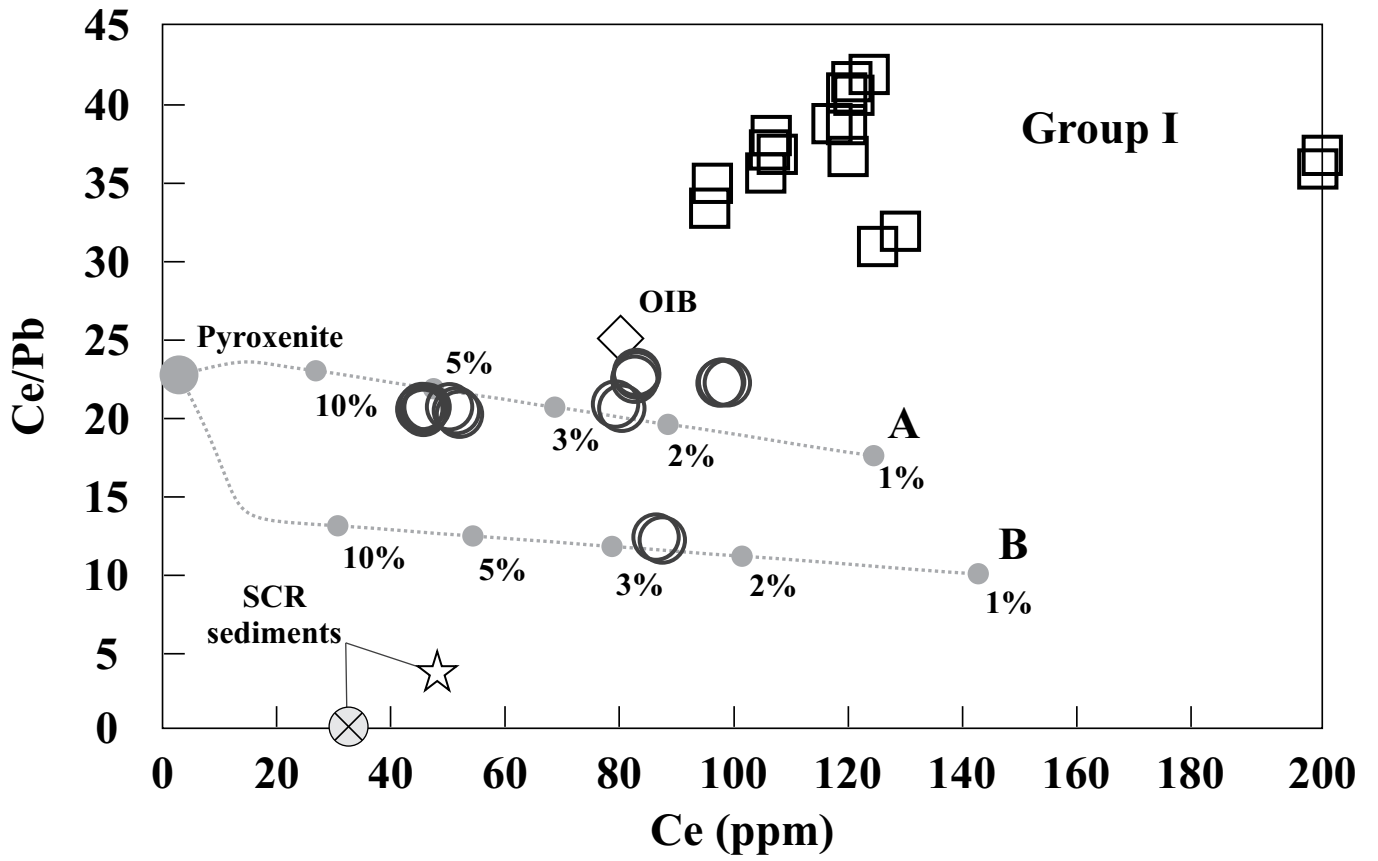


Figure 10

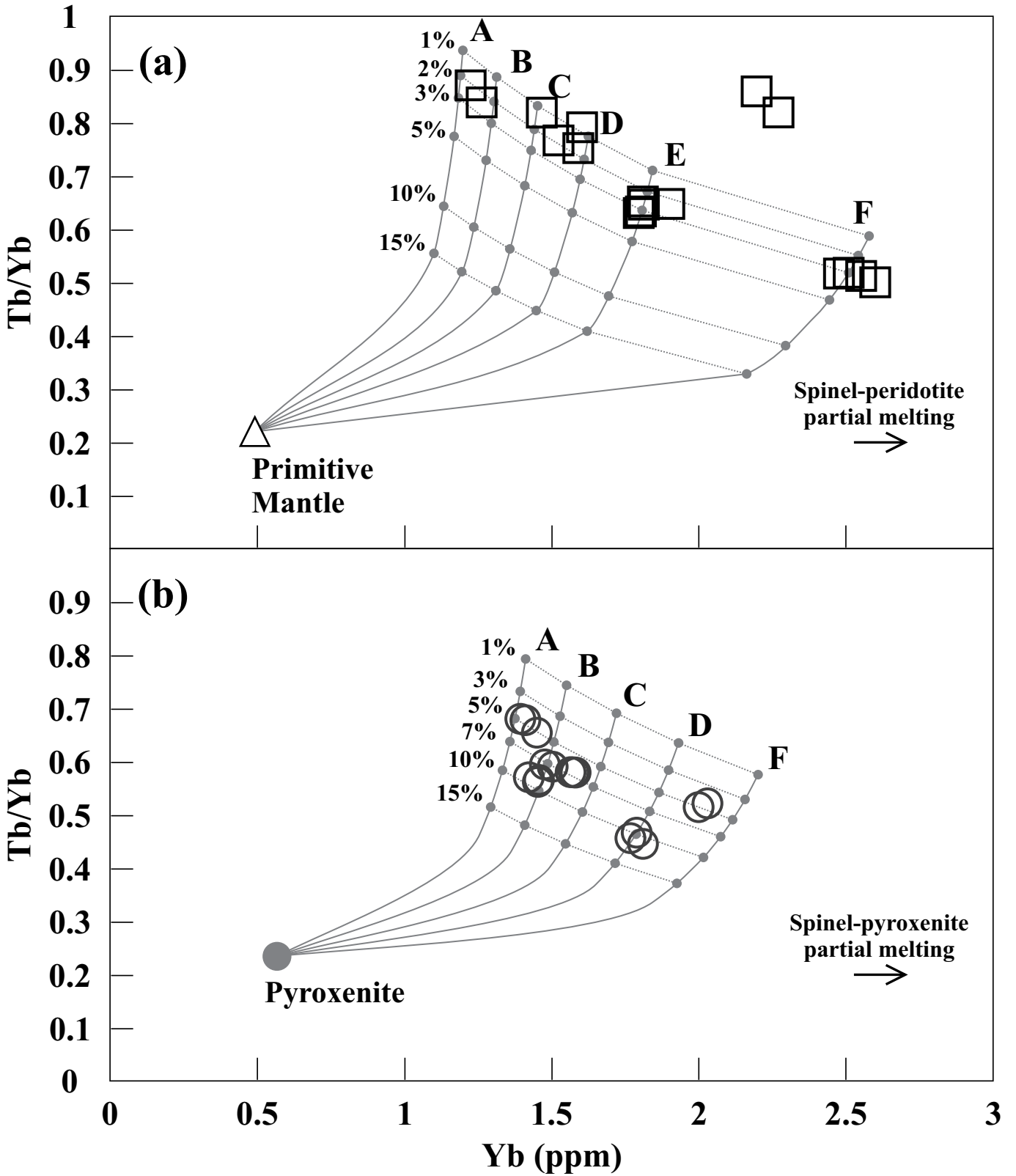
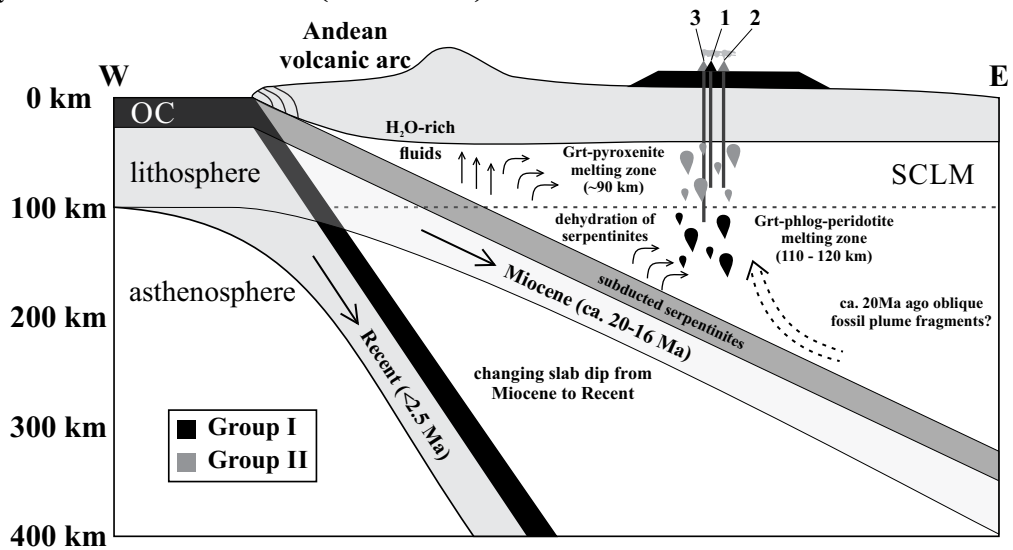
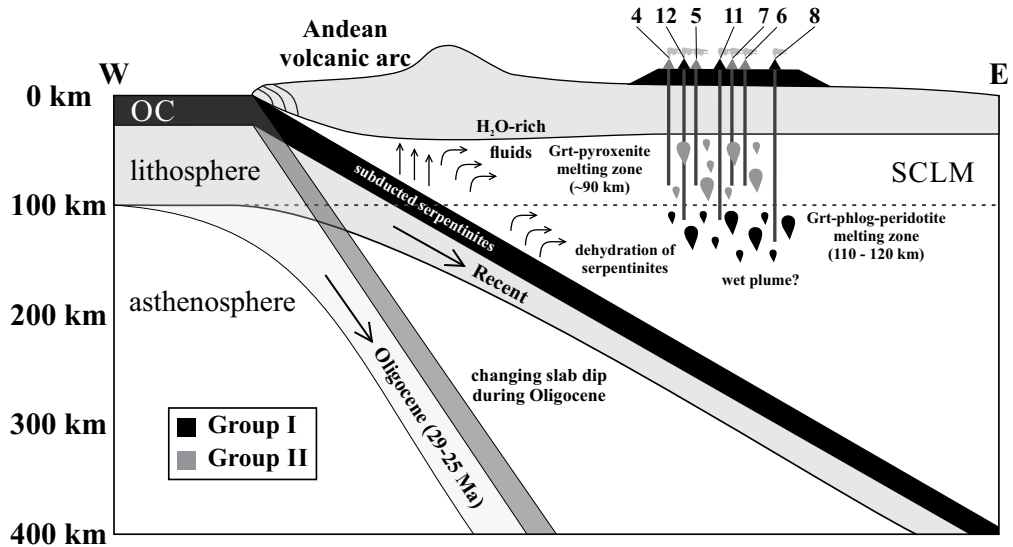


Figure 11

(a) Payenia Volcanic Province (36°S - 38°S)



(b) Somún Curá, Valle del Río Genoa and Paso de Indios areas (40°S - 45°S)



(c) Meseta Central and PAVF areas (49°S - 52°S)

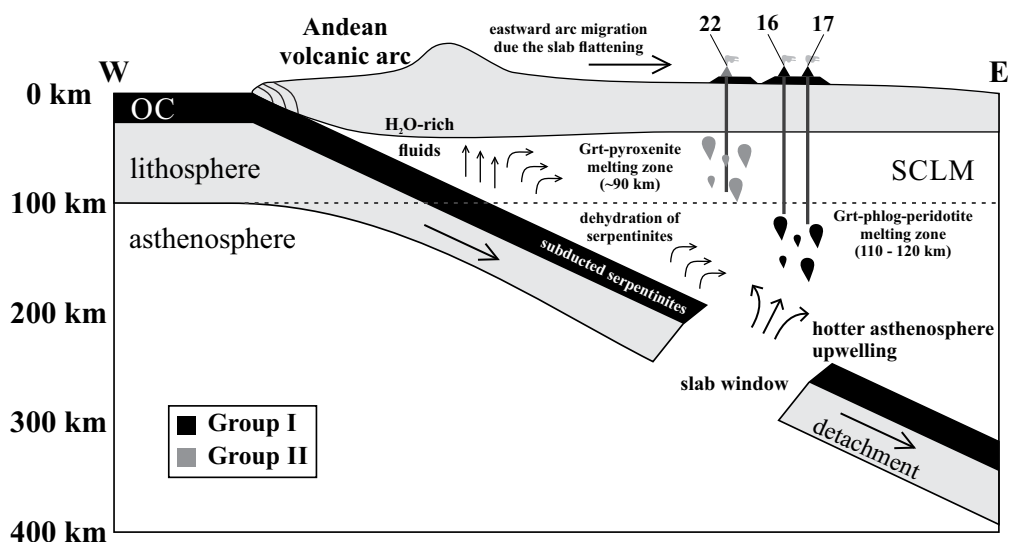


Table 1: Whole-rock geochemical data of Group I basalts

Group I									
Sample:	PM1-A1	PM1-A2	PM1-A3	PM1-A4	PM8-A1	PM8-B2	PM11-A1	PM11-A2	PM11-A3
Rock type:	BS	BS	BS	BS	MNeph	MNeph	BS	BS	BS
<i>Major elements (wt.%)</i>									
SiO ₂	43.48	43.32	43.49	43.55	40.41	40.44	42.50	42.35	42.34
TiO ₂	2.33	2.32	2.27	2.33	3.26	3.32	3.38	3.42	3.41
Al ₂ O ₃	14.73	14.77	14.83	14.77	9.23	9.33	12.86	12.91	12.88
Fe ₂ O ₃	12.01	12.05	11.58	11.81	14.76	14.82	13.31	13.74	13.63
MnO	0.21	0.21	0.21	0.21	0.22	0.23	0.19	0.19	0.20
MgO	9.82	9.77	9.80	9.84	16.37	16.07	11.80	11.59	11.57
CaO	11.13	11.13	11.19	11.05	10.29	10.40	11.09	11.02	11.05
Na ₂ O	3.94	4.02	4.16	4.05	3.07	2.94	3.40	3.30	3.44
K ₂ O	0.92	0.96	0.94	0.93	0.84	0.87	0.70	0.67	0.70
P ₂ O ₅	1.44	1.46	1.54	1.45	1.56	1.58	0.77	0.81	0.78
Mg-number	62	62	63	62	69	68	64	63	63
<i>Compatible elements (ppm)</i>									
V	238	242	232	228	176	175	256	257	262
Cr	263	252	260	265	493	473	391	385	384
Co	46	45	42	45	64	62	56	57	57
Ni	156	149	160	161	522	480	271	261	257
Zn	87	88	110	84	154	156	101	103	102
Ga	21	21	21	19	20	19	19	19	19
<i>Trace and rare earth elements (ppm)</i>									
Cs	0.60	0.76	0.68	0.54	0.80	0.78	0.68	0.55	0.67
Rb	19.93	21.35	20.32	19.83	18.74	21.98	22.95	23.13	23.65
Ba	522.17	530.02	526.32	519.13	670.66	654.89	509.28	510.54	497.69
Th	11.62	11.40	11.30	11.32	14.49	14.81	7.25	6.78	6.77
U	1.45	1.52	1.51	1.44	1.55	1.57	1.46	1.36	1.51
Nb	60.46	61.84	61.01	60.11	151.41	154.23	77.59	76.07	76.59
Ta	2.99	2.96	3.01	3.07	7.72	7.72	3.82	3.83	3.82
K	7603	7940	7788	7684	6949	7250	5796	5582	5846
La	67.55	67.67	67.23	67.34	120.08	119.64	64.27	62.35	62.14
Ce	120.49	120.85	123.52	119.58	200.22	201.18	119.56	117.01	119.83
Pb	2.91	2.98	2.95	2.94	5.59	5.48	3.09	3.02	3.27
Pr	14.39	14.31	15.06	14.22	24.05	24.16	14.08	13.84	14.07
Sr	1152	1154	1169	1138	1664	1744	897	953	882
P	6294	6350	6705	6338	6800	6878	3371	3536	3406
Nd	55.90	55.82	56.40	56.39	98.48	97.83	50.78	50.08	49.97
Sm	11.68	11.81	11.60	11.72	17.83	17.90	11.59	11.48	11.42
Zr	272.52	276.12	273.27	269.34	442.71	452.69	271.66	268.53	268.77
Hf	5.54	5.53	5.50	5.69	10.15	9.99	5.99	5.96	6.16
Eu	3.45	3.45	3.36	3.45	5.07	5.07	3.41	3.44	3.36
Ti	13981	13877	13603	13947	19533	19902	20243	20492	20437
Gd	9.37	9.35	9.32	9.42	15.82	15.44	9.52	9.07	9.40
Tb	1.28	1.29	1.30	1.31	1.89	1.86	1.17	1.13	1.14
Dy	6.20	6.20	6.21	6.20	8.52	8.70	5.45	5.33	5.47
Ho	1.16	1.17	1.18	1.15	1.42	1.47	0.96	0.97	0.96
Er	2.82	2.95	2.92	2.96	3.46	3.36	2.46	2.41	2.27
Tm	0.38	0.39	0.39	0.39	0.40	0.40	0.33	0.33	0.33
Yb	2.48	2.51	2.60	2.55	2.20	2.27	1.81	1.80	1.80
Lu	0.37	0.36	0.38	0.39	0.31	0.33	0.25	0.24	0.25

Table 1: Continued

Group I								
Sample:	PM12-A3	PM12-A4	PM16-A1	PM16-A3	PM17-A1	PM17-A2	PM17-A3	PM17-A4
Rock type:	BS	BS	BS	BS	BS	BS	BS	BS
<i>Major elements (wt.%)</i>								
SiO ₂	42.86	42.74	43.65	43.70	42.06	42.15	42.26	42.05
TiO ₂	3.26	3.30	3.56	3.59	3.58	3.58	3.64	3.60
Al ₂ O ₃	12.64	12.72	10.05	10.09	10.04	10.07	10.15	9.97
Fe ₂ O ₃	12.83	12.89	13.50	13.59	13.76	13.84	13.77	13.85
MnO	0.19	0.19	0.17	0.17	0.18	0.18	0.17	0.18
MgO	12.62	12.44	13.76	13.55	13.32	13.38	13.33	13.44
CaO	10.77	10.76	10.02	10.13	11.33	11.32	11.49	11.40
Na ₂ O	3.30	3.45	3.64	3.48	4.10	3.81	3.61	3.91
K ₂ O	0.75	0.73	0.75	0.77	0.69	0.71	0.67	0.66
P ₂ O ₅	0.79	0.79	0.90	0.92	0.94	0.95	0.92	0.94
Mg-number	66	66	67	66	66	66	66	66
<i>Compatible elements (ppm)</i>								
V	249	249	212	229	236	235	238	236
Cr	540	531	386	352	343	345	339	348
Co	54	54	67	65	67	66	66	67
Ni	290	290	318	307	297	306	288	304
Zn	150	150	134	138	128	127	130	129
Ga	19	20	20	20	19	19	20	19
<i>Trace and rare earth elements (ppm)</i>								
Cs	0.50	0.40	0.80	0.56	0.36	0.43	0.39	0.39
Rb	21.00	20.08	19.29	20.27	23.13	22.98	21.55	22.36
Ba	512.00	514.00	502.84	502.45	456.66	458.19	439.99	456.35
Th	6.67	6.92	6.65	6.49	6.11	6.05	6.27	5.96
U	1.60	1.58	1.34	1.33	1.37	1.31	1.43	1.30
Nb	71.92	72.02	64.79	65.90	68.20	68.25	67.88	67.76
Ta	3.67	3.70	2.80	2.98	3.18	3.17	3.27	3.14
K	6203	6019	6188	6418	5726	5882	5580	5491
La	66.06	68.08	50.21	49.96	57.38	56.69	58.69	56.82
Ce	125.00	129.00	96.08	95.60	107.44	105.41	106.07	106.38
Pb	4.05	4.05	2.75	2.87	2.92	2.96	2.86	2.80
Pr	14.70	15.10	11.11	10.88	12.58	12.29	12.55	12.45
Sr	810	827	884	894	944	932	932	933
P	3445	3440	3941	3995	4119	4160	4025	4102
Nd	50.21	50.26	47.08	45.84	54.00	53.92	56.22	53.67
Sm	10.29	10.32	10.94	10.67	12.08	12.04	12.06	12.12
Zr	256.36	252.49	243.46	241.03	250.45	245.03	270.08	254.65
Hf	6.02	6.04	5.13	5.23	5.61	5.40	5.96	5.57
Eu	3.01	3.02	3.03	3.02	3.36	3.35	3.37	3.35
Ti	19511	19764	21336	21530	21442	21480	21798	21556
Gd	8.66	8.99	7.90	7.95	8.66	8.65	8.73	8.72
Tb	1.18	1.23	1.07	1.06	1.20	1.17	1.27	1.20
Dy	5.90	6.04	5.00	4.95	5.93	5.86	6.49	5.87
Ho	0.99	0.99	0.87	0.85	0.99	1.01	1.10	0.99
Er	2.51	2.54	1.94	1.87	2.12	2.19	2.41	2.12
Tm	0.32	0.34	0.24	0.23	0.26	0.26	0.30	0.27
Yb	1.81	1.90	1.22	1.26	1.47	1.52	1.60	1.59
Lu	0.25	0.25	0.17	0.17	0.20	0.20	0.21	0.21

*Total iron reported as Fe₂O₃. BS = basanite; MNeph = melanephelinite. Major element results were normalized to 100%.

Table 2: Whole-rock geochemical data of Group II basalts

Group II									
Sample:	PM2A1	PM2A3	PM2-A4	PM3A1	PM3A2	PM3A3	PM4B2	PM4B4	PM5A2
Rock type:	TB	TB	TB	TB	TB	TB	BS	BS	MG
<i>Major elements (wt.%)</i>									
SiO ₂	47.07	47.11	46.84	46.85	46.63	46.62	46.30	46.07	51.78
TiO ₂	1.89	1.90	1.85	1.89	1.86	1.79	1.93	1.96	2.71
Al ₂ O ₃	14.56	14.48	14.71	15.24	15.11	15.00	14.80	14.96	15.70
Fe ₂ O ₃	12.03	12.00	11.92	11.86	11.77	11.83	10.94	11.03	11.52
MnO	0.17	0.16	0.17	0.17	0.17	0.18	0.17	0.17	0.15
MgO	9.75	9.76	9.85	9.48	9.45	9.74	9.98	9.95	4.19
CaO	8.73	8.72	8.77	8.92	9.40	9.27	8.60	8.53	8.14
Na ₂ O	3.83	3.91	3.96	3.58	3.63	3.61	3.89	3.97	3.70
K ₂ O	1.44	1.45	1.41	1.47	1.47	1.47	2.62	2.59	1.58
P ₂ O ₅	0.54	0.50	0.53	0.54	0.53	0.50	0.78	0.77	0.54
Mg-number	62	62	62	61	61	62	64	64	42
<i>Compatible elements (ppm)</i>									
V	184	174	185	189	197	201	208	205	209
Cr	319	312	331	275	279	296	360	350	52
Co	51	51	52	49	49	50	45	44	35
Ni	238	240	250	202	202	215	210	201	68
Zn	108	106	108	88	89	93	110	110	107
Ga	20	20	19	18	19	18	20	19	23
<i>Trace and rare earth elements (ppm)</i>									
Cs	0.62	0.51	0.64	0.86	0.73	0.59	2.00	2.10	0.85
Rb	29.33	29.83	29.29	28.81	29.14	29.27	64.00	62.00	22.99
Ba	353.72	337.22	334.42	399.47	369.43	380.13	905.00	925.00	660.02
Th	3.34	3.51	3.42	3.23	3.30	3.31	5.06	5.09	1.79
U	0.79	0.80	0.81	0.68	0.72	0.69	1.85	1.89	0.37
Nb	33.01	33.40	33.03	29.22	29.42	29.02	31.30	30.90	21.56
Ta	1.74	1.81	1.80	1.56	1.54	1.56	2.20	2.18	1.22
K	11984	12068	11730	12170	12206	12194	21720	21459	13081
La	23.01	23.25	23.47	23.36	22.32	22.52	42.83	42.80	20.04
Ce	50.06	51.79	51.24	45.48	44.84	45.25	86.20	87.30	45.78
Pb	2.43	2.57	2.51	2.24	2.19	2.19	7.00	7.20	2.23
Pr	5.90	5.90	5.94	5.85	5.72	5.86	11.20	11.30	6.43
Sr	630	625	638	611	612	615	1104	1130	624
P	2358	2199	2301	2369	2296	2162	3395	3380	2373
Nd	24.78	25.39	25.19	25.78	25.02	25.47	46.30	46.90	29.82
Sm	5.57	5.74	5.66	5.63	5.48	5.47	9.56	9.92	7.56
Zr	178.09	174.13	164.36	157.55	156.24	152.78	195.00	194.00	191.40
Hf	3.91	4.07	3.66	3.63	3.70	3.62	4.50	4.60	4.85
Eu	1.91	1.91	1.87	1.97	1.91	1.97	3.05	3.12	2.78
Ti	11332	11363	11103	11322	11122	10719	11547	11726	16238
Gd	4.98	4.94	4.86	5.43	5.43	5.46	8.50	8.58	6.62
Tb	0.81	0.82	0.82	0.84	0.81	0.81	1.03	1.06	1.04
Dy	4.19	4.23	4.20	4.74	4.64	4.67	5.44	5.55	5.39
Ho	0.72	0.77	0.75	0.90	0.87	0.86	0.97	0.99	1.01
Er	1.83	2.01	1.93	2.43	2.31	2.26	2.48	2.47	2.58
Tm	0.25	0.25	0.27	0.30	0.29	0.29	0.33	0.34	0.35
Yb	1.42	1.45	1.46	1.79	1.77	1.81	2.00	2.03	2.12
Lu	0.21	0.21	0.21	0.27	0.26	0.27	0.27	0.27	0.30

Table 2: Continued

Group II									
Sample:	PM5A3	PM6A1	PM6A2	PM6A3	PM7A1	PM7A2	PM22-A1	PM22-A2	PM22-A3
Rock type:	MG	TB	TB	TB	TB	TB	MG	MG	MG
<i>Major elements (wt.%)</i>									
SiO ₂	51.98	47.41	47.46	47.36	46.33	46.41	51.08	50.94	51.02
TiO ₂	2.86	2.80	2.81	2.78	2.43	2.29	2.47	2.49	2.49
Al ₂ O ₃	15.66	15.14	15.12	15.22	14.48	14.54	15.10	15.16	15.12
Fe ₂ O ₃	11.64	12.41	12.42	12.38	12.18	12.08	10.31	10.30	10.27
MnO	0.13	0.15	0.15	0.15	0.16	0.17	0.13	0.13	0.13
MgO	4.11	7.58	7.61	7.62	9.47	9.59	7.70	7.67	7.76
CaO	7.97	8.28	8.20	8.26	8.81	8.87	6.14	6.15	5.95
Na ₂ O	3.55	3.49	3.48	3.46	3.56	3.54	4.08	4.15	4.24
K ₂ O	1.58	1.98	1.99	1.98	1.83	1.81	2.14	2.16	2.16
P ₂ O ₅	0.51	0.75	0.75	0.80	0.75	0.71	0.85	0.86	0.86
Mg-number	41	55	55	55	61	61	60	60	60
<i>Compatible elements (ppm)</i>									
V	179	186	181	177	180	197	143	141	139
Cr	31	133	129	151	295	287	234	228	228
Co	33	51	51	47	35	49	39	39	39
Ni	51	155	160	160	230	232	208	206	201
Zn	113	132	133	160	89	102	128	127	130
Ga	22	23	22	24	19	19	23	24	23
<i>Trace and rare earth elements (ppm)</i>									
Cs	0.54	0.57	0.54	0.56	0.63	0.67	0.59	0.59	0.68
Rb	20.51	49.99	52.60	53.07	41.88	39.06	43.90	44.94	47.02
Ba	648.77	937.67	925.94	942.34	887.75	876.22	582.83	574.01	598.42
Th	1.84	5.00	5.13	4.97	4.94	4.92	4.87	4.79	4.70
U	0.39	0.92	0.93	0.91	1.12	1.11	1.31	1.34	1.34
Nb	21.90	62.57	62.60	62.58	61.03	61.27	49.06	49.92	50.08
Ta	1.21	3.27	3.24	3.25	3.26	3.24	2.66	2.62	2.59
K	13116	16449	16522	16432	15190	15015	17771	17898	17915
La	20.07	42.44	42.19	41.80	40.04	39.06	45.61	45.23	46.19
Ce	46.12	82.81	82.47	82.77	80.21	79.10	97.41	97.68	98.69
Pb	2.24	3.65	3.68	3.63	3.90	3.80	4.40	4.40	4.45
Pr	6.75	10.28	10.27	10.90	9.95	9.59	12.69	12.76	12.55
Sr	620	986	989	998	990	983	1197	1174	1216
P	2228	3273	3274	3502	3278	3077	3724	3762	3768
Nd	30.23	43.67	44.23	42.93	38.12	39.02	48.68	51.01	50.20
Sm	7.65	8.59	8.58	8.65	8.40	8.49	11.44	11.26	11.14
Zr	199.80	217.83	218.39	208.00	238.62	216.07	381.22	394.05	360.66
Hf	5.15	5.11	5.21	5.00	4.79	4.95	8.61	8.97	8.52
Eu	2.90	3.03	3.01	2.98	2.64	2.61	3.36	3.46	3.34
Ti	17116	16796	16867	16654	14543	13722	14795	14920	14945
Gd	6.88	7.97	7.93	7.93	6.75	6.76	7.95	7.96	7.97
Tb	1.07	0.95	0.95	0.96	0.88	0.89	0.91	0.91	0.92
Dy	5.43	4.53	4.37	4.49	4.27	4.28	5.11	5.18	5.16
Ho	1.01	0.73	0.73	0.74	0.77	0.81	0.95	0.99	0.96
Er	2.69	1.87	1.91	1.89	1.95	1.94	2.22	2.31	2.21
Tm	0.35	0.23	0.24	0.24	0.25	0.27	0.27	0.29	0.27
Yb	2.19	1.45	1.39	1.41	1.48	1.50	1.56	1.57	1.58
Lu	0.31	0.19	0.19	0.19	0.21	0.22	0.20	0.21	0.20

*Total iron reported as Fe₂O₃. BS = basanite; TB = trachybasalt; MG = mugearite. Major element results were normalized to 100%.

Table 3: CIPW norms and selected trace element ratios for Group I and II basalts

Group I																	
Sample:	PM1 -A1	PM1 -A2	PM1 -A3	PM1 -A4	PM8 -A1	PM8 -B2	PM11 -A1	PM11 -A2	PM11 -A3	PM12 -A3	PM12 -A4	PM16 -A1	PM16 -A3	PM17 -A1	PM17 -A2	PM17 -A3	PM17 -A4
<i>C.I.P.W. Norm (wt.%)</i>																	
Ol	16	15	15	16	26	26	17	17	17	19	18	20	19	17	17	17	17
Ne	11	12	12	12	11	10	10	10	11	9	10	9	8	16	14	13	15
Hy	-	-	-	-	-	-	-	-	-	-	-	-	-	-	-	-	-
Qtz	-	-	-	-	-	-	-	-	-	-	-	-	-	-	-	-	-
<i>Selected ratios in ppm</i>																	
Ce/Pb	41.4	40.5	41.8	40.6	35.8	36.7	38.66	38.73	36.63	30.87	31.85	34.91	33.32	36.77	35.57	37.04	37.96
Nb/U	41.6	40.6	40.4	41.7	97.7	98.3	53.10	55.82	50.62	44.95	45.58	48.23	49.58	49.83	52.12	47.48	52.16
Nb/La	0.89	0.91	0.91	0.89	1.26	1.29	1.21	1.22	1.23	1.09	1.06	1.29	1.32	1.19	1.20	1.16	1.19
Nb-Ta	20.2	20.9	20.2	19.5	19.6	19.9	20.29	19.88	20.06	19.60	19.49	23.15	22.09	21.44	21.50	20.78	21.58
Th/U	8.01	7.49	7.48	7.86	9.35	9.44	4.96	4.97	4.47	4.17	4.38	4.95	4.88	4.47	4.62	4.39	4.58
Ba/Th	44.9	46.5	46.5	45.8	46.3	44.2	70.21	75.34	73.53	76.76	74.28	75.56	77.39	74.71	75.71	70.13	76.63
Ba/Nb	8.64	8.57	8.63	8.64	4.43	4.25	6.56	6.71	6.50	7.12	7.14	7.76	7.62	6.70	6.71	6.48	6.73
Ba/La	7.73	7.83	7.83	7.71	5.58	5.47	7.92	8.19	8.01	7.75	7.55	10.01	10.06	7.96	8.08	7.50	8.03
K/Nb	126	128	128	129	46	47	75	73	76	86	84	96	97	84	86	82	81
K/La	113	117	116	114	58	61	90	90	94	94	88	123	128	100	104	95	97
K/Ce	63	66	63	64	35	36	48	48	49	50	47	64	67	53	56	53	52
Rb/Nb	0.33	0.35	0.33	0.33	0.12	0.14	0.30	0.30	0.31	0.29	0.28	0.30	0.31	0.34	0.34	0.32	0.33
<i>Selected normalized ratios</i>																	
Nb/Nb*	0.73	0.75	0.75	0.74	1.23	1.24	1.22	1.25	1.27	1.16	1.12	1.20	1.24	1.23	1.25	1.20	1.25
Pb/Pb*	0.69	0.71	0.67	0.70	0.79	0.77	0.74	0.74	0.79	0.93	0.90	0.83	0.88	0.78	0.81	0.77	0.76
K/K*	0.33	0.34	0.34	0.34	0.14	0.15	0.23	0.23	0.24	0.25	0.24	0.30	0.31	0.26	0.26	0.25	0.25
Eu/Eu*	1.01	1.00	0.99	1.01	0.92	0.93	0.99	1.03	0.99	0.98	0.96	1.00	1.00	1.01	1.01	1.01	1.00
Tb/Yb	2.36	2.35	2.28	2.34	3.92	3.74	2.95	2.88	2.88	2.98	2.96	3.97	3.83	3.74	3.50	3.61	3.43

Table 3: Continued

Group II																			
Sample:	PM2-A1	PM2-A3	PM2-A4	PM3-A1	PM3-A2	PM3-A3	PM4-B2	PM4-B4	PM5-A2	PM5-A3	PM6-A1	PM6-A2	PM6-A3	PM7-A1	PM7-A2	PM2-2-A1	PM2-2-A2	PM2-2-A3	
<i>C.I.P.W. Norm (wt.%)</i>																			
Ol	17	17	17	17	16	17	17	17	-	-	14	14	14	16	17	11	12	13	
Ne	6	6	7	5	7	7	12	12	-	-	3	2	2	6	6	-	-	-	
Hy	-	-	-	-	-	-	-	-	10	11	-	-	-	-	-	6	5	4	
Qtz	-	-	-	-	-	-	-	-	2	3	-	-	-	-	-	-	-	-	
<i>Selected ratios in ppm</i>																			
Ce/Pb	20.6	20.1	20.3	20.2	20.4	20.6	12.3	12.1	20.5	20.6	22.6	22.4	22.8	20.5	20.8	22.15	22.22	22.17	
Nb/U	41.6	41.8	40.5	42.6	41.1	41.8	16.9	16.3	58.6	56.3	68.3	67.2	69.0	54.4	55.3	37.38	37.31	37.27	
Nb/La	1.43	1.44	1.41	1.25	1.32	1.29	0.73	0.72	1.08	1.09	1.47	1.48	1.50	1.52	1.57	1.08	1.10	1.08	
Nb-Ta	19.0	18.4	18.3	18.6	19.0	18.5	14.2	14.1	17.6	18.0	19.1	19.3	19.2	18.6	18.9	18.43	19.03	19.33	
Th/U	4.22	4.40	4.20	4.72	4.61	4.77	2.74	2.69	4.86	4.74	5.47	5.52	5.48	4.41	4.45	3.71	3.58	3.50	
Ba/Th	105.77	96.09	97.80	123.68	111.93	114.91	178.85	181.73	369.25	352.41	187.45	180.37	189.57	179.56	178.09	119.75	119.75	127.25	
Ba/Nb	10.7	10.1	10.1	13.6	12.5	13.1	28.9	29.9	30.6	29.6	14.9	14.7	15.0	14.5	14.3	11.88	11.50	11.95	
Ba/La	15.3	14.5	14.2	17.1	16.5	16.8	21.1	21.6	32.9	32.3	22.0	21.9	22.5	22.1	22.4	12.78	12.69	12.96	
K/Nb	363	361	355	416	415	420	694	694	607	599	263	264	263	249	245	362	359	358	
K/La	521	519	500	521	547	542	507	501	653	653	388	392	393	379	384	390	396	388	
K/Ce	239	233	229	268	272	269	252	246	286	284	199	200	199	189	190	182	183	182	
Rb/Nb	0.89	0.89	0.89	0.99	0.99	1.01	2.04	2.01	1.07	0.94	0.80	0.84	0.85	0.69	0.64	0.89	0.90	0.94	
<i>Selected normalized ratios</i>																			
Nb/Nb*	1.28	1.25	1.25	1.14	1.16	1.14	0.72	0.71	1.22	1.22	1.46	1.44	1.47	1.47	1.50	1.12	1.15	1.15	
Pb/Pb*	1.39	1.45	1.42	1.36	1.35	1.33	2.22	2.26	1.28	1.25	1.23	1.25	1.19	1.36	1.36	1.23	1.23	1.25	
K/K*	1.22	1.21	1.18	1.30	1.33	1.34	1.66	1.65	1.76	1.75	0.89	0.90	0.90	0.86	0.86	1.05	1.05	1.04	
Eu/Eu*	1.11	1.10	1.09	1.09	1.07	1.10	1.04	1.04	1.20	1.22	1.12	1.12	1.10	1.07	1.05	1.08	1.12	1.09	
Tb/Yb	2.61	2.57	2.58	2.13	2.09	2.04	2.35	2.38	2.23	2.23	2.99	3.11	3.10	2.72	2.70	2.65	2.65	2.65	

Table 4: Sr-Nd-Pb isotopic data for selected Patagonian basalts analyzed in this study

Group I								
Sample:	$^{87}\text{Sr}/^{86}\text{Sr}$	$^{87}\text{Sr}/^{86}\text{Sr}_i$	$^{143}\text{Nd}/^{144}\text{Nd}$	$^{143}\text{Nd}/^{144}\text{Nd}_i$	ϵNd_i	$^{206}\text{Pb}/^{204}\text{Pb}$	$^{207}\text{Pb}/^{204}\text{Pb}$	$^{208}\text{Pb}/^{204}\text{Pb}$
PM1-A3	0.703204(10)	0.703190	0.512984(08)	0.512967	+6.4	18.493 (2)	15.565 (2)	38.425 (3)
PM1-A4	0.703193(17)	0.703179	0.512980(05)	0.512964	+6.4	18.490 (3)	15.563 (3)	38.423 (4)
PM8-A1	0.703945(09)	0.703941	0.512785(04)	0.512783	+2.8	18.597 (1)	15.585 (1)	38.631 (2)
PM8-B2b	0.703940(15)	0.703938	0.512778(12)	0.512776	+2.7	18.617 (1)	15.585 (1)	38.633 (2)
PM11-A1	0.703424(14)	0.703395	0.512871(07)	0.512845	+4.0	19.186 (2)	15.634 (2)	38.997 (3)
PM11-A3	0.703425(17)	0.703391	0.512872(08)	0.512842	+4.0	19.173 (2)	15.638 (2)	38.984 (3)
PM12-A3	0.703363(09)	0.703361	0.512859(12)	0.512857	+4.3	19.077 (2)	15.625 (2)	38.899 (3)
PM12-A4	0.703350(12)	0.703348	0.512858(09)	0.512856	+4.3	18.935 (2)	15.636 (2)	38.768 (2)
PM16-A1	0.703353(12)	0.703352	0.512919(06)	0.512917	+5.4	18.971 (4)	15.630 (4)	38.793 (6)
PM16-A3	0.703350(17)	0.703349	0.512910(09)	0.512908	+5.3	18.958 (6)	15.624 (5)	38.787 (6)
PM17-A1	0.703391(19)	0.703390	0.512891(06)	0.512890	+4.9	19.129 (1)	15.656 (1)	38.868 (2)
PM17-A4	0.703404(20)	0.703403	0.512897(07)	0.512896	+5.0	19.130 (2)	15.660 (1)	38.853 (2)
Group II								
Sample No.:	$^{87}\text{Sr}/^{86}\text{Sr}$	$^{87}\text{Sr}/^{86}\text{Sr}_i$	$^{143}\text{Nd}/^{144}\text{Nd}$	$^{143}\text{Nd}/^{144}\text{Nd}_i$	ϵNd_i	$^{206}\text{Pb}/^{204}\text{Pb}$	$^{207}\text{Pb}/^{204}\text{Pb}$	$^{208}\text{Pb}/^{204}\text{Pb}$
PM2-A3	0.703914(13)	0.703913	0.512705(03)	0.512704	+1.3	18.352 (5)	15.574 (4)	38.196 (3)
PM2-A4	0.703931(08)	0.703929	0.512708(06)	0.512707	+1.4	18.358 (5)	15.578 (5)	38.199 (4)
PM3-A1	0.703889(10)	0.703887	0.512704(07)	0.512703	+1.3	18.311 (4)	15.585 (4)	38.175 (2)
PM3-A2	0.703895(11)	0.703895	0.512695(07)	0.512695	+1.1	18.316 (5)	15.597 (5)	38.181 (2)
PM4-B2	0.704158(12)	0.704156	0.512625(08)	0.512625	-0.3	18.167 (3)	15.506 (3)	38.326 (3)
PM4-B4	0.704170(08)	0.704168	0.512625(04)	0.512624	-0.3	18.162 (3)	15.504 (6)	38.324 (3)
PM5-A2	0.704517(12)	0.704498	0.512629(06)	0.512605	-0.6	18.017 (2)	15.574 (2)	37.979 (3)
PM5-A3	0.704529(08)	0.704486	0.512613(06)	0.512591	-0.9	17.986 (2)	15.554 (2)	37.973 (2)
PM6-A1	0.704154(09)	0.704095	0.512732(06)	0.512709	+1.4	18.504 (2)	15.632 (2)	38.441 (6)
PM6-A3	0.704167(09)	0.704105	0.512734(05)	0.512710	+1.4	18.483 (2)	15.618 (2)	38.430 (6)
PM7-A1	0.704098(09)	0.704045	0.512766(07)	0.512738	+1.9	18.632 (2)	15.618 (2)	38.508 (2)
PM7-A2	0.704125(18)	0.704075	0.512758(05)	0.512730	+1.8	18.626 (2)	15.615 (2)	38.498 (2)
PM22-A1	0.704324(08)	0.704310	0.512677(04)	0.512668	+0.6	18.484 (2)	15.606 (2)	38.517 (2)
PM22-A2	0.704323(11)	0.704308	0.512672(05)	0.512663	+0.5	18.481 (4)	15.607 (3)	38.518 (2)

Initial Sr and Nd isotope composition were calculated using the respective K-Ar ages of each sample. Numbers in parentheses are 2σ of single analysis of each sample. Parent/daughter isotope ratios were recalculated using Rb, Sr, Sm and Nd concentrations from Table 1.

Table 5: Analytical values of the unspiked K–Ar ages

Group I						
Sample	K (wt%)	^{40}Ar rad ($10^{-8}\text{cm}^3\text{STP/g}$)	$^{38}\text{Ar}/^{36}\text{Ar}$	$(^{40}\text{Ar}/^{36}\text{Ar})$ initial ^a	Age (Ma)	Air Fraction (%)
PM1-A4	0.84 ± 0.017	63.38 ± 3.21	0.19138 ± 0.00127	306.65 ± 3.99	19.33 ± 1.05	32.14
PM8-A1	0.92 ± 0.018	13.39 ± 0.69	0.18717 ± 0.00089	-	3.76 ± 0.21	87.15
PM8-B2	0.62 ± 0.012	8.59 ± 0.44	0.18717 ± 0.00075	-	3.57 ± 0.20	82.16
PM11-A3	0.61 ± 0.012	76.39 ± 3.83	0.18875 ± 0.00063	-	32.08 ± 1.72	44.62
PM12-A4	2.26 ± 0.045	21.00 ± 1.07	0.18787 ± 0.00075	-	2.39 ± 0.13	84.29
PM16-A3	0.59 ± 0.012	3.96 ± 0.21	0.18718 ± 0.00096	-	1.73 ± 0.10	58.7
PM17-A1	0.51 ± 0.010	3.04 ± 0.17	0.188 ± 0.0009	-	1.53 ± 0.09	59.4
Group II						
Sample	K (wt%)	^{40}Ar rad ($10^{-8}\text{cm}^3\text{STP/g}$)	$^{38}\text{Ar}/^{36}\text{Ar}$	$(^{40}\text{Ar}/^{36}\text{Ar})$ initial ^a	Age (Ma)	Air Fraction (%)
PM2-A3	1.12 ± 0.022	3.4 ± 0.18	0.18922 ± 0.0008	-	0.78 ± 0.04	86.67
PM2-A4	1.23 ± 0.025	3.86 ± 0.21	0.1876 ± 0.00073	-	0.81 ± 0.05	93
PM3-A1	1.15 ± 0.023	4.23 ± 0.22	0.18774 ± 0.00078	-	0.95 ± 0.05	72.62
PM3-A2	1.16 ± 0.023	4.5 ± 0.24	0.18876 ± 0.00091	-	1.00 ± 0.057	84.2
PM4-B2	1.97 ± 0.040	5.72 ± 0.03	0.18836 ± 0.00105	-	0.75 ± 0.04	74.95
PM4-B4	2.02 ± 0.040	5.72 ± 0.29	0.18719 ± 0.00079	-	0.73 ± 0.04	72.68
PM5-A2	1.35 ± 0.027	112.84 ± 5.66	0.18992 ± 0.00154	-	21.36 ± 1.15	19.55
PM5-A3	1.27 ± 0.026	118.33 ± 5.93	0.18974 ± 0.00122	-	23.75 ± 1.27	19.8
PM6-A1	1.91 ± 0.038	221.56 ± 11.1	0.18971 ± 0.0014	-	29.56 ± 1.58	15.76
PM6-A3	1.94 ± 0.039	223.36 ± 11.19	0.18987 ± 0.00126	-	29.43 ± 1.57	17.25
PM7-A1	1.72 ± 0.035	213.5 ± 10.7	0.19048 ± 0.00099	-	31.61 ± 1.69	10.62
PM22-A1	2.14 ± 0.043	79.09 ± 3.97	0.18934 ± 0.00098	-	9.50 ± 0.51	38.81
PM22-A2	2.05 ± 0.041	77.91 ± 3.91	0.18904 ± 0.00098	-	9.75 ± 0.53	48.9

$(^{40}\text{Ar}/^{36}\text{Ar})$ initial = 296.0 is assumed. Error: 1σ .

^a $(^{40}\text{Ar}/^{36}\text{Ar})$ initial was estimated from the measured $^{38}\text{Ar}/^{36}\text{Ar}$ ratio, which was fractionated from the atmospheric value of 0.1880.

Table 6: Depths of magma segregation and potential temperature estimations of Groups I and II Patagonian basalts with MgO >9 wt.%; Ni >200 ppm and Cr >240 ppm

Group I													
Sample:	PM8 -A1	PM8 -B2	PM11 -A1	PM11 -A2	PM11 -A3	PM12 -A3	PM12 -A4	PM16 -A1	PM16 -A3	PM17 -A1	PM17 -A2	PM17 -A3	PM17 -A4
T _p ¹	1546	1538	1404	1399	1398	1424	1420	1448	1442	1450	1451	1448	1453
T _p ²	1563	1556	1436	1431	1431	1456	1452	1481	1475	1479	1480	1478	1482
P(Gpa)	4.1	4.0	3.5	3.5	3.5	3.5	3.5	3.4	3.4	3.6	3.6	3.6	3.6
Depth (km)	134	134	114	115	115	115	115	114	113	120	120	119	120
Mantle source	Asth	Asth	Asth	Asth	Asth	Asth	Asth	Asth	Asth	Asth	Asth	Asth	Asth
Group II													
Sample:	PM2 -A1	PM2 -A3	PM2- A4	PM3- A1	PM3- A2	PM3- A3	PM4- B2	PM4- B4	PM7- A1	PM7- A2			
T _p ¹	1312	1312	1317	1305	1306	1315	1324	1324	1308	1312			
T _p ²	1352	1352	1357	1346	1346	1355	1363	1364	1348	1352			
P(Gpa)	2.7	2.7	2.7	2.7	2.7	2.7	2.8	2.8	2.8	2.8			
Depth (km)	89	89	90	89	90	91	93	94	91	91			
Mantle source	LAB	LAB	LAB	LAB	LAB	LAB	LAB	LAB	LAB	LAB			

*Asth = asthenosphere; LAB = lithosphere-asthenosphere boundary.

¹Albarède (1992).

²Herzberg & Asimow (2008).

ARTIGO 2

SLAB-DERIVED COMPONENTS IN THE SUBCONTINENTAL LITHOSPHERIC MANTLE OF THE PALEOCENE-EOCENE SUBDUCTION ZONE BENEATH CHILEAN PATAGONIA: GEOCHEMISTRY AND Sr-Nd-Pb ISOTOPES OF MANTLE XENOLITHS AND THEIR HOST BASALTS

Assunto LITHOS5361 - Notice of manuscript number
Remetente Lithos <lithos-eo@elsevier.com>
Para <tiago.jalowitzki@ufrgs.br>
Data 2015-11-30 13:05



Dear Mr. Jalowitzki,

Your submission entitled "Slab-derived components in the subcontinental lithospheric mantle of the Paleocene-Eocene subduction zone beneath Chilean Patagonia: Geochemistry and Sr-Nd-Pb isotopes of mantle xenoliths and their host basalts" has been assigned the following manuscript number: LITHOS5361.

You will be able to check on the progress of your paper by logging on <http://ees.elsevier.com/lithos/> as Author.

Thank you for submitting your work to this journal.

Kind regards,

Lithos

1 **Slab-derived components in the subcontinental lithospheric**
2 **mantle of the Paleocene-Eocene subduction zone beneath**
3 **Chilean Patagonia: Geochemistry and Sr-Nd-Pb isotopes of**
4 **mantle xenoliths and their host basalts**

5

6 Tiago Jalowitzki ^{a,e*}, Fernanda Gervasoni ^b, Rommulo V. Conceição ^a, Yuji Orihashi ^c,
7 Gustavo W. Bertotto ^d, Hirochika Sumino ^e, Manuel Schilling ^f, Keisuke Nagao ^g, Diego
8 Morata ^{h,i}, Paul Sylvester ^j

9

10 ^a Programa de Pós-graduação em Geociências, Universidade Federal do Rio Grande do
11 Sul (UFRGS). Av. Bento Gonçalves, 9500 - Prédio 43129, Porto Alegre - RS, Brazil.

12 ^b Institut für Mineralogie, Westfälische-Wilhelms-Universität Münster, Germany.

13 ^c Earthquake Research Institute, the University of Tokyo, Yayoi 1-1-1, Bunkyo-Ku,
14 113-0032, Tokyo, Japan.

15 ^d INCITAP, CONICET - Universidad Nacional de La Pampa. Uruguay 151 (6300), Santa
16 Rosa, La Pampa, Argentina.

17 ^e Department of Basic Science, Graduate School of Arts and Sciences, the University of
18 Tokyo, 3-8-1 Komaba, Meguro-ku, Tokyo 153-8902, Japan.

19 ^f Instituto de Ciencias de la Tierra, Facultad de Ciencias, Universidad Austral de Chile,
20 Valdivia (5090000), Chile.

21 ^g Division of Polar Earth-System Sciences KOPRI (Korea Polar Research Institute), 26
22 Songdomirae-ro, Yeonsu-gu, Incheon 21990, Korea.

23 ^h Departamento de Geología, Facultad de Ciencias Físicas y Matemáticas, Universidad
24 de Chile, Plaza Ercilla 803, Santiago, Chile.

25 ⁱ Centro de Excelencia en Geotermia de los Andes (CEGA), Fondap-Conicyt, Chile.

26 ^j Department of Geosciences, Texas Tech University, 125 Science Building, Lubbock
27 TX 79409-1053, USA.

28

29 ***Corresponding author:** Programa de Pós-graduação em Geociências, Instituto de
30 Geociências, Universidade Federal do Rio Grande do Sul (UFRGS). Av. Bento
31 Gonçalves, 9500 - Prédio 43129, Bairro Agronomia, Porto Alegre - RS, Brazil. CEP:
32 91501970. Telephone number: +55(51)3308-7287.

33 **E-mail address:** tiago.jalowitzki@ufrgs.br (T. Jalowitzki).

34

35 **Abstract**

36 We report new whole-rock major, trace element and isotopic (Sr-Nd-Pb) data of
37 a suite of 17 anhydrous spinel-lherzolites hosted in Eocene lava flow yielding 54 Ma in
38 new K-Ar age. OIB-like alkaline basalts, hosting the mantle xenoliths, is located near
39 Coyhaique, Aysén region, current Chilean back-arc region, ~100 km east from the
40 current volcanic arc and ~320 km from the Chile trench. The host basalt has high MgO
41 (~10 wt%) and TiO₂ (>2.8 wt%) contents, and high L-REE/H-REE (e.g. Ce/Yb_N = 8.7),
42 Nb/(Ta-La) (>20; >1.4), Ce/Pb (>36) and Nb/U (>56) ratios. These chemical
43 characteristics suggest that this basalt was generated by small degrees of partial melting
44 (up to 6%) within the garnet stability field, probably a result from asthenospheric
45 upwelling through a slab window within the subducting Farallón-Aluk spreading ridge
46 in southern Patagonian province. Furthermore, the alkaline basalt shows initial ⁸⁷Sr/⁸⁶Sr
47 (0.703039–0.703058) and ¹⁴³Nd/¹⁴⁴Nd (0.512880–0.512874), similar to those of oceanic
48 island basalts with HIMU-like composition.

49 Mantle xenoliths hosted in alkaline basalts consist of coarse- to medium-grained spinel-
50 lherzolites, of which trace element compositions are characteristic of subduction zone,
51 such as pronounced negative Nb, Ta and Ti anomalies coupled with significant
52 enrichment of LILEs (e.g. U) and chalcophile elements (W, Pb and Sn). In terms of
53 REEs, the majority of the Coyhaique spinel-lherzolites studied here present flat patterns
54 from H-REE to L-REE, whereas some spinel-lherzolites show slightly L-REE
55 depletions (Ce/Yb_N = 0.5) to L-REE-enrichments (Ce/Yb_N = 2.2). Sr-Nd-Pb isotope
56 compositions of the studied spinel-lherzolites display the following ranges: ⁸⁷Sr/⁸⁶Sr =
57 0.70242–0.70430, ¹⁴³Nd/¹⁴⁴Nd = 0.512859–0.513242, ²⁰⁶Pb/²⁰⁴Pb = 18.212–18.729,
58 ²⁰⁷Pb/²⁰⁴Pb = 15.483–15.600, and ²⁰⁸Pb/²⁰⁴Pb = 37.914–38.524. The geochemical and
59 isotopic signatures of Coyhaique spinel-lherzolites require three mantle end-members:
60 Depleted MORBs Mantle (DMM), Prevalent Mantle (PREMA) and Enriched Mantle
61 (EMII) to explain their isotopic variation, which is significantly different from those of
62 host basalts. Furthermore, there is no evidence for influence of OIB-like asthenospheric
63 melts related to Farallón-Aluk asthenospheric slab window on the mantle wedge.
64 Therefore, these new geochemical data suggest that the Coyhaique spinel-lherzolites are
65 derived from a heterogeneous SCLM resulting from mixing between depleted

66 component and up to 15% of slab-derived components associated to the subduction of
67 Aluk oceanic plate. The enriched component added to the SCLM was metasomatized by
68 different extents of slab component resulting from melts of subducted Chile trench
69 sediments (up to 60% of CTS) and modified oceanic crusts (more than 40% of MOC)
70 prior to Farallón-Aluk ridge collision during Paleocene-Eocene time.

71

72 **Keywords:** Mantle peridotites; slab-derived metasomatism; Aluk plate subduction;
73 Andean back-arc, Chilean Patagonia.

74

75 **1. Introduction**

76

77 Patagonian mantle xenoliths represent direct samples of a subcontinental
78 lithospheric mantle (SCLM) related to an active subduction zone and are commonly
79 carried to the surface by alkaline magmatism located in the Andean back-arc region.
80 The geochemical and isotopic characteristics of the mantle xenoliths and their host
81 lavas, particularly those located close to the margin of the convergent plates, can
82 provide valuable information regarding heterogeneities in the SCLM caused by
83 subduction processes at the latitudes of the Southern and Austral Volcanic Zones (e.g.,
84 Bjerg et al., 2005; Conceição et al., 2005; Dantas et al., 2009; Faccini et al., 2013;
85 Gervasoni et al., 2012; Gorrington and Kay, 2000; Laurora et al., 2001; Ntaflos et al.,
86 2007; Rivalenti et al., 2004; Schilling et al., 2005, 2008; Stern et al., 1999).

87 In southern South America, the Andean volcanic arc is related to the convergent
88 boundary between the South American plate and both the Nazca and Antarctic plates at
89 the latitudes of the Southern Volcanic Zone (SVZ, 33°S – 46°S) and Austral Volcanic
90 Zone (AVZ, 49°S – 55°S) (e.g., Ramos, 1999). The Andean convergent margin allows a
91 (re)-fertilization of the SCLM through the subducting slab, which provides 1) pelagic
92 and continentally derived trench sediments, 2) water-rich fluids, 3) altered oceanic crust
93 (e.g., basalts, peridotites and serpentinites), 4) adakitic melts generated by the partial
94 melting of the subducted oceanic crust and 5) asthenospheric upwelling through slab
95 windows due to the subduction of the spreading ridges. Previous studies of plate
96 tectonic reconstructions have shown at least two active spreading ridge subductions
97 beneath the western margin of southern South America at the latitude of the Taitao
98 Peninsula during the Cenozoic: the Farallón-Aluk (Phoenix) ridge and the current Chile

99 spreading ridge (e.g., Aragón et al., 2013; Breitsprecher and Thorkelson, 2009; Cande
100 and Leslie, 1986; Somoza and Ghidella, 2005). The early Eocene to Recent successive
101 subductions of these spreading-ridges were responsible for both the modern and ancient
102 Patagonian slab windows.

103 To better understand the heterogeneities and tectonic evolution of the SCLM of
104 Southern Patagonia, we studied the petrography, whole-rock major and trace elements
105 and the Sr-Nd-Pb isotopic compositions of anhydrous spinel-peridotites carried by
106 Eocene (54 Ma) alkaline basalts located ~100 km east from the present volcanic arc, in
107 the Aysén Region of the Chilean Patagonia. Based on these new data, we discuss the
108 influence of the Aluk oceanic plate subduction beneath the Coyhaique area and the
109 interactions between the SCLM and the slab-derived components. Furthermore, we
110 consider the role of the Farallón-Aluk spreading ridge, which collided with the Chile
111 trench, generating a subsequent asthenospheric slab window beneath Patagonia during
112 the Paleocene-Eocene. Additionally, we also report new K-Ar ages and whole-rock
113 major, trace element and Sr-Nd isotopic compositions of the host alkali basalts
114 (Balmaceda Basalt) for comparison with the Coyhaique peridotites.

115

116 **2. Geological setting and samples**

117

118 The western margin of South America at the latitudes of the SVZ and AVZ has
119 undergone a long-lived history of subduction throughout the Cenozoic and that history
120 includes the subduction of at least two active ocean ridges (e.g., Aragón et al., 2013;
121 Breitsprecher and Thorkelson, 2009; Cande and Leslie, 1986; Somoza and Ghidella,
122 2005). Currently, the Patagonian western margin is recording the continuous subduction
123 of the Chile Ridge spreading centre, which intersects the Chile Trench at the latitude of
124 the Taitao Peninsula and forms a trench-ridge-trench triple junction (Cande and Leslie,
125 1986). The collision of the Farallón and Aluk oceanic plates against the South America
126 continental plate generated the Farallón-Aluk-South America triple junction, which
127 migrated southward along the South American trench during Paleocene-Eocene times.
128 This process allowed the opening of the first slab window beneath the Patagonian
129 province, as recorded by the alkaline Eocene plateau basalts of Central Patagonia
130 (Espinoza et al., 2005; Morata et al., 2000; Parada et al., 2001; Ramos and Kay, 1992).

131 The Cenozoic Patagonian continental back-arc province (34°S – 54°S) is
132 characterized by a widely distributed and voluminous tholeiitic main-plateau
133 accompanied with less-voluminous post-plateau magmatism (e.g., [Gorring et al., 1997](#)).
134 The post-plateau volcanism mainly comprises alkaline basaltic lava flows and
135 monogenetic cinder cones having an OIB-like signature and often hosts mantle
136 xenoliths. In the Chilean back-arc domain, the Aysén plateau basalts (ca. 46°S) occur
137 north of the General Carrera Lake and close to the international border between Chile
138 and Argentina ([Fig. 1](#)). The Cenozoic volcanism in this region is recorded by an Eocene
139 (60–46 Ma) sequence of olivine-phyric flood basalts ([Baker et al., 1981](#); [Butler et al.,](#)
140 [1991](#); [Demant et al., 1996](#); [Morata et al., 2000](#); [Parada et al., 2001](#)), which was divided
141 by [Parada et al. \(2001\)](#) into the Northern Magmatic Domain (NMD) and Southern
142 Magmatic Domain (SMD). The lava flow and mantle-derived xenoliths studied here
143 were first described by [Morata et al. \(2000\)](#), and they are located approximately 30 km
144 SE from the city of Coyhaique, only 100 km east of the modern volcanic arc and ~320
145 km from the Chile trench, in particular, are close to the Macá–Cay and Hudson
146 volcanoes. Consequently, the Coyhaique mantle xenoliths are among the closest to the
147 margin of the convergent plates, together with Cerro del Fraile and Chile Chico, which
148 are also located 280 to 300 km from the Chile Trench.

149 The host can be classified as an NMD basalt due to its alkaline affinity, OIB-like
150 geochemical signatures and depleted Sr-Nd isotope compositions ([Parada et al., 2001](#)).
151 The most plausible tectono-magmatic evolution that has been proposed to explain the
152 mantle source of the Eocene back-arc magmatism in this region implies asthenosphere
153 upwelling in response to the collision of the Farallón-Aluk ridge beneath the continental
154 margin during the Eocene and the consequent development of a slab window ([Demant](#)
155 [et al., 1996](#); [Morata et al., 2000](#); [Ramos and Kay, 1992](#)). The host basaltic rocks and 17
156 mantle xenoliths studied here were collected from the PM25 site in the Balmaceda
157 Basalt (45°46'S; 71°47'W) ([Fig. 2](#)) and were selected to be representative of the larger
158 collection. The studied mantle xenoliths reach up to 11 cm in size and are fresh, with
159 only a few xenoliths and with a reddish appearance in hand specimens, which is
160 probably caused by oxidation.

161

162 **3. Analytical techniques**

163

164 *3.1. Major and trace elements*

165

166 *3.1.1. Host basalts (HB)*

167

168 The whole-rock geochemistry of two basaltic rocks was performed using the
169 facilities of the Earthquake Research Institute at the University of Tokyo. Major and
170 selected trace element abundances (Sc, V, Cr, Co, Ni, Zn, Ga, Rb, Sr, Y, Zr, Nb and Ba)
171 were analysed using X-ray fluorescence (XRF, PW2400; Philips Japan Ltd.), and the
172 abundances of other trace elements (Cs, REEs, Ta, Hf, Pb, Th and U) were obtained
173 using an ICP–MS (Plasma Quad 3; VG Scienta Holdings AB) connected to a laser
174 ablation system using a frequency-quadrupled 213 nm Nd: YAG laser (UP-213; New
175 Wave Research Inc.). Both sets of data were obtained using the same glass beads, which
176 were prepared by mixing 1.8 g of rock powder with 3.6 g of lithium
177 metaborate/tetraborate flux. Then, 0.54 g of lithium nitrate were added into the sample
178 powder as an oxidizer, and the lithium nitrate and sample powder were mixed in a
179 torch-mixer for 3 min. The mixture was heated to 1200°C for 15 min in a 95%Pt-5%Au
180 crucible with 30-mm inner diameter used in an automatic bead sampler. Details of the
181 analytical procedures of the XRF and LA-ICP-MS methods are described in Tani et al.
182 (2002) and Orihashi and Hirata (2003), respectively.

183

184 *3.1.2. Mantle xenoliths*

185

186 The whole-rock geochemistry of the 17 mantle xenoliths was performed using
187 the facilities of The Earth Resources Research and Analysis (TERRA), Department of
188 Earth Sciences, Memorial University of Newfoundland, Canada. The major and trace
189 elements abundances were obtained using X-ray fluorescence (Bruker S8 Tiger
190 sequential wavelength-dispersive XRF) and ICP–MS (PerkinElmer ELAN DRCII). The
191 XRF data were obtained using glass beads, which were prepared by mixing 1.5 mg of
192 rock powder with 6.0 mg of lithium metaborate and 1.5 mg of lithium tetraborate. The
193 mixture was placed into a platinum crucible, and a few drops of lithium bromide were
194 added as a wetting agent. The crucibles were then placed in the Leco Fluxer and heated
195 at ~850°C for 8.5 minutes and fused at ~1050°C for 11.5 minutes. The ICP-MS data
196 were obtained by solution, where 0.1 g of sample powder were digested using the high

197 pressure digestion technique developed by Diegor et al. (2001). The total counting time
198 per mass, at one point per peak, was 10 s, and the dwell time per mass was 0.05 s. Three
199 external standards were used with different elements and with different concentrations.
200 Inner (internal) standards were also applied (Sc, In and Re U), with different
201 concentrations in each. The drift correction was performed with the In concentrations.
202 The external standards, inner standard (standard addition) and surrogate calibration for
203 Nb, Ta and Mo (using Zr and Hf) were used to address the interrelated matrix, drift and
204 interference problems (Jenner et al., 1990).

205

206 3.2. Sr-Nd-Pb isotopes

207

208 Sr-Nd-Pb isotopic ratios for 15 mantle xenoliths and two host basaltic samples
209 were measured at the Laboratório de Geologia Isotópica, Universidade Federal do Rio
210 Grande do Sul (UFRGS), Porto Alegre, Brazil. The samples (0.1 g) were leached with
211 cold 0.25 N HCl in an ultrasonic bath for 30 minutes to eliminate impurities. When
212 dried, the samples were weighed, and the mantle xenolith samples were spiked with a
213 mixed $^{87}\text{Rb}/^{84}\text{Sr}$ and $^{149}\text{Sm}/^{150}\text{Nd}$ tracer. However, the host basalt samples were
214 unspiked. Dissolution procedures were performed with HF, HNO₃ and HCl in Teflon
215 vials (Savillex®), which were warmed on a hot plate until complete material
216 dissolution. In the next stage, the sample solutions were diluted in 3 ml of HCl 2.5N and
217 stored in test tubes. An aliquot of 1 ml was used to separate the Rb, Sr and REE by
218 Cationic AG-50W-X8 (200–400 mesh) resin columns, followed by Sm and Nd
219 separation using anionic LN-B50-A (100–150 μ) resin. The Pb was separated using
220 anionic BioRad-AG1X (200–400 mesh) resin in an HBr solution. Individual solutions
221 of Rb, Sr, Sm, Nd and Pb were dried in Teflon vials (Savillex®) on a hot plate. The
222 residues were deposited onto single Ta (for Rb, Sr, Sm and Pb) and triple Ta–Re–Ta
223 (for Nd) filaments.

224 Mass spectrometric analyses of the radiogenic isotopes were performed using
225 two thermal ionization mass spectrometers (Sector 54; VG Scienta Holdings AB and
226 Triton; Thermo Scientific). The data were corrected for mass fractionation by
227 normalizing to $^{86}\text{Sr}/^{88}\text{Sr} = 0.1194$ and $^{146}\text{Nd}/^{144}\text{Nd} = 0.7219$. The replicate analyses of
228 NBS-987 and JNd-1 standards gave $^{87}\text{Sr}/^{86}\text{Sr} = 0.710254 \pm 19$ ($n = 4, 2\sigma$) and

229 $^{143}\text{Nd}/^{144}\text{Nd} = 0.512101 \pm 8$ ($n = 4$, 2σ). For Pb NBS-981, the variation from the
230 accepted values was less than 0.01%/a.m.u.

231

232 *3.3. K-Ar ages*

233

234 The new K-Ar ages for the two basaltic samples were analysed using the
235 unspiked sensitivity method. The Ar analyses were performed using a noble gas mass
236 spectrometry system (MS-III) at the Geochemical Research Center, Graduate School of
237 Science, University of Tokyo. The whole rock samples (0.3–0.6 g) were crushed and
238 sieved using a 60–80 mesh, wrapped in 10 μm thick aluminium foil and loaded into a
239 glass sample holder, which was connected to an extraction oven in which the samples
240 were fused at 1700°C in a vacuum and into which the evaporated gas for Ar purification
241 was introduced directly using a vacuum line. The Ar isotope analyses were performed
242 using a modified VG-5400 on a small amount of Ar gas ($<2 \times 10^{-7}$ cm^3 STP). When the
243 amount of Ar gas extracted from the sample exceeded this limit, it was reduced using a
244 known volume of the purification line. The errors in the ^{40}Ar sensitivity and $^{40}\text{Ar}/^{36}\text{Ar}$
245 ratio were estimated to be 5% and 0.2%, respectively, based on repeated measurements
246 of the atmospheric standard gas, which contained 1.5×10^{-7} cm^3 STP of ^{40}Ar . The errors
247 in the $^{40}\text{Ar}/^{36}\text{Ar}$ ratios were deduced from the statistical 1σ errors for the samples,
248 standard gases and blank correction. The K concentration for the aliquot of the rock
249 fractions used for the Ar analysis was determined using X-ray fluorescence (XRF,
250 PW2400; Philips Japan Ltd.) at the Earthquake Research Institute, University of Tokyo.
251 The details of the procedures are described in Nagao et al. (1991) and Orihashi et al.
252 (2004).

253

254 **4. Results**

255

256 *4.1. Host basalts*

257

258 Whole-rock trace element data (including REEs), K-Ar ages and Sr-Nd isotopic
259 compositions for the two host lavas are presented in Tables 1, 2 and 3, respectively. The
260 host volcanic rocks were classified as basalts that contain idiomorphic olivine and
261 clinopyroxene as phenocrysts and a fine-grained groundmass that consists of olivine,

262 clinopyroxene, plagioclase, oxides, glass and rare alkali feldspar. The lavas are
 263 relatively fresh, with incipient alteration of some the olivine phenocrysts along their
 264 rims, which were partially replaced by low-temperature iddingsite.

265 Considering the SiO₂ (~47.3 wt%) and alkalis (Na₂O + K₂O_{average} = 4.2 wt%)
 266 contents, these lavas were classified as alkaline basalts. The basalts have Mg# (>61),
 267 MgO (~10 wt%) and FeO*/MgO (~1.1) values, as well as high Cr and Ni contents
 268 (averages of 309 and 218 ppm, respectively), which indicate their relatively primitive
 269 character. They also show a high TiO₂ (>2.8 wt%) content associated with high Ce/Yb_N
 270 (8.7), Nb/Ta (>20), Ce/Pb (>36), Nb/U (>56), Nb/Nb* (>1.5) ratios and a low La/Nb
 271 (<0.7) ratio, similar to intraplate basalts from continental and oceanic settings
 272 worldwide.

273 The non-modal batch melting equation reported by Shaw (2006) [$C^L =$
 274 $C^S/(D+F(1-P))$] was applied to estimate the partial melting degree of the lavas from
 275 Coyhaique. The fractionated H-REE ratios (e.g., Tb/Yb_N = 2.45–2.60), as well as the
 276 calculated depths of the mantle source (87–89 km), suggest that these basalts were
 277 generated by a small degree of partial melting (up to 6%) within the garnet stability
 278 field, which implies a mantle source close to the lithosphere-asthenosphere boundary
 279 (LAB <100 km; e.g., Stern et al., 1999). The mantle potential temperatures (T_P)
 280 calculated for these lavas (1310–1366°C) overlap those estimated for the normal
 281 ambient mantle (~1350 ± 50°C; Herzberg and Asimow, 2008), which presents no
 282 evidence of a thermal anomaly. Estimates of the primary magma segregation pressures
 283 were obtained using the empirical equation of Albarède (1992) [$\ln P(\text{GPa}) =$
 284 $\{[5.04\text{MgO}/(\text{SiO}_2 + \text{MgO})] - 0.12\text{SiO}_2 + 7.47\}$], whereas the T_P were obtained using
 285 the methods proposed by Albarède (1992) [$T(\text{°C}) = 2000\text{MgO}/(\text{SiO}_2 + \text{MgO}) + 969$] and
 286 Herzberg and Asimow (2008) [$T(\text{°C}) = 935 + 33\text{MgO} - 0.37\text{MgO}^2 + 54P - 2P^2$; $P = \text{GPa}$].

287 Isotopically, these basalts have initial ⁸⁷Sr/⁸⁶Sr (0.703039–0.703058) and
 288 ¹⁴³Nd/¹⁴⁴Nd ratios (0.512874–0.512880) that are compatible with an HIMU reservoir
 289 (high-μ = elevated ²³⁸U/²⁰⁴Pb; Hanyu et al., 2014). However, it is necessary to reconfirm
 290 the existence of the HIMU component by analysing the lead isotopes of the host basalts.
 291 These values are similar to those reported for the Pali-Aike Volcanic Field (⁸⁷Sr/⁸⁶Sr =
 292 0.703166–0.703511 and ¹⁴³Nd/¹⁴⁴Nd = 0.512944–0.512862; Choo et al., 2012; D’Orazio
 293 et al., 2000), which represent the most depleted lavas among the entire set of Cenozoic
 294 Patagonian plateau lavas (D’Orazio et al., 2000). The age correction applied to the Sr-

295 Nd isotopic ratios was determined based on their respective new K-Ar dates, which
296 yielded 53.6 ± 2.9 Ma and 53.7 ± 2.9 Ma (Table 2). These ages are consistent with those
297 reported by Morata et al. (2000) (58.6 ± 2.0 Ma).

298 The Coyhaique host basalts can be temporally and chemically correlated with
299 the volcanic products of the Lower Basaltic Sequence (LBS) of Meseta de Chile Chico
300 (60–34 Ma; Baker et al., 1981; Charrier et al., 1979; Espinoza et al., 2005) and with the
301 NMD of the Balmaceda plateau basalts (51–44 Ma; Baker et al., 1981; Demant et al.,
302 1996; Parada et al., 2001). They also show affinities with Posadas plateau basalts, which
303 are located in the Argentinian back-arc (57–45 Ma, Kay et al., 2002; Ramos and Kay,
304 1992).

305 The Eocene magmatism between 44°S and 52°S has been attributed to the
306 development of an asthenospheric slab window in response to the collision of an active
307 oceanic spreading centre (Farallón-Aluk) between 53 and 42 Ma (Cande and Leslie,
308 1986; Demant et al., 1996; Espinoza et al., 2005; Kay et al., 2002; Morata et al., 2000;
309 Parada et al., 2001; Ramos and Kay, 1992). Thus, based on the similarity of the alkaline
310 basalts studied here with Eocene basalts discussed in the prior literature cited above, as
311 well as with kinematic plate reconstructions, we accept the model of asthenospheric
312 upwelling through a slab window within the subducting oceanic lithosphere in southern
313 Patagonia.

314

315 4.2. Mantle xenoliths

316

317 4.2.1. Petrography

318

319 An optical petrographic microscope was used to develop the mineral and textural
320 descriptions. An electron microscope (JSM-6610LV SEM) and energy dispersive
321 system (EDS) microanalysis were used to develop the semi-quantitative descriptions of
322 the mineral compositions. The modal proportions of the minerals were determined by
323 point-counting using 900–2800 points that covered the entire area of each relatively
324 large thin section (Table 4). The Coyhaique peridotites were classified as anhydrous
325 spinel (Sp)-lherzolites (Fig. 2a) and are composed of olivine (Ol = 42–63 vol. %),
326 orthopyroxene (Opx = 16–39 vol. %), clinopyroxene (Cpx = 10–20 vol. %) and spinel
327 (Sp = 2–4 vol. %) (Figs. 2b, 3a–b and 4a–b). Olivine (forsterite) and orthopyroxene

328 (enstatite) are the dominant minerals, with subordinate clinopyroxene (Cr-rich diopside)
329 and accessory spinel (chromium-aluminium spinel). In thin sections, it is possible to see
330 that the alteration has been developed mainly in olivine, which has been partially
331 transformed to red-brown to yellow iddingsite (Figs. 3c–d and 4d). As shown in Table
332 5, the iddingsite formation consists of the addition of Fe_2O_3 and SiO_2 and the removal
333 of MgO. The representative chemical compositions of the mineral phases shown in
334 Table 5 are similar to those reported by Morata et al. (2000).

335 Coarse- to medium-grained sp-lherzolites (grain sizes ranging from ~1 to ~17
336 mm) have a protogranular to porphyroclastic micro-texture (Mercier and Nicolas, 1975),
337 as evidenced by the presence of large orthopyroxene porphyroclasts with lobate grain
338 boundaries and smaller grains (neoblasts) (Fig. 2b). There is no obvious preferred
339 crystal orientation or strain-induced elongation, as well as whole mineral
340 recrystallization (equigranular texture). These textural characteristics imply an SCLM
341 with low strain and recrystallization rates resulting from the deformation of the primary
342 protogranular rock. Representative thin section photomicrographs of the studied
343 samples are presented in Figure 3a–f. The shapes of the olivine porphyroclasts (up to 7
344 mm in length) range from subhedral to anhedral, with straight to gently curved grain
345 boundaries, commonly fractured and often containing undulatory extinction and kink
346 bands (Fig. 3c–d). Orthopyroxenes porphyroclasts (up to 17 mm in length) evolving
347 locally to polygonal arrangements with 120° triple junctions sometimes display kinks
348 and contain numerous thin exsolution lamellae of clinopyroxene (Figs. 3e–f and 4e).
349 Clinopyroxene occurs as small dark green crystals (up to 5 mm in length), which
350 sometimes present spongy rims that are poor in Na_2O and Al_2O_3 but rich in CaO and
351 MgO (Fig. 4f and Table 5). This texture can indicate incongruent partial melting
352 induced by fluid penetration (e.g., Ionov et al., 1995) or by mineral breakdown induced
353 by decompression (e.g., Nelson and Montana, 1992). Spinel usually is black, however,
354 in some cases shows a brown colour. They are interstitial and typically holly leaf-
355 shaped (Figure 3a–b) and also occur as inclusions, especially in pyroxenes.

356

357 4.2.2. Whole-rock geochemistry

358

359 4.2.2.1. Major and trace element abundances

360

361 The whole-rock geochemical compositions and loss on ignition (LOI) data of the
362 17 Coyhaique sp-lherzolites are presented in Table 1. Most of the LOI values are
363 relatively low, ranging from 0.4 wt% to 1.2 wt% (average 0.6 wt%), which indicates
364 that secondary alteration was limited. However, sample PM25-15 has high LOI values
365 (close to 9 wt%), which can be explained by the abundant occurrence of iddingsite veins
366 recognized in the thin section.

367 Most sp-lherzolites show relatively low SiO₂ (usually < 44.7 wt%) and high
368 MgO (usually > 38.8 wt%) when compared to the primitive upper mantle (PUM -
369 McDonough and Sun, 1995; 44.9 wt% and 37.7 wt%, respectively) and depleted MORB
370 mantle (DMM - Workman and Hart, 2005; 44.7 wt% and 38.7 wt%, respectively). The
371 negative correlations between the MgO and basaltic components (e.g., SiO₂, Al₂O₃,
372 CaO and TiO₂) from fertile (close to PUM) to refractory compositions (Fig. 5a–d) can
373 be explained by partial melting and the extraction of basaltic liquid from the sp-
374 lherzolites. This suggests that the Coyhaique sp-lherzolites were derived from the same
375 fertile source but with different degrees of partial melting (Herzberg, 2004). In our
376 samples, Ni was positively correlated with MgO, which is consistent with its compatible
377 character during melt-peridotite equilibrium (Fig. 5e). Comparing other major and
378 compatible elements (e.g., Cr, Co, Zn) with MgO, most oxides showed some scatter
379 (not shown). It is well known that the chemical compositions of the SCLM are
380 correlated with the age of the overlying crust on the Al₂O₃ versus CaO diagram (e.g.,
381 Griffin et al., 2009). The sp-lherzolites studied here plotted into the field of the
382 Phanerozoic mantle, which reflects only a moderate depletion from primitive mantle
383 (PM) compositions (e.g., Griffin et al., 2009; Fig. 5f). The high contents of CaO (2.2–
384 3.7 wt%) and Al₂O₃ (2.7–4.0 wt%) observed in our samples indicate a fertile
385 composition, which is consistent with the high modal percent of both clinopyroxene and
386 spinel.

387 In general, on the PM-normalized multi-element diagram (Sun and McDonough,
388 1989; Fig. 6a–b), the sp-lherzolites studied here showed negative Nb, Ta and Ti
389 anomalies coupled with a significant enrichment in large ion lithophile elements (LILE;
390 e.g., U) and in chalcophile elements (W, Pb and Sn). On the other hand, Cs, Rb, Ba and
391 Sr do not show a well-defined pattern and vary from slightly negative to positive
392 anomalies. In the (PM)-normalized rare earth elements (REE) diagram (Fig. 6c), the
393 majority of the sp-lherzolites show flat patterns from heavy H-REE to light L-REE,

394 whereas some of the sp-lherzolites show a slightly L-REE depletion ($Ce/Yb_N = 0.5$;
 395 PM25-5, PM25-15 and PM25-35) to L-REE-enrichment ($Ce/Yb_N = 1.8$; PM25-18,
 396 PM25-21, PM25-25, PM25-26, PM25-28, PM25-30 and PM25-34). The H-REE
 397 abundances of most of the Coyhaique sp-lherzolites are similar to those of primitive
 398 mantle composition (e.g., $Yb_N = 0.92$ – 1.77). The difference from slightly depleted H-
 399 REEs ($Yb_N = 0.92 \times PM$) to slightly enriched H-REEs ($Yb_N = 1.77 \times PM$) suggests
 400 variable degrees of both partial melting and metasomatism. On the REE patterns, two
 401 sp-lherzolites (PM25-5 and PM25-35) present prominently negative Eu anomalies,
 402 whereas this element is only slightly depleted in four of the sp-lherzolites (PM25-25,
 403 PM25-28, PM25-30 and PM25-34).

404 Generally, both continental crust and depleted mantle reservoirs have
 405 subchondritic Nb/(Ta-La) and Ti/Zr (e.g., Rudnick et al., 2000). In fact, the sp-
 406 lherzolites studied here have Nb/Ta (5.18–15.71; usually < 10), Nb/La (0.06–0.48) and
 407 Ti/Zr (49.50–109.88) ratios lower than the average of C1 chondrite (Sun and
 408 McDonough, 1989; Nb/Ta = 17.6; Nb/La = 1.04; Ti/Zr = 115), which attests to the
 409 depleted signature of the SCLM beneath the Coyhaique location. However, the positive
 410 anomalies of the calcophile elements coupled with Ce/Pb (usually < 15) and Nb/U (< 5)
 411 ratios that are significantly lower than the PM and DMM values ($Ce/Pb = 25$ and 31 ;
 412 $Nb/U = 34$ and 46 , respectively), as well as strong negative Nb anomalies ($Nb/Nb^* =$
 413 0.07 – 0.38 , where $Nb/Nb^* = Nb_N / (Th_N \times La_N)^{1/2}$), indicate different degrees of the
 414 involvement of a subduction component in the genesis of the sp-lherzolites. Other
 415 marked features of this enrichment process are the high (Th-Ce)/Yb, Th/Sr, Pb/Ce ratios
 416 (Fig. 7a–d) and similar compositional ranges of the Coyhaique sp-lherzolites and Chile
 417 trench sediments (CTS) in terms of their (Ba-U-Pb-Sr)/Th ratios (see the discussion
 418 below).

419

420 4.2.2.2. Sr-Nd-Pb isotopes

421

422 The Sr-Nd-Pb isotopic data of sp-lherzolites and their host basalts studied here
 423 are given in Table 3, and the diagrams of $^{87}Sr/^{86}Sr$ vs. $^{143}Nd/^{144}Nd$ and $^{87}Sr/^{86}Sr$ –
 424 $^{207}Pb/^{204}Pb$ – $^{208}Pb/^{204}Pb$ vs. $^{206}Pb/^{204}Pb$ are shown in Figures 8a–d. Also plotted for
 425 comparison are the alkaline basalts from the Pali-Aike Volcanic Field (Choo et al.,
 426 2012; D’Orazio et al., 2000), Chile Ridge mid-ocean ridge basalts (MORBs; Bach et al.,

1996; Karsten et al., 1996; Sturm et al., 1999), Chile trench sediments (CTS; Jacques et al., 2013; Lucassen et al., 2010), altered oceanic crust (AOC; Hauff et al., 2003), modified oceanic crust (MOC, see section 5.2.1) (Karsten et al., 1996), Andean volcanic arc basalts (Hickey et al., 1986; Hickey-Vargas et al., 1989) and the slab melt with a mixture of 40% CTS and 60% MOC proposed in this study (see details below). The following mantle reservoir end-member compositions are also plotted: DMM (Workman and Hart, 2005), HIMU (Hanyu et al., 2014), Enriched Mantle-1 (EM-1; Salters and Sachi-Kocher, 2010), Enriched Mantle-2 (EM-2; Workman et al., 2004) and Prevalent Mantle (PREMA; Wörner et al., 1986).

The Coyhaique sp-lherzolites have $^{87}\text{Sr}/^{86}\text{Sr}$ ratios ranging from 0.702422 to 0.704390 and $^{143}\text{Nd}/^{144}\text{Nd}$ ratios ranging from 0.512859 to 0.513242 ($\epsilon\text{Nd} = +4.3$ to $+11.8$). The Pb isotope ratios for sp-lherzolites vary over the ranges of $^{206}\text{Pb}/^{204}\text{Pb} = 18.212\text{--}18.729$, $^{207}\text{Pb}/^{204}\text{Pb} = 15.483\text{--}15.600$ and $^{208}\text{Pb}/^{204}\text{Pb} = 37.914\text{--}38.524$ (Table 3). Regarding the modern mantle components, most of the sp-lherzolites are placed in the depleted field relative to present-day Bulk Silicate Earth (BSE; Zindler and Hart, 1986) and Chondritic Uniform Reservoir (ChUR; Jacobsen and Wasserburg, 1980) in the Sr-Nd diagram (Fig. 8a). The combined Sr-Nd-Pb isotopic signatures of the sp-lherzolites displayed a large range of variations, evidencing a significant heterogeneity in the SCLM beneath the Coyhaique location. The less radiogenic Sr-Pb and more radiogenic Nd isotopic compositions, which are similar to the depleted component (DMM or PREMA), have flat to depleted L-REE patterns. The variation in the Sr-Nd-Pb isotopic compositions of the sp-lherzolites overlap with those obtained from the Chile Ridge basalts, confirming the depleted characteristics of the Coyhaique sp-lherzolites. In contrast, samples with more radiogenic Sr-Pb and less radiogenic Nd isotopic compositions show slight L-REE enrichment (PM25-25, PM25-26, PM25-28, PM25-30 and PM25-34), which suggests a later stage of metasomatism (EMII reservoir). Along with the Sr-Nd-Pb isotopic signatures of the DMM-PREMA-EM mantle end-members, the variation in the chemical compositions for the Coyhaique sp-lherzolites allows us to identify the mixing between these three mantle end-members (Figs. 7a–d and 8a–d).

457

458 **5. Discussion**

459

460 *5.1. Partial melting and depletion*

461

462 Compared to the PM and DMM components, most of the sp-lherzolites studied
463 here showed a depletion in the basaltic components (e.g., SiO₂, Al₂O₃, CaO and TiO₂)
464 and a relative enrichment in MgO, which can be explained by different degrees of
465 partial melting (Fig. 5a–d). However, the high and variable H-REE contents of the sp-
466 lherzolites (e.g., Yb_N = 0.92–1.77; usually >1.0) are difficult to explain with a
467 progressive melt depletion process of a spinel-peridotite source composed of olivine,
468 orthopyroxene, clinopyroxene and spinel. It is important to emphasize that our samples
469 are garnet-free, and there is no petrographic evidence (e.g., symplectite texture) that
470 suggests that the SCLM beneath Coyhaique was previously stable at a deeper-level, in
471 the garnet stability field.

472 Considering that there is no petrographic evidence of intergranular percolation
473 of the host basalt melt, which would explain the enrichment in L-REE enrichment in
474 some spinel-peridotites, the extent of partial melting (F) can be evaluated using the non-
475 modal batch melting equation reported by Shaw (2006) [$C^S = ((D-PF)C)/((1-F)(D+F(1-
476 P)))$]. Here, the REEs were selected to calculate F because they do not change
477 significantly during partial melting due to their similar bulk partition coefficients and,
478 moreover, would be less disturbed by cryptic metasomatism in comparison with the
479 other incompatible elements. We modelled the partial melting using both the PM (Sun
480 and McDonough, 1989) and DMM (Workman and Hart, 2005) as starting compositions
481 for the spinel and garnet stability fields (Fig. 7a). The modal compositions employed
482 here are the PM and DMM compositions (McDonough, 1990 and Workman and Hart,
483 2005, respectively). The mineral/melt partition coefficients for the REEs were taken
484 from Niu and Hékinian (1997) and Shaw (2006), whereas the melt modes are those
485 proposed by Johnson (1998).

486 The geochemical modelling using the REE abundances fails to reproduce the
487 REE patterns of the Coyhaique sp-lherzolites on simple partial melting from both sp-
488 and grt-facies fertile mantle peridotite (PM-like) or depleted mantle peridotite (DMM)
489 (Fig. 7a). Regarding that fact, we chose a mixture of 85% DMM and 15% slab-derived
490 component as a source (see details below). Based on this model, the estimates of the
491 partial melting degrees using the REE abundances indicate that the sp-lherzolites

492 became residues after <6% of non-modal batch melting from a metasomatized depleted
493 mantle source by up to 15% of a slab-derived component.

494

495 *5.2. The slab-derived components in the Coyhaique depleted lithospheric mantle*

496

497 As mentioned above, the Coyhaique sp-lherzolites represent samples from a
498 residual depleted SCLM. However, the non-modal batch melting model applied to them
499 suggests that these samples are not simple residues from the partial melting of the
500 spinel-facies PM or DMM (Fig. 6a). Indeed, all of the sp-lherzolites studied here have a
501 signature that is typical of most arc magmas in terms of the trace element compositions,
502 i.e., high ratios of LILE/(HFSE-REE) and strong negative Nb and Ta anomalies. There
503 are several potential processes capable of enriching the lithospheric mantle in
504 continental margin subduction zones: 1) dehydration from subducted an AOC and
505 sediments, 2) accretion of sediments derived from the continental crust and oceanic
506 seafloor, 3) slab melts (e.g., adakites) produced from the partial melting of subducted
507 oceanic crust and 4) asthenospheric upwelling through slab windows.

508 Typical fluid-mobile (e.g., LILE) over fluid-immobile (e.g., HFSE and REE)
509 trace elements ratios are useful to estimate the proportion of slab-derived components
510 into the mantle (e.g., Jacques et al., 2013). To evaluate the role of the metasomatic
511 component in the Coyhaique sp-lherzolites, we employed the Ce/Yb, (Th-Pb)/Ce, (Ba-
512 U-Pb-Sr)/Th, Sr/Y and La/Yb ratios, as well as the $^{87}\text{Sr}/^{86}\text{Sr}$ vs. $^{143}\text{Nd}/^{144}\text{Nd}$ and
513 $^{87}\text{Sr}/^{86}\text{Sr}$ – $^{207}\text{Pb}/^{204}\text{Pb}$ – $^{208}\text{Pb}/^{204}\text{Pb}$ vs. $^{206}\text{Pb}/^{204}\text{Pb}$ diagrams (Figs. 7a–d and 8a–d, not all
514 of the ratios are shown). For the above results, we have assumed several scenarios to
515 explain the potential metasomatic component of the depleted SCLM beneath the
516 Coyhaique location, such as aqueous fluids and/or melts derived from dehydration
517 and/or melting reactions in the down-going southeast Pacific oceanic crust (OC) and
518 Chile trench sediments associated with the subducted Aluk oceanic plate.

519

520 *5.2.1. Sediments and oceanic crust*

521

522 The oceanic crust (altered or not) and overlying sediments contribute important
523 input fluxes to the subduction system. Because subducted sediments have much higher
524 selected trace element ratios [e.g., (Th-Ce)/Yb, Th/Sr, Pb/Ce] and (^{207}Pb – ^{208}Pb)/ ^{204}Pb

525 isotopic ratios than those of AOC, it is possible to model the contribution of oceanic
526 crust, including AOC (Hauff et al., 2003; Staudigel et al., 1996), and the overlying layer
527 of subducted sediments into the SCLM beneath the Coyhaique location. Thus, to
528 distinguish the slab components that metasomatized the Coyhaique sp-lherzolites, we
529 assumed that the composition of the metabasaltic sample from the Chile Ridge (sample
530 D42-4, Segment 3; Karsten et al., 1996) to the CTS average (Jacques et al., 2013; Kilian
531 and Behrmann, 2003; Lucassen et al., 2010; Shinjoe et al., 2013) was 40:60 in the
532 following quantitative models. In Figure 8a–d, the sample D42-4 is labelled as a
533 modified ocean crust (MOC), which is thought to have been generated from the melting
534 of a depleted mantle source with a contamination of ~11.6% AOC and ~0.4% sediments
535 at depth (Karsten et al., 1996). The trace element and Sr-Nd-Pb isotopic compositions
536 of the CTS are similar to those of the primitive Andean volcanic arc basalts (e.g.,
537 Hickey et al., 1986; Hickey-Vargas et al., 1989), which means that the CTS are
538 composed of pelagic sediments with a significant input of terrigenous sediments eroded
539 from materials of the Andean volcanic arc. In terms of the radiogenic isotopes (Fig. 8a–
540 d), the composition of the CTS lies almost between EM-1 and EM-2 mantle
541 components.

542 The $(^{207}\text{Pb}-^{208}\text{Pb})/^{204}\text{Pb}$ isotopic ratios and Th/Yb vs. Sr/Th trace element ratios
543 show a good correlation, which precludes the role of AOC on the generation of the
544 SCLM beneath the Coyhaique location (Figs. 7d and 8c–d). However, it is difficult to
545 explain the variation in the Coyhaique sp-lherzolites obtained in this study on the basis
546 of a simple two-component mixing model between DMM average (Workman and Hart,
547 2005) and EM components (a slab-derived component). Alternatively, our results
548 suggest that the Coyhaique sp-lherzolites were variably modified by slab melts released
549 from a combination of MOC plus CTS (Figs. 7a–d and 8a–d). Then, assuming a
550 depleted SCLM source metasomatized by slab melts (85% DMM + 15% slab melt) as
551 the starting material, non-modal batch melting curves are also shown in all of the plots
552 that involve trace element ratios (Figs. 7 and 8). The curves of the above model on
553 Ce/Yb vs. Yb and Th/Yb vs. Sr/Th diagrams suggest that the variations in the sp-
554 lherzolites represent those of residues left after varying degrees of melt extraction
555 (<6%), which is identical to the modelling applied in section 5.1. On the other hand, on
556 the Pb/Ce vs. Pb diagram (Fig. 7c), the curve of the non-modal batch melting did not
557 agree with the variation in the Coyhaique sp-lherzolites. In addition, their $(^{207}\text{Pb}-$

558 $^{208}\text{Pb}/^{204}\text{Pb}$ isotopic ratios suggest that the Pb budget must be dominated by the DMM
559 component rather than the slab melt component because slab melt components of only
560 less than 5% are required to produce the wide range of the Coyhaique sp-lherzolites
561 (Figs. 7c and 8c–d).

562 To summarize, our model suggests that the Coyhaique sp-lherzolites might be
563 the melting residue of a heterogeneous SCLM, which resulted from metasomatism of
564 different extents (<15%) by the slab melt released from subducted CTS and the MOC
565 prior to the Farallón-Aluk ridge collision during Paleocene-Eocene times.

566

567 *5.2.2. Dehydrated fluids from the subducted sediments and oceanic crust*

568

569 As mentioned above, the geochemical and isotope signatures of the Coyhaique
570 sp-lherzolites can be attributed to the interaction with slab melts of the subducted CTS
571 and MOC. However, we cannot preclude the possibility that the dehydration of the
572 subducted slab also metasomatized the sp-lherzolites. It is widely accepted that the
573 dehydration of a slab produces an enrichment of the highly incompatible chalcophile
574 elements (e.g., W, Pb and Sn) as well as elevated (Rb-Ba-U-Sr)/Th ratios because Rb,
575 Ba, U and Sr (e.g., LILE) are preferentially incorporated into the fluid phases, whereas
576 Th is transferred efficiently with the slab only when sediment melts are involved (e.g.,
577 [Hawkesworth et al., 1997](#); [Noll et al., 1996](#)). The Coyhaique sp-lherzolites have Ba/Th
578 (12.24–171.46; CTS = 50–400), U/Th (0.25–0.99; CTS = 0.11–0.91), Sr/Th (37.04–
579 273.35; CTS = 19.24–138.16) and Pb/Th (0.28–2.62; CTS = 1.35–3.39) ratios that are
580 similar to those of the CTS, which is consistent with cryptic metasomatism by a
581 dehydration-induced silicate melt rather than by dehydrated fluid. The absence of modal
582 metasomatism supports this argument because a hydrated mineral phase (e.g., pargasite,
583 phlogopite, phengite and serpentine) was not found in the sp-lherzolites studied here,
584 implying a metasomatic enrichment without a significant input of aqueous fluid.

585

586 *5.2.3. Modern adakitic melts derived from oceanic crust partial melting*

587

588 In the southern Patagonia province, late Miocene to Recent adakitic magmatism
589 and its metasomatism were described in Cerro Pampa ([Kay et al., 1993](#); [Orihashi et al.,](#)
590 [2013](#)), Cook Island ([Stern and Kilian, 1996](#)) and Cerro del Fraile ([Faccini et al., 2013](#);

591 Kilian and Stern, 2002). In general, Sr/Y vs. Y and La/Yb vs. Yb discriminant diagrams
592 are applied to classify adakites (e.g., Castillo, 2006). Hence, the product of adakitic
593 metasomatism is expected to have 1) a high Sr/Y ratio with a high Sr concentration, 2)
594 high La/Yb ratio with L-REE to M-REE enrichments over the H-REE, 3) high SiO₂
595 contents with less negative Nb-Ta anomalies and 4) low ⁸⁷Sr/⁸⁶Sr ratios and low MgO
596 content (e.g., Martin et al., 2005; Castillo, 2006; Moyen, 2009). In contrast with the
597 product of adakitic metasomatism in peridotites from Cerro del Fraile (CF; Kilian and
598 Stern, 2002), the Coyhaique sp-lherzolites show a lower Sr concentration (<30 ppm; CF
599 = 48 ppm) with a weak Sr spike on the multi-element diagram (Fig. 6a), as well as
600 significantly lower Sr/Y (3.0–6.1; CF = 37) and La/Yb ratios (0.62–3.8; CF = 10)
601 coupled with a slight L-REEs enrichment on the REE pattern (Fig. 6c). Moreover, all of
602 the Coyhaique sp-lherzolites have the same or more mafic compositions, i.e., lower
603 SiO₂ and higher MgO contents, than the DMM and PM components (Fig. 5a). Based on
604 the results discussed above, we cannot exclude the scenario where the Coyhaique
605 spinel-lherzolites might be less influenced by an adakitic melt. However, it is important
606 to note that the occurrence of modern adakites appears to be mainly restricted to the
607 subduction of young oceanic lithosphere (≤25 Ma; Defant and Drummond, 1990;
608 Martin et al., 2005; Castillo, 2006; Moyen, 2009), thus, Coyhaique sp-lherzolites should
609 require an ancient (e.g., Paleocene-Eocene) adakitic melt metasomatism.

610

611 *5.3. Role of the Paleocene-Eocene slab window components in the Coyhaique depleted* 612 *mantle*

613

614 Plate tectonic models associated with geochronological and geochemical data of
615 Eocene OIB-like magmatism indicate subduction of the Farallón-Aluk spreading ridge
616 beneath the southern Patagonian province and likely permit the formation of the
617 Farallón-Aluk slab window beneath the Aysén region during Paleocene to Eocene times
618 (e.g., Aragón et al., 2013; Breitsprecher and Thorkelson, 2009; Cande and Leslie, 1986;
619 Morata et al., 2000; Parada et al., 2001; Ramos and Kay, 1992). To find evidence of a
620 sub-slab asthenospheric mantle metasomatism due to the opening of a Paleocene-
621 Eocene slab window in the sp-lherzolites, we compared the geochemistry of these
622 xenoliths with those of the host basalts having an OIB-like signature. The comparison
623 revealed that the sp-lherzolites differ strongly from the host basalts in composition. For

624 example, the sp-lherzolites show 1) a depletion of basaltic components (e.g., Al₂O₃,
625 CaO and TiO₂) (Fig. 5b-d), 2) prominent negative Nb-Ta anomalies coupled with
626 positive U and Pb anomalies on the PM-normalized multi-element diagram (Fig. 6a-b),
627 3) a mantle array of depleted mantle components between the DMM and PREMA
628 extended to the EM-component in Sr-Nd-Pb isotopic composition (Fig. 8a-d) and 4) a
629 slightly depleted and flat to slightly enriched L-REE/H-REE pattern (Fig. 6c). On the
630 other hand, their host basalts have marked positive Nb-Ta anomalies coupled with
631 negative U and Pb anomalies on the PM-normalized multi-element diagram, HIMU-like
632 isotope signatures (Fig. 8a) and a strong L-REE/H-REE enrichment pattern (Fig. 6c).
633 Thus, the geochemical and isotopic differences between the Coyhaique sp-lherzolites
634 and their host basalts indicate the absence of slab window-induced metasomatism to the
635 SCLM beneath Coyhaique.

636

637 *5.4. Geodynamic implications*

638

639 In tectonic settings in which slab windows beneath a back-arc region result from
640 the subduction of spreading ridges, magmas released from the sub-slab asthenosphere
641 would be largely uncontaminated by the supra-slab mantle components and have OIB or
642 MORB-like magma compositions (e.g., Gorrying et al., 2003). Thus, the Coyhaique
643 basalts with an OIB-like signature incorporate the upwelling of a deeper asthenosphere
644 beneath the Aysén region. Our new K-Ar age of 54 Ma for the Coyhaique basalts as
645 well as a previous K-Ar age of 58.6 Ma (Morata et al., 2000) allow that the eruption
646 was linked to the formation of a slab window due to a ridge-trench collision along the
647 Andean margin during the Paleocene-Eocene and the inference that the Farallón-Aluk
648 ridge collided against the western border of South America at the latitude of studied
649 area (45°46'S) during 59–54 Ma. The process of slab detachment allowed the
650 infiltration of the chemically enriched sub-slab asthenosphere within the slab gap and,
651 consequently, the enrichment of a depleted SCLM that has a strong OIB-like signature,
652 which probably took a few million years to occur because the enriched material needed
653 to be convectively transported into the SCLM (Ferrari, 2004). Based on our
654 geochemical data, the Coyhaique basalts studied here are thought to have occurred in
655 the sub-slab asthenosphere, but there is no evidence that OIB-like asthenospheric melts,
656 which occurred in the Farallón-Aluk spreading ridge subduction and subsequently in the

657 asthenospheric slab window, had much influence on the Coyhaique sp-lherzolites. Thus,
658 we conclude that the exhumation of the Coyhaique sp-lherzolites at the surface occurred
659 during the initial stages of the Farallón-Aluk spreading ridge collision with the Chile
660 trench. The Coyhaique sp-lherzolites, which represent the Paleocene-Eocene SCLM,
661 obviously have the characteristics of a slab-derived component. Thus, we suggest that
662 the slab-derived components originated from an MOC melt mixed with ancient
663 (Paleocene or older?) sediment subducted into the depleted SCLM between the South
664 American plate and the subducting Aluk (Phoenix) plate.

665

666 **6. Conclusions**

667

668 The studied Eocene host alkaline basalts (Balmaceda Basalt) located near
669 Coyhaique have a primitive character due to their relatively high Mg# (>61), MgO (~10
670 wt%), Cr (>300 ppm) and Ni (>200 ppm) contents. The strong OIB-like affinity of these
671 samples is supported by marked positive Nb-Ta anomalies coupled with negative U and
672 Pb anomalies on the (PM)-normalized multi-element diagram, high trace element ratios
673 [e.g., Ce/Yb_N = 8.7, Nb/(Ta-La) (>20; >1.4), Ce/Pb (>36), Nb/U (>56)], a low initial
674 ⁸⁷Sr/⁸⁶Sr (0.703039–0.703058) and a high initial ¹⁴³Nd/¹⁴⁴Nd (0.512880–0.512874).
675 These basalts were generated by small degrees of partial melting (up to 6%) that
676 resulted from asthenospheric upwelling through slab windows related to the Farallón-
677 Aluk ridge collision and the subduction beneath southern Patagonia.

678 The coarse- to medium-grained sp-lherzolites hosted in the alkaline basalts have
679 protogranular to porphyroclastic micro-textures, which indicate low strain and
680 recrystallization rates. The slight depletion in SiO₂ and moderate enrichment in MgO
681 compared to the PUM and DMM compositions, as well as the negative correlations
682 between MgO and the basaltic components (e.g., Al₂O₃, CaO and TiO₂), indicate that
683 the Coyhaique sp-lherzolites are solid residues derived from the same fertile source with
684 different degrees of partial melting. The majority of the sp-lherzolites show flat patterns
685 from H-REE to L-REE, whereas some samples show slight L-REE depletion (Ce/Yb_N =
686 0.5) to L-REE enrichment (Ce/Yb_N = 1.8). Remarkably, all of the studied sp-lherzolites
687 have trace element compositions typical of most arc magmas, such as pronounced
688 negative Nb-Ta-Ti anomalies coupled with a significant enrichment of LILE (e.g., U)
689 and chalcophile elements (W, Pb and Sn). The correlations among the trace element

690 ratios [e.g., (Th-Pb)/Ce, (Ba-U-Pb-Sr)/Th] and Sr-Nd-Pb isotopic ratios ($^{87}\text{Sr}/^{86}\text{Sr} =$
691 $0.702422\text{--}0.704900$; $^{143}\text{Nd}/^{144}\text{Nd} = 0.512883\text{--}0.513242$; $^{206}\text{Pb}/^{204}\text{Pb} = 18.212\text{--}18.729$;
692 $^{207}\text{Pb}/^{204}\text{Pb} = 15.483\text{--}15.600$; $^{208}\text{Pb}/^{204}\text{Pb} = 37.914\text{--}38.524$) point to the mixing of
693 depleted mantle components (at least 85% of DMM or PREMA) with an enriched slab-
694 derived component (up to 15%). According to our model, the slab-derived component
695 in the depleted SCLM may contain up to 60% of subducted CTS and more than 40% of
696 MOC melts produced prior to the Farallón-Aluk ridge collision during Paleocene-
697 Eocene times. Conversely, there is no evidence that OIB-like asthenospheric melts
698 induced by the Farallón-Aluk asthenospheric slab window had less influence on the
699 SCLM in the depleted SCLM.

700

701 **Acknowledgements**

702 The study presented herein was supported by the National Council of Technological and
703 Scientific Development – CNPq, Brazil, JSPS KAKENHI Grant Numbers 21403012 &
704 15H02630 awarded to Y. O. and the Earthquake Research Institute (ERI) cooperative
705 research program, University of Tokyo. We are thankful to N. Hokanishi for her help
706 with the XRF analysis and M. Assis, A. Martins, G. Raupp and L. Carniel for their help
707 with the isotopic procedures.

708

709 **References**

710

711 Albarède, F., 1992. How deep do common basalts form and differentiate? *Journal of*
712 *Geophysical Research* 97, 10997-11009.

713

714 Aragón, E., Pinotti, L., D'Eramo, F., Castro, A., Rabbia, O., Coniglio, J., Demartis, M.,
715 Hernando, I., Cavarozzi, C.E., Aguilera, Y.E., 2013. The Farallón-Aluk ridge collision
716 with South America: Implications for the geochemical changes of slab window magmas
717 from fore- to back-arc. *Geoscience Frontiers* 4, 377-388.

718

719 Bach, W., Erzinger, J., Dosso, L., Bollinger, C., Bougault, H., Etoubleau, J., Sauerwein,
720 J., 1996. Unusually large Nb-Ta depletions in North Chile ridge basalts at 36°50' to
721 38°56'S: major element, trace element, and isotopic data. *Earth and Planetary Science*
722 *Letters* 142, 223-240.

723

724 Baker, P.E., Rea, W.J., Skarmeta, J., Caminos, R., Rex, D.C., 1981. Igneous History of
725 the Andean Cordillera and Patagonian Plateau around Latitude 46°S. Philosophical
726 Transactions Royal Society of London 303, 105-149.

727

728 Bjerg, E.A., Ntaflos, Th., Kurat, G., Dobosi, G., Labudía, C.H., 2005. The upper mantle
729 beneath Patagonia, Argentina, documented by xenoliths from alkali basalts. Journal of
730 South American Earth Sciences 18, 125-145.

731

732 Boutonnet, E., Arnaud, N., Guivel, C., Lagabrielle, Y., Scalabrino, B., Espinoza, F.,
733 2010. Subduction of the South Chile active spreading ridge: A 17 Ma to 3 Ma magmatic
734 record in central Patagonia (western edge of Meseta del Lago Buenos Aires, Argentina).
735 Journal of Volcanology and Geothermal Research 189, 319-339.

736

737 Breitsprecher, K., Thorkelson, D.J., 2009. Neogene kinematic history of Nazca–
738 Antarctic–Phoenix slab windows beneath Patagonia and the Antarctic Peninsula.
739 Tectonophysics 464, 10-20.

740

741 Butler, R.F., Hervé, F., Munizaga, F., Beck, M.E., Burmester, R.F., Oviedo, E., 1991.
742 Paleomagnetism of the Patagonian Plateau basalts, southern Chile and Argentina.
743 Journal of Geophysical Research 96, 6023-6034.

744

745 Cande, S.C., Leslie, R.B., 1986. Late Cenozoic Tectonic of the Southern Chile trench.
746 Journal of Geophysical Research 91, 471-496.

747

748 Castillo, P.R., 2006. An overview of adakite petrogenesis. Chinese Science Bulletin
749 51(3), 257-268.

750

751 Charrier, R., Linares, E., Niemeyer, H., Skármeta, J., 1979. K-Ar ages of basalt flows of
752 Meseta Buenos Aires in southern Chile and their relation to the southeast Pacific triple
753 junction. Geology 7, 436-439.

754

- 755 Choo, M.K., Lee, M.J., Lee, J.I., Kim, K.H., Park, K.-H., 2012. Geochemistry and Sr–
756 Nd–Pb isotopic constraints on the petrogenesis of Cenozoic lavas from the Pali Aike
757 and Morro Chico area (52°S), southern Patagonia, South America. *Island Arc* 21, 327–
758 350.
- 759
- 760 Conceição, R.V., Mallmann, G., Koester, E., Schilling, M., Bertotto, G.W., Rodriguez-
761 Vargas, A., 2005. Andean subduction-related mantle xenoliths: isotopic evidence of Sr–
762 Nd decoupling during metasomatism. *Lithos* 82, 273–287.
- 763
- 764 Dantas, C., Grégoire, M., Koester, E., Conceição, R.V., Rieck Jr., N., 2009. The
765 lherzolite–websterite xenolith suite from Northern Patagonia (Argentina): Evidence of
766 mantle–melt reaction processes. *Lithos* 107, 107–120.
- 767
- 768 Defant, M.J., Drummond, M.S., 1990. Derivation of some modern arc magmas by
769 melting of young subducted lithosphere. *Nature* 367, 662–665.
- 770
- 771 Demant, A., Hervé, F., Pankhurst, R.J., Suárez, M., 1996. Geochemistry of Early
772 Tertiary back-arc basalts from Aysén, Southern Chile (44–46°S): Geodynamic
773 implications. In *Third International Symposium on Andean Geodynamics*, No. 3, Actas,
774 p. 555–558. St. Malo, France.
- 775
- 776 Diegor, W., Longerich, H., Abrajano, T., Horn, I., 2001. Applicability of a high
777 pressure digestion technique to the analysis of sediment and soil samples by inductively
778 coupled plasma-mass spectrometry. *Analytica Chimica Acta* 431, 195–207.
- 779
- 780 D’Orazio, M., Agostini, S., Mazzarini, F., Innocenti, F., Manetti, P., Haller, M., Lahsen,
781 A., 2000. The Pali Aike Volcanic Field, Patagonia: slab-window magmatism near the
782 tip of South America. *Tectonophysics* 321, 407–427.
- 783
- 784 Espinoza, F., Morata, D., Pelleter, E., Maury, R. C., Suárez, M., Lagabrielle, Y., Polvé,
785 M., Bellon, H., Cotten, J., De la Cruz, R., Guivel, C., 2005. Petrogenesis of the Eocene
786 and Mio–Pliocene alkaline basaltic magmatism in Meseta Chile Chico, southern

- 787 Patagonia, Chile: Evidence for the participation of two slab windows. *Lithos* 82, 315-
788 343.
- 789
- 790 Faccini, B., Bonadiman, C., Coltorti, M., Grégoire, M., Siena, F., 2013. Oceanic
791 Material Recycled within the Sub-Patagonian Lithospheric Mantle (Cerro del Fraile,
792 Argentina). *Journal of Petrology* 54, 1211-1258.
- 793
- 794 Ferrari, L., 2004. Slab detachment control on mafic volcanic pulse and mantle
795 heterogeneity in central Mexico. *Geology* 32, 77-80.
- 796
- 797 Gervasoni, F., Conceição, R.V., Jalowitzki, T.L.R., Schilling, M.E., Orihashi, Y.,
798 Nakai, S., Sylvester, P., 2012. Heterogeneidades do manto litosférico subcontinental no
799 extremo sul da Placa Sul-americana: influência da subducção atual e interações
800 litosfera-astenosfera sob o Campo Vulcânico de Pali Aike. *Pesquisas em Geociências*
801 39, 269-285.
- 802
- 803 Gorrington, M.L., Kay, S.M., 2000. Carbonatite metasomatized peridotite xenoliths from
804 southern Patagonia: implications for lithospheric processes and Neogene plateau
805 magmatism. *Contributions to Mineralogy and Petrology* 140, 55-72.
- 806
- 807 Gorrington, M.L., Kay, S.M., Zeitler, P.K., Ramos, V.A., Rubiolo, D., Fernandez, M.I.,
808 Panza, J.L., 1997. Neogene Patagonian plateau lavas: continental magmas associated
809 with ridge collision at the Chile Triple Junction. *Tectonics* 16, 1-17.
- 810
- 811 Gorrington, M.L., Singer, B., Gowers, J., Kay, S.M., 2003. Plio-Pleistocene basalts from
812 the Meseta del Lago Buenos Aires, Argentina: evidence for asthenosphere–lithosphere
813 interactions during slab window magmatism. *Chemical Geology* 193, 215-235.
- 814
- 815 Griffin, W.L., O'Reilly, S.Y., Afonso, J.C., Begg, G.C., 2009. The Composition and
816 Evolution of Lithospheric Mantle: a Re-evaluation and its Tectonic Implications.
817 *Journal of Petrology* 50, 1185-1204.
- 818

- 819 Hanyu, T., Kawabata, H., Tatsumi, Y., Kimura, J.-I., Hyodo, H., Sato, K., Miyazaki, T.,
820 Chang, Q., Hirahara, Y., Takahashi, T., Senda, R., Nakai, S., 2014. Isotope evolution in
821 the HIMU reservoir beneath St. Helena: Implications for the mantle recycling of U and
822 Th. *Geochimica et Cosmochimica Acta* 143, 232-252.
- 823
- 824 Hauff, F., Hoernle, K., Schmidt, A., 2003. Sr-Nd-Pb composition of Mesozoic Pacific
825 oceanic crust (Site 1149 and 801, ODP Leg 185): Implications for alteration of ocean
826 crust and the input into the Izu-Bonin-Mariana subduction system. *Geochemistry,
827 Geophysics, Geosystems* 4, 1-30.
- 828
- 829 Hawkesworth, C.J., Turner, S.P., McDermott, F., Peate, D.W., van Calsteren, P., 1997.
830 U-Th Isotopes in Arc Magmas: Implications for Element Transfer from the Subducted
831 Crust. *Science* 276, 551-555.
- 832
- 833 Herzberg, C., 2004. Geodynamic Information in Peridotite Petrology. *Journal of
834 Petrology* 45, 2507-2530.
- 835
- 836 Herzberg, C., Asimow, P.D., 2008. Petrology of some oceanic island basalts:
837 PRIMELT2.XLS software for primary magma calculation. *Geochemistry, Geophysics,
838 Geosystems* 9, 1-25.
- 839
- 840 Hickey, R.L., Frey, F.A., Gerlach, D.C., 1986. Multiple sources for basaltic arc rocks
841 from the southern volcanic zone of the Andes (34°–41°S): trace element and isotopic
842 evidence for contributions from subducted oceanic crust, mantle, and continental crust.
843 *Journal of Geophysical Research* 91, 5963-5983.
- 844
- 845 Ionov, D.A., Prikhod'ko, V.S., O'Reilly, S.Y., 1995. Peridotite xenoliths in alkali
846 basalts from the Sikhote-Alin southeastern Siberia, Russia: trace-element signatures of
847 mantle beneath a convergent continental margin. *Chemical Geology* 120, 275-294.
- 848
- 849 Jacobsen, S.B., Wasserburg, G.J., 1980. Sm-Nd isotopic evolution of chondrites. *Earth
850 and Planetary Science Letters* 50, 139-155.
- 851

- 852 Jacques, G., Hoernle, K., Gill, J., Hauff, F., Wehrmann, H., Garbe-Schönberg, D., van
853 den Bogaard, P., Bindeman, I., Lara, L.E., 2013. Across-arc geochemical variations in
854 the Southern Volcanic Zone, Chile (34.5–38.0°S): Constraints on mantle wedge and
855 slab input compositions. *Geochimica et Cosmochimica Acta* 123, 218-243.
856
- 857 Jenner, G.A., Longrich, H.P., Jackson, S.E., Fryer, B.J., 1990. ICP-MS - a powerful
858 tool for high-precision trace-element analysis in earth sciences: evidence from analysis
859 of selected U.S.G.S. reference samples. *Chemical Geology* 83, 133-148.
860
- 861 Johnson, K.T.M., 1998. Experimental determination of partition coefficients for rare
862 earth and high-field-strength elements between clinopyroxene, garnet, and basaltic melt
863 at high pressures. *Contributions to Mineralogy and Petrology* 133, 60-68.
864
- 865 Karsten, J.L., Klein, E.M., Sherman, S.B., 1996. Subduction zone geochemical
866 characteristics in ocean ridge basalts from the southern Chile Ridge: Implications of
867 modern ridge subduction systems for the Archean. *Lithos* 37, 143-161.
868
- 869 Kay, S.M., Ramos, V.A., Marquez, M., 1993. Evidence in Cerro Pampa Volcanic Rocks
870 for Slab-Melting Prior to Ridge-Trench Collision in Southern South America. *The*
871 *Journal of Geology* 101, 703-714.
872
- 873 Kay, S.M., Ramos, V.R., Gorrington, M.L., 2002. Geochemistry of Eocene plateau basalts
874 related to ridge collision in Southern Patagonian. In: XV Congreso Geológico
875 Argentino. *Actas* 3, 60-65.
876
- 877 Kilian, R., Stern, C.R., 2002. Constraints on the interaction between slab melts and the
878 mantle wedge from adakitic glass in peridotite xenoliths. *European Journal of*
879 *Mineralogy* 14, 25-36.
880
- 881 Kilian, R., Behrmann, J.H., 2003. Geochemical constraints on the sources of Southern
882 Chile Trench sediments and their recycling in arc magmas of the Southern Andes.
883 *Journal of the Geological Society* 160, 57-70.
884

- 885 Laurora, A., Mazzucchelli, M., Rivalenti, G., Vannucci, R., Zanetti, A., Barbieri, M.A.,
886 Cingolani, C.A., 2001. Metasomatism and melting in carbonated peridotite xenoliths
887 from the mantle wedge: the Gobernador Gregores case (Southern Patagonia). *Journal of*
888 *Petrology* 42, 69-87.
- 889
- 890 Lucassen, F., Wiedicke, M., Franz, G., 2010. Complete recycling of a magmatic arc:
891 evidence from chemical and isotopic composition of Quaternary trench sediments in
892 Chile (36°–40°S). *International Journal of Earth Sciences* 99, 687-701.
- 893
- 894 Martin, H., Smithies, R.H., Rapp, R., Moyen, J.-F., Champion, D., 2005. An overview
895 of adakite, tonalite–trondhjemite–granodiorite (TTG), and sanukitoid: relationships and
896 some implications for crustal evolution. *Lithos* 79, 1-24.
- 897
- 898 McDonough, W.F., 1990. Constraints on the composition of the continental lithospheric
899 mantle. *Earth and Planetary Science Letters* 101, 1-18.
- 900
- 901 McDonough, W.F., Sun, S.-S., 1995. Composition of the Earth. *Chemical Geology* 120,
902 223-253.
- 903
- 904 Mercier, J.C., Nicolas, A., 1975. Textures and fabrics of upper-mantle peridotites as
905 illustrated by xenoliths from basalt, *Journal of Petrology* 16, 454-487.
- 906
- 907 Morata, D., de la Cruz, R., Suárez, M., Demant, A., 2000. Mantle xenoliths and
908 xenocrysts in the late Paleocene Patagonian continental flood basalts from Aysen, S.
909 Chile. In: IX Congreso Geológico Chileno. Actas 2, 226-229.
- 910
- 911 Moyen, J.-F., 2009. High Sr/Y and La/Yb ratios: The meaning of the “adakitic
912 signature”. *Lithos* 112, 556-574.
- 913
- 914 Nagao, K., Ogata, A., Miura, Y., Matsuda, J., Akimoto, S., 1991. Highly reproducible
915 13 and 17 ka K-Ar ages of two volcanic rocks. *Geochemical Journal* 25, 447-451.
- 916

- 917 Nelson, S.T., Montana, A., 1992. Sieve-textured plagioclase in volcanic rocks produced
918 by rapid decompression. *American Mineralogist* 77, 1242-1249.
919
- 920 Niu, Y., Hékinian, R., 1997. Basaltic liquids and harzburgitic residues in the Garrett
921 Transform: a case study at fast-spreading ridges. *Earth and Planetary Science Letters*
922 146, 243-258.
923
- 924 Noll Jr., P.D., Newsom, H.E., Leeman, W.P., Ryan, J.G., 1996. The role of
925 hydrothermal fluids in the production of subduction zone magmas: Evidence from
926 siderophile and chalcophile trace elements and boron. *Geochimica et Cosmochimica*
927 *Actas* 60, 587-611.
928
- 929 Ntaflos, Th., Bjerg, E.A., Labudia, C.H., Kurat, G., 2007. Depleted lithosphere from the
930 mantle wedge beneath Tres Lagos, southern Patagonia, Argentina. *Lithos* 94, 46-65.
931
- 932 Orihashi, Y., Hirata T., 2003. Rapid quantitative analysis of Y and REE abundances in
933 XRF glass bead for selected GSJ reference rock standards using UV laser ablation ICP-
934 MS. *Geochemical Journal* 37, 401-412.
935
- 936 Orihashi, Y., Naranjo, J. A., Motoki, A., Sumino, H., Hirata, D., Anma, R., Nagao, K.,
937 2004. Quaternary volcanic activity of Hudson and Lautaro volcanoes, Chilean
938 Patagonia: new constraints from K-Ar ages. *Andean Geology* 31, 207-224.
939
- 940 Orihashi, Y., Anma, R., Motoki, A., Haller, M.J., Hirata, D., Iwano, H., Sumino, H.,
941 Ramos, V.A., 2013. Evolution history of the crust underlying Cerro Pampa, Argentine
942 Patagonia: Constraint from LA-ICPMS U–Pb ages for exotic zircons in the Mid-
943 Miocene adakite. *Geochemical Journal* 47, 235-247.
944
- 945 Parada, M.A., Lahsen, A., Palacios, C., 2001. Ages and geochemistry of Mesozoic-
946 Eocene back-arc volcanic rocks in the Aysén region of the Patagonian Andes, Chile.
947 *Andean Geology* 28, 25-46.
948

- 949 Pankhurst, R.J., Weaver, S.D., Hervé, F., Larrondo, P., 1999. Mesozoic-Cenozoic
950 evolution of the North Patagonian Batholith in Aysén, southern Chile. *Journal of the*
951 *Geological Society of London* 156, 673-694.
- 952
- 953 Ramos, V.A., 1999. Plate tectonic setting of the Andean Cordillera. *Episodes* 22, 183-
954 190.
- 955
- 956 Ramos, V.A., Kay, S.M., 1992. Southern Patagonian plateau basalts and deformation:
957 back-arc testimony of ridge collisions, *Tectonophysics* 205, 261-282.
- 958
- 959 Rivalenti, G., Mazzucchelli, M., Laurora, A., Ciuffi, S.I.A., Zanetti, A., Vannucci, R.,
960 Cingolani, C.A., 2004. The backarc mantle lithosphere in Patagonia, South America.
961 *Journal of South American Earth Sciences* 17, 121-152.
- 962
- 963 Rudnick, R.L., Barth, M., Horn, I., McDonough, W.F., 2000. Rutile-Bearing Refractory
964 Eclogites: Missing Link Between Continents and Depleted Mantle. *Science* 287, 278-
965 281.
- 966
- 967 Salters, V.J.M., Sachi-Kocher, A., 2010. An ancient metasomatic source for the Walvis
968 Ridge basalts. *Chemical Geology* 273, 151-167.
- 969
- 970 Schilling, M., Conceição, R.V., Mallmann, G., Koester, E., Kawashita, K., Hervé, F.,
971 Morata, D., Motoki, A., 2005. Spinel-facies mantle xenoliths from Cerro Redondo,
972 Argentine Patagonia: Petrographic, geochemical, and isotopic evidence of interaction
973 between xenoliths and host basalt. *Lithos* 82, 485-502.
- 974
- 975 Schilling, M., Carlson, R.W., Conceição, R.V., Dantas, C., Bertotto, G.W., Koester, E.,
976 2008. Re-Os isotope constraints on subcontinental lithospheric mantle evolution of
977 southern South America. *Earth and Planetary Science Letters* 268, 89-101.
- 978
- 979 Shaw, D.M., 2006. *Trace Elements in Magmas: A Theoretical Treatment*. Cambridge
980 University Press, 256pp.
- 981

- 982 Shinjoe, H., Orihashi, Y., Naranjo, J.A., Hirata, D., Hasenaka, T., Fukuoka, T., Sano,
983 T., Anma, R., 2013. Boron and other trace element constraints on the slab-derived
984 component in Quaternary volcanic rocks from the Southern Volcanic Zone of the
985 Andes. *Geochemical Journal* 47, 185-199.
- 986
- 987 Staudigel, H., Plank, T., White, B., Schminck, H.-U., 1996. Geochemical Fluxes During
988 Seafloor Alteration of the Basaltic Upper Oceanic Crust: DSDP Sites 417 and 418. In:
989 Subduction top to bottom. *Geophysical Monograph*. Bebout, G.E., Scholl, D.W., Kirby,
990 S.H. and Platt, J.P. (Editors), American Geophysical Union, Washington, D.C. 96: 19-
991 38.
- 992
- 993 Stern, C.R., Kilian, R., 1996. Role of the subducted slab, mantle wedge and continental
994 crust in the generation of adakites from the Andean Austral Volcanic Zone.
995 *Contributions to Mineralogy and Petrology* 123, 263-281.
- 996
- 997 Stern, C.R., Kilian, R., Olker, B., Hauri, E.H., Kyser, T.K., 1999. Evidence from mantle
998 xenoliths for relatively thin (<100 km) continental lithosphere below the Phanerozoic
999 crust of southernmost South America. *Lithos* 48, 217-235.
- 1000
- 1001 Streckeisen, A., 1979. Classification and nomenclature of volcanic rocks, lamprophyres,
1002 carbonatites, and melilitic rocks: Recommendations and suggestions of the IUGS
1003 subcommission on the systematics of igneous rocks. *Geology* 7, 331-335.
- 1004
- 1005 Sturm, M.E., Klein, E.M., Graham, D.W., Karsten, J., 1999. Age constraints on crustal
1006 recycling to the mantle beneath the southern Chile Ridge: He-Pb-Sr-Nd isotope
1007 systematics. *Journal of Geophysical Research* 104, 5097-5114.
- 1008
- 1009 Sun, S., McDonough, W.F., 1989. Chemical and isotopic systematics of oceanic basalts,
1010 implications for mantle composition and processes. In: *Magmatism in the Ocean Basins*
1011 (Saunders, A.D. and Norry, M.J., editors). *Geological Society (Special Publications)* 42,
1012 313-345.
- 1013

1014 Tani, K., Orihashi, Y., Nakada, S., 2002. Major and trace component analysis of silicate
1015 rocks using fused glass bead by X-ray Fluorescence spectrometer: Evaluation of
1016 analytical precision for third, sixth and eleventh dilution fused glass beads. Tech. Res.
1017 Rep., ERI, Univ. Tokyo 8, 26-36.

1018

1019 Workman, R.K., Hart, S.R., 2005. Major and trace element composition of the depleted
1020 MORB mantle (DMM). Earth and Planetary Science Letters 231, 53-72.

1021

1022 Workman, R.K., Hart, S.R., Jackson, M., Regelous, M., Farley, K.A., Blusztajn, J.,
1023 Kurz, M., Staudigel, H., 2004. Recycled metasomatized lithosphere as the origin of the
1024 Enriched Mantle II (EM2) end-member: Evidence from the Samoan Volcanic Chain.
1025 Geochemistry, Geophysics, Geosystems 5, 1-44.

1026

1027 Wörner, G., Zindler, A., Staudigel, H., Schmincke, H.U., 1986. Sr, Nd, and Pb isotope
1028 geochemistry of Tertiary and Quaternary alkaline volcanics from West Germany. Earth
1029 and Planetary Science Letters 79, 107-119.

1030

1031 Zindler, A., Hart, S. 1986. Chemical Geodynamics. Annual Review of Earth and
1032 Planetary Sciences 14, 493-57.

1033

1034 **Figure captions**

1035

1036 **Figure 1.** (a) Present-day tectonic setting of southern South America, modified from
1037 [Boutonnet et al. \(2010\)](#). SVZ = Southern Volcanic Zone, AVZ = Austral Volcanic
1038 Zone, CTJ = Chile Triple Junction, CC = Meseta de Chile Chico, MLBA = Meseta del
1039 Lago Buenos Aires, MV = Meseta de las Vizcachas and PAVF = Pali-Aike Volcanic
1040 Field. (b) Simplified geological map of the Patagonian Cordillera between 43°30' and
1041 47°30'S showing the main geological units (modified from [Pankhurst et al., 1999](#)).
1042 LOFZ = Liquiñe-Ofqui Fault Zone. The circle indicates the location of the studied
1043 samples.

1044

1045 **Figure 2.** (a) Mineral proportions (wt.%) of the Coyhaique mantle xenoliths plotted on
1046 the ternary classification diagram from [Streckeisen \(1979\)](#). These data are from [Table 4](#).

1047 (b) Petrographic characteristics of a representative coarse-grained, protogranular to
1048 porphyroclastic, lower strain and recrystallized, Coyhaique spinel-lherzolite (PM25-05).
1049 Abbreviations: Ol = olivine; Opx = orthopyroxene; Cpx = clinopyroxene; Sp = spinel.
1050

1051 **Figure 3.** Photomicrograph showing different textures observed in the Coyhaique
1052 lherzolites. The photographs show both natural and plane-polarized light in thin
1053 sections: (a–b) Interstitial spinel and its typical holly-leaf texture; (c–d) fractured olivine
1054 with undulatory extinction (and kink bands) and occurrence of iddingsite; (e–f)
1055 orthopyroxene porphyroclast containing thin exsolution lamellae of clinopyroxene,
1056 especially in their central parts.

1057
1058 **Figure 4.** Scanning electron microscope images (BSE) of the Coyhaique lherzolites. (a)
1059 Coarse- to medium-grained lherzolite with protogranular to porphyroclastic textures
1060 evidenced by large olivine and orthopyroxene porphyroclasts with lobate grain
1061 boundaries; (b) Coarse- to medium-grained lherzolite with spinel holly-leaf; (c) olivine
1062 porphyroclast containing an iddingsite vein; (d) detail of the iddingsite vein; (e)
1063 clinopyroxene exsolution lamellae in a orthopyroxene porphyroclast; (f) spongy
1064 reaction rim in clinopyroxene.

1065
1066 **Figure 5.** Whole-rock MgO variation diagrams for selected major elements (wt.%) of
1067 the Coyhaique lherzolites (a–d). The negative correlations between MgO and the main
1068 oxides vary from fertile (close to PUM) to slight refractory compositions and indicate
1069 different degrees of partial melting. Ni is positively correlated with MgO, consistent
1070 with its compatible character during melt-peridotite equilibrium (e). The Al₂O₃ versus
1071 CaO diagram (f) reported by [Griffin et al. \(2009\)](#) indicates that the lherzolites studied
1072 here show a moderate depletion from primitive mantle compositions and plot into the
1073 field of the Phanerozoic mantle. For comparison, values of the primitive upper mantle
1074 (PUM; [McDonough and Sun, 1995](#)) and depleted MORB mantle (DMM; [Workman and
1075 Hart, 2005](#)) are shown.

1076
1077 **Figure 6.** Primitive mantle-normalized incompatible trace elements (a–b) and REE (c)
1078 diagrams of the whole-rock samples. The normalized values were reported by [Sun and
1079 McDonough \(1989\)](#). For comparison, values of the host basalts (HB), depleted MORB

1080 mantle (DMM; Workman and Hart, 2005), modified oceanic crust (MOC is represented
 1081 by Chile Ridge metabasalt, sample D42-4, Segment 3; Karsten et al., 1996), Chile
 1082 trench sediments average (CTS; Jacques et al., 2013; Kilian and Behrmann, 2003;
 1083 Lucassen et al., 2010; Shinjoe et al., 2013) and metasomatized lithospheric peridotite
 1084 mantle source (85% DMM + 15% slab melt) are shown. See the text for more details.

1085

1086 **Figure 7.** Selected trace element ratio diagrams. (a–b) Ce/Yb, vs. Yb, (c) Pb/Ce vs. Ce
 1087 and (d) Th/Yb vs. Sr/Th diagrams illustrating the geochemical characteristics of the
 1088 Coyhaique sp-lherzolites and their host basalts (HB). For comparison, the primitive
 1089 mantle (PM; Sun and McDonough, 1989), depleted MORB mantle (DMM; Workman
 1090 and Hart, 2005), modified oceanic crust (MOC is represented by Chile Ridge
 1091 metabasalt, sample D42-4, Segment 3; Karsten et al., 1996), Chile trench sediments
 1092 (CTS; Jacques et al., 2013; Kilian and Behrmann, 2003; Lucassen et al., 2010; Shinjoe
 1093 et al., 2013), altered oceanic crust (AOC; Staudigel et al., 1996), slab melt (60% CTS +
 1094 40% MOC), Andean volcanic arc basalts (Hickey et al., 1986; Hickey-Vargas et al.,
 1095 1989) and metasomatized lithospheric peridotite mantle source (85% DMM + 15% slab
 1096 melt) are shown. Two-component mixing curves between DMM-AOC, DMM-
 1097 CTS_{average} and DMM-Slab melt were calculated (b–d). The white filled circles along the
 1098 mixing dashed curves indicate the percentage of the metasomatic component in the
 1099 mixture as follow: 2%, 4%, 6%, 8%, 10%, 15%, 20% and 50%. The melting trends
 1100 from the PM, DMM and metasomatized lithospheric peridotite mantle source (85%
 1101 DMM + 15% slab melt) compositions are shown by solid curves. The circles on each
 1102 solid curve correspond to the residues from the partial melting of the spinel-facies,
 1103 whereas the squares represent the residues from the partial melting of the garnet-facies
 1104 (a, c and d). Each filled circle/square along the solid curves indicates the percentage of
 1105 partial melting as follow: 2%, 4%, 6%, 8%, 10%, 12% and 14%. The source modes
 1106 assumed here for partial melting from the DMM and metasomatized lithospheric
 1107 peridotite in the spinel and garnet stability fields are from Workman and Hart (2005),
 1108 whereas the PM modal compositions are from McDonough (1990).

1109

1110 **Figure 8.** $^{87}\text{Sr}/^{86}\text{Sr}$ vs. $^{143}\text{Nd}/^{144}\text{Nd}$ (a) and $^{87}\text{Sr}/^{86}\text{Sr}$ – $^{207}\text{Pb}/^{204}\text{Pb}$ – $^{208}\text{Pb}/^{204}\text{Pb}$ vs.
 1111 $^{206}\text{Pb}/^{204}\text{Pb}$ (b–d) isotope variations of whole-rock from selected Coyhaique sp-
 1112 lherzolites. The data for comparison are indicated in the text. The dashed line represents

1113 mixing between the depleted MORB mantle (DMM; [Workman and Hart, 2005](#)) and slab
1114 melt (60%CTS + 40%MOC). See the text for more details about the enriched end-
1115 member component. The mixing lines between the DMM and slab melt are marked at
1116 intervals of 1%, 2%, 5% and 10%, with increasing contribution from the latter
1117 component.

1118

1119 **Table captions**

1120

1121 **Table 1.** Whole-rock major and trace element compositions for the Coyhaique mantle
1122 xenoliths, determined by XRF and ICP-MS. The total iron is reported as Fe₂O₃. The
1123 major element results were normalized to 100%. PM25-A1 and PM25-A3 are
1124 representative host basalt samples. Mg-number = $Mg/(Mg+Fe^{+2})$.

1125

1126 **Table 2.** Whole-rock analytical values of the host basalt unspiked K-Ar ages.

1127

1128 **Table 3.** Whole-rock Rb-Sr, Sm-Nd and Pb-Pb isotopic data for the selected Coyhaique
1129 mantle xenoliths analysed in this study plus two representative host basalts (samples
1130 PM25-A1 and PM25-A3). The numbers in the parentheses indicate the 2σ errors in the
1131 last digits.

1132

1133 **Table 4.** Classification and modal mineralogies for the Coyhaique mantle xenoliths.
1134 The modal proportions of the minerals were determined by point-counting with 900–
1135 2800 points covering the entire area of the relatively large thin sections. Abbreviations:
1136 Ol = olivine; Opx = orthopyroxene; Cpx = clinopyroxene; Sp = spinel. The textures are
1137 from [Mercier and Nicolas \(1975\)](#), and the rock types are from [Streckeisen \(1979\)](#).

1138

1139 **Table 5.** Representative SEM-EDS analyses of the mineral assemblage from the
1140 Coyhaique mantle xenoliths. Total iron reported as FeO and Mg-number =
1141 $Mg/(Mg+Fe^{+2})$. Abbreviations: Ol = olivine; Opx = orthopyroxene; Cpx =
1142 clinopyroxene; Sp = spinel; Id = iddingsite; Cpx reaction = spongy texture.

Figure 1

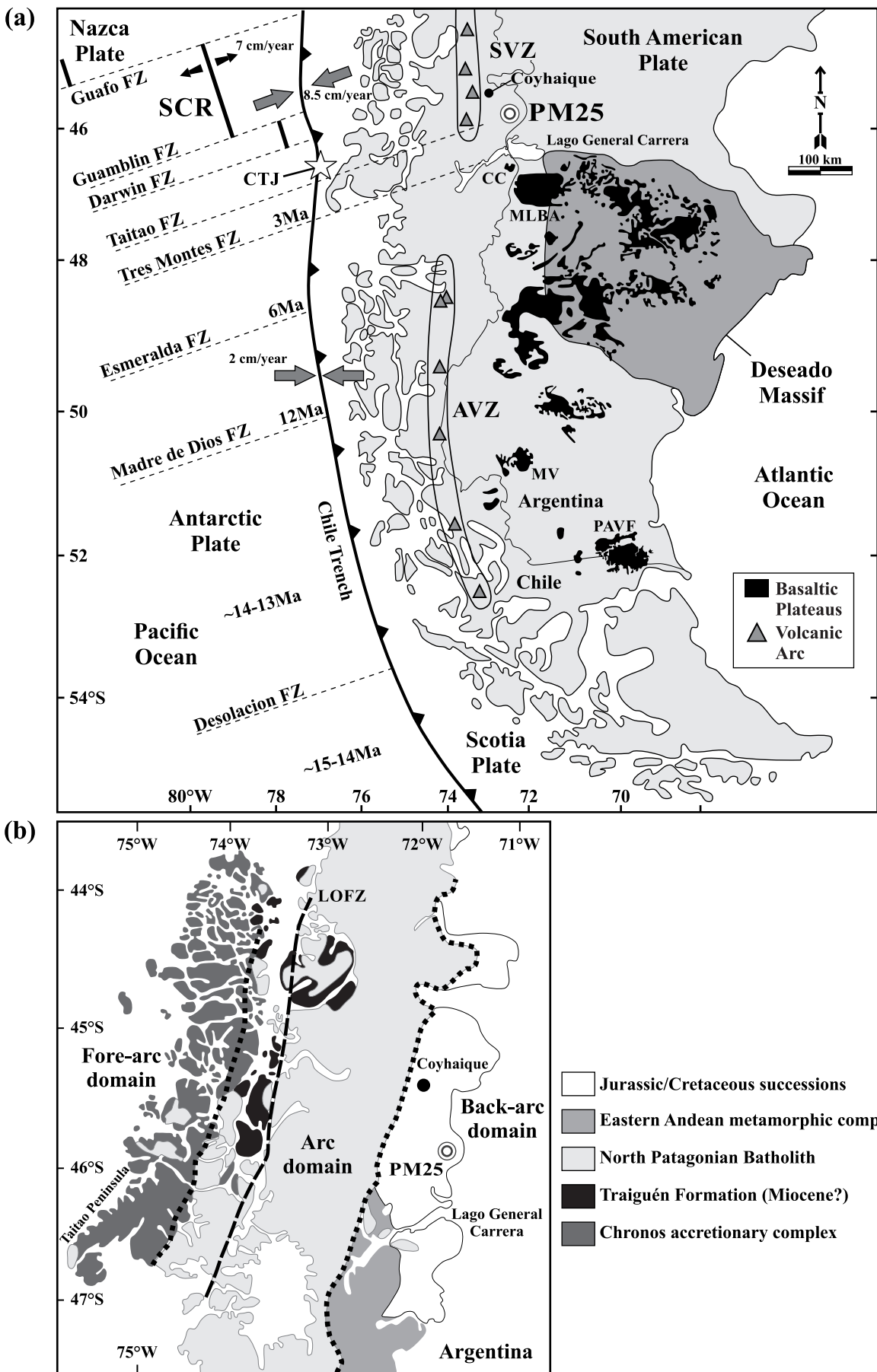


Figure 2

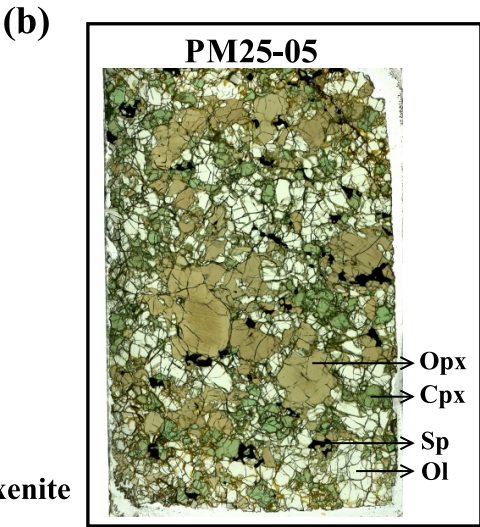
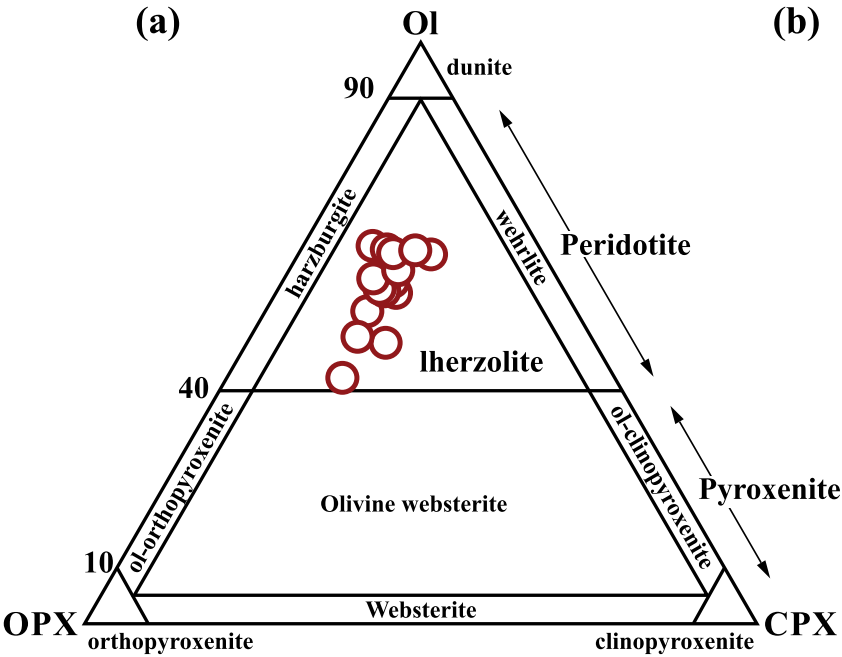


Figure 3

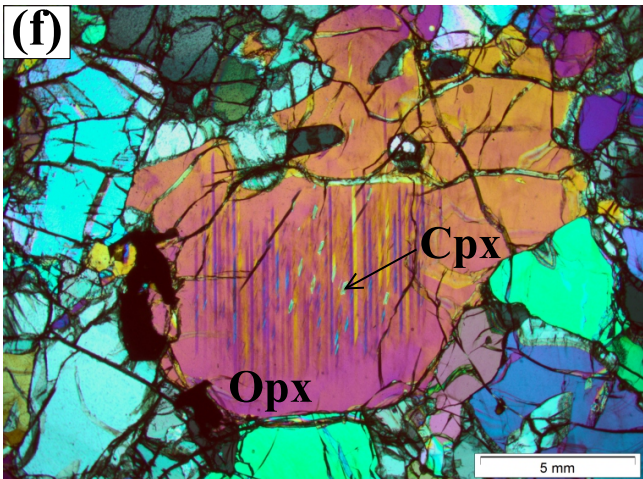
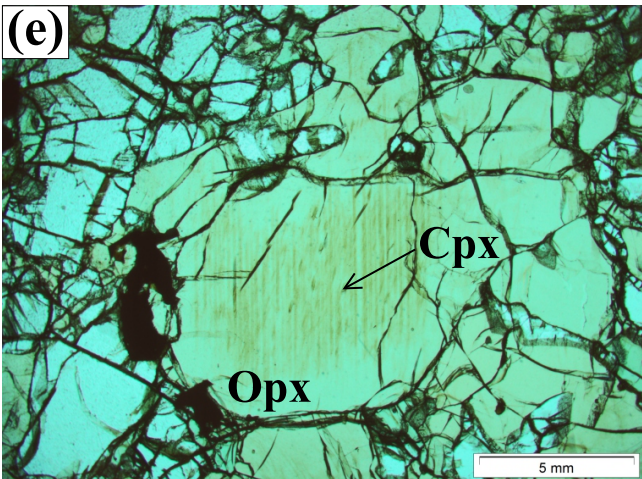
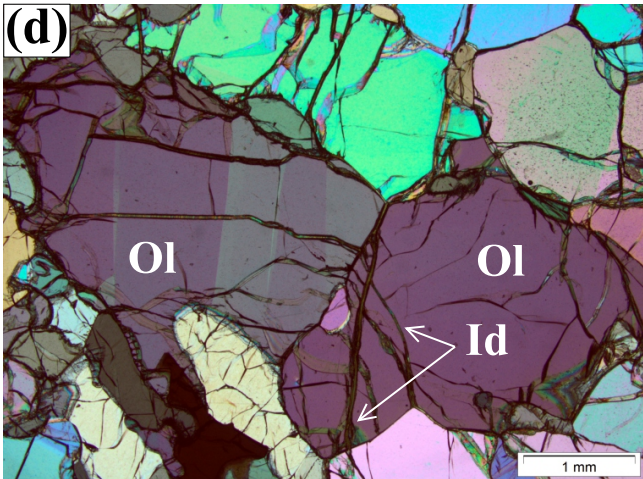
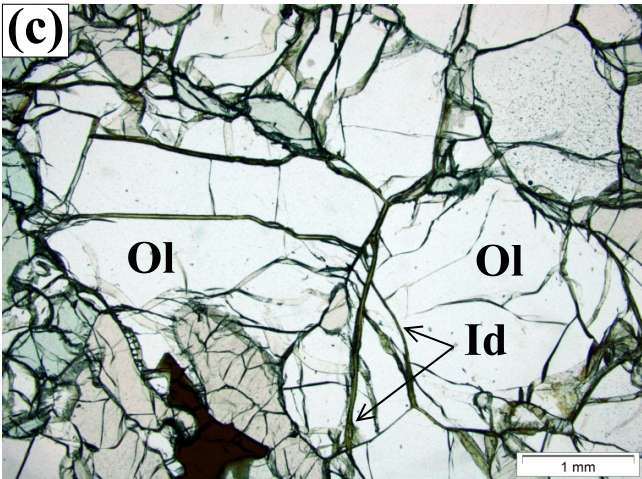
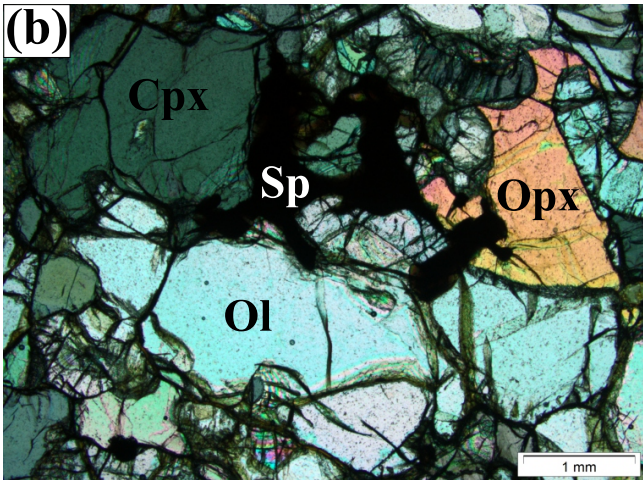
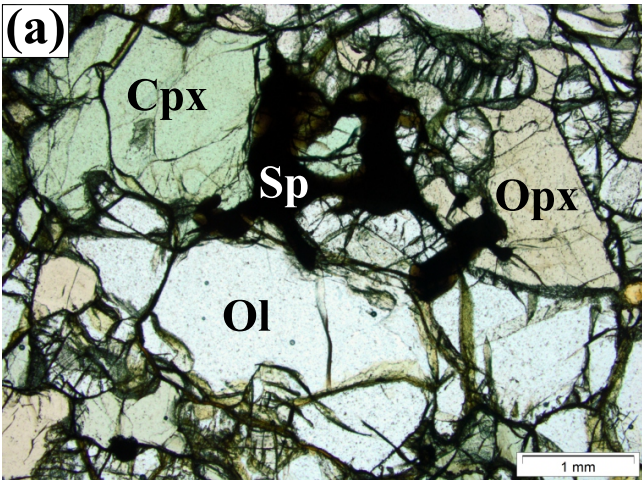


Figure 4

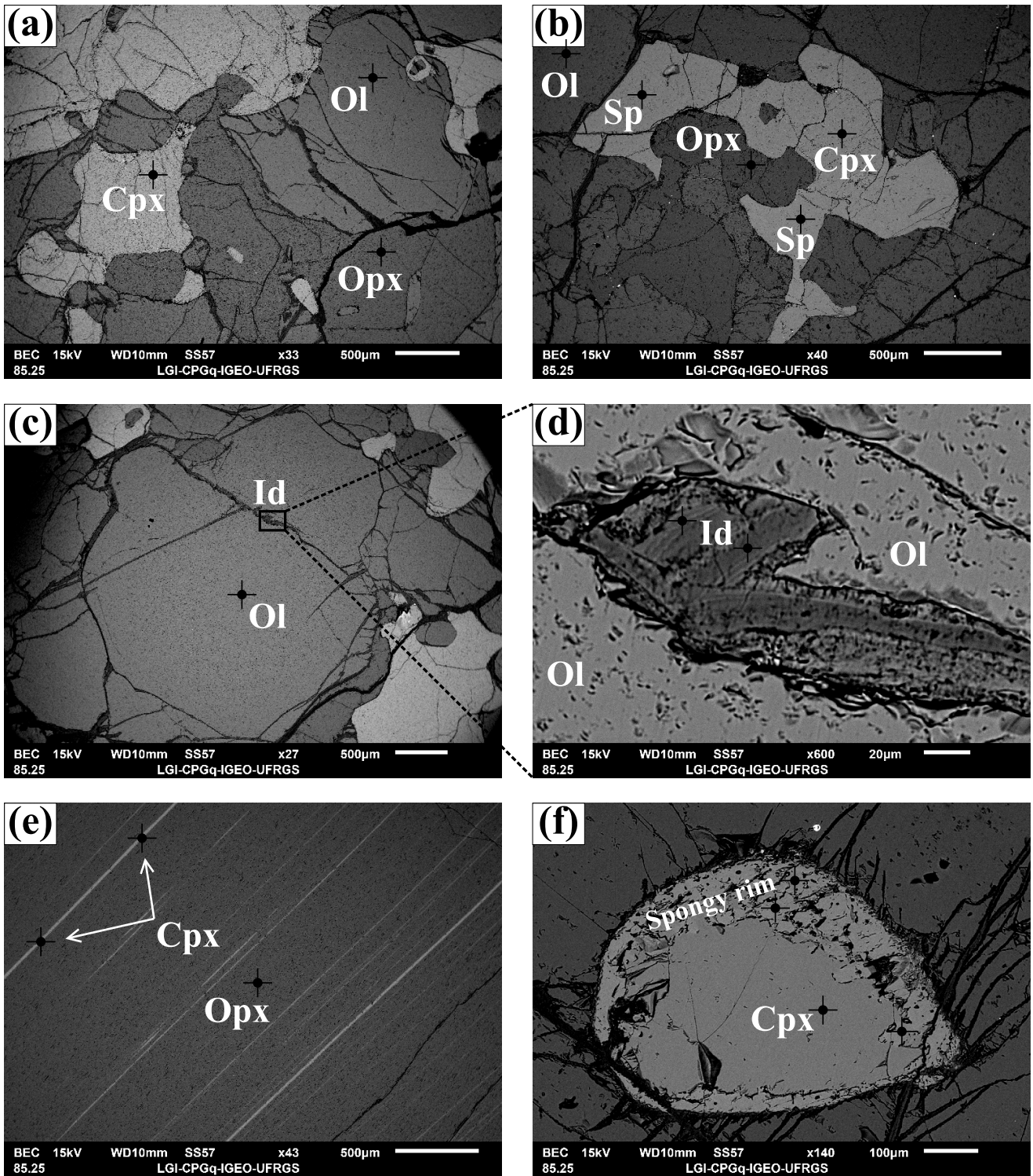


Figure 5

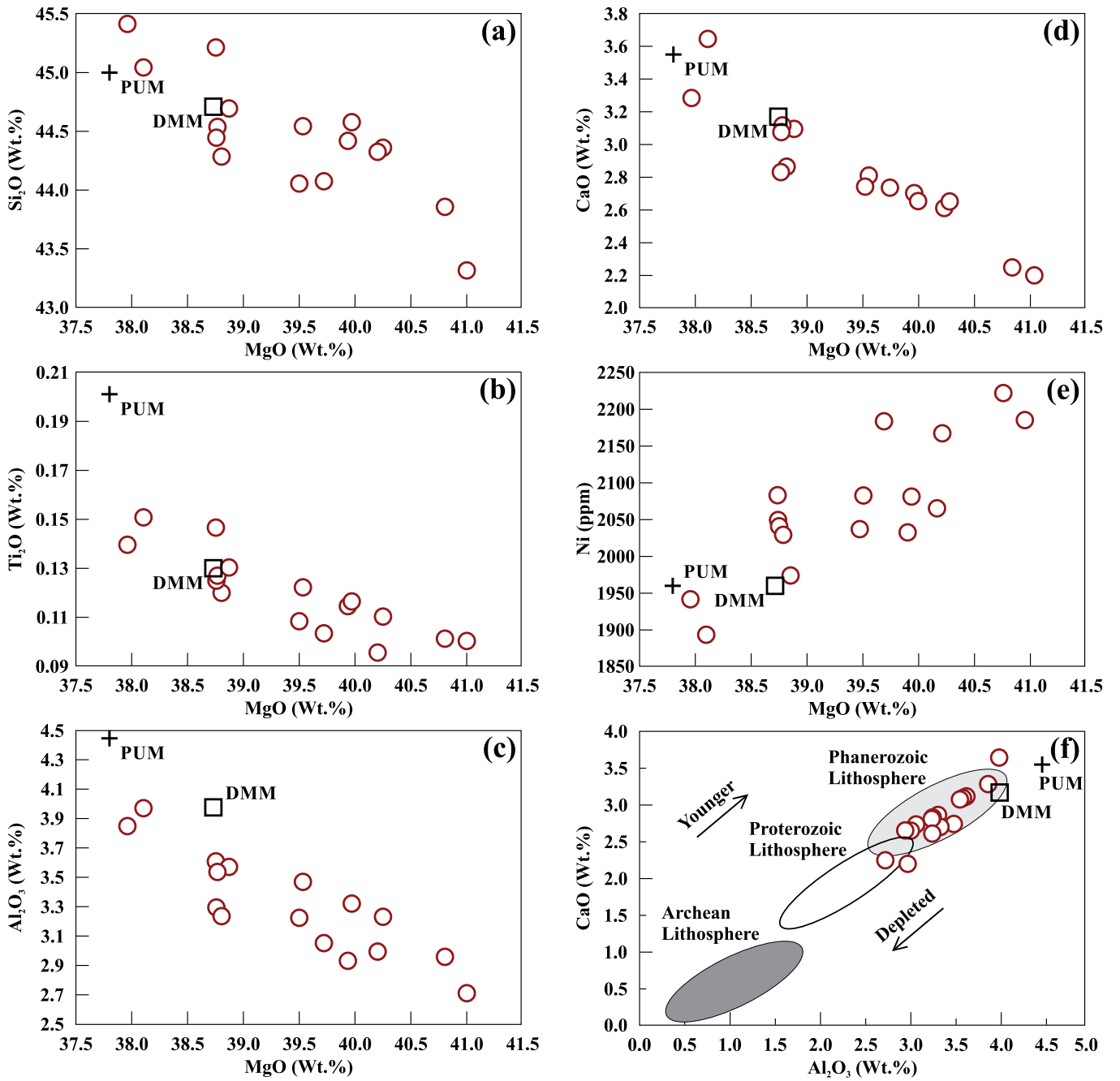


Figure 6

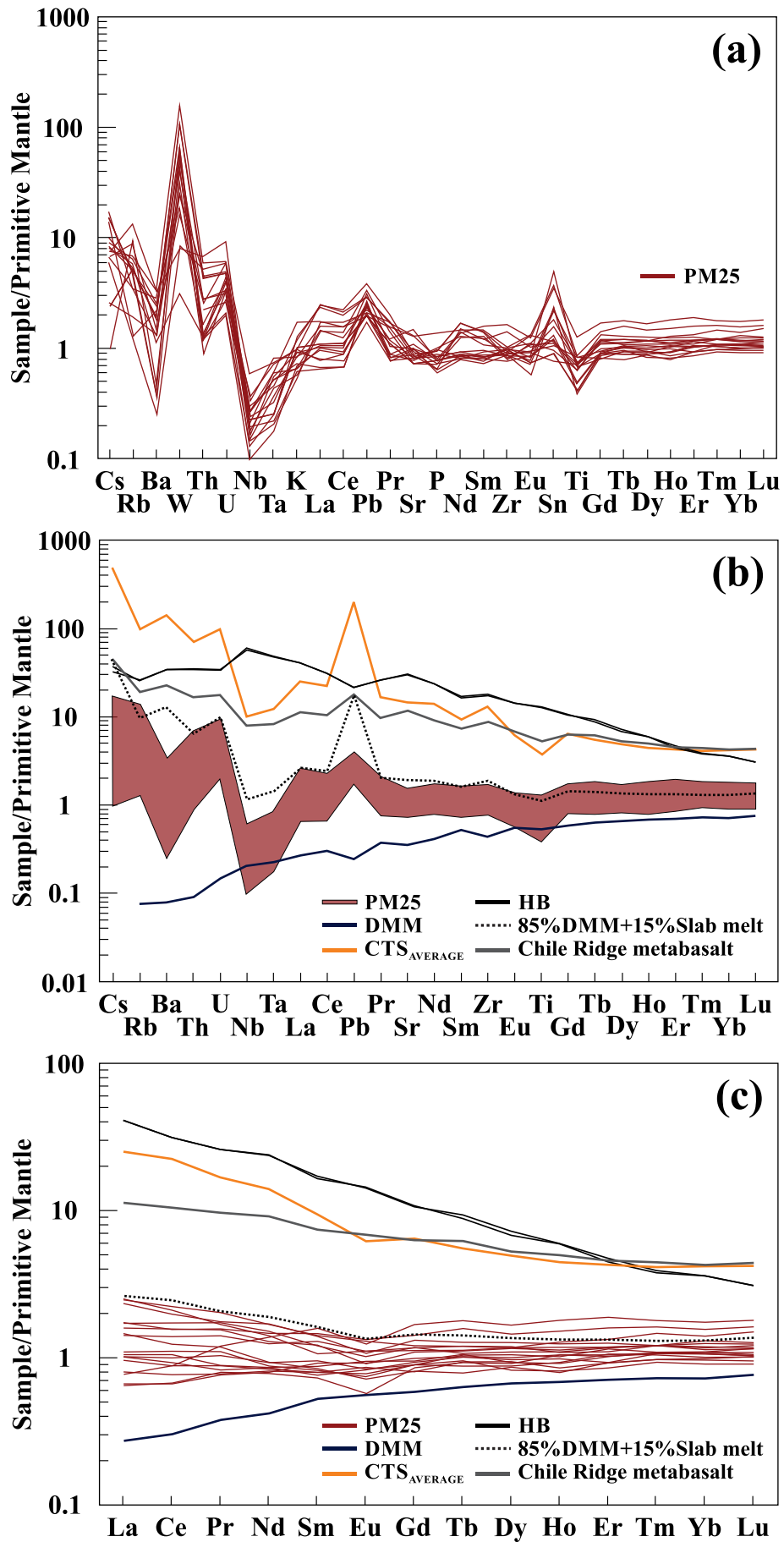


Figure 7

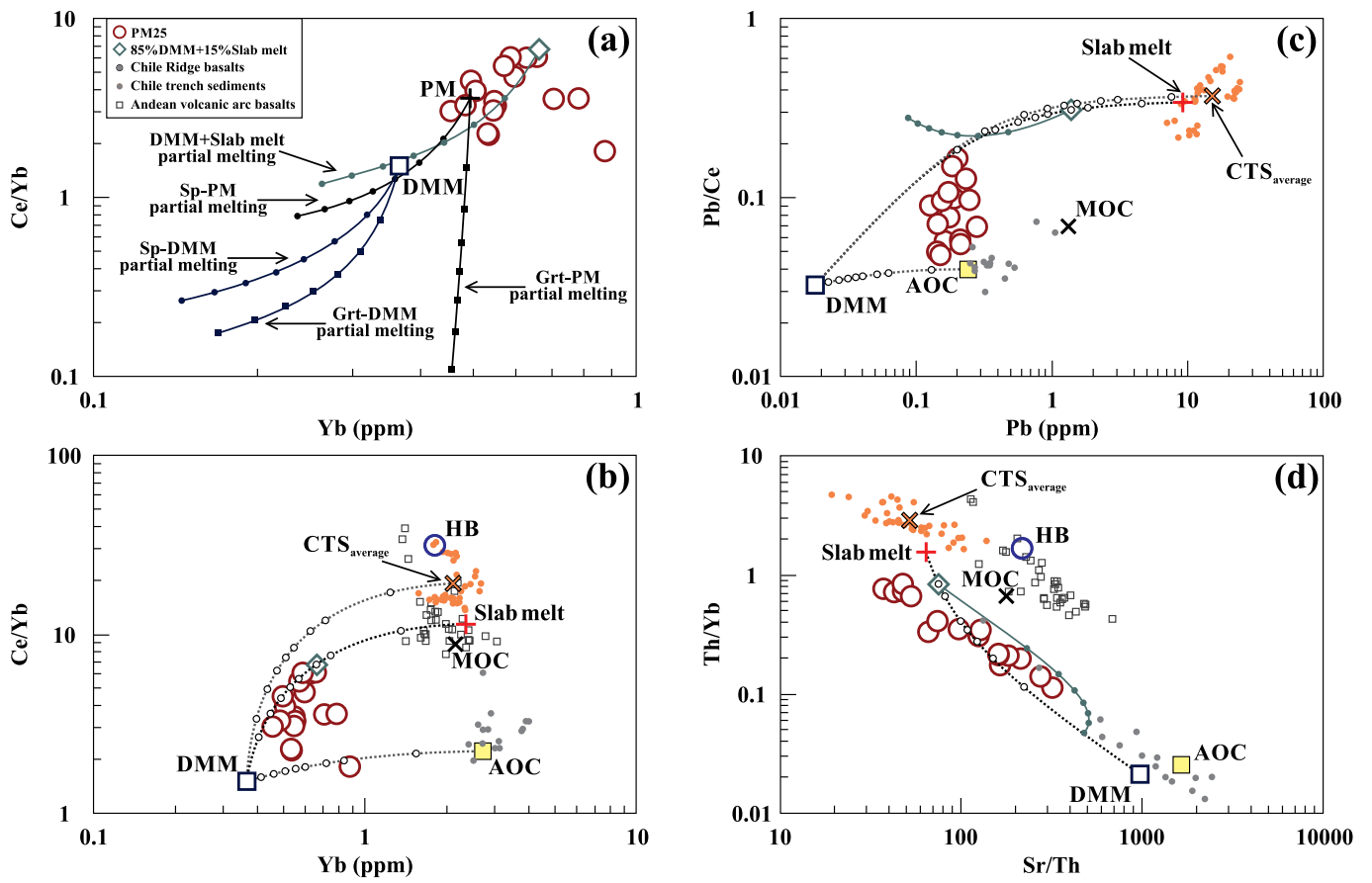


Figure 8

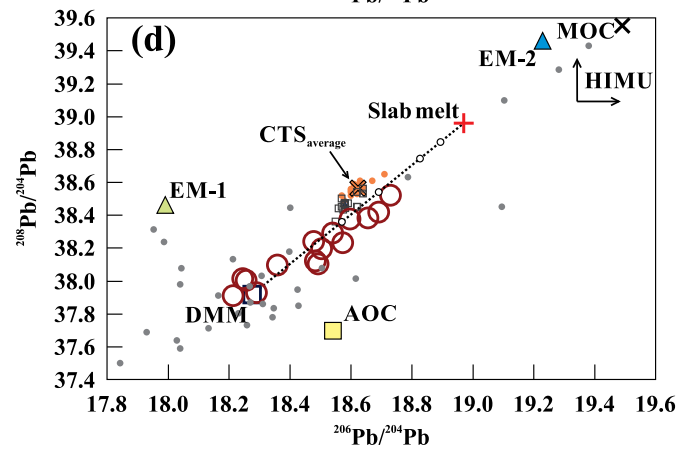
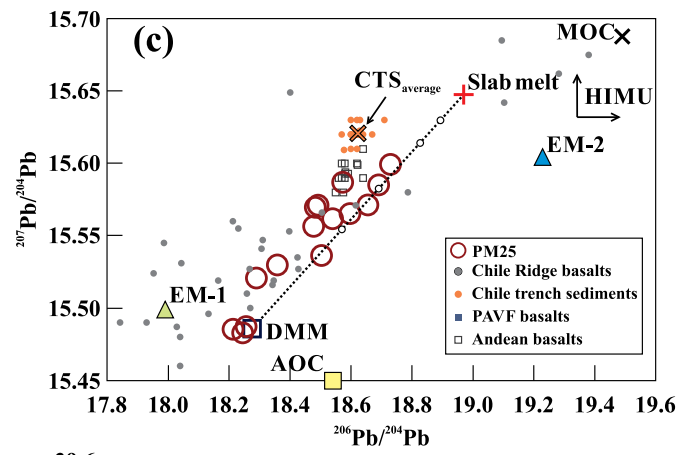
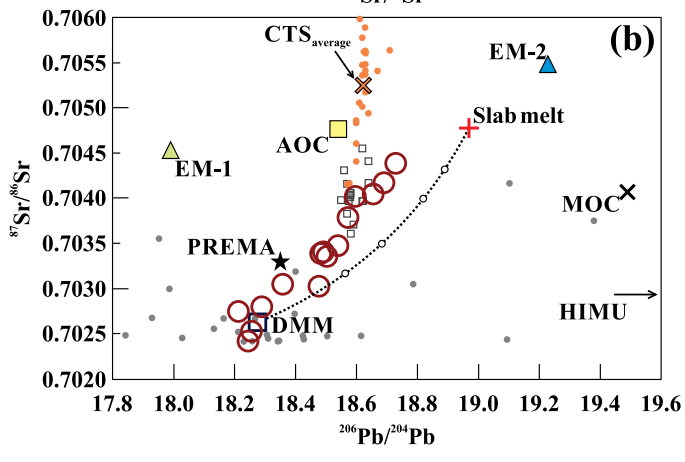
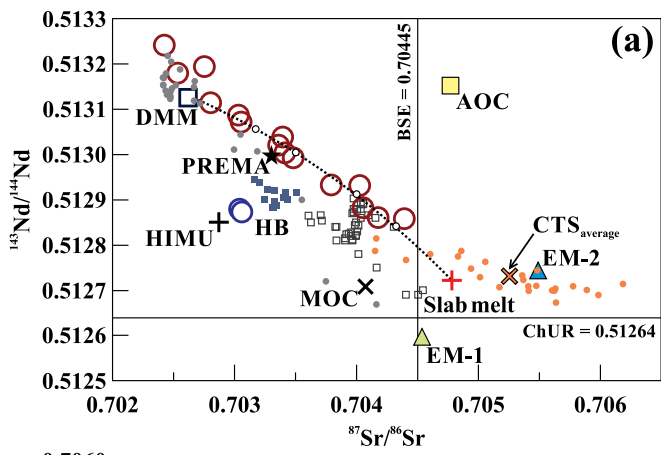


Table 1.

Sample:	PM25-5	PM25-9	PM25-12	PM25-15	PM25-17	PM25-18	PM25-21	PM25-22	PM25-25	PM25-26
<i>Major elements (wt.%)</i>										
SiO ₂	45.04	44.08	44.42	44.54	44.45	43.32	-	45.21	44.06	44.29
TiO ₂	0.15	0.10	0.12	0.15	0.12	0.10	-	0.13	0.12	0.13
Al ₂ O ₃	3.97	3.06	3.33	3.61	3.54	2.96	-	3.24	3.47	3.30
Fe ₂ O ₃	9.64	9.94	9.11	9.37	9.63	10.03	-	9.72	9.66	10.24
MnO	0.14	0.14	0.13	0.13	0.13	0.14	-	0.13	0.14	0.14
MgO	38.10	39.72	39.93	38.77	38.76	41.00	-	38.75	39.50	38.80
CaO	3.65	2.74	2.70	3.12	3.08	2.20	-	2.83	2.74	2.86
Na ₂ O	0.26	0.19	0.22	0.27	0.26	0.20	-	0.22	0.25	0.20
K ₂ O	0.02	0.02	0.02	0.02	0.01	0.03	-	0.02	0.03	0.03
P ₂ O ₅	0.02	0.02	0.02	0.02	0.02	0.02	-	0.02	0.02	0.02
Mg-number	88.67	88.78	89.66	89.12	88.85	89.00	-	88.76	89.00	88.24
LOI%	0.69	0.91	0.75	0.76	0.41	0.57	-	0.52	1.18	0.37
<i>Compatible elements (ppm)</i>										
V	88.52	64.34	65.55	73.94	75.02	62.23	77.97	68.83	69.47	71.24
Cr	3088.24	2830.32	2994.28	3002.14	2909.01	2538.11	2982.40	2907.71	2957.17	2773.40
Co	176.44	104.44	117.65	114.47	119.24	162.24	126.32	185.90	122.95	141.57
Ni	1893.40	2184.03	2032.74	2041.12	2049.59	2185.63	1985.53	2083.38	2037.14	2029.43
Cu	23.85	20.68	18.96	28.28	28.28	21.22	20.92	20.59	26.68	23.78
Zn	21.53	31.67	32.20	26.67	34.78	26.37	24.50	27.67	23.65	30.74
<i>Trace and rare earth elements (ppm)</i>										
Cs	0.07	0.14	0.02	0.12	0.05	0.06	0.06	0.12	0.07	0.80
Rb	3.29	2.23	1.25	3.09	5.76	8.75	4.40	3.24	4.11	3.46
Ba	2.79	20.12	9.23	2.47	10.53	23.77	23.01	16.66	17.94	12.49
W	1.48	0.40	1.12	0.71	0.98	3.57	0.16	1.49	0.54	0.35
Th	0.10	0.12	0.24	0.08	0.10	0.51	0.58	0.11	0.24	0.22
U	0.06	0.08	0.07	0.08	0.04	0.13	0.20	0.05	0.07	0.13
Nb	0.26	0.12	0.13	0.20	0.07	0.22	0.15	0.11	0.09	0.43
Ta	0.03	0.02	0.02	0.02	0.01	0.02	0.02	0.02	0.01	0.03
K	247.73	230.00	144.21	184.34	177.16	300.76	439.55	215.42	321.17	246.45
La	0.54	0.71	0.99	0.46	0.67	1.73	1.21	0.73	1.63	1.75
Ce	1.59	1.80	2.51	1.20	1.59	4.02	2.81	1.90	3.57	3.80
Pb	0.17	0.23	0.25	0.20	0.15	0.28	0.16	0.19	0.21	0.21
Pr	0.34	0.29	0.40	0.21	0.25	0.57	0.44	0.25	0.49	0.47
Sr	31.94	21.33	15.57	20.81	16.68	18.79	27.48	23.36	17.90	27.97
P	73.94	80.99	68.54	70.34	93.30	90.35	-	74.73	90.51	77.96
Nd	1.90	1.28	1.71	1.10	1.15	2.32	2.02	1.18	2.34	1.95
Sm	0.72	0.43	0.58	0.42	0.36	0.64	0.66	0.39	0.63	0.48
Zr	18.77	9.80	8.99	11.09	8.75	10.49	11.56	9.97	9.24	11.38
Hf	1.03	0.52	0.55	0.60	0.73	0.50	0.55	1.17	0.51	0.45
Eu	0.21	0.14	0.19	0.16	0.15	0.22	0.23	0.16	0.18	0.19
Sn	0.62	0.21	0.16	0.27	0.90	0.20	0.66	0.18	0.19	0.32
Ti	1671.81	629.63	847.86	965.38	895.63	959.87	1123.14	1091.30	889.13	977.96
Gd	1.02	0.54	0.68	0.60	0.49	0.73	0.86	0.58	0.80	0.71
Tb	0.20	0.11	0.12	0.11	0.10	0.13	0.17	0.12	0.14	0.13
Dy	1.25	0.79	0.88	0.75	0.70	0.88	1.09	0.70	0.95	0.89
Y	7.03	4.14	5.16	4.25	3.75	4.59	5.76	3.82	5.52	4.86
Ho	0.30	0.17	0.21	0.17	0.14	0.20	0.25	0.15	0.21	0.18
Er	0.92	0.56	0.65	0.51	0.45	0.58	0.78	0.50	0.61	0.54
Tm	0.13	0.08	0.11	0.08	0.07	0.09	0.12	0.08	0.09	0.09
Yb	0.87	0.55	0.70	0.53	0.48	0.65	0.78	0.55	0.59	0.63
Lu	0.14	0.09	0.11	0.08	0.07	0.10	0.12	0.08	0.09	0.09

Table 1. Continued

Sample:	PM25-27	PM25-28	PM25-30	PM25-31	PM25-34	PM25-35	PM25-38	PM25-A1	PM25-A3
<i>Major elements (wt.%)</i>									
SiO ₂	44.36	44.41	44.70	44.58	44.54	44.33	43.86	47.30	47.34
TiO ₂	0.11	0.14	0.12	0.11	0.11	0.10	0.10	2.80	2.85
Al ₂ O ₃	3.00	3.85	3.57	2.94	3.23	3.24	2.72	13.77	14.14
Fe ₂ O ₃	9.25	8.93	9.20	9.38	9.46	9.19	9.93	12.13	12.10
MnO	0.13	0.13	0.13	0.14	0.13	0.13	0.13	0.17	0.17
MgO	40.25	37.96	38.87	39.97	39.53	40.20	40.80	10.27	9.75
CaO	2.65	3.28	3.10	2.65	2.81	2.61	2.25	8.90	8.79
Na ₂ O	0.25	0.26	0.28	0.19	0.15	0.18	0.17	3.06	3.23
K ₂ O	0.02	0.01	0.02	0.02	0.02	0.02	0.03	1.07	1.09
P ₂ O ₅	0.01	0.02	0.02	0.02	0.01	0.01	0.02	0.53	0.55
Mg-number	89.60	89.38	89.32	89.40	89.22	89.65	89.05	62.64	61.46
LOI%	0.47	0.60	0.74	0.46	0.59	0.47	0.79	-	-
<i>Compatible elements (ppm)</i>									
V	61.76	82.45	82.60	67.83	65.49	64.67	64.95	234.11	236.48
Cr	3046.46	2990.17	3051.82	3013.49	2802.28	2779.19	2546.81	308.11	310.67
Co	126.92	110.55	173.27	129.51	135.37	94.49	101.64	48.98	47.85
Ni	2167.62	1941.71	1974.10	2081.52	2083.02	2065.54	2222.45	228.26	207.69
Cu	20.38	31.86	27.61	19.16	25.06	20.50	24.08	-	-
Zn	27.15	20.86	28.72	28.73	20.12	28.06	25.75	127.08	122.40
<i>Trace and rare earth elements (ppm)</i>									
Cs	0.02	0.06	0.11	0.01	0.05	0.05	0.02	0.26	0.30
Rb	6.73	3.74	0.83	6.48	2.28	0.85	3.41	16.89	16.46
Ba	3.49	8.05	15.55	3.36	9.24	1.78	13.54	246.61	242.22
W	-	0.06	1.29	0.92	0.53	0.17	2.38	-	-
Th	0.19	0.11	0.11	0.14	0.38	0.45	0.37	3.02	2.98
U	0.06	0.09	0.10	0.09	0.10	0.13	0.10	0.74	0.72
Nb	0.19	0.24	0.19	0.17	0.11	0.14	0.16	41.72	44.12
Ta	0.02	0.03	0.02	0.01	0.01	0.01	0.01	2.01	2.06
K	164.23	210.18	167.10	236.52	135.13	156.09	257.45	8908.26	9068.09
La	0.71	1.11	1.02	0.56	1.20	0.45	0.77	28.60	28.62
Ce	1.67	2.83	2.23	1.39	3.11	1.22	2.00	56.57	56.49
Pb	0.15	0.14	0.17	0.13	0.15	0.18	0.14	1.55	1.56
Pr	0.23	0.43	0.33	0.22	0.49	0.22	0.31	7.29	7.29
Sr	18.69	17.25	17.46	17.57	20.12	21.41	15.56	654.87	644.07
P	61.47	96.25	81.34	85.32	62.74	57.73	75.08	2330.19	2418.67
Nd	1.18	1.77	1.28	1.12	2.08	1.08	1.21	32.62	32.91
Sm	0.34	0.55	0.38	0.36	0.54	0.33	0.37	7.72	7.44
Zr	11.39	10.25	9.91	10.63	16.09	9.93	11.01	205.45	198.74
Hf	1.39	0.61	0.34	1.17	0.39	0.44	1.36	4.49	4.40
Eu	0.14	0.16	0.12	0.13	0.17	0.10	0.13	2.43	2.46
Sn	0.23	0.13	0.39	0.40	0.21	0.42	0.15	-	-
Ti	648.78	938.71	1089.34	887.31	833.91	508.28	544.90	16766.08	17057.70
Gd	0.56	0.66	0.49	0.54	0.71	0.52	0.54	6.42	6.53
Tb	0.11	0.12	0.09	0.10	0.12	0.10	0.10	1.03	0.97
Dy	0.73	0.87	0.65	0.62	0.82	0.68	0.66	5.42	5.09
Y	3.94	4.61	3.55	3.44	4.74	4.71	3.59	26.38	25.00
Ho	0.16	0.19	0.13	0.14	0.18	0.17	0.16	0.99	0.99
Er	0.45	0.58	0.45	0.42	0.57	0.50	0.52	2.31	2.19
Tm	0.08	0.09	0.07	0.07	0.09	0.08	0.08	0.29	0.28
Yb	0.54	0.60	0.49	0.45	0.57	0.53	0.50	1.80	1.80
Lu	0.08	0.09	0.08	0.07	0.09	0.08	0.08	0.23	0.23

Table 2.

Sample	K (wt%)	^{40}Ar rad ($10^{-8}\text{cm}^3\text{STP/g}$)	$^{38}\text{Ar}/^{36}\text{Ar}$	Age (Ma)	Air Fraction (%)
PM25-A1	0.92 ± 0.02	193.84 ± 9.71	0.1893 ± 0.0010	53.7 ± 2.9	43.0
PM25-A3	0.84 ± 0.02	176.82 ± 8.86	0.1895 ± 0.0007	53.6 ± 2.9	41.7

For calculation of ^{40}Ar rad, ($^{40}\text{Ar}/^{36}\text{Ar}$) initial = 296.0 is assumed. Error: 1σ .

Table 3.

Sample	Rb	Sr	⁸⁷ Sr/ ⁸⁶ Sr	Sm	Nd	¹⁴³ Nd/ ¹⁴⁴ Nd	εNd	²⁰⁶ Pb/ ²⁰⁴ Pb	²⁰⁷ Pb/ ²⁰⁴ Pb	²⁰⁸ Pb/ ²⁰⁴ Pb
PM25-5	0.38	15.63	0.702531(13)	3.69	17.64	0.513181(14)	+10.6	18.255(08)	15.487(07)	38.007(16)
PM25-9	0.91	12.74	0.703052(11)	2.63	17.06	0.513073(17)	+8.5	18.358(16)	15.530(14)	38.100(34)
PM25-12	0.18	10.25	0.703410(07)	2.51	10.66	0.513005(16)	+7.1	18.491(4)	15.571(04)	38.107(09)
PM25-15	0.29	14.37	0.702750(06)	2.96	13.54	0.513195(06)	+10.9	18.212(4)	15.486(04)	37.914(09)
PM25-17	0.17	11.14	0.703359(13)	3.29	17.08	0.513022(15)	+7.5	18.503(15)	15.537(12)	38.199(31)
PM25-21	0.36	11.27	0.703392(12)	3.14	14.22	0.513040(12)	+7.8	18.482(04)	15.570(04)	38.125(08)
PM25-22	0.83	12.88	0.702802(12)	8.37	15.52	0.513155(11)	+9.3	18.289(15)	15.521(13)	37.932(30)
PM25-25	0.13	6.81	0.704050(14)	7.49	15.03	0.512883(07)	+4.8	18.655(19)	15.572(16)	38.386(39)
PM25-26	0.29	14.37	0.704024(09)	3.33	30.46	0.512932(13)	+5.7	18.596(03)	15.566(02)	38.380(05)
PM25-27	0.33	9.82	0.703030(04)	3.23	15.82	0.513088(14)	+8.8	18.477(06)	15.557(05)	38.243(12)
PM25-28	0.49	13.41	0.704175(09)	4.19	22.90	0.512862(09)	+4.4	18.690(09)	15.585(08)	38.422(19)
PM25-30	0.48	16.65	0.704390(10)	2.81	15.59	0.512859(12)	+4.3	18.729(06)	15.600(05)	38.524(12)
PM25-31	0.07	11.14	0.703479(10)	3.34	24.94	0.512994(06)	+6.9	18.539(07)	15.562(06)	38.294(15)
PM25-34	0.09	6.66	0.703791(04)	2.58	11.97	0.512934(16)	+5.8	18.572(04)	15.587(03)	38.236(08)
PM25-35	0.23	11.62	0.702422(12)	2.40	9.46	0.513242(12)	+11.8	18.244(05)	15.483(04)	38.017(11)
PM25-A1 ^a	16.89	654.87	0.703112(15)	7.72	32.62	0.512925(06)	-	-	-	-
PM25-A1 ^b	-	-	0.703058(15)	-	-	0.512874(06)	+5.6	-	-	-
PM25-A3 ^a	16.46	644.07	0.703094(09)	7.44	32.91	0.512929(07)	-	-	-	-
PM25-A3 ^b	-	-	0.703039(09)	-	-	0.512880(07)	+5.7	-	-	-

For host basalts, initial Sr and Nd isotope compositions were calculated using the respective K-Ar ages of each sample (see Table 2). Parent/daughter isotope ratios were recalculated using Rb, Sr, Sm and Nd concentrations from Table 1.

^a Measured isotopic ratios.

^b Age corrected isotopic ratios (initial ratios).

Table 4.

Lithology: Lherzolite

Samples: PM25-5 PM25-9 PM25-12 PM25-15 PM25-17 PM25-18 PM25-21 PM25-22 PM25-25

Modal composition (Vol.%)

% Ol	47.2	62.6	48.5	55.2	56.8	56.5	62.1	56.3	57.6
% Opx	29.6	23.3	33.2	24.0	25.0	23.3	16.2	25.9	26.0
% Cpx	19.9	10.1	15.6	17.2	15.7	15.8	19.1	15.7	12.9
% Sp	3.3	4.0	2.8	3.6	2.4	4.4	2.6	2.1	3.5

Lithology: Lherzolite

Samples: PM25-26 PM25-27 PM25-28 PM25-30 PM25-31 PM25-34 PM25-35 PM25-38

Modal composition (Vol.%)

% Ol	58.0	61.8	41.7	62.3	59.0	56.2	52.1	61.5
% Opx	25.2	17.8	38.7	21.7	21.9	26.1	29.4	21.1
% Cpx	15.1	16.3	16.9	12.4	15.7	14.7	14.7	13.5
% Sp	1.6	4.2	2.7	3.6	3.5	3.0	3.8	3.9

Table 5.

Sample:	PM25-9	PM25-5	PM25-9	PM25-5	PM25-9	PM25-5
Mineral phase:	Ol	Opx	Cpx	Sp	Id	Cpx reaction
SiO ₂	40.02	53.94	50.70	-	49.20	51.92
Al ₂ O ₃	-	5.67	7.48	58.61	-	4.09
FeO	10.84	6.35	3.01	11.16	17.11	3.68
MgO	49.14	33.28	15.78	22.14	33.69	18.24
CaO	-	0.76	20.17	-	-	21.17
Na ₂ O	-	-	2.11	-	-	0.90
Cr ₂ O ₃	-	-	0.74	8.09	-	-
Mg-number	89.97	91.21	91.21	79.70	79.58	90.75

ARTIGO 3

NOBLE GAS COMPOSITION OF SUBCONTINENTAL LITHOSPHERIC MANTLE: AN EXTENSIVELY DEGASSED EARTH RESERVOIR OF SOUTHERN HEMISPHERE

Assunto Submission Confirmation
Remetente Earth and Planetary Science Letters
<eps1@elsevier.com>
Para <tiago.jalowitzki@ufrgs.br>
Data 2015-12-01 00:03



Dear Mr. Jalowitzki,

Your submission entitled "Noble gas composition of subcontinental lithospheric mantle: an extensively degassed Earth reservoir of Southern Hemisphere" has been received by Earth and Planetary Science Letters. The article type you selected is: Letters.

You may check on the progress of your paper by logging on to the Elsevier Editorial System as an author. The URL is <http://ees.elsevier.com/eps1/>.

Your manuscript will be given a reference number once an Editor has been assigned.

Thank you for submitting your work to this journal.

Kind regards,
Editorial Office
Earth and Planetary Science Letters

1 **Noble gas composition of subcontinental lithospheric mantle:**
2 **an extensively degassed Earth reservoir of Southern**
3 **Hemisphere**

4

5 Tiago Jalowitzki ^{a,b*}, Hirochika Sumino ^{b†}, Rommulo V. Conceição ^a, Yuji Orihashi ^c,
6 Keisuke Nagao ^{b*}, Gustavo W. Bertotto ^d, Eduardo Balbinot ^e, Manuel Schilling ^f,
7 Fernanda Gervasoni ^g

8

9 ^a Programa de Pós-graduação em Geociências, Universidade Federal do Rio Grande do
10 Sul (UFRGS). Av. Bento Gonçalves, 9500 – Prédio 43129, Porto Alegre – RS, Brazil.

11 E-mail: tiago.jalowitzki@ufrgs.br; rommulo.conceicao@ufrgs.br

12 ^b Geochemical Research Center, Graduate School of Science, the University of Tokyo,
13 7-3-1 Hongo, Bunkyo-ku, Tokyo 113-0033, Japan.

14 ^c Earthquake Research Institute, the University of Tokyo, 1-1-1 Yayoi, Bunkyo-Ku,
15 Tokyo 113-0032, Japan. E-mail: oripachi@eri.u-tokyo.ac.jp

16 ^d CONICET – Universidad Nacional de La Pampa. Uruguay 151 (6300), Santa Rosa, La
17 Pampa, Argentina. E-mail: gwbertotto@yahoo.com.ar

18 ^e Department of Physics, University of Surrey, Guildford GU2 7XH, UK. E-mail:
19 e.balbinot@surrey.ac.uk

20 ^f Instituto de Ciencias de la Tierra, Facultad de Ciencias, Universidad Austral de Chile,
21 Valdivia, Código postal 5090000, Región de Los Ríos, Chile. E-mail:

22 manuel.schilling@uach.cl

23 ^g Institut für Mineralogie, Westfälische–Wilhelms–Universität Münster, Germany. E-
24 mail: gervasoni.fe@uni-muenster.de

25 † Present address: Department of Basic Science, Graduate School of Arts and Sciences,
26 the University of Tokyo, 3-8-1 Komaba, Meguro-ku, Tokyo 153-8902, Japan. E-mail:
27 sumino@igcl.c.u-tokyo.ac.jp

28 * Present address: Division of Polar Earth-System Sciences, KOPRI (Korea Polar
29 Research Institute), 26 Songdomirae-ro, Yeonsu-gu, Incheon 406-840, Korea. E-mail:
30 nagao@kopri.re.kr

31

32 ***Corresponding author:** Programa de Pós-graduação em Geociências, Instituto de
33 Geociências, Universidade Federal do Rio Grande do Sul (UFRGS). Av. Bento
34 Gonçalves, 9500 – Prédio 43129, Bairro Agronomia, Porto Alegre – RS, Brazil. CEP:
35 91501970. Telephone number: +55(51)3308-7140.

36 **E-mail address:** tiago.jalowitzki@ufrgs.br (T. Jalowitzki).

37

38 **Abstract**

39 Southern Andean Patagonia is one of the few sites where interactions between oceanic
40 and continental lithosphere due to the subduction of an active spreading ridge beneath
41 continent can be investigated. In order to characterize the noble gas composition of
42 Patagonian subcontinental lithospheric mantle (SCLM) we present the first noble gas
43 and new lithophile (Sr–Nd–Pb) isotopic data for mantle xenoliths from Pali–Aike
44 Volcanic Field and Gobernador Gregores. Based on noble gas isotopic compositions
45 determined by stepwise crushing method, Patagonian SCLM reflects a mixing between
46 air and two mantle components: a strongly radiogenic/nucleogenic SCLM and a
47 MORB–like endmembers.
48 Pali–Aike mantle xenoliths represent the degassed local SCLM with higher
49 $(U+Th+K)/(^3He, ^{22}Ne, ^{36}Ar)$ ratios than MORB source, varying over the range of

50 $^3\text{He}/^4\text{He}_{\text{AVERAGE}} = 6.87 \pm 0.04R_A$ and $^{21}\text{Ne}/^{22}\text{Ne}_{(\text{E})}$ between 0.085 and 0.092. The
51 $^{40}\text{Ar}/^{36}\text{Ar}$ ratios vary from the near-atmospheric ratio (510) up to 16400, with
52 $^{40}\text{Ar}/^{36}\text{Ar}_{(\text{E})}$ ranging between 31100^{+9400}_{-6800} and 54000^{+14200}_{-9600} . In addition, $^3\text{He}/^{22}\text{Ne}$
53 ratios for the local SCLM endmember are higher (between 12.03 ± 0.15 and $13.66 \pm$
54 0.37) than depleted MORBs ($^3\text{He}/^{22}\text{Ne} = 8.31\text{--}9.75$). Noble gas component observed in
55 Gobernador Gregores mantle xenoliths is characterized by isotopic compositions over
56 the range of MORBs in terms of helium ($^3\text{He}/^4\text{He}_{\text{AVERAGE}} = 7.24 \pm 0.09R_A$), but with
57 slightly nucleogenic neon ($^{21}\text{Ne}/^{22}\text{Ne}_{(\text{E})}$ between 0.065 and 0.079). The $^{40}\text{Ar}/^{36}\text{Ar}$ ratios
58 vary from the near-atmospheric ratio (380) up to 6560, with $^{40}\text{Ar}/^{36}\text{Ar}_{(\text{E})}$ ranging
59 between 8100^{+1400}_{-700} and 17700^{+4400}_{-3100} . The low $^{40}\text{Ar}/^{36}\text{Ar}$ ratios (usually < 4000)
60 attest that these rocks were significantly affected by atmospheric contamination
61 associated with recycled oceanic lithosphere in the Patagonian SCLM.
62 Finally, Xe isotopic measurements of some samples from both localities show
63 $^{129}\text{Xe}/^{132}\text{Xe}_{(\text{E})} = 1.0833^{+0.0216}_{-0.0053}$ and $^{136}\text{Xe}/^{132}\text{Xe}_{(\text{E})} = 0.3761^{+0.0246}_{-0.0034}$ values, as well
64 as a well-defined trend of $^{129}\text{--}^{136}\text{Xe}/^{132}\text{Xe}$ ratios. These results allow us to define a
65 SCLM indistinguishable from the MORB source.
66 Based on these new data, we conclude that the highly radiogenic/nucleogenic signature
67 of Pali-Aike mantle xenoliths represents an intrinsic feature of the SCLM reservoir
68 beneath southern Patagonia. This signature could have been homogenized during the
69 last 14 Ma, after rapid passage and northward migration of the Chile Triple Junction and
70 its slab window at this latitude. On the other hand, the less radiogenic/nucleogenic
71 MORB-like component identified in Gobernador Gregores mantle xenoliths could be
72 explained by recent metasomatism of the SCLM due to the asthenospheric mantle
73 upwelling in response to the opening of a slab window beneath Patagonia because of
74 South Chile Ridge subduction.

75

76 **Keywords:** noble gas isotopes, subcontinental lithospheric mantle, radiogenic isotopes,
77 mantle xenoliths, southern Patagonia.

78

79 **1. Introduction**

80

81 Ultramafic mantle–derived xenoliths from wedges overlying subduction zones
82 associated with ridge subduction and slab window formation are very rare. Patagonia,
83 the southernmost portion of South America, is one of the few sites where active
84 subduction of a spreading ridge and its consequences for ridge axis magmatism can be
85 investigated in the Earth. Since middle Miocene, Chile active spreading ridge subducts
86 beneath South America, resulting in a slab-free zone, or slab window, and provides gaps
87 through which asthenospheric mantle can flow. Thus, the collision of Chile Ridge
88 against the Chile trench offers an opportunity to investigate the composition of
89 subcontinental lithospheric mantle (SCLM), represented by the occurrence of mantle
90 xenoliths in this particular geological setting, and the influence of the shallow
91 asthenospheric mantle beneath the Andean continental back–arc region.

92 Abundant occurrence of spinel– and/or garnet–bearing mantle xenoliths hosted
93 by intra–plate alkaline basalts found in Pali–Aike Volcanic Field (PAVF in Fig. 1) and
94 Gobernador Gregores (GG in Fig. 1) provides invaluable information about the nature
95 and processes involved in the evolution of the southern Patagonian SCLM.

96 Subcontinental mantle xenoliths often have low amounts of noble gas trapped in their
97 fluid inclusions (e.g., *Gautheron et al., 2005*), however, they are powerful tracers of
98 mantle sources. Although the noble gas isotopic ratios of mid–ocean–ridge basalts
99 (MORBs) and ocean island basalts (OIBs) are relatively well defined (e.g., *Sarda et al.,*

100 1988; Hiyagon *et al.*, 1992; Burnard *et al.*, 1997; Moreira *et al.*, 1998; Trieloff *et al.*,
101 2000; Mukhopadhyay, 2012), the composition of SCLM source remains poorly known.
102 This limitation is enhanced by the significant contribution of air-like component in
103 noble gas composition of mantle-derived xenoliths. It complicates the characterization
104 of SCLM endmember because these rocks, generally, display a binary mixture between
105 SCLM and an atmospheric component (e.g., Buikin *et al.*, 2005; Gautheron *et al.*, 2005;
106 Hopp *et al.*, 2004; Poreda and Farley, 1992).

107 In order to determine the noble gas composition of Patagonian SCLM at the
108 latitude of Austral Volcanic Zone (AVZ; 49°S – 55°S), we present the first He–Ne–Ar,
109 Kr and Xe isotopic ratios plus new lithophile isotopes (Sr–Nd–Pb) in whole-rocks and
110 minerals separate from anhydrous and hydrous peridotites.

111

112 **Figure 1**

113

114 **2. Geological setting**

115

116 Geodynamically, the Patagonian continental back-arc represents a complex
117 region formed by several continental accretion events related to the subduction of
118 different oceanic plates (e.g., Pankhurst *et al.*, 2006), some of them containing seismic
119 and aseismic ridges (e.g., Chile Ridge and Juan Fernandez Ridge).

120 At present, the Patagonian western margin is characterized by the continuous
121 subduction of Nazca and Antarctic oceanic plates beneath the South American
122 continental plate, resulting in the formation of the Andean volcanic arc. The southern
123 part of this arc has been divided into Southern Volcanic Zone (SVZ, 33°S – 46°S) and
124 Austral Volcanic Zone (AVZ, 49°S – 55°S), that are separated by a volcanic gap. The

125 interruption of the volcanism has been attributed to the subduction of the South Chile
126 Ridge (SCR), which divides Nazca and Antarctic plates.

127 Approximately 16 Ma ago the active oceanic ridge spreading center (South Chile
128 Ridge – SCR) collided with the Chile trench at the latitude of Tierra del Fuego (55°S),
129 and formed a ridge–trench–trench triple junction (Chile Triple Junction – CTJ; [Cande
130 and Leslie, 1986](#)). The triple point has since migrated northwards to its present position
131 (46.5°S, north of the Taitao Peninsula). The subduction of four oblique active ridge
132 segments that entered the trench at 12 Ma (SCR–2), 6 Ma (SCR–1), 3 Ma (SCR0), and
133 0.3 Ma (SCR1) has resulted in the formation of a series of slab windows beneath the
134 South American plate (e.g., [Cande and Leslie, 1986](#)). The subduction of these segments
135 are associated with the asthenospheric mantle upwelling and with the extensive eruption
136 of plateau lavas from late Miocene to the recent times (e.g., [Gorring *et al.*, 1997](#);
137 [D’Orazio *et al.*, 2000](#)).

138 During the Cenozoic, mantle xenoliths hosted by alkaline basalts were widely
139 distributed in the Andean back–arc, southern Patagonia, at the latitude of AVZ (49°S –
140 52°S) (e.g., [Stern *et al.*, 1999](#); [Gorring and Kay, 2000](#); [Laurora *et al.*, 2001](#); [Rivalenti *et*
141 *al.*, 2004](#); [Gervasoni *et al.*, 2012](#)). The studied ultramafic xenoliths were sampled from
142 Gobernador Gregores (GG; PM23) volcanic center and from Pali–Aike Volcanic Field
143 (PAVF; PM14 and PM18) ([Fig. 1](#)).

144 Gobernador Gregores is located ~400 km east from Chile trench, in the
145 southwestern border of the Deseado Massif, and lies within the Meseta Central. The
146 xenoliths were brought to the surface by Plio–Pleistocene alkaline basalts and hawaiites
147 that composed a post–plateau sequence (ca. 3.5 Ma; [Gorring *et al.*, 1997](#)). The samples
148 studied here are spinel–bearing ultramafic xenoliths with anhydrous or hydrous
149 (amphibole ± phlogopite ± apatite) assemblages that locally contain glass, similar to

150 those found in previous works (Gorring and Kay, 2000; Laurora *et al.*, 2001; Rivalenti
151 *et al.*, 2004). Based on the whole-rock geochemistry of xenoliths, Gorring and Kay
152 (2000) suggested carbonatite metasomatism to the SCLM of GG. On the other hand,
153 based on trace element mineral compositions, Laurora *et al.* (2001) and Rivalenti *et al.*
154 (2004) concluded that this carbonatite metasomatism is unlikely at GG, and they
155 identified a hydrous Si-rich fluid/melt (carrying K₂O and P₂O₅) derived from the
156 subducted slab as the contaminant phase. Thermobarometric estimates of GG mantle
157 xenoliths indicate that the lithosphere has depths from 46 up to 70 km (P = 1.4–2.1
158 GPa) and a range of temperature of 870–1185°C (Gorring and Kay, 2000; Laurora *et*
159 *al.*, 2001; Rivalenti *et al.*, 2004), with higher temperatures for hydrous samples.

160 Two different localities of PAVF (4500 km², D’Orazio *et al.*, 2000) are
161 considered in this study: 1) Laguna Ana (PM14); and 2) Laguna Timone (PM18).
162 PAVF represents the southernmost Patagonian plateau basalts in the Andean back-arc,
163 being ~400 km distant south from GG and east from the modern Chile trench (Fig. 1).
164 PAVF is composed by more than 450 monogenetic volcanic centers (tuff-rings, maars,
165 spatter and scoria cones), mainly classified as alkaline basalts and basanites, with minor
166 olivine basalts (e.g., D’Orazio *et al.*, 2000). The mantle xenoliths hosted by Pali-Aike
167 post-plateau alkaline basalts (3.78–0.17 Ma; e.g., D’Orazio *et al.*, 2000 and references
168 therein; Jalowitzki *et al.*, unpublished data) comprise spinel, spinel-garnet, and garnet
169 harzburgites and lherzolites with hydrous phases (e.g., pargasitic amphibole and Ti-
170 phlogopite) (e.g., Stern *et al.*, 1999). These K-bearing minerals may occur as
171 glimmeritic veins (Gervasoni *et al.*, 2012). The PAVF SCLM is mineralogically and
172 chemically similar to the global asthenospheric source of MORB at the transition zone
173 from lithosphere to asthenosphere, which currently occurs at <100 km (Stern *et al.*,
174 1999). Based on the enrichment of chalcophile elements (W, Pb, Mo, Sn), Gervasoni *et*

175 *al.* (2012) suggested cryptic metasomatism to the PAVF SCLM, which probably is
176 related to the current subduction of Antarctic plate under the South–American plate.
177 These authors proposed that the occurrence of glimmerite, as well as K–rich minerals
178 (phlogopite and pargasite) in mantle xenoliths samples indicate modal metasomatism by
179 asthenospheric fluids. The estimated pressure and temperature are between 1.9 a 2.4GPa
180 and 970–1160°C (Stern *et al.*, 1999), indicating depths of 63 up to 80 km to the SCLM
181 beneath PAVF.

182

183 **3. Analytical techniques**

184

185 **3.1. Noble gas isotopes**

186

187 Fifteen whole–rock spinel peridotite samples from GG were selected for noble
188 gas measurements. Noble gas were extracted from all samples by heating method and 5
189 samples among them that contain larger amounts of noble gases were selected to the
190 analysis by crushing, including 2 samples of olivine separates (Supplementary Table S1
191 and Supplementary Table S2). It is important to emphasize that due to the different
192 number of crushing strokes that was applied for each sample, we have carried out 30
193 measurements by the crushing method (Supplementary Table S1). In the case of PAVF,
194 20 whole–rock xenoliths, including garnet and spinel or only spinel peridotites, were
195 selected for noble gas analysis by heating method and those 8 samples with larger
196 amount of gases, being 2 olivine separates, were also analyzed by crushing
197 (Supplementary Tables S1–S2). For crushing experiments, the total of measurements
198 was of 52, according with the number of strokes applied for each sample
199 (Supplementary Table S1).

200 The analyses of noble gases were performed using two modified–VG5400 noble
201 gas mass spectrometers (MS–III and MS–IV) in the Geochemical Research Center,
202 Graduate School of Science, University of Tokyo. The studied mantle xenoliths are
203 relatively fresh without significant alterations. The selected samples were coarsely
204 crushed using an agate mortar and the superficial slices of the samples were discarded in
205 order to avoid the contamination generated due to the contact with their host basalt and
206 by weathering alteration. The selected mantle xenoliths were sieved into three size
207 fractions (0.5–1; 1–2 and > 2mm). The size fractions >1 mm have the greater amount of
208 fluid inclusions in the mineral grains, and these fractions were therefore used for further
209 processing. The mineral separates were handpicked under a binocular microscope and
210 those altered were removed. After that, they were twice washed with ethanol (EtOH
211 99.5%) in an ultrasonic bath for 30min, washed in de–ionized water and then dried at
212 150°C during 24 hours in the oven, followed by a final purification by handpicking
213 under the binocular microscope. Both single step heating and stepwise crushing
214 methods were applied.

215 The single step heating experiments were applied to obtain He, Ne and Ar
216 isotopic ratios in whole–rock samples (~0.5 g), which were wrapped in Al–foil 10µm
217 and loaded in branches of a sample holder that admit up to 24 samples at once without
218 breaking the vacuum condition. Samples analyzed by heating method were dropped into
219 the heating furnace, which is heated until they completely melted at approximately
220 1800°C, and then the evaporated gas was purified, separated and analyzed in the mass
221 spectrometer.

222 All noble gas isotopic ratios (He, Ne, Ar, Kr, Xe) were obtained by stepwise
223 crushing in vacuum to release noble gases trapped in fluid inclusions of whole–rock and
224 olivine separates (see [Supplementary Tables S1–S4](#)). For crushing experiments, the

225 final separates with weights >1 g were crushed in a stainless-steel tube with sequential
226 number of strokes of a nickel piston driven from outside the vacuum by a solenoid
227 magnet (Sumino *et al.*, 2001). Different number of strokes were applied to crush the
228 samples and, thus, releases the gases that were trapped in their fluid inclusions. The
229 number of strokes applied was 100, 500, 1000 and 2000 (the last was applied repeatedly
230 while the sample had enough amounts of noble gases). Those samples, which contain
231 great amount of gases, were selected to analyze the separated olivines.

232 After loading the samples in sample holder and in crushers, the whole system of
233 extraction and purification line is baked out over 250°C for 24 hours to reduce
234 atmospheric contamination. Following purification and separation of noble gases by a
235 charcoal trap cooled by liquid nitrogen or by cryogenically cooled trap made by porous
236 sintered stainless steel, their isotopic compositions were measured. ³He and ⁴He ion
237 beams were detected in a double collector system, in which ³He was by ion counting
238 and ⁴He by Faraday cup collectors. Daly multiplier collector was used for Ar analysis,
239 whereas ion-counting collector detected Ne, Kr and Xe isotopes. Full details for the
240 mass spectrometric systems are described at Sumino *et al.* (2001). Based on
241 reproducibility of He standard of Japan (HESJ) and calibrated air standard, experimental
242 uncertainties for concentrations of each noble gases were estimated as 5% for He and
243 Ar, and 10% for Ne, Kr and Xe. During Ne analyses, corrections for ⁴⁰Ar⁺⁺ on ²⁰Ne⁺
244 and CO₂⁺⁺ on ²²Ne⁺ were <5%. Uncertainties assigned to the observed isotopic ratios
245 are one standard deviation (1σ), including uncertainties of blank corrections and mass
246 discrimination. Blanks were running using the same procedure as the samples. Heating
247 blanks are: ⁴He = (2–4)×10⁻¹¹ cm³STP; ²⁰Ne = (1–9)×10⁻¹² cm³STP; and ⁴⁰Ar = (2–
248 12)×10⁻⁹ cm³STP, whereas crushing blanks are: ⁴He = (2–4)×10⁻¹¹ cm³STP; ²⁰Ne = (2–

249 $4) \times 10^{-13} \text{ cm}^3 \text{STP}$; and $^{40}\text{Ar} = (3-5) \times 10^{-10} \text{ cm}^3 \text{STP}$. Blank corrections were applied
250 assuming atmospheric isotopic composition.

251

252 **3.1. Sr–Nd–Pb isotopes**

253

254 Sr–Nd isotopic ratios for 7 whole–rock samples were measured at Laboratório
255 de Geologia Isotópica, Universidade Federal do Rio Grande do Sul (UFRGS), Porto
256 Alegre, Brazil. In addition, Sr–Nd isotope compositions were measured on separates of
257 orthopyroxene, clinopyroxene and phlogopite from the garnet–spinel harzburgite
258 PM18–17. The samples (0.1g) were leached with cold 0.25N HCl in an ultrasonic bath
259 for 30 minutes in order to eliminate impurities. Afterwards, the dried samples were
260 weighed and spiked with mixed $^{87}\text{Rb}/^{84}\text{Sr}$ and $^{149}\text{Sm}/^{150}\text{Nd}$ tracer. These samples were
261 processed using standard dissolution procedures with HF, HNO_3 and HCl in Teflon
262 vials (Savillex®), warmed on a hot plate until complete material dissolution. In next
263 stage, sample solutions were diluted in 3ml of HCl 2.5N and stored in test tubes. An
264 aliquot of 1 ml was used in order to separate the Rb, Sr, and REE by Cationic AG–
265 50W–X8 (200–400 mesh) resin columns, followed by Sm and Nd separation using
266 anionic LN–B50–A (100–200 mesh) resin. Pb was separated using anionic BioRad–
267 AG1X (200–400 mesh) resin in HBr solution. Individual solutions of Rb, Sr, Sm, Nd
268 and Pb were dried in Teflon vials (Savillex®) on a hot plate. Residues were deposited
269 onto single Ta (for Rb, Sr, Sm and Pb), and triple Ta–Re–Ta (for Nd) filaments.

270 Mass spectrometric analyses for radiogenic isotopes were performed in a multi–
271 collector VG Sector 54 thermal ionization mass spectrometer. Data were corrected for
272 mass fractionation by normalizing to $^{86}\text{Sr}/^{88}\text{Sr} = 0.1194$ and $^{146}\text{Nd}/^{144}\text{Nd} = 0.7219$.
273 Replicate analyses of NBS–987 and JNDI standards gave $^{87}\text{Sr}/^{86}\text{Sr} = 0.710254 \pm 12$ (n =

274 7, 2σ) and $^{143}\text{Nd}/^{144}\text{Nd} = 0.512101 \pm 8$ ($n = 4, 2\sigma$). For Pb NBS–981 and NBS–982,
275 variation of accepted values was less than 0.01%/a.m.u.

276

277 **4. Samples and petrography**

278

279 Samples studied here are rounded, reach up to 60 cm and usually without any
280 noticeable interaction with their host basalt, and present no evidence of weathering and
281 serpentinization.

282 Lithologically, GG mantle xenoliths studied here are coarse-grained hydrous
283 and anhydrous spinel–peridotites, comprising 11 lherzolites and 4 wehrlites (see
284 [Supplementary Table S5](#)). On the other hand, PAVF xenoliths are coarse-grained which
285 either contain garnet and spinel or only spinel. PAVF peridotites studied here comprise
286 6 garnet–spinel–lherzolites (2 with amphibole); 5 garnet–spinel–harzburgites (2 with
287 phlogopite); 4 spinel–lherzolites; and 5 spinel–harzburgites ([Supplementary Table S5](#)).
288 GG peridotites are, in average, coarser grained than PAVF peridotites.

289 Both GG and PAVF peridotites are mainly composed by coarse olivine and
290 orthopyroxene crystals with subordinate clinopyroxene. The hydrous phases are
291 amphibole and phlogopite. Olivine often displays undulatory extinction and share
292 equilibrium triple junctions with orthopyroxene. Clinopyroxene occurs as an interstitial
293 phase, whereas spinel is an intergranular phase. Ortho– and clinopyroxene display
294 abundant exsolution lamellae. Carbonate can occur as veins and pockets; and apatite is
295 locally present as an accessory mineral in GG samples.

296 Detailed petrographic descriptions of GG mantle xenoliths were made by
297 [Gorring and Kay \(2000\)](#); [Laurora *et al.* \(2001\)](#); and [Zaffarana *et al.* \(2014\)](#) among

298 others, whereas PAVF mantle xenoliths were described by Stern *et al.* (1999); Zaffarana
299 *et al.* (2014); and Gervasoni *et al.* (2012) among others.

300

301 **5. Results and discussion**

302

303 **5.1. Helium**

304

305 Results of noble gas isotope measurements by single step heating and stepwise
306 crushing extraction methods for both localities studied here (GG and PAVF) are
307 presented in [Supplementary Tables S1–S4](#). ^4He concentrations obtained by heating
308 experiments show a widely and variable range between $15\text{--}5300\times 10^{-8}\text{ cm}^3\text{STP/g}$
309 (PAVF) and $36\text{--}1210\times 10^{-8}\text{ cm}^3\text{STP/g}$ (GG). $^3\text{He}/^4\text{He}$ versus total ^4He concentrations of
310 each sample analyzed by crushing ([Fig. 2a](#)) also show a large variability, ranging from
311 $36\text{ to }1560\times 10^{-8}\text{ cm}^3\text{STP/g}$ (PAVF) and from $16\text{ to }750\times 10^{-8}\text{ cm}^3\text{STP/g}$ (GG). There is
312 no significant difference between $^3\text{He}/^4\text{He}$ ratios with progressive number of strokes
313 applying in stepwise crushing methods ([Fig. 2b](#)). The total ^4He concentrations found in
314 separated olivine crystals are lower than obtained in whole-rocks (see [Supplementary](#)
315 [Table S1](#)).

316

317 **Figure 2**

318

319 Two samples of GG [$8.18\text{--}8.36 R_A$; where $1R_A$ corresponds to the atmospheric
320 ratio of 1.4×10^{-6} ; ([Ozima and Podosek, 1983](#))] and most samples of PAVF (7.1--
321 $10.38R_A$) analyzed by heating have slightly high $^3\text{He}/^4\text{He}$ ratios compared with values
322 obtained by crushing (see [Supplementary Tables S1– S2](#)). Differently, every wehrlites

323 (3.60–4.82 R_A), and one lherzolite (5.45 R_A; PM23–2) of GG show low ³He/⁴He ratios.
324 ³He/⁴He ratios observed in the heating experiments that are respectively lower and
325 higher than the range defined using the crushing method probably reflect radiogenic ⁴He
326 and cosmogenic ³He production. In order to verify whether the lower ³He/⁴He ratios
327 observed in some GG peridotites are related to the contribution of slab–derived
328 metasomatism or whether it is related to the post–eruption production of ⁴He from
329 radioactive decay of U and Th, we compare the ³He/⁴He ratios obtained by stepwise
330 crushing and single step heating using the sample PM23–34. This sample has low
331 ³He/⁴He ratio (4.18 R_A) when analyzed by heating method, however, when analyzed by
332 crushing method, it shows higher ³He/⁴He = 7.21 R_A (see [Supplementary Tables S1–](#)
333 [S2](#)). This observation clearly indicates that the He in matrix is more affected by
334 radiogenic ⁴He than in fluid inclusions. It is generally assumed that the gas extracted by
335 crushing avoids the effect of the cosmogenic and radiogenic helium from the matrix
336 (³He and ⁴He, respectively). Consequently, in this study we assumed that ³He/⁴He ratios
337 obtained by crushing represent the SCLM beneath PAVF and GG. Importantly, coupled
338 crushing/melting experiments carried out on those samples with the highest amounts of
339 ⁴He, ²¹Ne and ⁴⁰Ar showed quite similar results ([Supplementary Tables S1–S2](#)).
340 Moreover, no systematic difference of noble gas isotopes were found between olivine
341 and whole–rock samples analyzed by crushing method, which indicates that our whole–
342 rock results represent noble gas composition in mantle source.

343 Therefore, excluding those samples analyzed by heating that display the effect of
344 cosmogenic and radiogenic excess produced in the matrix (³He and ⁴He, respectively),
345 peridotites from PAVF and GG show a narrow range of helium isotopic ratios
346 (³He/⁴He_{PAVF} = 6.84–6.90 R_A; ³He/⁴He_{GG} = 7.17–7.37 R_A) ([Supplementary Table S1](#)
347 [and Fig. 2a–b](#)). Representative ³He/⁴He ratios of PAVF peridotites overlap those values

348 defined to the SCLM worldwide [$6 \pm 1 R_A$; (Gautheron and Moreira, 2002; Gautheron
349 *et al.*, 2005)] and HIMU-like mantle source [$^3\text{He}/^4\text{He} = 5\text{--}7R_A$; (e.g., Moreira and Kurz,
350 2001)]. On the other hand, the values obtained for GG peridotites overlap the field
351 defined for global MORBs [$8 \pm 1 R_A$; (Sarda *et al.*, 1988; Moreira *et al.*, 1998)] and are
352 quite similar with the North Chile Ridge MORBs [$\text{NCR} = 7.77 \pm 0.23R_A$; Niedermann
353 and Bach, 1998].

354

355 5.2. Neon

356

357 Most data from both PAVF and GG contain neon isotopic ratios distinguishable
358 from air [$^{20}\text{Ne}/^{22}\text{Ne}_{\text{AIR}} = 9.80 \pm 0.08$; $^{21}\text{Ne}/^{22}\text{Ne}_{\text{AIR}} = 0.0290 \pm 0.0003$; (Ozima and
359 Podosek, 1983)] considering 1σ analytical uncertainties (Figs. 3 and 4). PAVF and GG
360 peridotites are characterized by high $^{21}\text{Ne}/^{22}\text{Ne}$ relative to MORB trend for a given
361 $^{20}\text{Ne}/^{22}\text{Ne}$, which indicates endmembers more nucleogenic than global MORB source.
362 Mixing lines between a mantle endmember and atmospheric composition allow define
363 MORB-like and a more nucleogenic mantle reservoirs in the Ne three-isotope diagram
364 (Figs. 3 and 4). It is important to note that only neon isotopic ratios distinguishable from
365 air with 1σ analytical uncertainties were plotted. In addition, heating data was removed
366 from this discussion because of concern with mass fractionation during heating
367 extraction resulting from difference in diffusivities of isotopes, so only the data obtained
368 with each crushing step are used.

369 Well-defined linear trends in Ne three-isotope diagram (Figs. 3 and 4) were
370 used to determine extrapolated mantle source $^{21}\text{Ne}/^{22}\text{Ne}$ [hereafter $^{21}\text{Ne}/^{22}\text{Ne}_{(\text{E})}$] of each
371 studied mantle xenolith at $^{20}\text{Ne}/^{22}\text{Ne} = 12.5$ [Ne-B; (Trieloff *et al.*, 2000)] with high
372 reliability. $^{21}\text{Ne}/^{22}\text{Ne}_{(\text{E})}$ ratios were determined by x and y error weighted least squares

373 regression forced through the atmospheric composition [$y = a_0(x-0.029)+9.8$]. Mantle
374 xenoliths from PAVF show $^{21}\text{Ne}/^{22}\text{Ne}_{(\text{E})}$ (corrected for atmospheric contamination) ratio
375 ranging from 0.085 ± 0.001 (PM18–35WR) to 0.094 ± 0.003 (PM14–15Ol) and
376 PAVF_{AVERAGE} of 0.090 ± 0.002 (Fig. 3). Extrapolated $^{21}\text{Ne}/^{22}\text{Ne}$ ratios of PAVF
377 samples are significantly nucleogenic than MORB ($^{21}\text{Ne}/^{22}\text{Ne}_{(\text{E})} = 0.060$; Sarda *et al.*,
378 1988; Moreira *et al.*, 1998), European SCLM ($^{21}\text{Ne}/^{22}\text{Ne}_{(\text{E})} = 0.071$; Bukin *et al.*, 2005),
379 and Mangaia HIMU ($^{21}\text{Ne}/^{22}\text{Ne}_{(\text{E})} = 0.077$; Hanyu *et al.*, 2011) endmembers. Based on
380 this comparison, it is possible to conclude that PAVF_{SCLM} is characterized by far more
381 nucleogenic Ne than previous defined Earth endmembers.

382 Gobernador Gregores, represented by sample PM23–1, is undistinguished of
383 NCR MORBs ($^{21}\text{Ne}/^{22}\text{Ne}_{(\text{E})} = 0.063$; Niedermann and Bach, 1998) considering the
384 analytical uncertainties and, therefore, this sample would represent Ne local MORB–
385 like component with $^{21}\text{Ne}/^{22}\text{Ne}_{(\text{E})} = 0.065 \pm 0.002$ (Fig. 4). Consequently, the sample
386 PM14–4 (PAVF; $^{21}\text{Ne}/^{22}\text{Ne}_{(\text{E})} = 0.071 \pm 0.001$) and the other peridotites from
387 GG_{AVERAGE} ($^{21}\text{Ne}/^{22}\text{Ne}_{(\text{E})} = 0.077 \pm 0.001$) represent three–component mixing between
388 atmospheric component and two mantle endmembers: MORB–like and a more
389 radiogenic/nucleogenic SCLM (Figs. 3 and 4).

390

391 **Figure 3**

392

393 **Figure 4**

394

395 **5.3. Helium–neon systematics**

396

397 Since He–Ne isotope systematics is coupled (Honda *et al.*, 1993), the increase in
398 $^{21}\text{Ne}/^{22}\text{Ne}$ should be associated with decrease of $^3\text{He}/^4\text{He}$ due to the constant $^{21}\text{Ne}/^4\text{He}$
399 production in the mantle [4.5×10^{-8} ; (Yatsevich and Honda, 1997)]. $^4\text{He}/^3\text{He}$ and
400 $^{21}\text{Ne}/^{22}\text{Ne}_{(\text{E})}$ isotopic ratios of GG and PAVF peridotites can be explained by binary
401 mixing hyperbola between a MORB and an even more degassed SCLM
402 (radiogenic/nucleogenic) components (Fig. 5). Local SCLM is represented by data
403 points for PAVF mantle xenoliths ($^{21}\text{Ne}/^{22}\text{Ne}_{(\text{E})} = 0.090$; $^4\text{He}/^3\text{He} = 104000$), whereas
404 MORB sources employed in modelling are the global ($^{21}\text{Ne}/^{22}\text{Ne}_{(\text{E})} = 0.060$; $^4\text{He}/^3\text{He} =$
405 90000 ; Sarda *et al.*, 1988; Moreira *et al.*, 1998) and NCR MORBs ($^{21}\text{Ne}/^{22}\text{Ne}_{(\text{E})} =$
406 0.063 ; $^4\text{He}/^3\text{He} = 92000$; Niedermann and Bach, 1998). The equation employed for
407 mixing hyperbola is from Hopp and Trieloff (2008), where straight line means equal
408 $^3\text{He}/^{22}\text{Ne}$ ratios [$r = 1$, where $r = (^3\text{He}/^{22}\text{Ne})_{\text{SCLM}} / (^3\text{He}/^{22}\text{Ne})_{\text{MORB}}$], whereas hyperbolic
409 mixing line ($r = 5$) requires endmember components with different $^3\text{He}/^{22}\text{Ne}$ ratios.

410

411 **Figure 5**

412

413 Figure 5 demonstrates that during the mixing, sample PM14–4 (PAVF) plots
414 along a hyperbolic mixing curve ($r = 5$) and shows He isotopic ratios of intrinsic SCLM,
415 whereas their Ne is affected by MORB–like component. Asthenospheric mantle
416 upwelling through Patagonian slab window would have slightly metasomatized
417 $\text{PAVF}_{\text{SCLM}}$ with MORB–like signature after the collision of SCR with Chile trench ca.
418 14 Ma. We suggest that this intrinsic metasomatism was unable to overprint the noble
419 gas composition of PAVF mantle xenoliths because of rapid northward migration of
420 Chile Triple Junction. Thus, He was probably been diluted or homogenized during the
421 last 14 Ma (see details about Rb–Sr isochron in section 5.8) because it is more diffusive

422 than Ne and could be easily homogenized. Similarly, PM23–1 (GG) xenolith data also
423 plots along the same hyperbola ($r = 5$). However, this sample shows the less
424 radiogenic/nucleogenic $^4\text{He}/^3\text{He}$ and $^{21}\text{Ne}/^{22}\text{Ne}_{(\text{E})}$ isotopic ratios, suggesting that it is
425 largely dominated by MORB–like component, especially when compared with NCR
426 MORBs. Two samples from GG (PM23–32 and PM23–34) plot close to the linear
427 mixing between SCLM and MORB endmembers [$(^3\text{He}/^{22}\text{Ne})_{\text{SCLM}}/(^3\text{He}/^{22}\text{Ne})_{\text{MORB}} = 1$],
428 resulting from different extents of MORB–like component in Patagonian SCLM.
429 Therefore, we argue that less radiogenic/nucleogenic MORB–like component identified
430 in GG samples could be explained by recent metasomatism of the SCLM due to
431 asthenospheric mantle upwelling in response to the opening of Patagonian slab window,
432 which is a consequence of SCR subduction..

433 In order to avoid the influence of shallow level air contaminant in the $^3\text{He}/^{22}\text{Ne}$
434 ratios (Supplementary Table S6), we calculate mantle source from measured He and Ne
435 isotope ratios in studied mantle xenoliths following the “method 1” proposed by Tucker
436 and Mukhopadhyay (2014). For calculations, we used the $^4\text{He}/^3\text{He}$ and $^{21}\text{Ne}/^{22}\text{Ne}_{(\text{E})}$
437 ratios of each studied sample, as well as the $(^4\text{He}/^{21}\text{Ne})_{\text{production}}$ of 2.2×10^7 (Yatsevich
438 and Honda, 1997), the initial primordial composition of $^{21}\text{Ne}/^{22}\text{Ne}$ [0.0313; (Trieloff
439 and Kunz, 2005)] and $^4\text{He}/^3\text{He}$ [6024 or 120 R_A ; (Mahaffy *et al.*, 1998)]. Uncertainties
440 in $^3\text{He}/^{22}\text{Ne}$ were propagated from uncertainties in $^4\text{He}/^3\text{He}$ and $^{21}\text{Ne}/^{22}\text{Ne}_{(\text{E})}$.

441 $^3\text{He}/^{22}\text{Ne}$ values for the PAVF_{SCLM} endmember shows higher ratios ($12.03 \pm$
442 0.15 to 13.66 ± 0.37) than depleted MORBs ($^3\text{He}/^{22}\text{Ne} = 8.31\text{--}9.75$; Tucker and
443 Mukhopadhyay, 2014). Local MORB–like component (PM23–1; $^3\text{He}/^{22}\text{Ne} = 8.39 \pm$
444 0.14) and sample PM14–4 (PAVF; $^3\text{He}/^{22}\text{Ne} = 9.01 \pm 0.17$) show values over the range
445 of depleted MORBs, whereas other samples from GG vary between 10.44 ± 0.11 and

446 11.27 ± 0.12 . It argues for a SCLM reservoir more degassed than depleted MORBs,
447 which is consistent with the pattern observed in Ne isotopes.

448 Comparatively, even if He–Ne component of PAVF_{SCLM} is less radiogenic in He
449 isotopes, it is more nucleogenic in Ne than European (DW1 sample with
450 $^4\text{He}/^3\text{He}=120000$, $^{21}\text{Ne}/^{22}\text{Ne}_{(E)} = 0.07$; Buikin *et al.*, 2005) and Arabic (SA86–121/1
451 sample with $^4\text{He}/^3\text{He} = 116000$, $^{21}\text{Ne}/^{22}\text{Ne}_{(E)} = 0.07$; Hopp *et al.*, 2004) SCLMs (also see
452 sections 5.1 and 5.2). Moreover, calculated $^3\text{He}/^{22}\text{Ne}$ ratios for European SCLM (7.47;
453 Buikin *et al.*, 2005) and Arabic SCLM (7.74; Hopp *et al.*, 2004) are similar to those
454 defined for MORBs (7.52 ± 1.13 ; Honda and McDougall, 1998), but significantly lower
455 than those found in Patagonian SCLM. It suggests that Patagonian SCLM have
456 experienced a different evolution from MORBs and other SCLMs. Our preferred model
457 to explain the higher $^3\text{He}/^{22}\text{Ne}$ ratios observed in Patagonian SCLM is based on the
458 greater solubility of He related to Ne (e.g., Yamamoto *et al.*, 2009; Tucker and
459 Mukhopadhyay, 2014). The difference of solubility implies in preferential degassing of
460 Ne into the atmosphere and increase $^3\text{He}/^{22}\text{Ne}$ ratio of the mantle during depletion of
461 these peridotites due to melt extraction.

462

463 **5.4. Argon**

464

465 $^{40}\text{Ar}/^{36}\text{Ar}$ ratios obtained by heating and crushing extractions range over 380–
466 4830 in GG and over 420–17700 in PAVF peridotites (Supplementary Tables S1–S2).
467 The values close to the atmospheric ratio [296; Ozima and Podosek, 1983], especially
468 those from GG peridotites, indicate atmospheric contamination, which probably
469 occurred during exposure to the surface. The highest $^{40}\text{Ar}/^{36}\text{Ar}$ ratios determined in this
470 study were obtained in sample PM14–4 ($^{40}\text{Ar}/^{36}\text{Ar}_{\text{HEATING}} = 17700 \pm 160$;

471 $^{40}\text{Ar}/^{36}\text{Ar}_{\text{CRUSHING}} = 16400 \pm 120$), which implies in a relatively small contribution of
472 atmospheric Ar in this sample. Our results are similar to the highest $^{40}\text{Ar}/^{36}\text{Ar}$ values
473 measured at mantle xenolith from European SCLM (16200 ± 200 , [Buikin *et al.*, 2005](#);
474 and 17000 ± 1100 , [Dunai and Baur, 1995](#)). However, all measured $^{40}\text{Ar}/^{36}\text{Ar}$ ratios are
475 significantly lower than maximum MORB source estimate, which range from ~ 28000
476 up to 44000 (e.g., [Burnard *et al.*, 1997](#); [Moreira *et al.*, 1998](#); [Tucker *et al.*, 2012](#)).
477 Considering that $^{40}\text{Ar}/^{36}\text{Ar}$ ratios are a mixing between mantle sources and atmospheric
478 component, we can only infer the mantle source composition by using neon–argon
479 isotope correlations, which will be presented bellow (section 5.5).

480

481 **5.5. Neon–argon systematics**

482

483 In general, mixing between isotopic ratios with different denominators are
484 hyperbolas. In Ne–Ar systematic, the curvature of two endmembers hyperbola is
485 defined by $k = (^{36}\text{Ar}/^{22}\text{Ne})_{\text{A}} / (^{36}\text{Ar}/^{22}\text{Ne})_{\text{B}}$. However, when calculated $^{36}\text{Ar}/^{22}\text{Ne}$ values
486 are similar to the atmospheric ratio (18.8; [Ozima and Podosek, 1983](#)) (see
487 [Supplementary Table S6](#)), it is reasonable to assume a linear mixing
488 $[(^{36}\text{Ar}/^{22}\text{Ne})_{\text{MANTLE}} / (^{36}\text{Ar}/^{22}\text{Ne})_{\text{AIR}} = 1]$ ([Sumino *et al.*, 2006](#)). Values for $^{36}\text{Ar}/^{22}\text{Ne}$ of
489 each sample were obtained through a division between their calculated total ^{36}Ar and
490 total ^{22}Ne concentrations. It is important empathize that $^{36}\text{Ar}/^{22}\text{Ne}$ ratios, as well as
491 other data used in discussion of extrapolated values, were calculated considering
492 datasets that differ from atmospheric ratios with 1σ analytical uncertainties.

493 Except for samples PM14–4 ($^{36}\text{Ar}/^{22}\text{Ne} = 3.29 \pm 0.02$) and PM23–1 ($^{36}\text{Ar}/^{22}\text{Ne} =$
494 9.96 ± 0.06), most studied mantle xenoliths show similar $^{36}\text{Ar}/^{22}\text{Ne}$ ratios to the air
495 (14.76 ± 0.09 to 25.56 ± 0.13) ([Supplementary Table S6](#)). We restrict hyperbolic

496 extrapolations to those samples that significantly differ from air in terms of $^{36}\text{Ar}/^{22}\text{Ne}$
497 ratios (PM14–4 and PM23–1) (Fig. 6).

498 With purpose to obtain the best–fit hyperbola reflecting two–component mixing
499 between air and mantle endmembers, we applied the approach proposed by Parai *et al.*
500 (2012). This method consists in a total least–squares hyperbolic fit, where the fit process
501 is based on chi–square statistics computed using the orthogonal error weighted distances
502 using a Markov Chain Monte Carlo (MCMC) optimization. This method uses a
503 hyperbola with two free parameters to fit the data. The first describes the curvature of
504 the model (k), and the second is the model value at a fixed value in the abscissa (Neon–
505 B $^{20}\text{Ne}/^{22}\text{Ne} = 12.5$). Moreover, the model implies in force best–fit hyperbola to pass
506 through the atmospheric composition. It is important to note that large uncertainties
507 observed in extrapolated $^{40}\text{Ar}/^{36}\text{Ar}$ ratios are related to significant air contribution in
508 both $^{40}\text{Ar}/^{36}\text{Ar}$ and $^{20}\text{Ne}/^{22}\text{Ne}$ ratios, which fall rather close to the air.

509 Extrapolating regression lines to Neon–B $^{20}\text{Ne}/^{22}\text{Ne} = 12.5$, we found
510 $^{40}\text{Ar}/^{36}\text{Ar}_{(\text{E})}$ ratios for intrinsic PAVF_{SCLM} over the range of 31100^{+9400}_{-6800} up to
511 54000^{+14200}_{-9600} (Fig. 6). This interval is in agreement with that proposed for European
512 SCLM ($^{40}\text{Ar}/^{36}\text{Ar} = 34000\text{--}52000$; Buikin *et al.*, 2005) and substantially higher than
513 sample 2IID43 popping rock (25000; Moreira *et al.*, 1998) and MORB reservoir (41500
514 ± 9000 ; Tucker *et al.*, 2012). In order to compare previous data with best–fit hyperbola
515 given by our approach, we fitted the $^{40}\text{Ar}/^{36}\text{Ar}_{(\text{E})}$ for popping rock (25700^{+1200}_{-1100} ;
516 Moreira *et al.*, 1998), sample DW1 from European SCLM (13400^{+4900}_{-2300} ; Buikin *et*
517 *al.*, 2005), and depleted MORB sample RC28063D–2 (38600 ± 350 ; Tucker *et al.*,
518 2012) (Fig. 6).

519 High $^{40}\text{Ar}/^{36}\text{Ar}_{(\text{E})}$ observed in Patagonian SCLM endmember implies an even
520 more degassed Earth reservoir than MORB source with high $\text{K}/^{36}\text{Ar}$ ratio, which is

521 accompanied by high (U+Th)/(³He, ²²Ne) isotopic ratios. On the other hand, GG mantle
522 xenoliths show lower values than those observed in PAVF samples, implying a
523 significant contribution from atmospheric argon with ⁴⁰Ar/³⁶Ar_(E) between 8100⁺¹⁴⁰⁰₋₇₀₀
524 and 17700⁺⁴⁴⁰⁰₋₃₁₀₀. It could indicate an effective recirculation of atmospheric Ar
525 associated with recycled oceanic lithosphere in Patagonian SCLM as observed in mantle
526 peridotites from subduction zones (e.g., Matsumoto *et al.*, 2001; Kim *et al.*, 2005;
527 Sumino *et al.*, 2010; Hopp and Ionov, 2011).

528

529 **Figure 6**

530

531 **5.6. Krypton**

532

533 Krypton isotopic ratios were determined by crushing and are listed in
534 [Supplementary Table S3](#). All ⁸⁶Kr/⁸²Kr and ⁸⁴Kr/⁸²Kr isotopic ratios measured in this
535 study are indistinguishable from atmospheric compositions at 1σ analytical
536 uncertainties. Holland *et al.* (2009) obtained a linear trend from atmospheric values to
537 compositions with non-air ratios plotting their Kr isotopic data in ⁸⁶Kr/⁸²Kr versus
538 ⁸⁴Kr/⁸²Kr. As an alternative approach, we plotted our results in this diagram and three
539 samples (PM14–15; PM18–23 and PM23–1) show distinctly non-atmospheric ⁸⁶Kr/⁸²Kr
540 and ⁸⁴Kr/⁸²Kr ratios, falling in the linear trend defined between air and AVCC (average
541 carbonaceous chondrite; see Holland *et al.*, 2009 for details). However, due large
542 uncertainties in ⁸⁶Kr/⁸²Kr ratios, these results cannot be considered.

543

544 **5.7. Xenon**

545

546 Xenon isotopic data were obtained by crushing and are presented in
 547 [Supplementary Table S4](#). Because of large analytical uncertainty of ^{130}Xe -normalized
 548 ratios, we decided to use $^{129}\text{Xe}/^{132}\text{Xe}$ and $^{136}\text{Xe}/^{132}\text{Xe}$ isotopic ratios to discuss our data.
 549 However, assuming 1σ analytical uncertainties, we found $^{129}\text{Xe}/^{130}\text{Xe}$ and $^{136}\text{Xe}/^{130}\text{Xe}$
 550 values ranging from air composition to $^{129}\text{Xe}/^{130}\text{Xe}_{\text{PAVF}} = 7.12 \pm 0.47$ and
 551 $^{136}\text{Xe}/^{130}\text{Xe}_{\text{PAVF}} = 2.43 \pm 0.21$ ($^{129}\text{Xe}/^{130}\text{Xe}_{\text{AIR}} = 6.5$; $^{136}\text{Xe}/^{130}\text{Xe}_{\text{AIR}} = 2.18$; [Ozima and](#)
 552 [Podosek, 1983](#)).

553 Xe isotopic ratios for some samples from GG (PM23–1 and PM23–32) and
 554 PAVF (PM14–4, PM14–15, PM18–23 and PM18–35) are clearly distinguishable from
 555 those of air with 1σ analytical uncertainties [$^{129}\text{Xe}/^{132}\text{Xe}_{\text{AIR}} = 0.9832$; $^{136}\text{Xe}/^{132}\text{Xe}_{\text{AIR}} =$
 556 0.3294 ; [Ozima and Podosek, \(1983\)](#)]. In three–isotope diagram of $^{129}\text{Xe}/^{132}\text{Xe}$ versus
 557 $^{136}\text{Xe}/^{132}\text{Xe}$ ([Fig. 7](#)), PAVF_{SCLM} defines a correlation line undistinguishable of mixing
 558 line between air and depleted MORB (e.g., [Staudacher and Allègre, 1982](#); [Kunz et al.,](#)
 559 [1998](#); [Tucker et al., 2012](#)). The best–fit hyperbola for Xe isotopic compositions was
 560 obtained using the same approach described above (section 5.5). Because of our limited
 561 number of data points, it was possible to define the extrapolated Xe ratios for samples
 562 PM14–4 ($^{129}\text{Xe}/^{132}\text{Xe}_{(\text{E})} = 1.0833^{+0.0216}_{-0.0053}$; $^{136}\text{Xe}/^{132}\text{Xe}_{(\text{E})} = 0.3761^{+0.0246}_{-0.0034}$) and
 563 PM14–15 ($^{129}\text{Xe}/^{132}\text{Xe}_{(\text{E})} = 1.0556^{+0.0614}_{-0.0040}$; $^{136}\text{Xe}/^{132}\text{Xe}_{(\text{E})} = 0.3720^{+0.0401}_{-0.0056}$) ([Fig.](#)
 564 [8](#)). For consistent comparison, we applied the same approach used here to fit Xe
 565 isotopic composition of sample RC28063D–2, which was assumed as representative of
 566 the depleted MORB mantle group ([Tucker et al., 2012](#)). These extrapolations yielded a
 567 mantle source $^{129}\text{Xe}/^{132}\text{Xe} = 1.1156^{+0.0442}_{-0.0124}$ and $^{136}\text{Xe}/^{132}\text{Xe} = 0.3850^{+0.0156}_{-0.0061}$,
 568 which is consistent with the estimated values of $^{129}\text{Xe}/^{132}\text{Xe} = 1.1180$ and $^{136}\text{Xe}/^{132}\text{Xe} =$
 569 0.3851 obtained by these authors ([Fig. 8](#)). Based on these results, we conclude that
 570 additional measurements on these mantle xenoliths in the future will be able to better

571 constrain Xe of SCLM endmember. However, at this moment we can infer that
572 Patagonian SCLM shows at least a similar excess of ^{129}Xe and ^{136}Xe to that of MORB
573 reservoir.

574

575 **Figure 7**

576

577 **Figure 8**

578

579 **5.8. He–Ne and lithophile isotopes (SCLM or HIMU reservoirs?)**

580

581 In this study, we report new isotopic data and radiometric ages for whole-rock
582 and separate minerals with noble gas data previously measured (Supplementary Table
583 S7). Sr–Nd–Pb isotopic compositions of both suites are very similar with $^{87}\text{Sr}/^{86}\text{Sr} =$
584 $0.702811\text{--}0.703259$, $^{143}\text{Nd}/^{144}\text{Nd} = 0.512847\text{--}0.512993$, $^{206}\text{Pb}/^{204}\text{Pb} = 17.99\text{--}19.09$,
585 $^{207}\text{Pb}/^{204}\text{Pb} = 15.34\text{--}15.72$, and $^{208}\text{Pb}/^{204}\text{Pb} = 37.53\text{--}38.59$. These results are in
586 agreement with those previously reported by (Stern *et al.*, 1999) and (Gorring and Kay,
587 2000) for samples from same localities. Sr–Nd isotopic signature of PAVF and GG
588 mantle xenoliths requires a depleted component because they plot between Chile Ridge
589 MORBs (Klein and Karsten, 1995; Bach *et al.*, 1996) and HIMU–OIBs [high- $\mu =$
590 elevated $^{238}\text{U}/^{204}\text{Pb}$ (Hart *et al.*, 1992)] (Fig. 9a). Pb isotope ratios for PAVF and GG
591 overlap the field of Chile Ridge MORBs (Klein and Karsten, 1995; Bach *et al.*, 1996),
592 with $^{206}\text{Pb}/^{204}\text{Pb}$ ratios significantly lower than HIMU endmember (Fig. 9b).

593

594 **Figure 9**

595

596 Although our samples display some noble gas affinities with HIMU, such as
597 radiogenic helium and nucleogenic neon, the less radiogenic lead isotopic ratios than
598 those observed in this mantle reservoir [e.g., $^{206}\text{Pb}/^{204}\text{Pb} > 20.5$; Hanyu *et al.*, 2014]
599 argue against the contribution of this component in SCLM beneath PAVF and GG (Fig.
600 9b). Relationships between He–Ne isotopes also demonstrate that Patagonian SCLM
601 have distinct signature than Mangaia HIMU endmember (Hanyu *et al.*, 2011). Our
602 samples are considerably more nucleogenic (extrapolated $^{21}\text{Ne}/^{22}\text{Ne}_{\text{SCLM}} = 0.090$;
603 $^{21}\text{Ne}/^{22}\text{Ne}_{\text{HIMU}} = 0.077$) and less radiogenic ($^4\text{He}/^3\text{He}_{\text{SCLM}} = 104000$; $^4\text{He}/^3\text{He}_{\text{HIMU}} =$
604 113200) than HIMU component (Fig. 5; also see sections 5.2 and 5.3). We further note
605 that Patagonian SCLM have $^3\text{He}/^{22}\text{Ne}$ ratios (average of 13.20) higher than HIMU
606 (9.38).

607 Additionally, the formation age of phlogopite, which is a key mineral to
608 determine the time of metasomatic imprint and its potential association with geotectonic
609 events, was calculated through of an Rb–Sr isochron including whole–rock,
610 clinopyroxene and phlogopite. The obtained age is $13.64 \pm 0.83\text{Ma}$ with initial $^{87}\text{Sr}/^{86}\text{Sr}$
611 $= 0.702903 \pm 0.000005$ (2σ) (MSWD = 1.16; Fig. 10). Besides its unique radiogenic Pb
612 isotopic composition, this age allow us to rule out the presence of HIMU component
613 due the necessity of a long–term preservation [>1 Ga (Hauri and Hart, 1993)] of
614 recycled oceanic crust and lithosphere to generate the HIMU signature. Moreover, this
615 age suggests concomitant formation of this K–rich mineral with subduction and
616 dehydration of the southeast extension of Chile Ridge (SCR–3) during ca. 14–13 Ma
617 ago [e.g., Cande and Leslie, (1986); D’Orazio *et al.*, (2000)].

618

619 **Figure 10**

620

621 **6. Conclusions**

622

623 We present the first noble gas data and new Sr–Nd–Pb isotopes of mantle
624 xenoliths from subcontinental lithospheric mantle beneath southern Patagonia. Based on
625 noble gas isotopic compositions determined by stepwise crushing method we conclude:

626

627 1) Heterogeneous SCLM beneath Pali–Aike Volcanic Field and Gobernador Gregores
628 represents mixing between air and two mantle endmembers: a degassed and depleted
629 SCLM with radiogenic/nucleogenic composition and MORB–like component.

630 2) Pali–Aike mantle xenoliths represent the intrinsic local SCLM reservoir with higher

631 $(U+Th+K)/(^3He, ^{22}Ne, ^{36}Ar)$ ratios than MORB source, which would have been

632 homogenized during the last 14 Ma, after the rapid passage and northward migration of

633 Chile Triple Junction and its slab window at this latitude. This mantle reservoir is

634 characterized by radiogenic $^3He/^4He_{AVERAGE} = 6.87 \pm 0.04 R_A$ and nucleogenic mantle

635 neon with $^{21}Ne/^{22}Ne$ average of 0.090, with $^3He/^{22}Ne$ ratios higher (up to 13.66 ± 0.37)

636 than depleted MORBs (8.31–9.75). $^{40}Ar/^{36}Ar$ ratios vary from near–atmospheric ratio

637 (510) up to 16400, with $^{40}Ar/^{36}Ar_{(E)}$ reaching 54000^{+14200}_{-9600} .

638 3) The less radiogenic/nucleogenic MORB–like component identified in Gobernador

639 Gregores mantle xenoliths could be explained by recent metasomatism of the SCLM

640 due to asthenospheric mantle upwelling in response to the opening of Patagonian slab

641 window, which is consequence of SCR subduction. These mantle xenoliths are

642 characterized by $^3He/^4He_{AVERAGE} = 7.24 \pm 0.09R_A$, and by slightly nucleogenic mantle

643 neon with $^{21}Ne/^{22}Ne = 0.065$. The $^{40}Ar/^{36}Ar$ ratios usually are less than 4000, with

644 $^{40}Ar/^{36}Ar_{(E)}$ ranging between 8100^{+1400}_{-700} and 17700^{+4400}_{-3100} . It indicates that these

645 rocks were significantly affected by atmospheric contamination associated with
646 recycled oceanic lithosphere.
647 4) $^{129}\text{Xe}/^{136}\text{Xe}/^{132}\text{Xe}$ isotopic ratios that are distinguishable from air with 1σ analytical
648 uncertainties form a mixing line between air and MORB endmembers with
649 $^{129}\text{Xe}/^{132}\text{Xe}_{(E)} = 1.0833^{+0.0216}_{-0.0053}$ and $^{136}\text{Xe}/^{132}\text{Xe}_{(E)} = 0.3761^{+0.0246}_{-0.0034}$. It suggests
650 that Patagonian SCLM shows, at least, a similar excess of ^{129}Xe and ^{136}Xe to that of
651 MORB reservoir.

652

653 **Acknowledgments:** This study was supported by National Council of Technological
654 and Scientific Development – CNPq, Brazil and by the Graduate School of Science
655 cooperative research program, the University of Tokyo conceded to T.J., and by the
656 Japan Society for the Promotion of Science (JSPS) Grant-in-Aid for Scientific Research
657 (B) Nos. 23340169 and 26287139, the Sumitomo Foundation No.100191, and Inamori
658 Foundation conceded to H.S. We are thankful to G. Salerno for his help in mathematical
659 models and to Prof. E. Koester and A. Martins for their support in Sr–Nd–Pb analysis.

660

661 **References**

662

663 Bach, W., Erzinger, J., Dosso, L., Bollinger, C., Bougault, H., Etoubleau, J.,
664 Sauerwein, J., 1996. Unusually large Nb–Ta depletions in North Chile ridge basalts at
665 $36^{\circ}50'$ to $38^{\circ}56'S$: major element, trace element, and isotopic data. *Earth Planet. Sci.*
666 *Lett.* 142, 223–240.

667

668 Buikin, A., Trieloff, M., Hopp, J., Althaus, T., Korochantseva, E., Schwarz, W.H.,
669 Altherr, R., 2005. Noble gas isotopes suggest deep mantle plume source of late
670 Cenozoic mafic alkaline volcanism in Europe. *Earth Planet. Sci. Lett.* 230, 143–162.
671

672 Burnard, P.G., Graham, D.W., Turner, G., 1997. Vesicle-specific noble gas analyses of
673 “popping rock”: Implications for primordial noble gases in Earth. *Science* 276, 568–
674 571.
675

676 Cande, S.C., Leslie, R.B., 1986. Late Cenozoic Tectonic of the Southern Chile trench. *J.*
677 *Geophys. Res.* 91, 471–496.
678

679 D’Orazio, M., Agostini, S., Mazzarini, F., Innocenti, F., Manetti, P., Haller, M., Lahsen,
680 A., 2000. The Pali Aike Volcanic Field, Patagonia: slab–window magmatism near the
681 tip of South America. *Tectonophysics* 321, 407–427.
682

683 Dunai, T.J., Baur, H., 1995. Helium, neon, and argon systematics of the European
684 subcontinental mantle: implications for its geochemical evolution. *Geochim.*
685 *Cosmochim. Acta* 59, 2767–2783.
686

687 Gautheron, C.E., Moreira, M., 2002. Helium signature of the subcontinental lithospheric
688 mantle. *Earth Planet. Sci. Lett.* 199, 39–47.
689

690 Gautheron, C.E., Moreira, M., Allègre, C., 2005. He, Ne and Ar composition of the
691 European lithospheric mantle. *Chem. Geol.* 217, 97–112.
692

693 Gervasoni, F., Conceição, R.V., Jalowitzki, T.L.R., Schilling, M.E., Orihashi, Y.,
694 Nakai, S., Sylvester, P., 2012. Heterogeneidades do manto litosférico subcontinental no
695 extremo sul da Placa Sul–americana: influência da subducção atual e interações
696 litosfera–astenosfera sob o Campo Vulcânico de Pali Aike. *Pesq. Geoc.* 39, 269–285.
697
698 Gorrington, M.L., Kay, S.M., 2000. Carbonatite metasomatized peridotite xenoliths from
699 southern Patagonia: implications for lithospheric processes and Neogene plateau
700 magmatism. *Contrib. Mineral. Petrol.* 140, 55–72.
701
702 Gorrington, M.L., Kay, S.M., Zeitler, P.K., Ramos, V.A., Rubiolo, D., Fernandez, M.I.,
703 Panza, J.L., 1997. Neogene Patagonian plateau lavas: continental magmas associated
704 with ridge collision at the Chile Triple Junction. *Tectonics* 16, 1–17.
705
706 Hanyu, T., Tatsumi, Y., Senda, R., Miyazaki, T., Chang, Q., Hirahara, Y., Takahashi,
707 T., Kawabata, H., Suzuki, K., Kimura, J.–I., 2011. Geochemical characteristics and
708 origin of the HIMU reservoir: A possible mantle plume source in the lower mantle.
709 *Geochem. Geophys. Geosyst.* 12, Q0AC09. doi:10.1029/2010GC003252.
710
711 Hanyu, T., Kawabata, H., Tatsumi, Y., Kimura, J.–I., Hyodo, H., Sato, K., Miyazaki, T.,
712 Chang, Q., Hirahara, Y., Takahashi, T., Senda, R., Nakai, S., 2014. Isotope evolution in
713 the HIMU reservoir beneath St. Helena: Implications for the mantle recycling of U and
714 Th. *Geochim. Cosmochim. Acta* 143, 232–252.
715
716 Hart, S.R., Hauri, E.H., Oschmann, L.A., Whitehead, J.A., 1992. Mantle Plumes and
717 Entrainment: Isotopic Evidence. *Science* 256: 517–520.

718

719 Hauri, E.H., Hart, S.R., 1993. Re–Os isotope systematics of HIMU and EMII oceanic
720 island basalts from the South Pacific Ocean. *Earth Planet. Sci. Lett.* 114, 353–371.

721

722 Hiyagon, H., Ozima, M., Marty, B., Zashu, S., Sakai, H., 1992. Noble gases in
723 submarine glasses from mid–oceanic ridges and Loihi seamount: Constraints on the
724 early history of the Earth. *Geochim. Cosmochim. Acta* 56, 1301–1316.

725

726 Holland, G., Cassidy, M., Ballentine, C.J., 2009. Meteorite Kr in Earth’s Mantle
727 Suggests a Late Accretionary Source for the Atmosphere. *Science* 326, 1522–1525.

728

729 Honda, M., McDougall, I., 1998. Primordial helium and neon in the Earth – a
730 speculation on early degassing. *Geophys. Res. Lett.* 25, 1951–1954.

731

732 Honda, M., McDougall, I., Patterson, D., 1993. Solar noble gases in the Earth: The
733 systematics of helium–neon isotopes in mantle derived samples. *Lithos* 30, 257–265.

734

735 Hopp, J., Trieloff, M., 2008. Helium deficit in high– $^3\text{He}/^4\text{He}$ parent magmas:
736 Predegassing fractionation, not a “helium paradox”. *Geochem. Geophys. Geosyst.* 9,
737 Q03009, doi:10.1029/2007GC001833.

738

739 Hopp, J., Ionov, D.A., 2011. Tracing partial melting and subduction-related
740 metasomatism in the Kamchatkan mantle wedge using noble gas compositions. *Earth*
741 *Planet. Sci. Lett.* 302, 121–131.

742

743 Hopp, J., Trieloff, M., Altherr, R., 2004. Neon isotopes in mantle rocks from the Red
744 Sea region reveal large-scale plume–lithosphere interaction. *Earth Planet. Sci. Lett.*
745 219, 61–76.
746
747 Klein, M.E., Karsten, J.L., 1995. Ocean–ridge basalts with convergent–margin
748 geochemical affinities from the Chile Ridge. *Nature* 374, 52–57.
749
750 Kim, K.H., Nagao, K., Tanaka, T., Sumino, H., Nakamura, T., Okuno, M., Lock, J.B.,
751 Youn, J.S., Song, J., 2005. He–Ar and Nd–Sr isotopic compositions of ultramafic
752 xenoliths and host alkali basalts from the Korean peninsula. *Geoch. J.* 39, 341–356.
753
754 Kunz, J., Staudacher, Th., Allègre, C.J., 1998. Plutonium–Fission Xenon Found in
755 Earth’s Mantle. *Science* 280, 877–880.
756
757 Laurora, A., Mazzucchelli, M., Rivalenti, G., Vannucci, R., Zanetti, A., Barbieri, M.A.,
758 Cingolani, C.A., 2001. Metasomatism and melting in carbonated peridotite xenoliths
759 from the mantle wedge: the Gobernador Gregores case (southern Patagonia). *J. Petrol.*
760 42, 69–87.
761
762 Mahaffy, P.R., Donahue, T.M., Atreya, S.K., Owen, T.C., Niemann, H.B., 1998.
763 Galileo probe measurements of D/H and $^3\text{He}/^4\text{He}$ in Jupiter’s atmosphere. *Space Sci.*
764 *Rev.* 84, 251–263.
765
766 Matsumoto, T., Chen, Y., Matsuda, J., 2001 Concomitant occurrence of primordial and
767 recycled noble gases in the Earth’s mantle. *Earth Planet. Sci. Lett.* 185, 35–47.

768

769 Moreira, M., Kurz, M.D., 2001. Subducted oceanic lithosphere and the origin of the
770 “high μ ” basalt helium isotopic signature. *Earth Planet. Sci. Lett.* 189, 49–57.

771

772 Moreira, M., Kunz, J., Allègre, C., 1998. Rare gas systematics in popping rock: isotopic
773 and elemental compositions in the upper mantle. *Science* 279, 1178–1181.

774

775 Mukhopadhyay, S., 2012. Early differentiation and volatile accretion recorded in deep–
776 mantle neon and xenon. *Nature* 486, 101–104.

777

778 Niedermann, S., Bach, W., 1998. Anomalously nucleogenic neon in North Chile Ridge
779 basalt glasses suggesting a previously degassed mantle source. *Earth Planet. Sci. Lett.*
780 160, 447–462.

781

782 Ozima, M., Podosek, F.A., 1983. *Noble Gas Geochemistry* (Cambridge Univ. Press,
783 Cambridge, 367p).

784

785 Pankhurst, R.J., Rapela, C.W., Fanning, C.M., Márquez, M., 2006. Gondwanide
786 continental collision and the origin of Patagonia. *Earth–Sci. Reviews* 76, 235–257.

787

788 Parai, R., Mukhopadhyay, S., Standish, J.J., 2012. Heterogeneous upper mantle Ne, Ar
789 and Xe isotopic compositions and a possible Dupal noble gas signature recorded in
790 basalts from the Southwest Indian Ridge. *Earth Planet. Sci. Lett.* 359–360, 227–239.

791

792 Poreda, R.J., Farley, K.A., 1992. Rare gases in Samoan xenoliths. *Earth Planet. Sci.*
793 *Lett.* 113, 129–144.
794
795 Rivalenti, G., Zanetti, A., Mazzucchelli, M., Vannucci, R., Cingolani, C.A., 2004.
796 Equivocal carbonatite markers in the mantle xenoliths of the Patagonia backarc: the
797 Gobernador Gregores case (Santa Cruz Province, Argentina). *Contrib. Mineral. Petrol.*
798 147, 647–670.
799
800 Sarda, P., Staudacher, T., Allègre, C.J., 1988. Neon isotopes in submarine basalts. *Earth*
801 *Planet. Sci. Lett.* 91, 73–88.
802
803 Staudacher, Th., Allègre, C.J., 1982. Terrestrial xenology. *Earth Planet. Sci. Lett.* 60,
804 389–406.
805
806 Stern, C.R., Kilian, R., Olker, B., Hauri, E.H., Kyser, T.K., 1999. Evidence from mantle
807 xenoliths for relatively thin (<100 km) continental lithosphere below the Phanerozoic
808 crust of southernmost South America. *Lithos* 48, 217–235.
809
810 Sumino, H., Nagao, K., Notsu, K., 2001. Highly sensitive and precise measurement of
811 helium isotopes using a mass spectrometer with double collector system. *J. Mass*
812 *Spectrom. Soc. Jpn.* 49, 61–68.
813
814 Sumino, H., Kaneoka, I., Matsufuji, K., Sobolev, A.V., 2006. Deep mantle origin of
815 kimberlite magmas revealed by neon isotopes. *Geophys. Res. Lett.* 33, L16318.
816 doi:10.1029/2006GL027144.

817

818 Sumino, H., Burgess, R., Mizukami, T., Wallis, S.R., Holland, G., Ballentine, C.J.,
819 2010. Seawater-derived noble gases and halogens preserved in exhumed mantle wedge
820 peridotite. *Earth Planet. Sci. Lett.* 294, 163–172.

821

822 Trieloff, M., Kunz, J., 2005. Isotope systematics of noble gases in the Earth's mantle:
823 possible sources of primordial isotopes and implications for mantle structure. *Phys.*
824 *Earth Planet. Inter.* 148, 13–38.

825

826 Trieloff, M., Kunz, J., Clague, D.A., Harrison, D., Allègre, C.J. 2000. The nature of
827 pristine noble gases in mantle plumes. *Science* 288, 1036–1038.

828

829 Tucker, J.M., Mukhopadhyay, S., 2014. Evidence for multiple magma ocean outgassing
830 and atmospheric loss episodes from mantle noble gases. *Earth Planet. Sci. Lett.* 393,
831 254–265.

832

833 Tucker, J.M., Mukhopadhyay, S., Schilling, J.–G., 2012. The heavy noble gas
834 composition of the depleted MORB mantle (DMM) and its implications for the
835 preservation of heterogeneities in the mantle. *Earth Planet. Sci. Lett.* 355–356, 244–254.

836

837 Yamamoto, J., Nishimura, K., Sugimoto, T., Takemura, K., Takahata, N., Sano, Y.,
838 2009. Diffusive fractionation of noble gases in mantle with magma channels: Origin of
839 low He/Ar in mantle-derived rocks. *Earth Planet. Sci. Lett.* 280, 167–174.

840

841 Yatsevich, I., Honda, M., 1997. Production of nucleogenic neon in the Earth from
842 natural radioactive decay. *J. Geophys. Res.*102, 10291–10298.
843
844 Zaffarana, C., Tommasi, A., Vauchez, A., Grégoire, M., 2014. Microstructures and
845 seismic properties of south Patagonian mantle xenoliths (Gobernador Gregores and Pali
846 Aike). *Tectonophysics* 621, 175–197.

847

848 **Figure captions**

849

850 **Figure 1.** Present–day tectonic setting of Southern South America. Circles indicate
851 studied samples localities as follow: Laguna Ana (PM14 – 52°04'34"S; 69°47'17"W);
852 Laguna Timone (PM18 – 52°01'39"S; 70°12'53"W); Gobernador Gregores (PM23 –
853 48°34'02"S; 70°10'59"W).

854

855 **Figure 2.** Relationship between $^3\text{He}/^4\text{He}$ (in R_A) versus total ^4He concentration (in 10^{-8}
856 cm^3 STP/g) (a) and cumulative number of strokes (b). Uncertainties are 1σ and only
857 crushing experiments are reported. It is important to highlight that in some cases
858 uncertainties are smaller than the symbol size. No significant variation with increasing
859 number of strokes could be recorded. Typical MORB [$8 \pm 1 R_A$; (Sarda *et al.*, 1988;
860 Moreira *et al.*, 1998)] and SCLM [$6 \pm 1 R_A$; (Gautheron and Moreira, 2002; Gautheron
861 *et al.*, 2005)] ranges are indicated. PAVF peridotites clearly shows strong affinity with
862 SCLM domain, whereas GG peridotites fall in MORB range. WR = whole–rock, Ol =
863 olivine.

864

865 **Figure 3.** Ne three–isotope diagram showing all individual single step heating and
866 stepwise crushing results of PAVF that differ 1σ of air. Uncertainties given correspond
867 to 1σ . It is important to highlight that in some cases uncertainties are smaller than
868 symbol size. All samples of PAVF peridotites represent an endmember more
869 nucleogenic than typical MORB. Well–defined slopes for SCLM (PAVF_{AVERAGE})
870 represent a mixing between air and a strongly nucleogenic endmember, which allow us
871 to determine extrapolated mantle source $^{21}\text{Ne}/^{22}\text{Ne}_{(E)}$ at $^{20}\text{Ne}/^{22}\text{Ne} = 12.5$ with high
872 precision. For each sample, we calculated a tendency line applying a data regression
873 including air point and using uncertainties as weight. There are no significant
874 differences between coupled crushing/melting experiments. See text for references.
875

876 **Figure 4.** Ne three–isotope diagram showing all individual stepwise crushing results of
877 GG peridotites that differ 1σ of air. Uncertainties given correspond to 1σ . It is important
878 to highlight that in some cases uncertainties are smaller than symbol size. For
879 comparison, typical MORB–line (Sarda *et al.*, 1988; Moreira *et al.*, 1998) and North
880 Chile Ridge MORB–line (Niedermann and Bach, 1998) are shown. All samples of GG
881 peridotites represent an endmember more nucleogenic than typical MORB. Well–
882 defined slopes for each sample represent a mixing between air and a mantle
883 endmember, which allow us to determine extrapolated mantle source $^{21}\text{Ne}/^{22}\text{Ne}_{(E)}$ at
884 $^{20}\text{Ne}/^{22}\text{Ne} = 12.5$ with high precision. For each sample, we calculated a tendency line
885 applying a data regression including air point and using uncertainties as weight. See text
886 for references.
887

888 **Figure 5.** $^4\text{He}/^3\text{He}$ versus $^{21}\text{Ne}/^{22}\text{Ne}_{(E)}$ for Southern Patagonia peridotites. $^{21}\text{Ne}/^{22}\text{Ne}$
889 ratios extrapolated to a mantle endmember value of $^{20}\text{Ne}/^{22}\text{Ne} = 12.5$ (Trieloff *et al.*,

890 2000). Aiming to avoid in situ produced radiogenic/nucleogenic and cosmogenic
891 effects, as well as elemental fractionation, only crushed samples were considered. Thus,
892 $^4\text{He}/^3\text{He}$ $^{21}\text{Ne}/^{22}\text{Ne}_{(\text{E})}$ are total crushing results for each sample that differ 1σ from air.
893 Uncertainties given correspond to 1σ . It is important to highlight that in some cases
894 uncertainties are smaller than the symbol size. He–Ne relationship can be explained by
895 mixing lines between MORBs and assumed local SCLM endmembers. Mixing lines are
896 presented for r ranging from 1 to 5 [where $r = (^3\text{He}/^{22}\text{Ne})_{\text{SCLM}}/(^3\text{He}/^{22}\text{Ne})_{\text{MORB}}$]. For
897 comparison, European SCLM (sample DW1; Buikin *et al.*, 2005) and Mangaia HIMU
898 (Hanyu *et al.*, 2011) reservoirs were plotted.

899

900 **Figure 6.** Ar–Ne isotope systematics corrected for shallow–level air contamination. For
901 each sample, stepwise crushing generates an array reflecting variable degrees of
902 atmospheric contamination. For samples with well–defined mixing array, we calculated
903 best–fit to extrapolated mantle $^{40}\text{Ar}/^{36}\text{Ar}_{(\text{E})}$ at $^{20}\text{Ne}/^{22}\text{Ne}=12.5$. In order to determine
904 mantle source $^{40}\text{Ar}/^{36}\text{Ar}$, we applied two approaches (see text for more details): 1) linear
905 mixing data regression [$(^{36}\text{Ar}/^{22}\text{Ne})_{\text{MANTLE}}/(^{36}\text{Ar}/^{22}\text{Ne})_{\text{AIR}} = 1$] including air point and
906 using uncertainties as weight to those samples with similar $^{36}\text{Ar}/^{22}\text{Ne}$ ratios to air; and
907 2) best–fit hyperbola extrapolations to those samples that significantly differ from the
908 air in terms of $^{36}\text{Ar}/^{22}\text{Ne}$ ratios (PM14–4 and PM23–1). Grey lines show 100 models
909 randomly sampled from the chi-squared distribution up to 3σ from the best–fit one. For
910 comparison, we fitted the $^{40}\text{Ar}/^{36}\text{Ar}_{(\text{E})}$ for popping rock (Moreira *et al.*, 1998), sample
911 DW1 from European SCLM (Buikin *et al.*, 2005), and depleted MORB sample
912 RC28063D–2 (Tucker *et al.*, 2012). Our results indicate a SCLM endmember with more
913 radiogenic argon isotopic composition than MORB, between 31000 and 54000, similar
914 to previous suggested by Buikin *et al.* (2005) ($^{40}\text{Ar}/^{36}\text{Ar} = 34000\text{--}52000$).

915

916 **Figure 7.** Plot of $^{129}\text{Xe}/^{132}\text{Xe}$ versus $^{136}\text{Xe}/^{132}\text{Xe}$ ratios of step-crushes (a) and total
917 crushing (b) for PAVF and GG peridotites, defines a correlation line similar to MORB–
918 line (Staudacher and Allègre, 1982; Kunz *et al.*, 1998; Tucker *et al.*, 2012). Excess of
919 fissionogenic ^{136}Xe suggest an enrichment of ^{238}U in Southern Patagonia SCLM. Data that
920 differ 1σ from atmospheric ratios are shown and uncertainties are 1σ . It is important to
921 highlight that, in some cases, uncertainties are smaller than symbol size.

922

923 **Figure 8.** Ar–Xe mixing systematics for those samples that are distinguishable from air
924 values with 1σ analytical uncertainties (PM14–4 and PM14–15). Best-fit hyperbolae for
925 these samples yielded extrapolated mantle $^{129-136}\text{Xe}/^{132}\text{Xe}_{(\text{E})}$ at $^{20}\text{Ne}/^{22}\text{Ne} = 12.5$. We
926 applied the approach described in section 5.5 to fit Xe isotopic composition of our
927 samples. Grey lines show 100 models randomly sampled from the chi-squared
928 distribution up to 3σ from the best-fit one. For comparison, a representative sample of
929 depleted MORB mantle (RC28063D–2; Tucker *et al.*, 2012) was plotted. These
930 extrapolations suggest that Patagonian SCLM shows similar excess of ^{129}Xe and ^{136}Xe
931 to that of MORB reservoir.

932

933 **Figure 9.** $^{87}\text{Sr}/^{86}\text{Sr}$ versus $^{143}\text{Nd}/^{144}\text{Nd}$ (a) and $^{206}\text{Pb}/^{204}\text{Pb}$ versus $^{208}\text{Pb}/^{204}\text{Pb}$ (b) isotope
934 variations of whole-rock and mineral separates from selected PAVF and GG
935 peridotites. For comparison, data from HIMU (Hanyu *et al.*, 2011, 2014), PAVF (Stern
936 *et al.*, 1999) and GG (Gorring and Kay, 2000) samples plus Chile Ridge MORBs [NCR
937 from Bach *et al.* (1996) and SCR from Klein and Karsten (1995)] are also plotted.
938 Mantle reservoirs after (Hart *et al.*, 1992).

939

940 **Figure 10.** Rb–Sr mineral isochron for a garnet–spinel harzburgite from PAVF (PM18–
941 17). Uncertainties are 1σ of the mean refer to last digit of $^{87}\text{Sr}/^{86}\text{Sr}$ ratio. The 1σ
942 uncertainties are smaller than size of the symbols.

943

944 **Supplementary material**

945 **Table captions**

946

947 **Table S1.** He, Ne and Ar concentrations (in $\text{cm}^3\text{STP/g}$) and isotopic ratios measured in
948 peridotites from Southern Patagonia by crushing experiments. Total Ne isotopic ratios
949 and their uncertainties were calculated considering results that differ 1σ from air.

950

951 **Table S2.** He, Ne and Ar concentrations (in $\text{cm}^3\text{STP/g}$) and isotopic ratios measured in
952 whole–rock peridotites from Southern Patagonia by heating experiments.

953

954 **Table S3.** Krypton concentrations (in $\text{cm}^3\text{STP/g}$) and isotopic ratios measured in
955 peridotites from Southern Patagonia by crushing experiments.

956

957 **Table S4.** Xenon concentrations (in $\text{cm}^3\text{STP/g}$) and isotopic ratios measured in
958 peridotites from Southern Patagonia by crushing experiments. Numbers in parentheses
959 indicate 1σ uncertainties in last digits.

960

961 **Table S5.** Sample location and lithologies.

962

963 **Table S6.** Mantle source compositions.

964

965 **Table S7.** Rb–Sr, Sm–Nd and Pb–Pb isotopic data for selected Patagonian peridotites
966 analyzed in this study. Numbers in parentheses indicate 2σ uncertainties in the last
967 digits. WR = whole rock, Opx = orthopyroxene, Cpx = clinopyroxene, Phlog =
968 phlogopite.

Figure 1

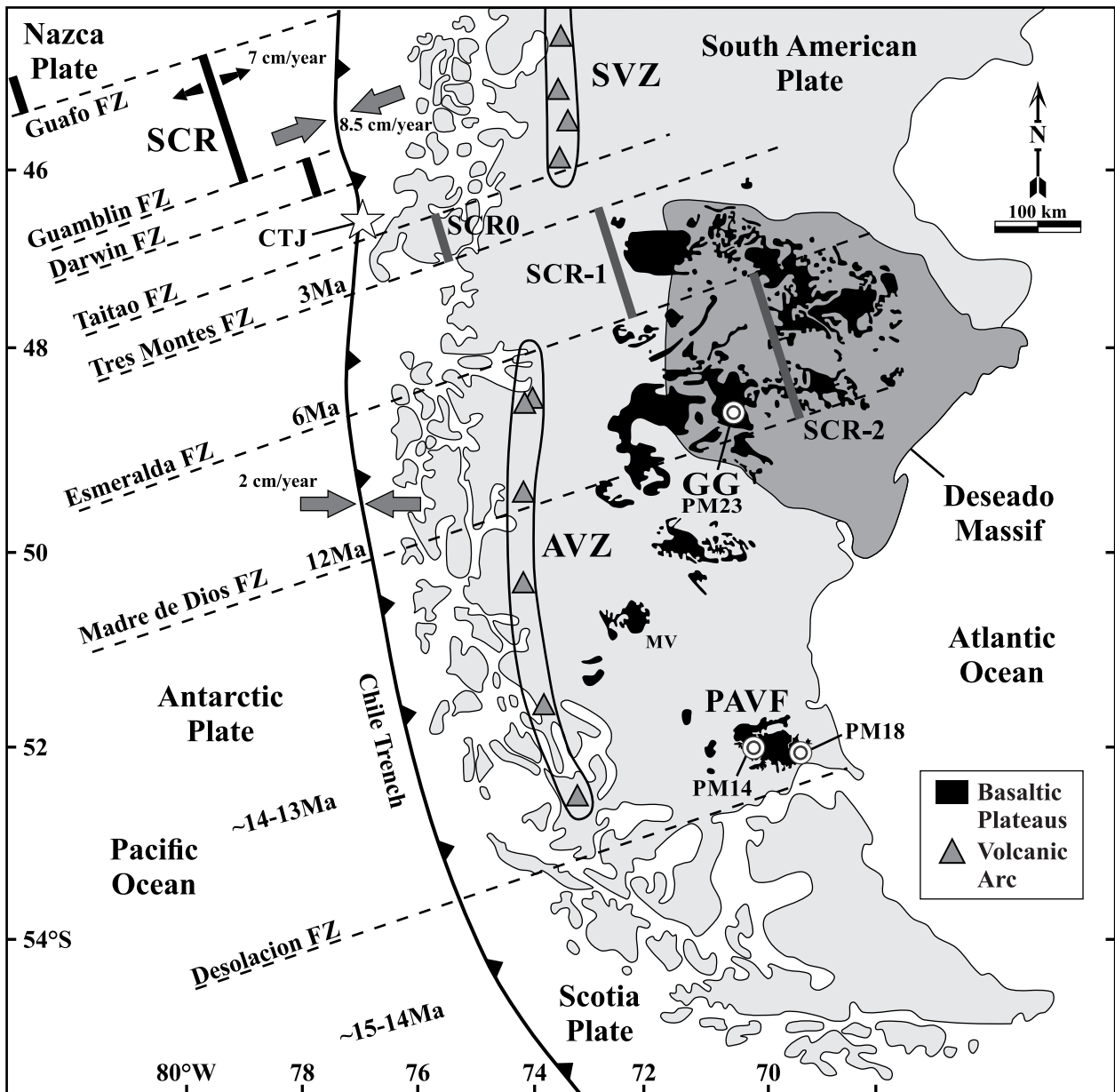


Figure 2

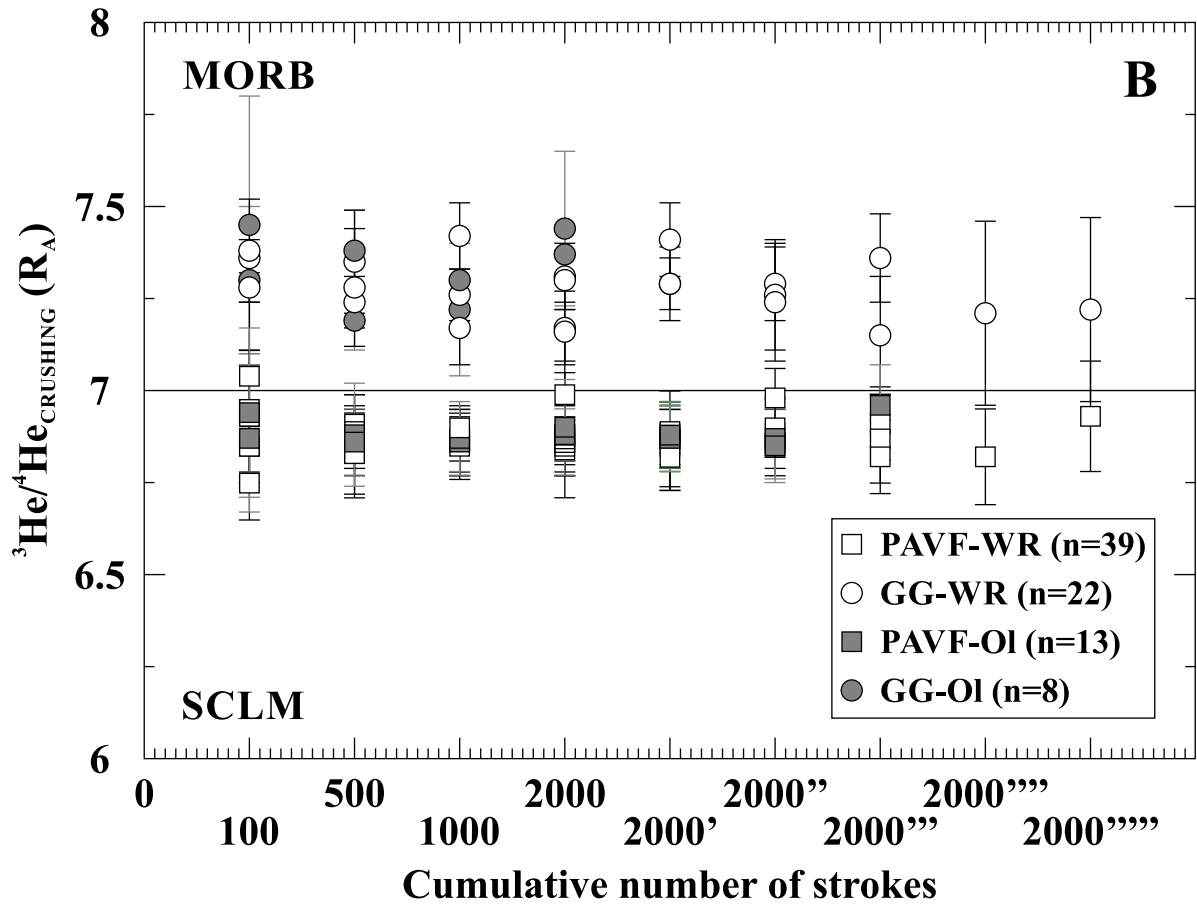
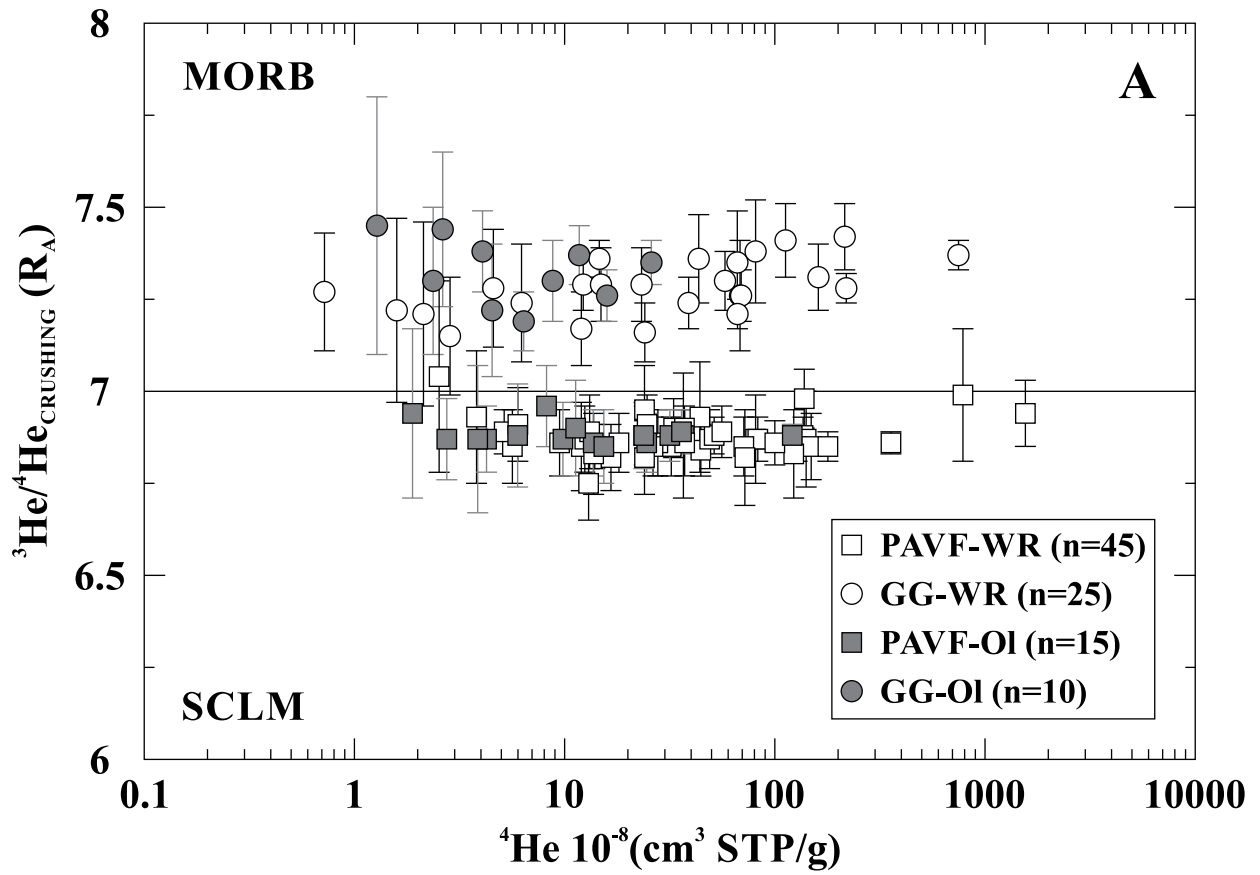


Figure 3

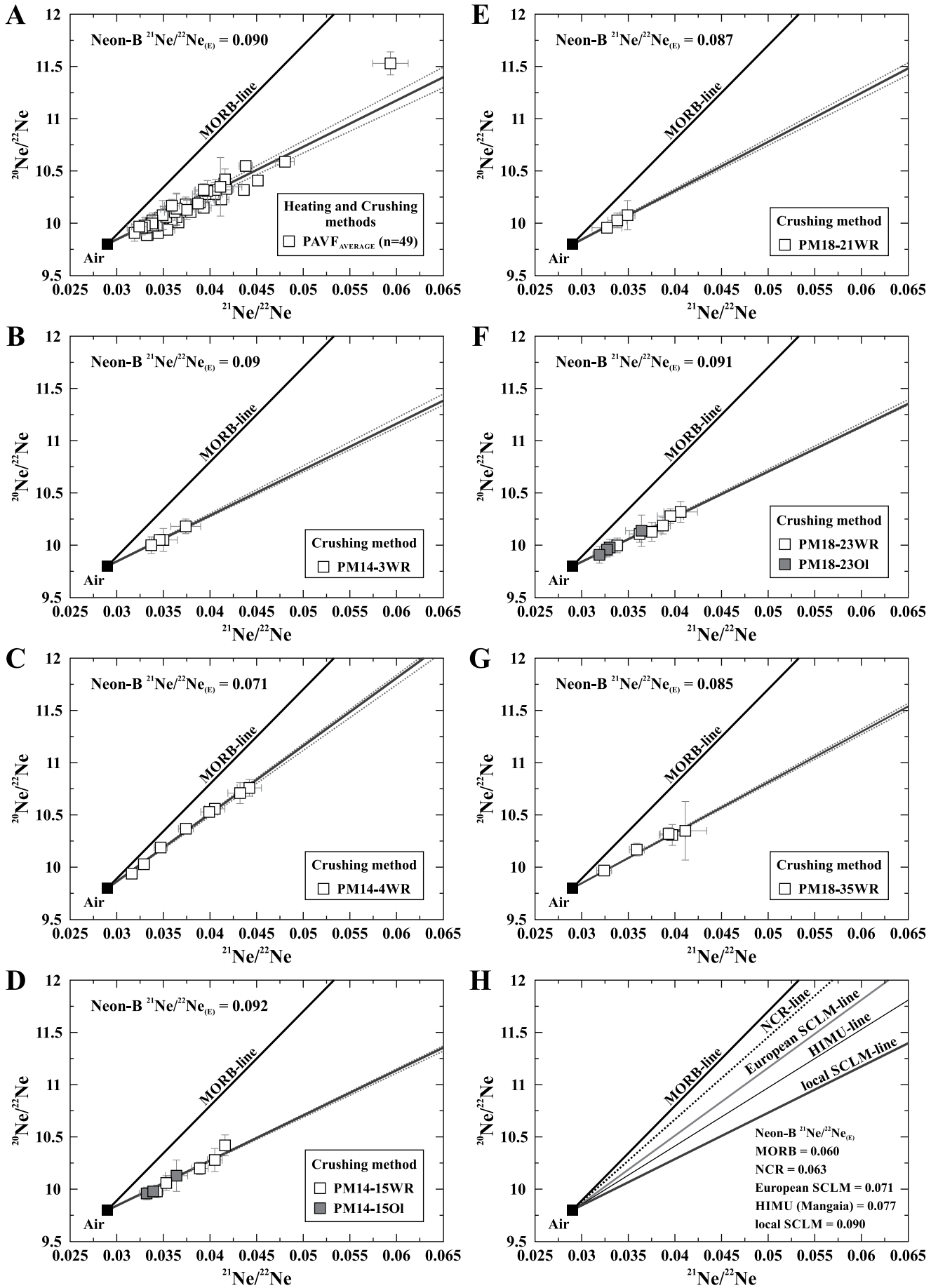


Figure 4

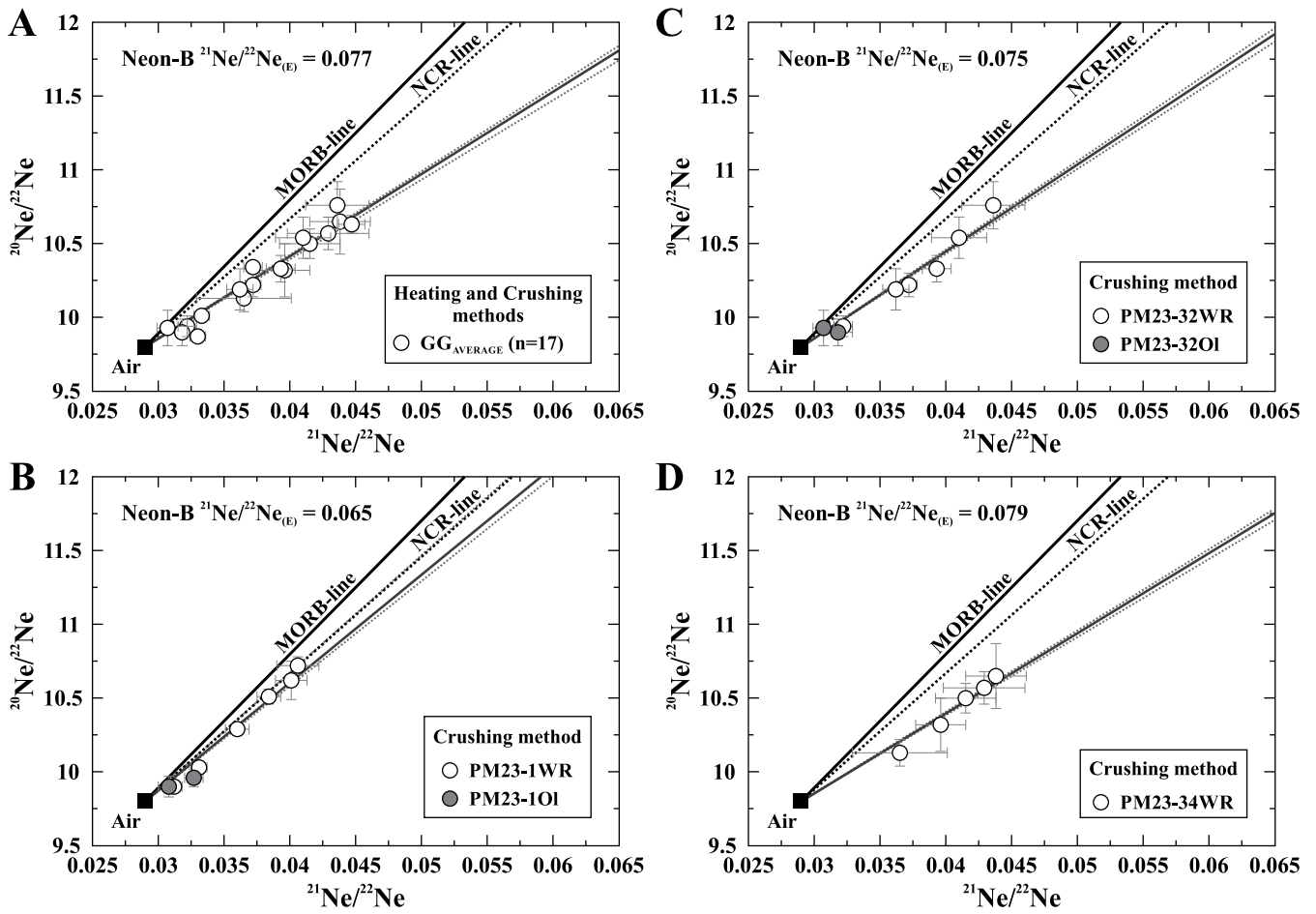


Figure 5

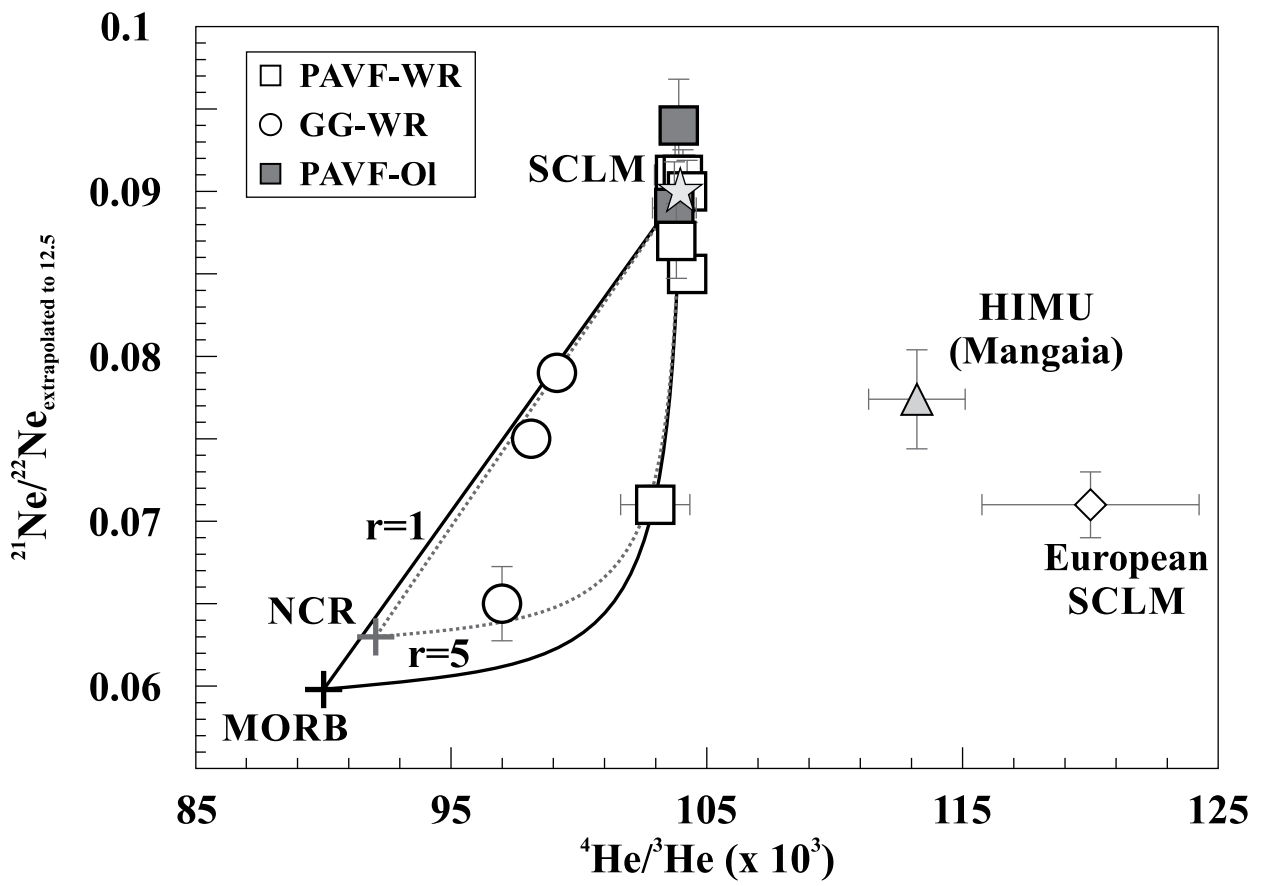


Figure 6

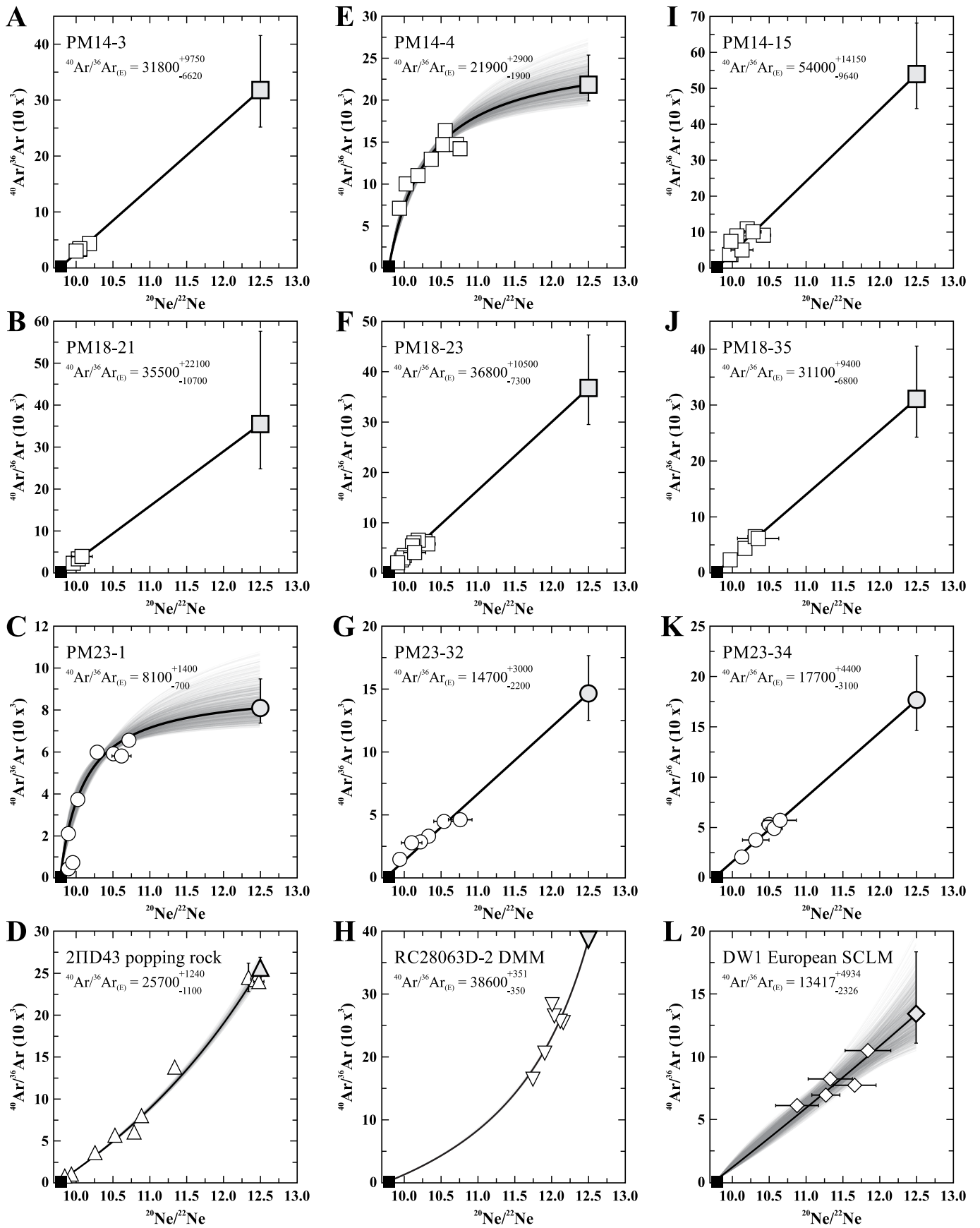


Figure 7

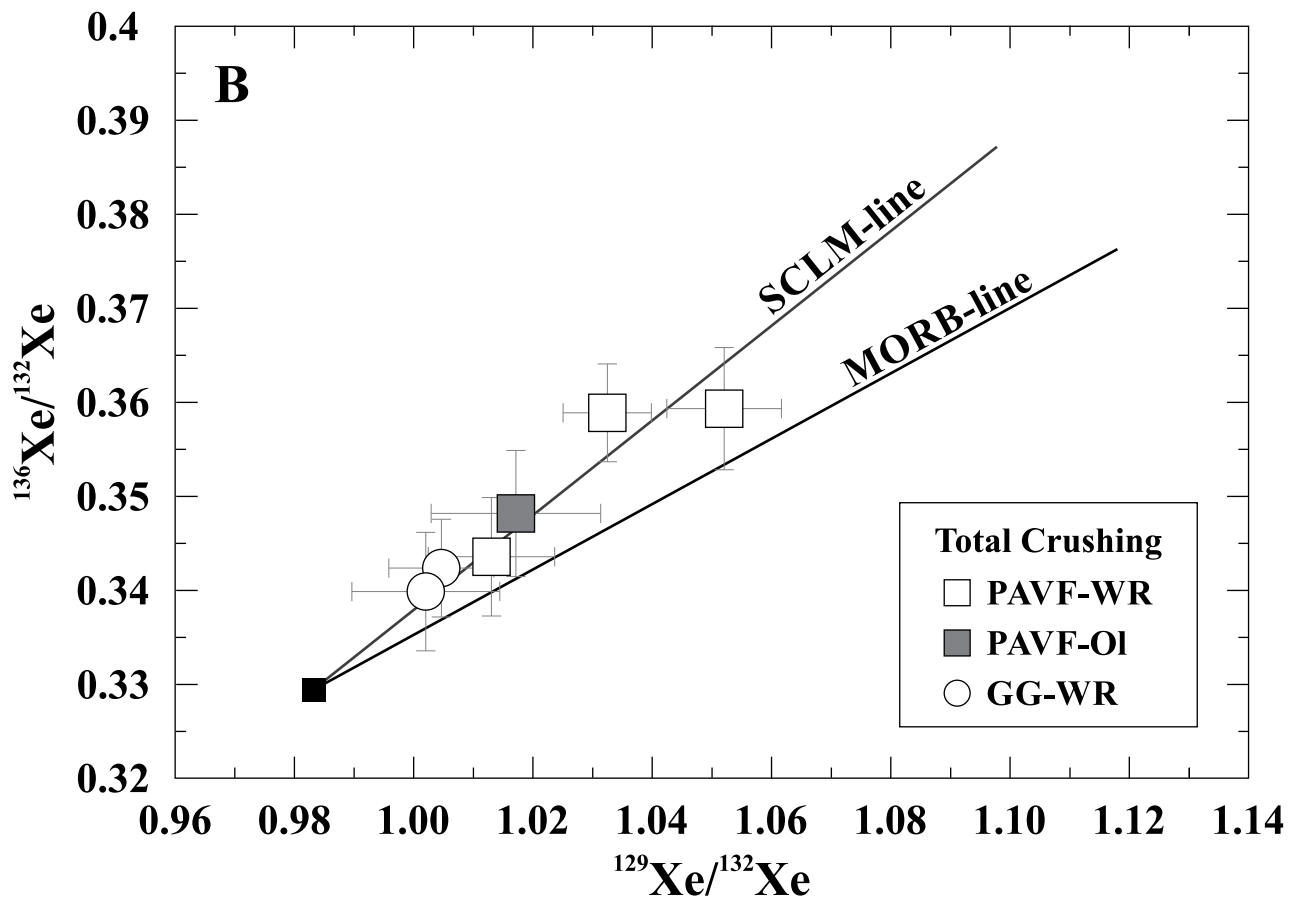
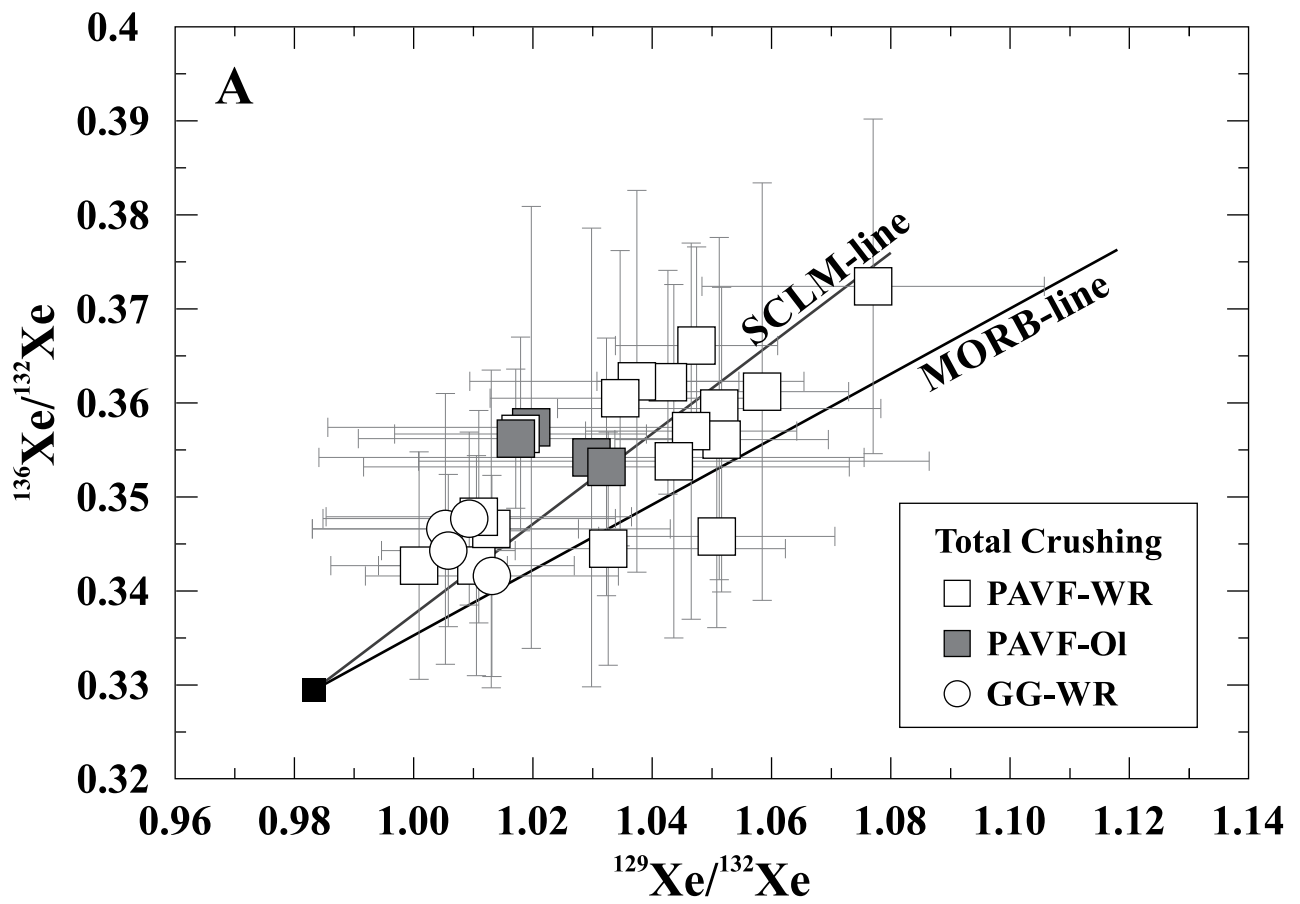


Figure 8

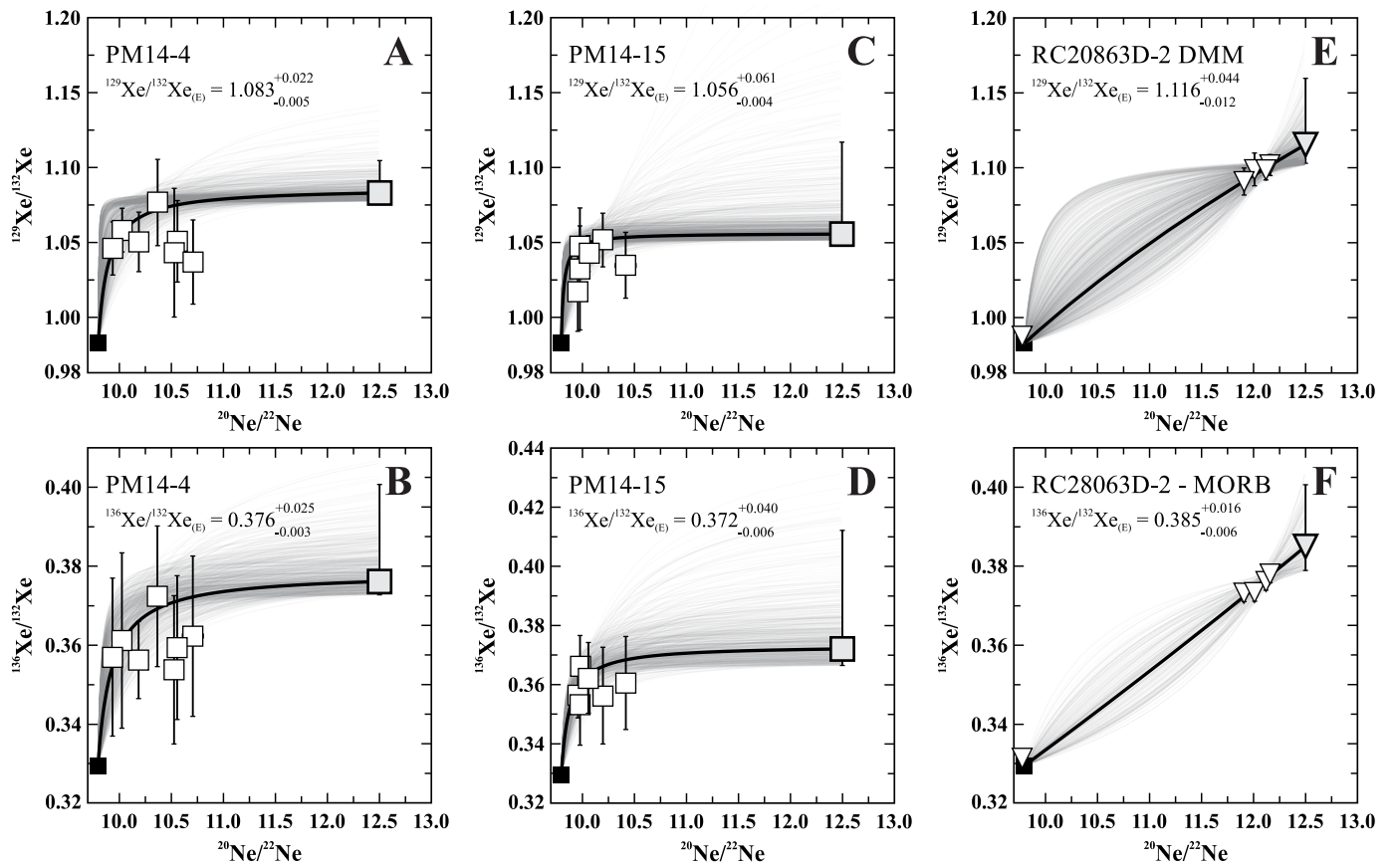


Figure 9

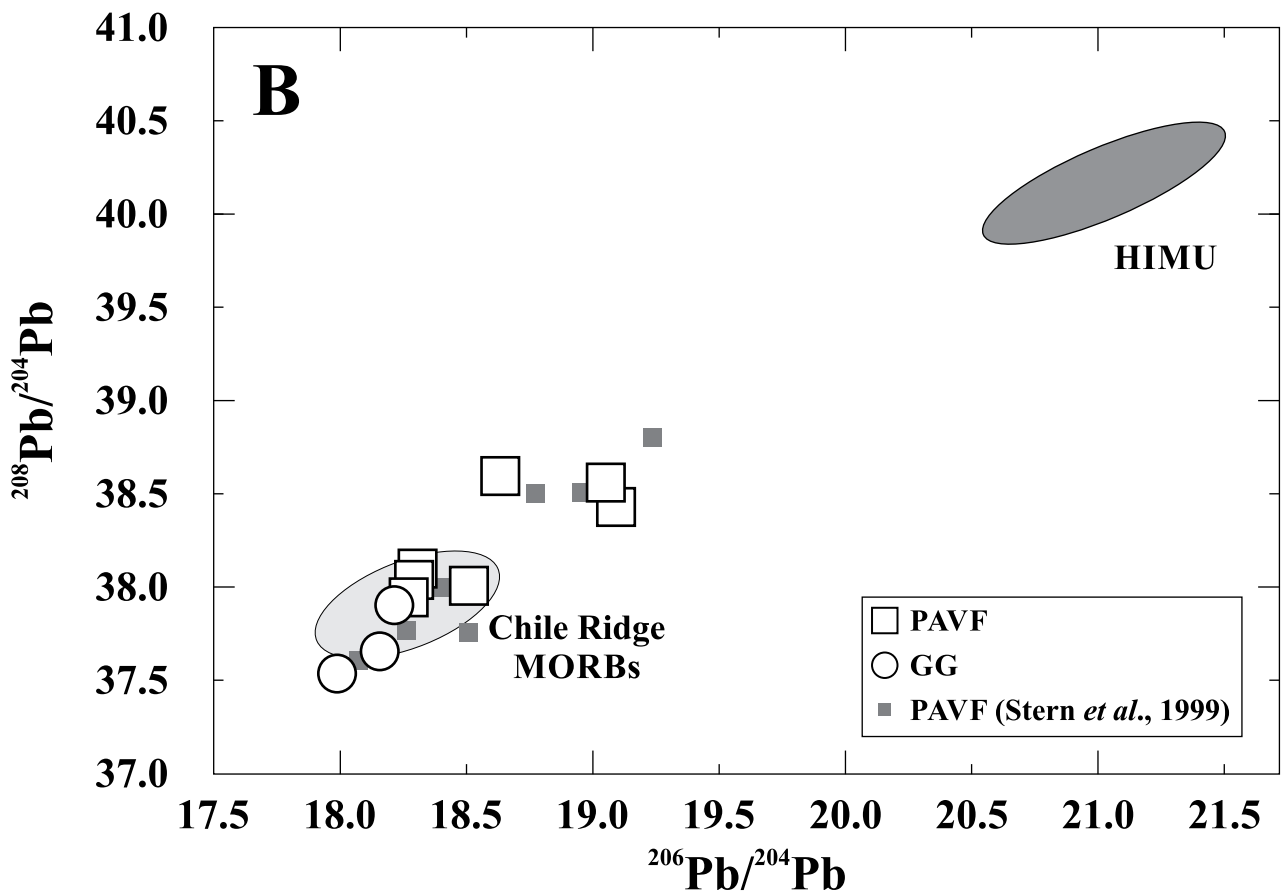
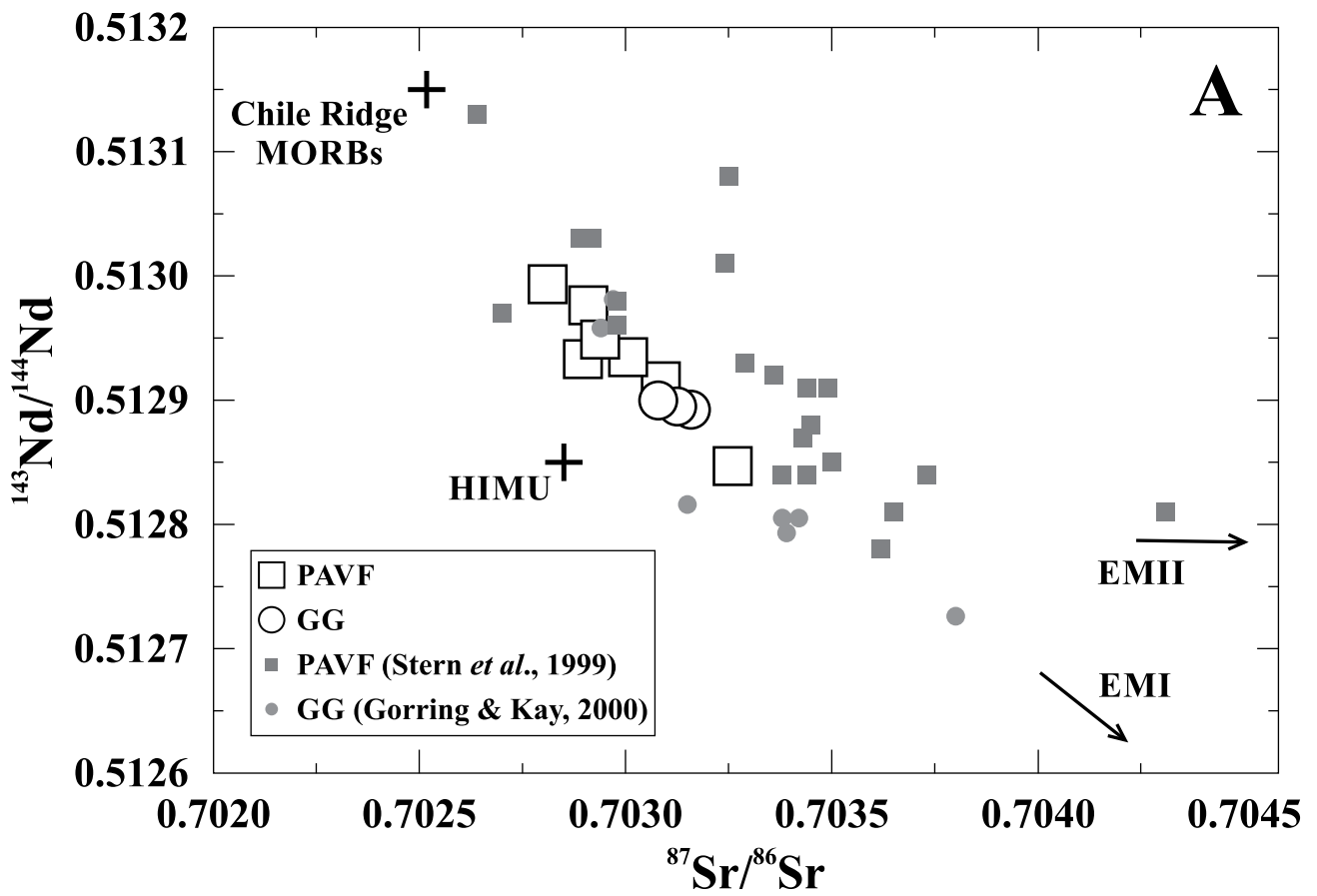


Figure 10

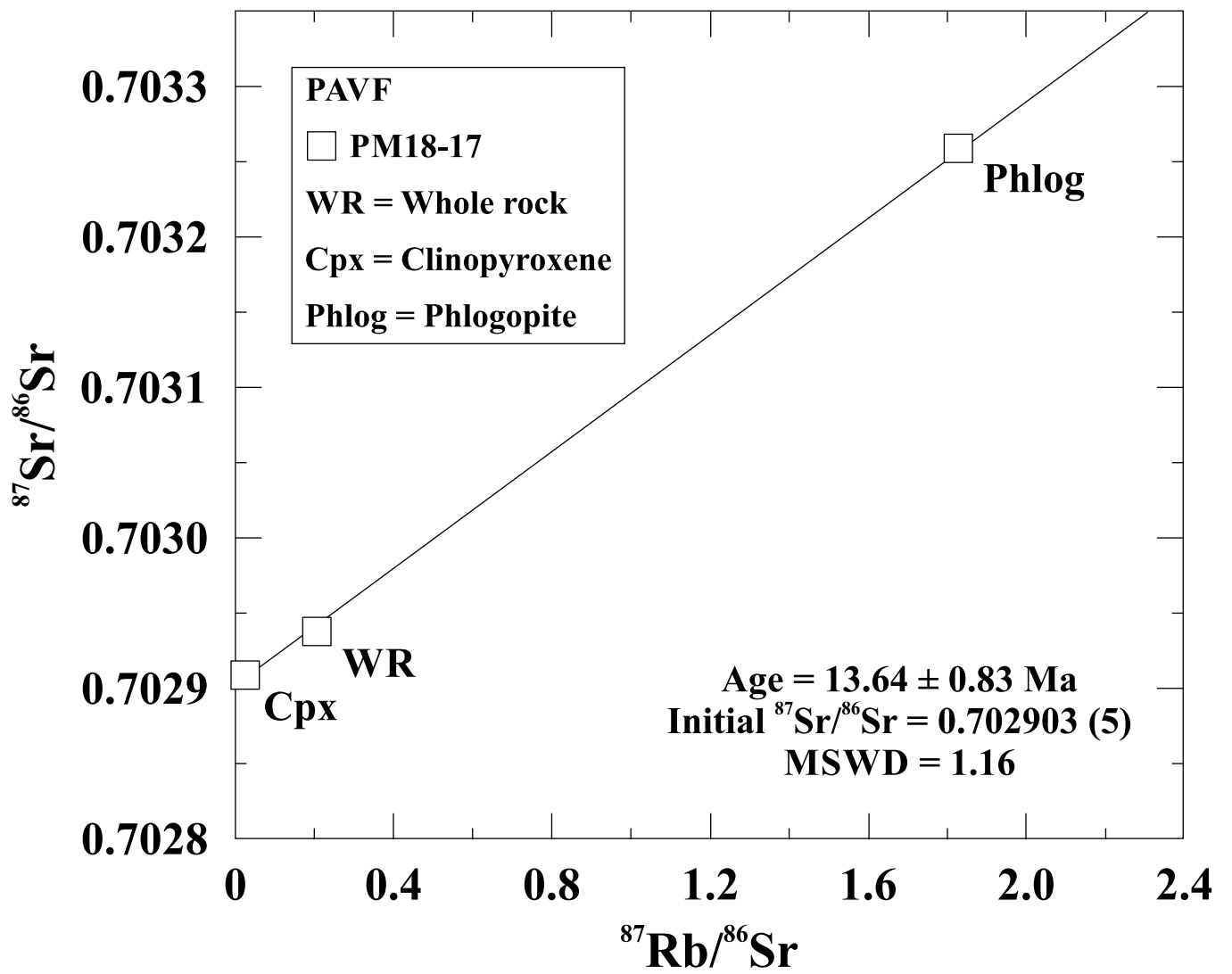


Table S1. He, Ne and Ar concentrations (in cm³STP/g) and isotopic ratios measured in peridotites from Southern Patagonia by crushing experiments. Total Ne isotopic ratios and their uncertainties were calculated considering the results that differ 1σ of air.

Samples	⁴ He×10 ⁻⁸	³ He/ ⁴ He (R _A)	²⁰ Ne×10 ⁻⁸	²⁰ Ne/ ²² Ne	²¹ Ne/ ²² Ne	⁴⁰ Ar×10 ⁻⁸	⁴⁰ Ar/ ³⁶ Ar
Laguna Ana (PAVF)							
PM14-3WR (1.1g)							
100x	3.81	6.93 ± 0.18	0.0006	9.81 ± 0.18	0.0321 ± 0.0012	1.99	1327 ± 44
500x	13.74	6.83 ± 0.11	0.0018	9.89 ± 0.09	0.0312 ± 0.0005	5.84	1984 ± 4
1000x	27.77	6.86 ± 0.09	0.0023	10.00 ± 0.08	0.0337 ± 0.0006	9.04	3011 ± 11
2000x	44.47	6.84 ± 0.07	0.0030	10.05 ± 0.05	0.0346 ± 0.0007	14.26	3432 ± 11
2000'x	23.93	6.88 ± 0.08	0.0014	10.05 ± 0.11	0.0350 ± 0.0015	8.21	3296 ± 9
2000''x	13.91	6.85 ± 0.06	0.0007	10.18 ± 0.07	0.0374 ± 0.0016	5.50	4328 ± 15
Total	127.65	6.85 ± 0.04	0.0099	10.05 ± 0.06	0.0346 ± 0.0005	44.84	2919 ± 5
PM14-4WR (1.13g)							
100x	24.24	6.95 ± 0.12	0.0002	9.91 ± 0.16	0.0305 ± 0.0023	9.27	5518 ± 27
500x	122.73	6.83 ± 0.12	0.0152	9.94 ± 0.03	0.0316 ± 0.0006	45.00	7115 ± 38
1000x	148.92	6.85 ± 0.09	0.0115	10.03 ± 0.04	0.0329 ± 0.0006	49.61	10016 ± 68
2000x	785.33	6.99 ± 0.18	0.0436	10.19 ± 0.03	0.0347 ± 0.0007	59.72	11029 ± 60
2000'x	140.63	6.87 ± 0.13	0.0056	10.35 ± 0.04	0.0374 ± 0.0008	49.05	13012 ± 93
2000''x	137.72	6.98 ± 0.08	0.0048	10.53 ± 0.05	0.0399 ± 0.0009	49.95	14736 ± 179
2000'''x	81.22	6.87 ± 0.12	0.0040	10.56 ± 0.05	0.0405 ± 0.0011	27.65	16373 ± 115
2000''''x	71.78	6.82 ± 0.13	0.0019	10.71 ± 0.10	0.0432 ± 0.0013	26.42	14730 ± 92
2000''''x	43.62	6.93 ± 0.15	0.0012	10.76 ± 0.08	0.0442 ± 0.0013	14.61	14209 ± 197
Total	1556.19	6.94 ± 0.09	0.0879	10.19 ± 0.06	0.0349 ± 0.0005	331.30	11027 ± 15
PM14-15WR (1.14g)							
100x	12.60	6.75 ± 0.10	0.0026	9.83 ± 0.08	0.0307 ± 0.0008	11.10	2063 ± 7
500x	56.26	6.89 ± 0.07	0.0075	9.84 ± 0.05	0.0312 ± 0.0004	41.12	4092 ± 14
1000x	82.62	6.87 ± 0.06	0.0061	9.98 ± 0.06	0.0343 ± 0.0007	64.13	7430 ± 21
2000x	99.75	6.86 ± 0.06	0.0072	10.06 ± 0.07	0.0353 ± 0.0005	79.33	8948 ± 119
2000'x	49.30	6.87 ± 0.08	0.0023	10.20 ± 0.06	0.0389 ± 0.0009	40.56	10926 ± 78
2000''x	32.93	6.90 ± 0.08	0.0013	10.42 ± 0.10	0.0416 ± 0.0005	28.39	9132 ± 26
2000'''x	23.93	6.82 ± 0.10	0.0010	10.28 ± 0.11	0.0405 ± 0.0008	23.18	10085 ± 58
Total	357.38	6.86 ± 0.03	0.0279	10.09 ± 0.06	0.0361 ± 0.0005	287.81	6845 ± 12
PM14-15Ol (1.5g)							
100x	3.86	6.87 ± 0.20	0.0009	9.83 ± 0.10	0.0315 ± 0.0015	1.96	1496 ± 3
500x	13.67	6.86 ± 0.09	0.0016	9.83 ± 0.08	0.0321 ± 0.0007	6.40	2410 ± 14
1000x	24.57	6.86 ± 0.08	0.0035	9.82 ± 0.06	0.0313 ± 0.0008	15.40	2634 ± 6
2000x	31.65	6.88 ± 0.07	0.0025	9.96 ± 0.06	0.0332 ± 0.0008	16.21	3773 ± 13
2000'x	23.79	6.88 ± 0.09	0.0017	9.98 ± 0.05	0.0339 ± 0.0004	11.83	3750 ± 17
2000''x	15.36	6.85 ± 0.10	0.0007	10.13 ± 0.15	0.0364 ± 0.0012	7.54	5032 ± 17
2000'''x	8.20	6.96 ± 0.11	0.0004	9.82 ± 0.12	0.0355 ± 0.0018	4.52	4437 ± 14
Total	121.10	6.88 ± 0.03	0.0113	9.99 ± 0.06	0.0339 ± 0.0005	63.86	3228 ± 5
Laguna Timone (PAVF)							
PM18-21WR (1.11g)							
100x	2.53	7.04 ± 0.26	0.0004	9.39 ± 0.19	0.0316 ± 0.0017	1.60	1376 ± 42
500x	13.15	6.89 ± 0.10	0.0014	9.96 ± 0.05	0.0327 ± 0.0016	5.58	2329 ± 6
1000x	18.13	6.86 ± 0.08	0.0014	10.03 ± 0.07	0.0338 ± 0.0010	6.65	3347 ± 10
2000x	12.48	6.87 ± 0.09	0.0011	10.08 ± 0.14	0.0349 ± 0.0008	5.85	3929 ± 14
2000'x	5.16	6.89 ± 0.06	0.0004	9.63 ± 0.12	0.034 ± 0.0022	2.62	2800 ± 6
Total	51.45	6.88 ± 0.05	0.0048	10.02 ± 0.06	0.0337 ± 0.0005	22.29	2799 ± 5
PM18-23WR (1.15g)							
100x	5.64	6.85 ± 0.10	0.0009	9.88 ± 0.12	0.0316 ± 0.0010	3.24	1933 ± 6
500x	24.69	6.91 ± 0.08	0.0025	10.00 ± 0.07	0.0338 ± 0.0006	15.05	3485 ± 8
1000x	37.15	6.90 ± 0.06	0.0027	10.11 ± 0.08	0.0362 ± 0.0011	24.43	5403 ± 20
2000x	36.71	6.88 ± 0.17	0.0022	10.19 ± 0.08	0.0387 ± 0.0008	26.48	6564 ± 18
2000'x	16.62	6.82 ± 0.09	0.0012	10.13 ± 0.09	0.0375 ± 0.0010	12.86	6017 ± 25
2000''x	9.46	6.86 ± 0.09	0.0007	10.28 ± 0.07	0.0395 ± 0.0014	8.22	6273 ± 16
2000'''x	5.99	6.91 ± 0.10	0.0004	10.32 ± 0.10	0.0406 ± 0.0018	5.70	5804 ± 14

Total	136.27	6.88 ± 0.05	0.0107	10.12 ± 0.05	0.0351 ± 0.0009	95.99	5057 ± 9
PM18-35WR (1.51g)							
100x	32.16	6.85 ± 0.08	0.0037	9.97 ± 0.05	0.0324 ± 0.0008	14.55	2350 ± 6
500x	71.19	6.85 ± 0.08	0.0042	10.17 ± 0.06	0.0359 ± 0.0008	32.76	4384 ± 9
1000x	37.25	6.86 ± 0.09	0.0018	10.31 ± 0.10	0.0397 ± 0.0014	19.56	6482 ± 38
2000x	26.34	6.85 ± 0.08	0.0014	10.32 ± 0.06	0.0393 ± 0.0009	15.48	6376 ± 24
2000'x	12.01	6.85 ± 0.12	0.0007	10.35 ± 0.28	0.0411 ± 0.0023	7.75	6162 ± 25
Total	178.94	6.85 ± 0.04	0.0117	10.15 ± 0.05	0.0360 ± 0.0004	90.11	4424 ± 8
PM18-23OI (1.5g)							
100x	1.89	6.94 ± 0.23	0.0004	9.78 ± 0.10	0.0298 ± 0.0004	1.56	514 ± 4
500x	5.98	6.88 ± 0.14	0.0014	9.91 ± 0.08	0.0319 ± 0.0007	5.22	2044 ± 6
1000x	9.82	6.87 ± 0.10	0.0017	9.96 ± 0.07	0.0327 ± 0.0006	5.88	2643 ± 10
2000x	11.29	6.90 ± 0.13	0.0018	9.98 ± 0.08	0.0330 ± 0.0007	10.06	3020 ± 6
2000'x	4.25	6.87 ± 0.09	0.0005	10.14 ± 0.15	0.0364 ± 0.0017	4.28	4101 ± 12
2000''x	2.75	6.87 ± 0.11	0.0004	9.73 ± 0.12	0.0326 ± 0.0006	2.85	3317 ± 5
Total	35.97	6.89 ± 0.06	0.0061	9.97 ± 0.05	0.0329 ± 0.0005	29.85	2287 ± 5
Gobernador Gregores (GG)							
PM23-1WR (1.13g)							
100x	81.02	7.38 ± 0.14	0.0124	9.78 ± 0.03	0.0299 ± 0.0006	12.03	834 ± 3
500x	66.33	7.35 ± 0.14	0.0232	9.90 ± 0.03	0.0312 ± 0.0006	45.67	2102 ± 7
1000x	215.00	7.42 ± 0.09	0.0096	10.03 ± 0.03	0.0331 ± 0.0006	33.68	3745 ± 16
2000x	161.15	7.31 ± 0.09	0.0040	10.29 ± 0.04	0.0360 ± 0.0009	22.90	6020 ± 27
2000'x	112.47	7.41 ± 0.10	0.0023	10.51 ± 0.05	0.0384 ± 0.0009	13.88	5915 ± 26
2000''x	68.32	7.26 ± 0.15	0.0012	10.72 ± 0.06	0.0406 ± 0.0016	10.30	6564 ± 24
2000'''x	43.45	7.36 ± 0.12	0.0008	10.62 ± 0.13	0.0401 ± 0.0012	6.32	5810 ± 26
Total	747.74	7.37 ± 0.04	0.0535	10.04 ± 0.06	0.0329 ± 0.0005	144.78	2683 ± 6
PM23-32WR (1.15g)							
100x	14.63	7.36 ± 0.05	0.0011	9.94 ± 0.07	0.0322 ± 0.0007	4.14	1470 ± 5
500x	38.89	7.24 ± 0.07	0.0014	10.19 ± 0.14	0.0362 ± 0.0010	10.84	2785 ± 5
1000x	69.15	7.26 ± 0.07	0.0028	10.22 ± 0.08	0.0372 ± 0.0006	17.09	2855 ± 6
2000x	57.95	7.30 ± 0.08	0.0020	10.33 ± 0.09	0.0393 ± 0.0011	15.35	3311 ± 10
2000'x	23.23	7.29 ± 0.10	0.0007	10.54 ± 0.14	0.0410 ± 0.0021	13.26	4484 ± 13
2000''x	14.89	7.29 ± 0.10	0.0004	10.76 ± 0.16	0.0436 ± 0.0024	4.60	4616 ± 19
Total	218.74	7.28 ± 0.04	0.0085	10.24 ± 0.05	0.0374 ± 0.0004	65.28	3067 ± 5
PM23-34WR (1.23g)							
100x	0.72	7.27 ± 0.16	0.0001	9.44 ± 0.29	0.0313 ± 0.0028	0.73	583 ± 2
500x	4.58	7.28 ± 0.16	0.0002	10.13 ± 0.09	0.0365 ± 0.0036	2.00	2076 ± 4
1000x	12.01	7.17 ± 0.10	0.0005	10.32 ± 0.18	0.0396 ± 0.0019	5.19	3758 ± 19
2000x	24.07	7.16 ± 0.08	0.0007	10.50 ± 0.10	0.0415 ± 0.0023	4.99	5309 ± 26
2000'x	12.26	7.29 ± 0.07	0.0004	10.65 ± 0.22	0.0438 ± 0.0023	5.91	5717 ± 23
2000''x	6.24	7.24 ± 0.16	0.0002	10.57 ± 0.11	0.0429 ± 0.0031	2.74	4910 ± 26
2000'''x	2.85	7.15 ± 0.16	0.0192	11.35 ± 0.05	0.0315 ± 0.0004	1.86	3168 ± 8
2000''''x	2.13	7.21 ± 0.25	0.0001	10.09 ± 0.40	0.0410 ± 0.0033	1.51	2539 ± 9
2000''''x	1.59	7.22 ± 0.25	0.0001	9.67 ± 0.27	0.0395 ± 0.0048	1.22	2610 ± 9
Total	66.45	7.21 ± 0.04	0.0215	10.45 ± 0.05	0.0411 ± 0.0003	26.14	3365 ± 6
PM23-1OI (1.55g)							
100x	1.28	7.45 ± 0.35	0.0019	9.74 ± 0.05	0.0296 ± 0.0005	0.83	383 ± 1
500x	4.07	7.38 ± 0.11	0.0034	9.90 ± 0.07	0.0308 ± 0.0008	2.36	436 ± 1
1000x	8.78	7.30 ± 0.11	0.0044	9.71 ± 0.04	0.0293 ± 0.0006	3.66	534 ± 3
2000x	11.73	7.37 ± 0.08	0.0023	9.96 ± 0.06	0.0327 ± 0.0007	3.15	728 ± 2
Total	25.86	7.35 ± 0.06	0.0120	9.92 ± 0.07	0.0300 ± 0.0007	10.00	533 ± 1
PM23-32OI (1.51g)							
100x	2.37	7.30 ± 0.20	0.0012	9.54 ± 0.10	0.0290 ± 0.0010	1.66	419 ± 1
500x	6.39	7.19 ± 0.08	0.0011	9.93 ± 0.12	0.0307 ± 0.0008	2.55	535 ± 1
1000x	4.52	7.22 ± 0.18	0.0007	9.90 ± 0.09	0.0318 ± 0.0011	1.75	625 ± 1
2000x	2.63	7.44 ± 0.21	0.0006	9.53 ± 0.11	0.0314 ± 0.0009	1.28	547 ± 1
Total	15.91	7.26 ± 0.07	0.0035	9.92 ± 0.07	0.0311 ± 0.0007	7.23	522 ± 1

Table S2. He, Ne and Ar concentrations (in cm³STP/g) and isotopic ratios measured in whole-rock peridotites from Southern Patagonia by heating experiments.

Samples	⁴ He×10 ⁻⁸	³ He/ ⁴ He (R _A)	²⁰ Ne×10 ⁻⁸	²⁰ Ne/ ²² Ne	²¹ Ne/ ²² Ne	⁴⁰ Ar×10 ⁻⁸	⁴⁰ Ar/ ³⁶ Ar
<i>Laguna Ana (PAVF)</i>							
PM14-1 (0.54g)	162	8.87 ± 0.11	0.0197	10.23 ± 0.05	0.0412 ± 0.0008	220	419 ± 1
PM14-3 (0.53g)	422	7.27 ± 0.11	0.0257	10.33 ± 0.04	0.0417 ± 0.0008	345	6418 ± 38
PM14-4 (0.53g)	5303	6.90 ± 0.10	0.0033	11.53 ± 0.11	0.0593 ± 0.0019	3135	17718 ± 159
PM14-5 (0.54g)	246	7.15 ± 0.14	0.0136	10.15 ± 0.04	0.0393 ± 0.0008	484	8189 ± 55
PM14-6 (0.53g)	394	7.10 ± 0.09	0.0234	10.59 ± 0.04	0.0480 ± 0.0010	104	3095 ± 9
PM14-7 (0.54g)	136	7.82 ± 0.14	0.0243	9.94 ± 0.04	0.0354 ± 0.0008	47	2223 ± 6
PM14-14 (0.66g)	286	7.49 ± 0.07	0.0164	10.41 ± 0.03	0.0451 ± 0.0005	87	3565 ± 15
PM14-15 (0.65g)	349	6.84 ± 0.06	0.0507	10.15 ± 0.03	0.0379 ± 0.0005	585	9803 ± 47
PM14-17 (0.66g)	44	8.98 ± 0.12	0.0164	9.89 ± 0.04	0.0333 ± 0.0005	12	1287 ± 4
PM14-19 (0.68g)	212	7.70 ± 0.11	0.0196	10.32 ± 0.03	0.0436 ± 0.0006	160	9785 ± 72
<i>Laguna Timone (PAVF)</i>							
PM18-2 (0.59g)	239	7.16 ± 0.07	0.0185	10.06 ± 0.04	0.0364 ± 0.0005	56	2513 ± 5
PM18-11 (0.64g)	43	8.04 ± 0.10	0.0083	10.03 ± 0.05	0.0359 ± 0.0007	27	2899 ± 5
PM18-13 (0.64g)	143	7.34 ± 0.08	0.0151	9.91 ± 0.05	0.0344 ± 0.0004	59	3798 ± 16
PM18-17 (0.64g)	30	8.47 ± 0.15	0.0169	9.78 ± 0.04	0.0315 ± 0.0003	68	620 ± 2
PM18-19 (0.62g)	108	7.39 ± 0.07	0.0211	9.89 ± 0.03	0.0332 ± 0.0004	35	1757 ± 6
PM18-21 (0.64g)	328	7.11 ± 0.06	0.0193	10.13 ± 0.04	0.0379 ± 0.0009	117	5883 ± 29
PM18-22 (0.67g)	104	7.50 ± 0.07	0.0113	10.01 ± 0.05	0.0366 ± 0.0006	35	1690 ± 6
PM18-23 (0.57g)	411	7.12 ± 0.06	0.0202	10.38 ± 0.04	0.0415 ± 0.0003	296	8836 ± 34
PM18-35 (0.59g)	329	7.11 ± 0.06	0.0119	10.55 ± 0.05	0.0438 ± 0.0007	144	7025 ± 22
PM18-36 (0.67g)	15	10.38 ± 0.20	0.0101	9.97 ± 0.04	0.0342 ± 0.0003	8	519 ± 1
<i>Gobernador Gregores (GG)</i>							
PM23-1 (0.51g)	1207	7.36 ± 0.12	0.0378	10.34 ± 0.03	0.0372 ± 0.0007	147	4831 ± 14
PM23-2 (0.50g)	83	5.45 ± 0.11	0.0019	9.60 ± 0.06	0.0330 ± 0.0011	10	376 ± 1
PM23-4 (0.51g)	52	8.36 ± 0.20	0.0088	9.88 ± 0.06	0.0380 ± 0.0008	11	661 ± 1
PM23-5 (0.50g)	78	7.06 ± 0.13	0.0088	9.87 ± 0.03	0.0375 ± 0.0008	9	834 ± 2
PM23-6 (0.53g)	82	3.60 ± 0.09	0.0832	9.85 ± 0.03	0.0303 ± 0.0005	11	662 ± 4
PM23-7 (0.51g)	105	3.80 ± 0.09	0.0516	9.84 ± 0.03	0.0307 ± 0.0006	12	829 ± 3
PM23-11 (0.50g)	114	7.17 ± 0.12	0.0240	9.87 ± 0.02	0.0330 ± 0.0006	22	722 ± 2
PM23-14 (0.49g)	112	7.21 ± 0.14	0.0176	10.01 ± 0.03	0.0333 ± 0.0006	89	3104 ± 7
PM23-15 (0.51g)	36	7.49 ± 0.17	0.0152	9.89 ± 0.05	0.0330 ± 0.0007	9	490 ± 1
PM23-17 (0.51g)	62	4.82 ± 0.12	0.0276	9.86 ± 0.03	0.0316 ± 0.0006	8	524 ± 1
PM23-18 (0.56g)	55	8.18 ± 0.15	0.0098	9.91 ± 0.06	0.0357 ± 0.0008	9	905 ± 2
PM23-20 (0.53g)	75	7.17 ± 0.11	0.0162	9.79 ± 0.04	0.0352 ± 0.0007	19	980 ± 3
PM23-31 (0.52g)	56	7.46 ± 0.15	0.0219	9.80 ± 0.03	0.0325 ± 0.0006	10	844 ± 2
PM23-32 (0.53g)	406	7.29 ± 0.09	0.0090	10.63 ± 0.06	0.0447 ± 0.0010	89	4720 ± 17
PM23-34 (0.52g)	126	4.18 ± 0.08	0.0060	9.93 ± 0.06	0.0398 ± 0.0010	20	1575 ± 5

Table S3. Krypton concentrations (in cm³STP/g) and isotopic ratios measured in peridotites from Southern Patagonia by crushing experiments.

Samples	⁸⁴ Kr×10 ⁻¹³	⁷⁸ Kr/ ⁸⁴ Kr	⁸⁰ Kr/ ⁸⁴ Kr	⁸² Kr/ ⁸⁴ Kr	⁸³ Kr/ ⁸⁴ Kr	⁸⁶ Kr/ ⁸⁴ Kr
<i>Laguna Ana (PAVF)</i>						
PM14-3WR (1.1g)						
100x	3.34	0.0069 ± 0.0036	0.0444 ± 0.0038	0.212 ± 0.008	0.207 ± 0.004	0.319 ± 0.008
500x	11.37	0.0063 ± 0.0019	0.0417 ± 0.0023	0.205 ± 0.004	0.209 ± 0.004	0.310 ± 0.006
1000x	14.85	0.0068 ± 0.0012	0.0437 ± 0.0011	0.196 ± 0.002	0.206 ± 0.005	0.306 ± 0.006
2000x	16.90	0.0064 ± 0.0012	0.0435 ± 0.0014	0.206 ± 0.003	0.205 ± 0.003	0.308 ± 0.002
2000'x	11.12	0.0066 ± 0.0017	0.0432 ± 0.0011	0.204 ± 0.005	0.208 ± 0.004	0.306 ± 0.004
2000''x	4.86	0.0060 ± 0.0018	0.0406 ± 0.0039	0.205 ± 0.011	0.210 ± 0.007	0.308 ± 0.005
Total	62.43	0.0065 ± 0.0007	0.043 ± 0.0007	0.203 ± 0.002	0.207 ± 0.002	0.308 ± 0.002
PM14-4WR (1.13g)						
100x	5.69	0.0056 ± 0.0019	0.0440 ± 0.0021	0.213 ± 0.005	0.209 ± 0.021	0.314 ± 0.009
500x	11.21	0.0112 ± 0.0010	0.0570 ± 0.0012	0.211 ± 0.003	0.209 ± 0.004	0.304 ± 0.005
1000x	15.03	0.0069 ± 0.0021	0.0455 ± 0.0012	0.210 ± 0.003	0.207 ± 0.004	0.308 ± 0.004
2000x	16.85	0.0072 ± 0.0014	0.0453 ± 0.0008	0.209 ± 0.006	0.206 ± 0.004	0.304 ± 0.005
2000'x	12.49	0.0060 ± 0.0019	0.0456 ± 0.0019	0.212 ± 0.004	0.207 ± 0.006	0.308 ± 0.006
2000''x	12.07	0.0073 ± 0.0014	0.0467 ± 0.0015	0.209 ± 0.005	0.207 ± 0.006	0.307 ± 0.004
2000'''x	5.31	0.0084 ± 0.0029	0.0617 ± 0.0022	0.214 ± 0.009	0.207 ± 0.003	0.306 ± 0.005
2000''''x	6.92	0.0069 ± 0.0019	0.0555 ± 0.0029	0.213 ± 0.005	0.211 ± 0.006	0.311 ± 0.007
2000''''x	4.43	0.0076 ± 0.0022	0.0487 ± 0.0017	0.214 ± 0.008	0.217 ± 0.006	0.314 ± 0.009
Total	90.00	0.0075 ± 0.0006	0.0489 ± 0.0005	0.211 ± 0.002	0.208 ± 0.002	0.307 ± 0.002
PM14-15WR (1.14g)						
100x	20.34	0.0062 ± 0.0014	0.0412 ± 0.0015	0.205 ± 0.005	0.206 ± 0.003	0.306 ± 0.004
500x	49.32	0.0068 ± 0.0005	0.0412 ± 0.0008	0.202 ± 0.002	0.204 ± 0.002	0.303 ± 0.003
1000x	35.97	0.0062 ± 0.0006	0.0424 ± 0.0010	0.203 ± 0.002	0.206 ± 0.003	0.304 ± 0.003
2000x	36.15	0.0054 ± 0.0011	0.0439 ± 0.0010	0.204 ± 0.002	0.204 ± 0.002	0.305 ± 0.003
2000'x	20.65	0.0065 ± 0.0010	0.0423 ± 0.0013	0.204 ± 0.003	0.206 ± 0.004	0.304 ± 0.003
2000''x	11.32	0.0056 ± 0.0012	0.0498 ± 0.0024	0.202 ± 0.002	0.209 ± 0.005	0.303 ± 0.003
2000'''x	9.58	0.0061 ± 0.0017	0.0477 ± 0.0020	0.205 ± 0.003	0.207 ± 0.003	0.305 ± 0.004
Total	183.34	0.0062 ± 0.0004	0.0429 ± 0.0004	0.203 ± 0.001	0.205 ± 0.001	0.304 ± 0.001
PM14-15OI (1.5g)						
100x	6.00	0.0053 ± 0.0016	0.0385 ± 0.0028	0.210 ± 0.007	0.208 ± 0.006	0.311 ± 0.012
500x	15.62	0.0063 ± 0.0015	0.0422 ± 0.0017	0.202 ± 0.003	0.206 ± 0.007	0.306 ± 0.004
1000x	25.29	0.0063 ± 0.0005	0.0429 ± 0.0009	0.204 ± 0.002	0.205 ± 0.004	0.305 ± 0.004
2000x	21.18	0.0071 ± 0.0013	0.0454 ± 0.0012	0.205 ± 0.002	0.207 ± 0.002	0.303 ± 0.005
2000'x	15.66	0.0060 ± 0.0016	0.0438 ± 0.0018	0.204 ± 0.003	0.205 ± 0.004	0.302 ± 0.005
2000''x	9.59	0.0069 ± 0.0013	0.0439 ± 0.0015	0.206 ± 0.003	0.208 ± 0.006	0.306 ± 0.004
2000'''x	6.29	0.0072 ± 0.0015	0.0432 ± 0.0025	0.205 ± 0.007	0.210 ± 0.006	0.307 ± 0.010
Total	99.63	0.0065 ± 0.0005	0.0433 ± 0.0006	0.205 ± 0.001	0.206 ± 0.002	0.305 ± 0.002
<i>Laguna Timone (PAVF)</i>						
PM18-21WR (1.11g)						
100x	3.05	0.0075 ± 0.0042	0.0399 ± 0.0047	0.202 ± 0.010	0.206 ± 0.007	0.316 ± 0.009
500x	8.86	0.0069 ± 0.0018	0.0420 ± 0.0018	0.205 ± 0.005	0.211 ± 0.006	0.309 ± 0.007
1000x	8.87	0.0064 ± 0.0014	0.0412 ± 0.0020	0.206 ± 0.003	0.209 ± 0.004	0.311 ± 0.005
2000x	6.87	0.0050 ± 0.0012	0.0423 ± 0.0032	0.204 ± 0.006	0.205 ± 0.006	0.312 ± 0.006
2000'x	3.31	0.0089 ± 0.0044	0.0413 ± 0.0035	0.205 ± 0.009	0.206 ± 0.007	0.305 ± 0.006
Total	30.96	0.0066 ± 0.0009	0.0415 ± 0.0012	0.205 ± 0.003	0.208 ± 0.003	0.310 ± 0.003
PM18-23WR (1.15g)						
100x	17.00	0.0064 ± 0.0017	0.0414 ± 0.0013	0.204 ± 0.003	0.205 ± 0.004	0.308 ± 0.005
500x	31.44	0.0029 ± 0.0006	0.0416 ± 0.0012	0.205 ± 0.003	0.204 ± 0.002	0.304 ± 0.004
1000x	37.91	0.0062 ± 0.0008	0.0426 ± 0.0013	0.205 ± 0.004	0.204 ± 0.004	0.305 ± 0.004
2000x	73.69	0.0062 ± 0.0009	0.0413 ± 0.0007	0.204 ± 0.002	0.205 ± 0.002	0.304 ± 0.002
2000'x	62.98	0.0057 ± 0.0010	0.0405 ± 0.0008	0.203 ± 0.002	0.202 ± 0.002	0.304 ± 0.002
2000''x	82.14	0.0062 ± 0.0008	0.0404 ± 0.0008	0.202 ± 0.002	0.202 ± 0.002	0.305 ± 0.003
2000'''x	54.10	0.0060 ± 0.0010	0.0397 ± 0.0007	0.202 ± 0.003	0.204 ± 0.003	0.305 ± 0.003
Total	359.25	0.0058 ± 0.0004	0.0409 ± 0.0003	0.203 ± 0.001	0.203 ± 0.001	0.305 ± 0.001

PM18-35WR (1.51g)

100x	26.11	0.0061 ± 0.0011	0.0424 ± 0.0018	0.206 ± 0.002	0.205 ± 0.003	0.303 ± 0.004
500x	24.32	0.0063 ± 0.0009	0.0470 ± 0.0014	0.204 ± 0.003	0.204 ± 0.003	0.301 ± 0.003
1000x	13.87	0.0067 ± 0.0008	0.0461 ± 0.0022	0.203 ± 0.004	0.208 ± 0.004	0.303 ± 0.004
2000x	12.81	0.0064 ± 0.0015	0.0442 ± 0.0020	0.205 ± 0.005	0.207 ± 0.004	0.306 ± 0.004
2000'x	7.62	0.0071 ± 0.0016	0.0449 ± 0.0030	0.204 ± 0.003	0.206 ± 0.005	0.307 ± 0.005
Total	84.74	0.0064 ± 0.0005	0.0448 ± 0.0009	0.205 ± 0.002	0.206 ± 0.002	0.303 ± 0.002

PM18-23OI (1.5g)

100x	27.97	0.0054 ± 0.0005	0.0406 ± 0.0016	0.204 ± 0.004	0.205 ± 0.004	0.308 ± 0.007
500x	13.18	0.0058 ± 0.0011	0.0426 ± 0.0014	0.206 ± 0.003	0.207 ± 0.003	0.309 ± 0.009
1000x	16.19	0.0064 ± 0.0012	0.0426 ± 0.0014	0.203 ± 0.005	0.206 ± 0.004	0.303 ± 0.004
2000x	16.24	0.0064 ± 0.0016	0.0434 ± 0.0012	0.205 ± 0.003	0.206 ± 0.003	0.302 ± 0.004
2000'x	5.47	0.0067 ± 0.0014	0.0439 ± 0.0028	0.209 ± 0.005	0.211 ± 0.004	0.307 ± 0.009
2000''x	4.72	0.0047 ± 0.0021	0.0438 ± 0.0034	0.209 ± 0.008	0.207 ± 0.005	0.315 ± 0.013
Total	83.77	0.0059 ± 0.0005	0.0422 ± 0.0007	0.205 ± 0.002	0.206 ± 0.002	0.306 ± 0.003

Gobernador Gregores (GG)**PM23-1WR (1.13g)**

100x	47.94	0.0065 ± 0.0007	0.0414 ± 0.0011	0.203 ± 0.003	0.202 ± 0.002	0.304 ± 0.003
500x	67.71	0.0067 ± 0.0005	0.0411 ± 0.0008	0.204 ± 0.002	0.202 ± 0.002	0.305 ± 0.002
1000x	33.87	0.0068 ± 0.0007	0.0420 ± 0.0010	0.205 ± 0.002	0.203 ± 0.003	0.305 ± 0.004
2000x	15.37	0.0067 ± 0.0014	0.0456 ± 0.0011	0.206 ± 0.004	0.205 ± 0.004	0.306 ± 0.004
2000'x	12.49	0.0072 ± 0.0018	0.0453 ± 0.0008	0.210 ± 0.005	0.208 ± 0.005	0.306 ± 0.004
2000''x	8.40	0.0069 ± 0.0016	0.0463 ± 0.0020	0.213 ± 0.003	0.212 ± 0.005	0.316 ± 0.007
2000'''x	6.68	0.0061 ± 0.0016	0.0430 ± 0.0028	0.211 ± 0.006	0.208 ± 0.003	0.313 ± 0.010
Total	192.46	0.0067 ± 0.0003	0.0423 ± 0.0005	0.205 ± 0.001	0.204 ± 0.001	0.306 ± 0.001

PM23-32WR (1.15g)

100x	12.65	0.0062 ± 0.0012	0.0412 ± 0.0018	0.202 ± 0.004	0.205 ± 0.005	0.305 ± 0.005
500x	17.72	0.0060 ± 0.0012	0.0421 ± 0.0012	0.203 ± 0.003	0.206 ± 0.002	0.307 ± 0.006
1000x	27.97	0.0064 ± 0.0010	0.0421 ± 0.0010	0.204 ± 0.003	0.204 ± 0.002	0.303 ± 0.003
2000x	21.77	0.0060 ± 0.0009	0.0428 ± 0.0010	0.205 ± 0.003	0.204 ± 0.002	0.304 ± 0.004
2000'x	9.14	0.0058 ± 0.0020	0.0380 ± 0.0009	0.204 ± 0.004	0.207 ± 0.003	0.309 ± 0.007
2000''x	5.79	0.0069 ± 0.0019	0.0414 ± 0.0023	0.205 ± 0.005	0.212 ± 0.006	0.309 ± 0.008
Total	95.04	0.0062 ± 0.0005	0.0417 ± 0.0005	0.204 ± 0.001	0.205 ± 0.001	0.305 ± 0.002

PM23-34WR (1.23g)

100x	2.21	0.0060 ± 0.0026	0.0350 ± 0.0036	0.206 ± 0.010	0.199 ± 0.010	0.315 ± 0.019
500x	3.64	0.0052 ± 0.0026	0.0423 ± 0.0035	0.199 ± 0.006	0.201 ± 0.008	0.308 ± 0.014
1000x	6.79	0.0057 ± 0.0035	0.0418 ± 0.0031	0.207 ± 0.009	0.209 ± 0.005	0.309 ± 0.071
2000x	10.44	0.0054 ± 0.0011	0.0440 ± 0.0015	0.203 ± 0.004	0.204 ± 0.005	0.305 ± 0.008
2000'x	5.58	0.0067 ± 0.0031	0.0413 ± 0.0031	0.204 ± 0.004	0.209 ± 0.008	0.311 ± 0.008
2000''x	3.71	0.0081 ± 0.0022	0.0403 ± 0.0028	0.208 ± 0.006	0.210 ± 0.003	0.310 ± 0.012
2000'''x	4.56	0.0063 ± 0.0012	0.0431 ± 0.0027	0.208 ± 0.009	0.212 ± 0.004	0.305 ± 0.008
2000''''x	1.52	0.0081 ± 0.0064	0.0417 ± 0.0020	0.205 ± 0.010	0.208 ± 0.010	0.304 ± 0.011
2000''''x	1.16	0.0070 ± 0.0053	0.0426 ± 0.0053	0.201 ± 0.011	0.204 ± 0.021	0.303 ± 0.014
Total	39.60	0.0062 ± 0.0009	0.0420 ± 0.0010	0.205 ± 0.002	0.207 ± 0.002	0.308 ± 0.013

PM23-1OI (1.55g)

100x	16.43	0.0062 ± 0.0021	0.0411 ± 0.0008	0.207 ± 0.003	0.204 ± 0.003	0.310 ± 0.004
500x	33.13	0.0059 ± 0.0013	0.0406 ± 0.0011	0.202 ± 0.002	0.203 ± 0.002	0.307 ± 0.002
1000x	37.80	0.0060 ± 0.0008	0.0405 ± 0.0008	0.205 ± 0.002	0.203 ± 0.002	0.309 ± 0.004
2000x	29.41	0.0066 ± 0.0015	0.0422 ± 0.0049	0.203 ± 0.002	0.204 ± 0.003	0.303 ± 0.003
Total	116.77	0.0061 ± 0.0007	0.0410 ± 0.0013	0.204 ± 0.001	0.204 ± 0.001	0.307 ± 0.002

PM23-32OI (1.51g)

100x	30.78	0.0097 ± 0.0010	0.0405 ± 0.0008	0.204 ± 0.002	0.204 ± 0.002	0.308 ± 0.004
500x	35.28	0.0068 ± 0.0009	0.0406 ± 0.0011	0.203 ± 0.003	0.202 ± 0.002	0.306 ± 0.002
1000x	19.36	0.0055 ± 0.0015	0.0412 ± 0.0018	0.204 ± 0.003	0.203 ± 0.002	0.306 ± 0.004
2000x	13.84	0.0068 ± 0.0015	0.0409 ± 0.0009	0.206 ± 0.003	0.203 ± 0.005	0.305 ± 0.005
Total	99.25	0.0075 ± 0.0006	0.0407 ± 0.0006	0.204 ± 0.001	0.203 ± 0.001	0.306 ± 0.002

Table S4. Xenon concentrations (in cm³STP/g) and isotopic ratios measured in peridotites from Southern Patagonia by crushing experiments. Numbers in parentheses indicate 1σ errors in the last digits.

Samples	¹³² Xe	¹²⁸ Xe	¹²⁹ Xe	¹³⁰ Xe	¹³¹ Xe	¹³⁴ Xe	¹³⁶ Xe
	[×10 ⁻¹³]	Normalized to ¹³² Xe					
Laguna Ana (PAVF)							
PM14-3WR (1.1g)							
100x	0.38	0.0819(146)	0.9614(594)	0.1491(030)	0.8196(086)	0.3805(044)	0.3269(012)
500x	1.40	0.0775(090)	0.9878(341)	0.1603(009)	0.7820(046)	0.3933(029)	0.3371(022)
1000x	2.06	0.0671(055)	0.9687(429)	0.1598(013)	0.7907(016)	0.3917(013)	0.3420(017)
2000x	3.44	0.0746(050)	0.9778(176)	0.1568(003)	0.7942(017)	0.4032(023)	0.3315(012)
2000'x	2.31	0.0786(060)	0.9743(207)	0.1570(008)	0.7999(023)	0.4009(014)	0.3378(016)
2000''x	2.31	0.0708(118)	0.9685(458)	0.1491(018)	0.8072(035)	0.3886(047)	0.3471(019)
Total	11.90	0.0739(033)	0.9740(140)	0.1560(005)	0.7966(012)	0.3960(012)	0.3379(007)
PM14-4WR (1.13g)							
100x	0.54	0.0841(150)	1.0345(247)	0.1740(022)	0.8068(056)	0.4036(030)	0.3457(030)
500x	2.12	0.0771(057)	1.0465(177)	0.1556(006)	0.7911(019)	0.4059(007)	0.3570(020)
1000x	2.01	0.0788(058)	1.0584(145)	0.1544(007)	0.7936(026)	0.4097(018)	0.3612(022)
2000x	2.85	0.0752(036)	1.0508(198)	0.1599(009)	0.7617(020)	0.4056(015)	0.3562(010)
2000'x	1.91	0.0827(093)	1.0770(287)	0.1538(013)	0.8044(032)	0.4231(022)	0.3724(018)
2000''x	2.02	0.0742(045)	1.0436(428)	0.1505(008)	0.7633(022)	0.4131(027)	0.3538(019)
2000'''x	1.24	0.0768(054)	1.0512(271)	0.1491(017)	0.7781(030)	0.3926(012)	0.3590(018)
2000''''x	1.41	0.0741(072)	1.0374(280)	0.1460(016)	0.7968(031)	0.4219(027)	0.3623(020)
2000''''x	0.71	0.0791(128)	1.0572(524)	0.1481(019)	0.7667(073)	0.4252(022)	0.3547(034)
Total	14.81	0.0773(022)	1.0521(096)	0.1542(004)	0.7826(010)	0.4108(007)	0.3593(007)
PM14-15WR (1.14g)							
100x	1.45	0.0648(051)	0.9916(243)	0.1422(012)	0.7619(033)	0.3829(024)	0.3422(028)
500x	6.08	0.0727(041)	1.0179(211)	0.1538(009)	0.7902(025)	0.3971(014)	0.3567(010)
1000x	4.69	0.0735(042)	1.0474(136)	0.1549(005)	0.7885(022)	0.4179(017)	0.3661(011)
2000x	5.95	0.0725(042)	1.0426(119)	0.1500(005)	0.7942(006)	0.4105(008)	0.3622(012)
2000'x	3.23	0.0757(056)	1.0516(179)	0.1549(006)	0.7864(010)	0.4108(020)	0.3561(016)
2000''x	2.51	0.0755(060)	1.0346(218)	0.1585(009)	0.7804(020)	0.4072(014)	0.3605(016)
2000'''x	1.90	0.0692(082)	1.0060(311)	0.1458(008)	0.7661(022)	0.3930(014)	0.3521(014)
Total	25.82	0.0727(019)	1.0324(074)	0.1386(003)	0.7860(008)	0.4055(006)	0.3589(005)
PM14-15Ol (1.5g)							
100x	0.45	0.0720(058)	0.9898(540)	0.1570(018)	0.8119(084)	0.3918(022)	0.3246(039)
500x	1.49	0.0707(084)	1.0197(341)	0.1576(011)	0.8007(028)	0.4096(011)	0.3574(023)
1000x	2.79	0.0743(076)	1.0094(262)	0.1492(007)	0.7700(032)	0.4000(017)	0.3388(014)
2000x	2.66	0.0705(053)	1.0171(264)	0.1499(007)	0.7909(015)	0.3966(010)	0.3562(007)
2000'x	1.92	0.0711(056)	1.0323(407)	0.1546(011)	0.7824(027)	0.4017(027)	0.3532(014)
2000''x	1.13	0.0752(117)	1.0359(479)	0.1535(011)	0.7746(026)	0.3964(023)	0.3364(024)
2000'''x	0.92	0.0735(106)	0.9943(636)	0.1460(016)	0.7984(059)	0.4217(039)	0.3570(033)
Total	11.35	0.0723(030)	1.0171(142)	0.1519(004)	0.7854(012)	0.4018(008)	0.3482(007)
Laguna Timone (PAVF)							
PM18-21WR (1.11g)							
100x	0.31	0.0858(187)	0.9787(341)	0.1560(023)	0.7388(052)	0.3814(043)	0.3228(029)
500x	0.91	0.0680(086)	0.9976(401)	0.1415(019)	0.7690(072)	0.3744(025)	0.2962(020)
1000x	1.01	0.0660(102)	0.9720(513)	0.1459(017)	0.7613(050)	0.3868(013)	0.3255(022)
2000x	0.97	0.0691(124)	0.9901(429)	0.1406(011)	0.7701(037)	0.3866(029)	0.3474(035)
2000'x	0.50	0.0697(162)	1.0202(541)	0.1457(017)	0.7896(062)	0.3649(047)	0.2731(027)
Total	3.69	0.0695(055)	0.9901(220)	0.1442(008)	0.7674(026)	0.3803(013)	0.3168(013)
PM18-23WR (1.15g)							
100x	2.57	0.0688(041)	0.9724(436)	0.1557(010)	0.8049(022)	0.3822(018)	0.3268(008)
500x	5.73	0.0723(042)	0.9936(107)	0.1556(009)	0.7925(016)	0.3860(012)	0.3376(011)
1000x	8.43	0.0744(035)	1.0109(256)	0.1576(005)	0.8020(019)	0.3983(010)	0.3479(011)
2000x	21.27	0.0744(024)	0.9885(107)	0.1562(004)	0.7936(011)	0.3897(005)	0.3361(004)
2000'x	17.33	0.0752(029)	0.9892(114)	0.1542(005)	0.7925(013)	0.3950(006)	0.3381(005)
2000''x	21.79	0.0739(032)	0.9757(079)	0.1537(004)	0.7847(008)	0.3933(006)	0.3395(006)
2000'''x	14.78	0.0730(031)	0.9797(131)	0.1537(004)	0.7905(013)	0.3923(007)	0.3354(009)

Total	91.91	0.0739(013)	0.9861(051)	0.1549(002)	0.7918(005)	0.3923(003)	0.3381(003)
PM18-35WR (1.51g)							
100x	3.34	0.0699(061)	1.0009(148)	0.1538(010)	0.7964(024)	0.3912(007)	0.3427(012)
500x	3.89	0.0753(061)	1.0105(164)	0.1543(012)	0.7890(022)	0.3993(010)	0.3427(012)
1000x	2.43	0.0706(139)	1.0326(297)	0.1526(012)	0.7890(024)	0.4059(016)	0.3445(012)
2000x	2.43	0.0731(038)	1.0130(300)	0.1536(013)	0.8007(032)	0.3918(015)	0.3466(017)
2000'x	1.23	0.0718(099)	1.0150(436)	0.1593(020)	0.7709(044)	0.3805(026)	0.3271(017)
Total	13.33	0.0724(036)	1.0130(106)	0.1542(006)	0.7913(012)	0.3954(006)	0.3436(006)
PM18-23OI (1.5g)							
100x	1.35	0.0813(098)	0.9809(315)	0.1534(016)	0.7721(023)	0.3845(032)	0.3337(019)
500x	1.35	0.0726(135)	0.9860(255)	0.1474(011)	0.7911(043)	0.3967(020)	0.3478(016)
1000x	1.70	0.6842(134)	0.9855(271)	0.1578(008)	0.7568(013)	0.3826(017)	0.3124(020)
2000x	1.77	0.0760(060)	0.9885(284)	0.1615(009)	0.7967(026)	0.3986(024)	0.3459(021)
2000'x	0.73	0.0717(189)	1.0298(457)	0.1607(014)	0.7805(046)	0.3966(031)	0.3542(024)
2000''x	0.51	0.0723(089)	0.9692(332)	0.1362(018)	0.7585(050)	0.3739(022)	0.3326(038)
Total	7.41	0.2151(129)	0.9887(128)	0.1548(005)	0.7778(013)	0.3901(010)	0.3207(009)
Gobernador Gregores (GG)							
PM23-1WR (1.13g)							
100x	3.67	0.0764(031)	0.9954(287)	0.1560(011)	0.7804(026)	0.3938(018)	0.3374(015)
500x	7.47	0.0774(048)	1.0058(112)	0.1565(006)	0.7919(008)	0.3995(010)	0.3443(008)
1000x	3.85	0.0758(058)	1.0131(212)	0.1557(011)	0.7775(021)	0.4032(009)	0.3416(011)
2000x	2.81	0.0792(066)	1.0053(223)	0.1611(004)	0.7928(018)	0.3950(025)	0.3466(014)
2000'x	2.10	0.0741(057)	0.9972(350)	0.1534(007)	0.7905(022)	0.3879(019)	0.3406(019)
2000''x	1.41	0.0687(061)	1.0063(300)	0.1530(010)	0.7947(023)	0.3988(018)	0.3374(023)
2000'''x	0.98	0.0655(107)	1.0083(545)	0.1558(013)	0.7789(036)	0.3923(028)	0.3474(024)
Total	22.29	0.0758(023)	1.0046(088)	0.1563(003)	0.7871(007)	0.3972(006)	0.3424(005)
PM23-32WR (1.15g)							
100x	0.93	0.0758(096)	1.0163(415)	0.1423(018)	0.8157(031)	0.4036(027)	0.3502(027)
500x	1.98	0.0719(070)	0.9910(317)	0.1587(010)	0.8080(021)	0.3994(016)	0.3367(010)
1000x	3.34	0.0730(036)	0.9809(259)	0.1559(012)	0.7765(027)	0.4023(018)	0.3388(011)
2000x	2.89	0.0729(075)	1.0093(245)	0.1474(011)	0.7952(030)	0.4037(016)	0.3477(009)
2000'x	1.74	0.0709(093)	1.0395(269)	0.1416(008)	0.7591(061)	0.3840(025)	0.3239(027)
2000''x	0.93	0.0761(068)	0.9941(389)	0.1503(010)	0.7757(025)	0.4125(030)	0.3442(014)
Total	11.80	0.0729(029)	1.0020(124)	0.1507(005)	0.7868(015)	0.4004(009)	0.3399(006)
PM23-34WR (1.23g)							
100x	0.14	0.0766(267)	0.9508(803)	0.1658(037)	0.7800(131)	0.4218(053)	0.3235(065)
500x	0.38	0.0709(110)	1.0388(539)	0.1569(022)	0.7720(064)	0.3964(051)	0.2699(031)
1000x	0.91	0.0634(100)	0.9704(330)	0.1422(022)	0.8074(037)	0.3869(009)	0.3113(017)
2000x	1.45	0.0760(070)	1.0028(395)	0.1503(011)	0.7891(027)	0.4148(036)	0.3410(014)
2000'x	0.82	0.0646(127)	0.9985(216)	0.1419(021)	0.7809(049)	0.3932(016)	0.3496(029)
2000''x	0.58	0.0757(076)	0.9575(337)	0.1624(012)	0.7942(077)	0.3911(041)	0.3191(025)
2000'''x	0.71	0.0723(084)	1.0231(722)	0.1402(013)	0.8048(034)	0.3739(036)	0.3328(035)
2000''''x	0.23	0.0616(216)	1.0501(844)	0.1548(028)	0.8105(118)	0.3855(033)	0.3398(054)
2000''''x	0.16	0.0876(249)	1.0404(737)	0.1751(031)	0.8246(110)	0.3815(060)	0.3740(073)
Total	5.38	0.0710(038)	0.9988(172)	0.1494(007)	0.7941(017)	0.3954(013)	0.3297(009)
PM23-1OI (1.55g)							
100x	1.02	0.0660(081)	0.9582(416)	0.1427(020)	0.7512(196)	0.3782(019)	0.3247(015)
500x	2.41	0.0696(071)	0.9863(287)	0.1551(009)	0.7993(030)	0.3847(020)	0.3403(013)
1000x	2.81	0.0707(041)	0.9798(274)	0.1513(011)	0.8023(024)	0.3875(025)	0.3391(018)
2000x	2.56	0.0716(044)	0.9833(254)	0.1612(009)	0.8071(037)	0.3979(011)	0.3399(017)
Total	8.79	0.0701(028)	0.9801(147)	0.1542(006)	0.7970(028)	0.3887(010)	0.3381(009)
PM23-32OI (1.51g)							
100x	1.26	0.0700(079)	1.0054(278)	0.1636(013)	0.8049(029)	0.3950(022)	0.3326(019)
500x	3.31	0.0727(033)	0.9838(227)	0.1497(004)	0.7890(015)	0.3950(013)	0.3322(010)
1000x	2.07	0.0780(098)	0.9793(371)	0.1525(010)	0.7930(031)	0.3975(027)	0.3425(017)
2000x	1.69	0.0732(094)	0.9797(548)	0.1549(008)	0.7784(029)	0.3940(018)	0.3211(011)
Total	8.34	0.0737(036)	0.9851(175)	0.1536(004)	0.7903(012)	0.3954(010)	0.3327(007)

Table S5. Sample location and lithologies.

Locality	Sample name	Rock type	Hydrous phase
Laguna Ana (PAVF)			
	PM14-1	Spinel lherzolite	-
	PM14-3	Garnet-spinel lherzolite	-
	PM14-4	Spinel lherzolite	-
	PM14-5	Spinel lherzolite	-
	PM14-6	Spinel lherzolite	-
	PM14-7	Spinel lherzolite	-
	PM14-14	Garnet-spinel lherzolite	pargasite
	PM14-15	Garnet-spinel harzburgite	-
	PM14-17	Spinel lherzolite	-
	PM14-19	Spinel lherzolite	-
Laguna Timone (PAVF)			
	PM18-2	Spinel lherzolite	-
	PM18-11	Garnet-spinel lherzolite	pargasite
	PM18-13	Garnet-spinel lherzolite	pargasite
	PM18-17	Garnet-spinel harzburgite	phlogopite
	PM18-19	Garnet-spinel lherzolite	pargasite
	PM18-21	Garnet-spinel lherzolite	-
	PM18-22	Garnet-spinel lherzolite	-
	PM18-23	Garnet-spinel harzburgite	-
	PM18-35	Spinel lherzolite	-
	PM18-36	Garnet-spinel lherzolite	pargasite/phlogopite
Gobernador Gregores (GG)			
	PM23-1	Spinel lherzolite	pargasite
	PM23-2	Spinel lherzolite	phlogopite
	PM23-4	Spinel lherzolite	phlogopite
	PM23-5	Spinel lherzolite	-
	PM23-6	Wehrlite	pargasite/phlogopite
	PM23-7	Wehrlite	pargasite/phlogopite
	PM23-11	Spinel lherzolite	pargasite/phlogopite
	PM23-14	Spinel lherzolite	pargasite/phlogopite
	PM23-15	Spinel lherzolite	-
	PM23-17	Wehrlite	pargasite
	PM23-18	Spinel lherzolite	-
	PM23-20	Spinel lherzolite	-
	PM23-31	Spinel lherzolite	-
	PM23-32	Spinel lherzolite	-
	PM23-34	Wehrlite	pargasite

Table S6. Mantle source compositions.

	$^{21}\text{Ne}/^{22}\text{Ne}_{(\text{E})}$	$^{40}\text{Ar}/^{36}\text{Ar}_{(\text{E})}$	$^3\text{He}/^{22}\text{Ne}$	$^{36}\text{Ar}/^{22}\text{Ne}$
PM14-3	0.090 ± 0.002	31800^{+9700}_{-6600}	13.15 ± 0.30	14.76 ± 0.09
PM14-4	0.071 ± 0.001	21900^{+2900}_{-1900}	9.01 ± 0.17	3.29 ± 0.02
PM14-15	0.091 ± 0.002	54000^{+14200}_{-9600}	13.63 ± 0.16	15.06 ± 0.09
PM18-21	0.087 ± 0.002	35500^{+22100}_{-10700}	12.53 ± 0.30	15.06 ± 0.09
PM18-23	0.091 ± 0.003	36800^{+10500}_{-7300}	13.66 ± 0.18	17.87 ± 0.09
PM18-35	0.085 ± 0.001	31100^{+9400}_{-6800}	12.03 ± 0.16	12.03 ± 0.15
PM23-1	0.065 ± 0.002	8100^{+1400}_{-700}	8.39 ± 0.26	9.66 ± 0.06
PM23-32	0.075 ± 0.001	14700^{+3000}_{-2200}	10.44 ± 0.15	25.26 ± 0.13
PM23-34	0.079 ± 0.001	17700^{+4400}_{-3100}	11.27 ± 0.16	24.85 ± 0.13

Table S7. Rb-Sr, Sm-Nd and Pb-Pb isotopic data for selected Patagonian peridotites analyzed in this study. Numbers in parentheses indicate 2σ errors in the last digits. WR = whole-rock, Opx = orthopyroxene, Cpx = clinopyroxene, Phlog = phlogopite.

<i>Pali-Aike Volcanic Field</i>					
Samples	PM18-17WR	PM18-17Opx	PM18-17Cpx	PM18-17Phlog	PM18-21WR
Rb (ppm)	0.21	0.33	0.44	22.09	0.49
Sr (ppm)	2.94	7.02	50.61	35.17	20.25
$^{87}\text{Rb}/^{86}\text{Sr}$	0.2064	0.1359	0.0252	1.8289	0.0699
$^{87}\text{Sr}/^{86}\text{Sr}$	0.702938(05)	0.702811(18)	0.702909(03)	0.703259(07)	0.702896(14)
Sm (ppm)	0.16	0.57	0.99	0.09	0.48
Nd (ppm)	0.51	1.35	5.96	0.42	1.34
$^{147}\text{Sm}/^{144}\text{Nd}$	0.1888	0.2548	0.1003	0.1281	0.2162
$^{143}\text{Nd}/^{144}\text{Nd}$	0.512949(09)	0.512993(15)	0.512976(16)	0.512847(12)	0.512933(14)
ϵNd	6.1	6.9	6.6	4.1	5.8
$^{206}\text{Pb}/^{204}\text{Pb}$	19.0939(52)	18.3083(20)	18.2732(24)	19.0534(81)	18.5114(32)
$^{207}\text{Pb}/^{204}\text{Pb}$	15.7246(43)	15.5828(17)	15.4276(20)	15.6127(70)	15.5339(28)
$^{208}\text{Pb}/^{204}\text{Pb}$	38.4275(11)	38.0979(52)	37.9431(51)	38.5583(56)	38.0055(67)
<i>Pali-Aike Volcanic Field</i>			<i>Gobernador Gregores</i>		
Samples	PM18-23WR	PM18-35WR	PM23-01WR	PM23-32WR	PM23-34WR
Rb (ppm)	0.19	0.20	0.24	0.18	0.40
Sr (ppm)	5.56	8.78	261.06	224.92	221.85
$^{87}\text{Rb}/^{86}\text{Sr}$	0.0982	0.0655	0.0026	0.0024	0.0052
$^{87}\text{Sr}/^{86}\text{Sr}$	0.703085(11)	0.703006(05)	0.703079(14)	0.703125(08)	0.703158(10)
Sm (ppm)	0.11	0.19	7.64	5.40	4.79
Nd (ppm)	0.55	0.75	26.03	27.78	28.38
$^{147}\text{Sm}/^{144}\text{Nd}$	0.1165	0.1503	0.1775	0.1176	0.1021
$^{143}\text{Nd}/^{144}\text{Nd}$	0.512915(08)	0.512935(14)	0.512900(12)	0.512895(16)	0.512892(11)
ϵNd	5.4	5.8	5.1	5.0	5.0
$^{206}\text{Pb}/^{204}\text{Pb}$	18.2943(23)	18.6360(11)	17.9895(28)	18.1584(21)	18.2161(44)
$^{207}\text{Pb}/^{204}\text{Pb}$	15.5631(21)	15.6176(98)	15.3436(25)	15.3701(87)	15.3974(95)
$^{208}\text{Pb}/^{204}\text{Pb}$	38.0372(50)	38.5939(23)	37.5346(58)	37.6538(32)	37.9016(71)